Multiscale Investigation and Resistivity-based Durability Modeling of EShC Containing Crystalline Admixtures

by

Pejman Azarsa

B.Sc., Azad University of Mashhad, 2009

M.Sc., Shahrood University of Technology, 2012

MEng., Illinois Institute of Technology, 2014

A Dissertation Submitted in Partial Fulfillment of the Requirements for the Degree of

DOCTOR OF PHILOSOPHY

in the Department of Civil Engineering

University of Victoria

Supervisory Committee

Multiscale Investigation and Resistivity-based Durability Modeling of EShC Containing Crystalline Admixtures

by

Pejman Azarsa

B.Sc., Azad University of Mashhad, 2009

M.Sc., Shahrood University of Technology, 2012

MEng., Illinois Institute of Technology, 2014

Supervisory Committee

Dr. Rishi Gupta, Supervisor

Department of Civil Engineering

Dr. Phalguni Mukhopadhyaya, Departmental Member, Supervisory Committee

Department of Civil Engineering

Dr. Caterina Valeo, Outside Member, Supervisory Committee

Department of Mechanical Engineering

Dr. Alexandre Brolo, Outside Member, Supervisory Committee

Department of Chemistry

Abstract

Supervisory Committee

Dr. Rishi Gupta, Supervisor

Department of Civil Engineering

Dr. Phalguni Mukhopadhyaya, Departmental Member, Supervisory Committee

Department of Civil Engineering

Dr. Caterina Valeo, Outside Member, Supervisory Committee

Department of Mechanical Engineering

Dr. Alexandre Brolo, Outside Member, Supervisory Committee

Department of Chemistry

It is well-known that concrete permeability is a good indicator of its expected durability until it remains uncracked. However, in various stages of its service life, different types of cracking in concrete can be developed due to exposure to different deterioration processes such as early plastic shrinkage or chloride-induced reinforcement corrosion. Although these cracks may not endanger concrete's structural performance from the mechanical point of view, they create a pathway for aggressive ions that can initiate degradation processes, lead to increase in concrete permeability and thus reduce its durability. Cracking in concrete might not be preventable, but its capability to naturally seal small cracks, named autogenous self-healing (SH), provides an additional feature to manufacture more durable concrete structures. However, natural self-healing capability of concrete is limited and therefore it is typically omitted in the design of concrete structures. Hence, more attention has been recently paid to Engineered Self-healing Concrete (EShC) which is associated with artificially triggered healing mechanisms into the cementitious matrix by incorporating various substances such as crystalline products. EShC helps in reducing concrete permeability; thus, increasing its service-life and durability. Due to formation of needle-shaped pore-blocking crystals, Crystalline Admixtures (CA), as a candidate from the Permeability-Reducing Admixtures (PRA) category, can be implemented into concrete mixtures to fabricate EShC concretes. Crystalline waterproofing technology is not new, but still is unknown to many researchers, engineers, and construction industry professionals. The lack of knowledge of its microstructure and self-healing properties

limits CA's proper usage in the construction industry. The techniques to assess the self-healing capability of mortar and concrete are not well-standardized yet. No research work has been done to address certain durability characteristics of this material (i.e. electrical resistivity (ER) or chloride diffusivity) especially when combined with Supplementary Cementitious Materials (SCM) and Portland Limestone Cement (PLC). Since the resistance of concrete against ions' penetration is a function of its permeability, it might be a straightforward and reliable parameter to rapidly evaluate concrete's durability during its intended service life. Hence, electrical resistivity measurement is considered as an indirect and alternative tool for other time-consuming permeability testing techniques to examine the CA's efficiency as it modifies the concrete's microstructure by crystals' deposition; thus, leads to permeability improvement.

In comparison to previous studies, on a larger scale, this thesis aims to systematically study the effects of CA on the microstructural features, self-healing properties and long-term durability and resistivity of cement-based materials and in addition, draw some comprehensive conclusions on the use of CA in new and repair applications. This study is divided into three major phases to propose all-inclusive work on using CA in construction industry. To satisfy the goals of each individual phase, a test matrix consisting of a series of four mixes with variables such as use of PLC or presence of CA in powder form is considered.

In order to address to the lack of research and industry knowledge discussed above, this PhD thesis includes the following phases: **Phase (I)** In this phase, the main focus is on the microstructural properties and the changes in the pore structure and chemical compositions of the cement phase of mortar mixes when treated with CA. These microstructural features are studied using Scanning Electron Microscope (SEM) and Scanning Transmission Electron Holography Microscope (STEHM). Moreover, physical and chemical characteristics of the hydration products are determined using image analysis and Energy Dispersive X-ray (EDX) Spectroscopy, respectively. **Phase (II)** This phase is allocated to macro-level investigation of durability characteristics such as chloride/water permeability and electrical resistivity of concrete structures containing CA and PLC cement. To non-destructively measure the chloride ion concentration in the field conditions, both changes in corrosion potential of rebars and concrete electrical resistivity in treated circular hollow-section steel reinforced columns exposed to simulated marine environment is monitored and compared over a 2-year period with control samples. In addition, laboratory-size concrete samples are studied to investigate the effects of CA presence on long-term resistivity, rapid chloride permeability, water permeability and chloride diffusivity of concrete. Later, a resistivity-based model is developed to predict long-term performance of concretes incorporating slag or metakaolin, studied in various environmental conditions. The long-term goal of this phase is to develop a standard design guideline and durability-based model. **Phase (III)** Using an innovative self-healing testing method [1], quantitative analysis of crack

closure ability and self-healing potential of CA treated and control concretes with OPC or PLC cement is accomplished during this phase.

The obtained results from first phase showed that hydrated CA particle revealed fine, compact, homogenous morphology examined by STEHM and its diffraction pattern after water-activation indicated nearly amorphous structure, however, diffuse rings, an evidence for short-range structural order and sub-crystalline region, were observed which requires further investigation. The SEM micrographs taken from specimen's fractured surface showed formation of pore-blocking crystals for all treated mixes while similar spots in un-treated sections were left uncovered. Although needle-shaped crystals were observed in the treated mortar specimens, but not all of them had shapes and chemical compositions other than ettringite (well-known to form needle-like crystals). Using backscatter SEM images and EDX spectrums, examination of polished mortar sections with and without CA also showed typical hydration phases, forming in the control system.

Results from phase II showed that concretes treated with CA had almost 50% lower water penetration depth and thus smaller permeability coefficient when compared with the virgin OPC or PLC concretes. According to salt ponding test results, the use of CA helped in enhancing the resistance to chloride penetration compared to control concrete. This improvement increases with increasing in concrete age. Strong linear relationship between Surface Resistivity (SR) and Bulk Resistivity (BR) data was observed which indicates that these test methods can be used interchangeably. The presence of SCM in concrete indicated considerable increase in both SR and BR compared to control concrete. Concretes incorporating slag or metakaolin have tendency to react more slowly (or rapidly in MK case), consume calcium hydroxide over time, form more Calcium Silicate Hydrate (C-S-H) gel, densify internal matrix, and also reduce OH- in the pores' solution; thus, increase concrete electrical resistivity. For laboratory specimens, environmental conditions such as temperature variation and degree of water saturation indicated considerable effects on electrical resistivity measurements. As temperature or water content of concrete decreases, its electrical resistivity greatly increases by more than 2-3 times from reference environmental condition. This is mostly because of variation or accessibility in electron mobility. Experimental results from field investigation showed that electrical resistivity readings were highly influenced by the presence of rebar and concrete moisture conditions. In addition, concrete cover thickness and CA addition into cementitious matrix had a negligible effect on its resistivity.

In the last phase, an optical microscope was used to measure the average crack width. OPC samples had an average measured crack width of 0.244 mm as compared to 0.245 mm for OPC-CA, 0.251 mm for PLC, and 0.247 mm for PLC-CA. Self-healing test results also showed 90% self-healing ratio for CA modified mix within few days after starting experiment. Addition of CA into the mix led to higher rates of healing

and full crack closure (width up to 250 µm) when compared to reference concrete. An empirical equation that relates water initial flow rate to the crack width ($Q \propto CW^3$) was also proposed in this phase. Presence of PLC and CA in the mixture resulted in positive improvement in crack-closing capability and self-healing ratio.

Table of Contents

List of Figures

List of Tables

Glossary

Abbreviation or Symbol	Definition
BD	Bulk Diffusion
BR	Bulk Resistivity
CA	Crystalline Admixtures
CH	Calcium Hydroxide
CSA	Calcium Sulfo-Aluminate
C-S-H	Calcium Silicate Hydrate
ECC	Engineered Cementitious Composite
E_{corr}	Corrosion Potential
EShC	Engineered Self-healing Concrete
EVA	Ethylene Vinyl Acetate
FA	Fly Ash
FIB	Focused Ion Beam
GGBS	Ground Granulated Blast-furnace Slag
HCP	Half-cell Potential
HPFRCC	High Performance Fiber Reinforced Cementitious Composite
MK	Metakaolin
NSC	Normal Strength Concrete
OPC	Ordinary Portland Cement
PC	Polycarbonate
PF	Polyethylene Fiber
PLC	Portland Limestone Cement
PMC	Polymer Modified Concrete
PVA	Poly Vinyl Alcohol
RCM	Rapid Chloride Migration
RCP	Rapid Chloride Permeability
SAP	Super Absorbent Polymer
SCM	Supplementary Cementitious Materials
SEM	Scanning Electron Microscope
SH	Self-healing
SR	Surface Resistivity
STEHM	Scanning Transmission Electron Holography Microscope
UPV	Ultrasonic Pulse Velocity
w/c	Water to cement ratio

Acknowledgment

First and foremost, I would like to express my special appreciation and thanks to my advisor Dr. Rishi Gupta, who has been a tremendous mentor for me. I appreciate all his contributes of time, ideas and funding to make my PhD experience productive and stimulating. I would like to thank him for encouraging my research and for allowing me to grow as a research scientist. His advice on both research as well as on my career have been invaluable. The joy and enthusiasm he has for research was contagious and motivational for me, even during tough times in the PhD pursuit. In addition to our academic collaboration, I greatly value the close personal rapport that Dr. Rishi and I have forged over the years. I quite simply cannot imagine a better advisor.

For this dissertation, I would like to thank my reading committee members: Dr. Phalguni Mukhopadhyaya, Dr. Caterina Valeo, and Dr. Alexandre Brolo for their time, interest, and helpful comments. I would also like to thank my oral defense committee member, Dr. Meghdad Hoseini, for his time and valuable feedback on a draft version of my thesis. I also want to thank you for letting my defense be an enjoyable moment, and for your brilliant comments and suggestions. I would also thank Dr. Elaine Humphery for her helpful guidance on the SEM and Dr. Arthur Blackburn for his support and advice on the TEM. Among many other things, I am thankful to both technician and administrative teams in Civil engineering department, especially Dr. Armando Tura and Matt Walker for their endless supports in providing any demand.

I gratefully acknowledge the funding sources that made my PhD work possible. The members of the Kryton Inc. group have contributed immensely to my personal and professional time at UVic, especially Mr. Alireza Biparva who played a crucial role in my academic career.

My time at UVic was made enjoyable in large part due to the many friends and groups that became a part of my life. I am grateful for time spent with Peiman Azarsa, Dr. Armando Tura, Adham El-Newihy, Laura Simandl, Dr. Mohit Garg, Harsh Rathod, Boyu Wang, Amir Salar Salehi, Kaveh Nazeri, Sara Daneshvar and Vahid Ahsani as I finished up my degree and for many other people and memories.

I am deeply thankful to my family, words cannot express how grateful I am to my parents and brothers (Pouya and Pedram) for their love, encouragement and all the sacrifices you did on my behalf. For my parents who raised me with love of science and supported me in all pursuits. For the presence of my brother, Peiman, at UVic for two of my years here. Thank you! Without them this thesis would never have been written.

Pejman Azarsa

University of Victoria

September 2018

Chapter 1 Introduction

1.1 Research Motivation

Concrete is the most widely used construction and building material all over the world due to its high compressive strength, relatively low cost, easy-forming ability. Permeability of concrete is a good indicator of its quality and durability although it is generally sensitive to crack formation at micro and macro levels. As long as a crack is not formed, the permeability of concrete is relatively low but cracking in concrete is inevitable. Cracks can be introduced into concrete due to many factors such as drying shrinkage, plastic shrinkage, service loading, limited tensile strength. Development of cracks into the concrete matrix create pathways for aggressive agents such as chlorides to endanger the structural durability and service life. Specifically, in the steel reinforced concrete structures, as cracks grow wider, chance of reinforcement exposure to harsh environments gets higher. As soon as the reinforcement begins to corrode due to carbonation or chloride ingress, the resulting rust occupies a greater volume than the steel. This expansion creates tensile stresses in concrete, which can eventually cause additional cracking, delamination, spalling and structural collapse. Hence, it is essential to monitor, control and repair concrete cracks; however, repairing cracks is not always a feasible task as cracks are not visible or accessible. As reported, costs related to repair works are also equal to half of the annual construction budget in Europe [2]. In the USA, the annual cost for maintaining existing bridges is around $5.2 billion [3], while in the UK, nearly 45% of the budget allocated for the construction industry is spent for repair and maintenance applications [4]. Furthermore, indirect costs are associated with concrete crack repair works due to loss in production and traffic jam occurrence. Although cracks in concrete may not be preventable, the inherent ability of concrete to heal itself to a certain level increases its service-life, thus making this material highly beneficial. This time dependent phenomenon is called “self-healing” of concrete.

Self-Healing (SH) is a significant topic of interest in engineering. However, studies related to it in the concrete world, have only started to appear in the last two decades. In concrete, there are various SH mechanisms including (1) on-going hydration; (2) calcium carbonate ($CaCO_3$) precipitation; (3) swelling

of cement matrix; (4) sedimentation of debris and loose cement particles in presence of water (5) admixture effect. In young concrete, continued hydration is the dominant healing mechanism because of its fairly high content of un-hydrated cement particles whereas calcite formation ($CaCO_3$) becomes the main mechanism at a later age. Different SH mechanisms which can initiate simultaneously are highly dependent upon the concrete age at the time of cracking. Based on the healing mechanisms, approaches to SH in concrete can be classified broadly into two main groups, namely autogenous healing and autonomous healing. Autogenous crack healing in concrete refers to SH properties resulting from the chemical and/or physical composition of cementitious matrix and is only effective for small crack widths up to 200 μm [5]. On other hand, autonomous crack healing is associated with artificially triggered mechanisms into the cementitious matrix and is presented mainly by some chemical or biological agents. Due to the small crack width closure, autogenous healing is not a reliable phenomenon to achieve noticeable healing effects. Hence, in recent years, greater attention has been paid to engineered healing concepts such as the use of microencapsulated healing agents [6]–[9], bacterial concrete [6], [10]–[13] or the use of crystalline admixtures [14]–[20].

Crystalline Admixtures (CA) are a type of Permeability Reducer Admixtures (PRAs) as described by the American Concrete Institute (ACI) Committee 212 [21]. Contrary to properties of hydrophobic or water-repellent materials, these products are hydrophilic which makes them react easily when moisture enters into the pores/cracks of concrete. After this reaction takes place, CA forms water insoluble pores/cracks blocking crystals that create very low permeability concrete due to increase in density of Calcium Silicate Hydrate (CSH, main cement hydration product) and higher resistance to water penetration. The matrix component which reacts is tri-calcium silicate (C_3S) and presence of water is also essential for the reaction. Depending on the crystalline promoter and a precipitate formed from calcium and water molecules, active chemicals contained in cement and sand form these products. As a result of crystalline depositions into concrete matrix, pressure resistance of modified matrix increases as high as 14 bars [21]. Although the effectiveness of these admixtures as a healing agent in reducing concrete permeability is well understood, no researcher evaluated their capabilities using durability tests, macro mechanical tests, microstructural

tests, and tests at the nanostructure level simultaneously. Also, no well-standardized method has been reported for measuring SH efficiency of concrete using these products. In addition, long term durability and resistivity monitoring of these materials in concrete have not been addressed. Furthermore, the interaction of these admixtures when combined with Portland Limestone Cement (PLC), which was only introduced in the Canadian markets 6-7 years ago, is not known. Consequently, this thesis is focusing on studying the long-term effects of PLC in combination with CA on durability characteristics of concrete from Nano to Macro levels. No well-documented research study found to address microstructural features and morphological/chemical characteristics of CA-treated composites. There is no well-standardized and reliable technique to indicate how to fabricate nano-size cement-based materials and quantitively examine them using STEHM. Research and industry knowledge gap on resistivity (CA-treated system) found to grasp the correlation of electrical resistivity and other durability properties (especially for in-service field concrete elements) and to understand the effect of various parameters such as rebar or crack presence, temperature, SCM, chemical admixtures, and water saturation degree.

1.2 Dissertation Outline and Objectives

This dissertation includes the current introductory Chapter 1 that provides the context and framework and links the following Chapters based on proposed research motivation and background information.

Chapter 2 is a brief introduction and reviews the history of self-healing phenomenon and its application in cementitious materials especially for cement-based systems containing CA (section 2.1). The objective of this section is to identify gaps in the current research knowledge on self-healing capacity of cementitious materials and to also understand the effects of CA on concrete self-healing as previously reported by literature. The literature review of self-healing subject in cement-based materials helped in setting up the experiments and analyzing the data. A comprehensive literature review of electrical resistivity method for concrete durability evaluation purposes, in the form of a published peer-review journal paper [22], is presented in this chapter (section 2.2). To determine the correlation between concrete resistivity and other durability properties such as water permeability, to evaluate the influential parameters on concrete

resistivity, and to assess the applicability and current challenges in using resistivity measurement techniques were the objectives of section 2.2. This published literature review gives better insights in understanding the context of concrete resistivity, used as main investigation tool in this study.

Chapter 3 is a peer-reviewed published journal paper [23] that its objective is set to develop technique for nano-size specimen fabrication and quantitative nano-scale investigation of CA, using one of the world's highest magnification STEHM (section 3.1). Microstructural features and hydration phases of mortars treated with four types of CA, studied by SEM and EDX analysis, is also introduced in section 3.2. In this section the objective was to quantify reduction in void volume using SEM when crystalline admixtures (CA) is used and to determine various hydration phases and chemical compositions of CA- and un-treated concrete by means of EDX spectroscopy. This chapter provides better understanding on morphology, hydration products, microstructural features, and chemical elements of cement-based composites modified with CA and PLC.

Chapter 4 is a journal manuscript (currently under review) that presents the use of CA in enhancing concrete self-healing and its certain durability parameters such water permeability and electrical resistivity. Different correlations between these durability parameters are also introduced. Based on self-healing results, a simple empirical equation is presented to correlate the water flow through concrete crack and width of crack. One of the objectives was to evaluate durability parameters (e.g. water/chloride permeability) and calculate transport properties of concrete specimens containing CA and PLC. The other objective of this chapter was to analyze the influence of CA and PLC with reference to the enhancement of self-healing mechanisms and to determine crack-closing capability and water-flow reduction of concretes treated with CA.

Chapter 5 presents a journal paper (under review) on the long-term changes in electrical resistivity of concretes modified by CA, metakaolin, and slag; examined in laboratory conditions for over 2 years period. A predictive resistivity model that considers effect of curing age, temperature and water content on resistivity measurements, is also introduced. Finally, long-term durability of steel reinforced concrete columns exposed to simulated corrosive environment in the field, investigated by resistivity and half-cell

potential testing techniques, is presented in section 5.2. The targeted objectives are to assess the effectiveness of CA-treated concrete elements in corrosive field environment using various NDT techniques and to develop an empirical resistivity-based model for concretes treated with CA and SCMs considering environmental factors such as temperature and water content. Assessing efficiency of CA on concrete electrical resistivity when other minerals present; establishing a correlation between bulk and surface electrical resistivity (BR & SR) of concrete with and without CA; addressing the influence of environmental conditions on resistivity of concrete tread CA, are also the objectives of this chapter.

Chapter 6 summarizes the main results and contributions of the entire work done in this project and suggests the possible future work.

1.3 Research Contributions

There is a dire demand to develop materials that are more durable and also to advance the state of smart materials that can be autogenically healed as it is beneficial especially for inaccessible sites such as underground tunnels, dams, below grade parking, water containment tanks, sewage plants, swimming pools. It is well understood that reduction in permeability can increase the durability of cementitious materials, increasing its service life, hence making the material more sustainable. Extending the serviceable life of new and existing structures has a direct and indirect impact on the environment as it reduces the demand for natural resources required for producing world's most used construction material- "concrete". Development of durable and 'self-healing' concrete can reduce steel corrosion (major deterioration process) in RC structures, reducing the possibility of catastrophic failures in many structures.

Through this long-term study, various research aspects related to developing "crack-free" and "self-healing" materials that can increase the durability of the cementitious material is identified. Developed a comprehensive mathematical model (macro-model) for durability design would be valuable as an educational tool, and a tool for decision makers to use in designing sustainable RC structures. The development of this model will contribute to construction industry and also advance the state-of-knowledge

about smart cementitious materials. The long-term monitoring of chloride ion penetration and measurement of electrical resistivity of specimens exposed to simulated conditions also leads to better understanding of the relationship between un-cracked permeability and chloride diffusion. Considerable and fully clarified model is not found between studies published in the literature to estimate long-term changes in electrical resistivity of concrete. Even though much efforts have been made to find better understanding about resistivity of concrete and its measurement technique in the laboratory, lack of understanding in how this parameter can accurately be determined in the real-world condition is still missing. Moreover, using the highest magnification STEHM in the Advanced Microscopy Facility (AMF) at UVic proceed the comprehension about the nanostructure and microstructure of cementitious materials modified using PLC and CA. In addition, improving the quantification of the concrete self-healing property, can have a noteworthy impact in the concrete industry to get better understanding about the reduction in permeability of cracked concrete. Therefore, this improvement will be also beneficial for engineers to consider larger crack width in designing RC structures, and thus lead to major cost savings on the future construction projects.

Overall, using the developed durable and self-healing concrete, structures' service life around world can be constructively extended; thus, it can help both the environment and the economy as it decreases the consumption of resources whilst also resulting in lower building/repair costs. It can also be socially beneficial as it can prevent steel corrosion, thus leading to safer, and more reliable buildings around the nation.

Chapter 2 Literature Review

In its first part, this chapter summarizes the literature review carried out on concrete self-healing and efficiency of crystalline additives in attaining it. The objective of this section is to identify gaps in the current research knowledge on self-healing capacity of cementitious materials and to also understand the effects of CA on concrete self-healing as previously reported by literature. The second part of this chapter includes a summary of published literature on electrical resistivity of concrete [22], one parameter that affects durability and which is a partial focus of this study. To determine the correlation between concrete resistivity and other durability properties such as water permeability, to evaluate the influential parameters on concrete resistivity, and to assess the applicability and current challenges in using resistivity measurement techniques were the objectives of next section.

2.1 Self-healing capability of crystalline admixtures treated concrete

2.1.1 Self-healing methods in cementitious materials

Self-healing (SH) properties was introduced into polymer materials for the first time in Malinskii *et al.*'s work [24] where the influences of the molecular weight of a polymer and the environment on cracks SH in polyvinyl acetate was investigated. Thereafter, Dry started working on the concept of self-healing in the concrete [25] and in the polymers [26]. However, the SH concept of materials has gained recognition after 2001 when White *et al.* [27] published their paper in Nature about SH in polymer based materials. They have reported a structural polymeric material with the ability to autonomically heal cracks [27]. A microencapsulated healing agent was incorporated into the material which is released as the crack opens. In their fracture experiments, as much as 75% toughness recovery was observed [27]. Intrinsic healing, capsule-based healing, and vascular healing are the three broad groups that can present SH in cementitious materials, in accordance with approaches which originate from SH of polymers [28]. Each approach has a different mechanism to heal the cracked region.

Intrinsic SH materials exhibit SH properties due to the composition of the cementitious matrix [5]. In this approach, healing relies on autogenous healing, improved autogenous healing or reaction of the polymeric substances inside polymer modified concrete [5]. Autogenous healing mechanism as mentioned previously has disadvantages such as limited size crack width closure and moisture demand for activation. Hence, to minimize the aforementioned disadvantages, the improved autogenous healing approach relies on restricting crack width and supplying required water for the healing process. To restrict the crack width, for the first time, it was proposed to use Polyethylene Fiber (PF) reinforced strain hardening Engineered Cementitious Composite (ECC) [29]. Later, cheaper materials such as Poly Vinyl Alcohol (PVA) fibers were used for crack width restriction [30]-[31]. In addition to control crack width, several researchers attempted to provide additional water by mixing Super Absorbent Polymer (SAP) with cementitious materials [32]–[34]. SAP, also called hydrogels, are cross-linked polymers which can absorb a large amount of water and substantially swell to create a soft and insoluble gel. In highly alkaline concrete environment, hydrogels' swelling capacity reduce when mixed into fresh concrete and once crack arises, they will swell again as moisture enters via the crack. Also, in this approach, improving the possibility of ongoing hydration or crystallization can promote intrinsic healing. Continued hydration can be improved via replacing part of cement in the concrete matrix with Fly Ash (FA) and Ground-Granulated Blast-Furnace Slag (GGBFS), as high amount of these binders remain un-hydrated at later age due to their low pozzolanic reactions and thus, promote autogenous healing [35]–[39]. Addition of expansive agents, geo-materials and chemical agents that can promote the deposition of crystals inside the crack, also improves autogenous healing of concrete [40]. Furthermore, Polymer Modified Concrete (PMC), which is made by dispersion of organic polymers inside the mixing water, were investigated by Abd-Emoaty to study its healing behavior [41]. As reported, healing in PMC occurs in the same way as in conventional concrete but on a larger extent and over longer period due to availability of more un-hydrated cement [41]. Other studies conducted by Yuan *et al.* [42], [43] suggest using Ethylene Vinyl Acetate (EVA) co-polymer particles into concrete mix and once crack forms, heating the samples up to 150 °C to melt EVA particles; hence, crack can be filled and healed by adhesive flow into it. However, high temperature (150 °C) may affect concrete surface and its properties.

With a material like PMC, it seems clear that different construction procedures are needed to take advantage of the unique properties of PMC. Some failures have occurred because of incompatibility between PMC and the concrete substrate as a result of the difference in coefficients of thermal expansion coupled with a high Polycarbonate (PC) modulus of elasticity. Thermal changes can produce high shear and tensile stresses at the interface near boundaries which may cause the repair to delaminate. First, it should be understood that one of the primary limitations of polymer-modified concretes is cost. The cost of polymers can range from 10 to 100 times that of Portland cement, and even considering that the specific gravity of cement is about $2\frac{1}{2}$ times that of polymer, the cost per unit volume of polymer composites is still considerably higher than Portland cement concrete. Another limitation is its inability to withstand high temperatures, particularly fires, and therefore the materials cannot be used as the structure for buildings housing people. A third limitation is the odor and/or toxicity and/or flammability of many of the monomers and resins during construction or fabrication. While these limitations only exist for the relatively short time until curing occurs, the use of these materials can create problems of safety and/or worker discomfort which must be taken into account during construction.

Originating from self-healing of polymers, another approach to integrate self-healing inside the concrete matrix is to trigger a healing agent into discrete capsules to create capsule-based SH materials. When the capsules are ruptured, the healing agent will be released in the damage domain and through different mechanisms will promote healing ability of concrete. Some of the healing agents react upon contact with air or moisture or heating, or upon contact with cementitious matrix itself. While other agents react when contacting a second component which is present in the matrix or provided by supplementary capsules. One interesting study in this area is to encapsulate $CaCO_3$ precipitating bacterial spores and their nutrients, calcium lactate ($CaC_6H_{10}O_6$), into expanded clay particles or directly into the fresh mix [10], [11], [44]. When a crack develops into the concrete matrix, in presence of water, both spores and nutrients dissolve, resulting in activation of the bacterial pores. The bacteria-based concrete was introduced by Jonker [44] for

the first time. One disadvantage of this approach was that the expanded clay particles showed 50% decrease in compressive strength of concrete.

One approach to achieve self-healing in materials is to create vascular system inside the matrix. By creating a network of hollow tubes that connect the interior and exterior of the structure, the healing agent can be injected through the tubes to develop a vascular-based SH material. When this approach is used in combination with a one-component healing agent, a one channel vascular system is applied, while a multiple channel system is used in combination with a multi-component healing agent [5]. Mihashi *et al.* embedded two glass pipes, which were connected to an external reservoir, into concrete beams. While one tube and connected-reservoir were filled with one component of the epoxy glue, the other tube and reservoir were filled with the second component. Upon crack formation both pipes broke and both components were released resulting in a polymerization reaction. However, as both components did not mix well, the strength regain was almost similar to specimens without included any healing agent.

Up to different crack size, both "autogenic" SH (natural SH) and "autonomic" SH (engineered SH) control and repair early-stage cracks in concrete structures by preventing permeation of driving factors for deterioration in one hand, and even by providing partial recovery of mechanical properties relevant to concrete serviceability and durability [5], [45]. However, in the last two decades, a huge amount of research work has been dedicated to Engineered Self-healing Concrete (EShC) concept in various directions of investigation as mentioned above including: SH engineered with fiber reinforcement [29]–[31], [46]–[50], bacteria-based concrete [44], SAP [32]–[34], and other proprietary chemical admixtures [21] such as PRAs and various modified calcium composite materials. In all SH mechanisms, presence of water (moisture) is essential, especially in the case of chemical agents in order to promote the crystals deposition inside the crack which is accessible in most of infrastructures exposed to rain or underground water [21]. In addition to water presence, several factors have an influence on the phenomenon of SH including the mix proportion [51], both cracks stress state and their steadiness state [52], and thermal and hygrometric conditions [53], [54]. Among those aforementioned proprietary chemical admixtures, Crystalline Admixture (CA) from

PRAs category has hydrophilic nature that cause them to increase density of Calcium Silicate Hydrate (C-S-H), generate pore-blocking crystals, or both, to resist ions ingress [21]. Crystalline-based technology has been used over the past two decades in the construction industry and its effectiveness on reducing concrete permeability is well-understood; however, only limited research work has been done to analyze the effects of these admixtures to the enhancement of SH mechanisms and long-term durability.

2.1.2 Efficiency of crystalline admixtures in concrete self-healing

Awni Al-Otoom *et al*. [14] experimentally investigated a new water-based crystallization technology to reduce permeability of concrete. This technology is dependent on the formation of sodium acetate crystals inside the pores of concrete. It was reported that an optimum solution of 20 wt. % sodium acetate delivers the best minimization of water penetration into concrete without altering the physical properties of the concrete. The treatment solution only penetrated 0.5 inch from the surface. A water to cement ratio of 0.65 was considered in this study which is not practical for most applications. In their investigation, reinforcement corrosion was not also examined. Although this is the first study in this field, so many uncertainties were observed in the results which opened another research area for further investigation.

The visual closure of crack produced by various additives in mortar specimens comparing with a reference Portland mortar using fly ash, expansive admixtures, silica fume, CA and limestone powder under water immersion condition were also studied by Jaroenratanapirom and Sahamitmongkol [55], [56]. It was reported that CA improved the SH process for cracks with less than 0.05 mm width at higher rate than the other additives types; however, they became inefficient for wider cracks.

SH potential of cement-based materials incorporating Calcium Sulfo-Aluminate (CSA) based expansive additive and CA has been investigated in Sisomphon *et al*.'s study [15]. CA is a synthetic cementitious material which contains reactive silica and some crystalline catalysts, whereas CSA is a commercial product normally used for shrinkage compensation. The effects of both CSA and CA on surface crack closing ability, water tightness and microstructures of pre-cracked mortar specimens were examined in [15]. In their experimental setup, the suitable dosages were set at 1.5% and 10% by mass of total cementitious

material, for CA and CSA, respectively and disc shape specimens were cast in plastic containers with a height of about 20 mm and 75 mm diameter. After the age of 28 days, a surface crack width between 100 and 400 µm were induced into specimens which already were reinforced with galvanized wire-mesh at the mid-height to obtain a desired crack width. After applying constant water head of 100 ± 5 mm, the surface crack width was measured on 20 different locations at 0, 3, 7, 14, 28 days wetting period. As an indicator of quantitative evaluation of SH, the change of surface crack width was considered. Within 28 days test period, for control mixes and CA/CSA addition samples, it was found that surface crack up to about 150 µm width and up to 250-400 µm have been completely closed. It was observed that calcium carbonate was the major healing product for those samples with admixtures, particularly on the mouth of cracks. Moreover, since the amount of leached Ca^{+2} from matrix plays an important role on the precipitation of calcium carbonate, it was concluded that calcium ion released from CSA/CA additions was responsible for better healing performance of treated mortar. Also, it was stated that the higher pH of samples with admixtures favors the precipitation of calcium carbonate [15]. However, using concrete instead of mortar and larger specimen size which give better simulation of real-world conditions have not been considered in this study. Furthermore, various curing and exposure conditions were not examined. In this study, it was also not explored that how much mechanical properties of materials were recovered after healing process.

Ferrara *et al*. [16] studied the effects of CA on the SH of concrete and their healing capability on the recovery of mechanical properties. They evaluated the influences of the SH phenomena on the recovery of stiffness and load-bearing capacity by means of 3-point bending (3pb) test before and after conditioning [16]. In addition to that, Ultrasonic Pulse Velocity (UPV) tests and microstructural observations have been performed. In Ferrara's experimental setup [16], concrete was treated by an addition of 1% CA and cast into the slabs 1 m long × 0.5 m wide and 50 mm thick. Thereafter, slabs were cut into prismatic "beam like" specimens, each 500 mm long and about 100 mm wide and cured in a fog room for a period ranging between 35 and 42 days at 20 °C temperature, 95% Relative Humidity (RH) and under wet towels. The beam specimens were pre-cracked up to different levels of residual crack opening (100 and 200 µm) using the

three-point bending test set-up to assess the SH capacity of treated concrete. Three exposure conditions that have been examined in this study were water immersion, air exposure, and accelerated temperature cycles. For water immersion condition, it was reported that the presence of CA sped up the crack healing process and recovered the bending stiffness and load-bearing capacity of concrete. In the case of air exposure, CA treated concrete was highly effective in crack healing and in recovering of material's mechanical properties, while no reliable recovery either of material continuity nor of its mechanical behavior was observed in the absence of CA. However, for specimens in accelerated exposure condition, no definite conclusion was stated due to high dispersion of obtained results. It was also found that a crack closure above 70-80% is necessary to start recovery of stiffness and load bearing capacity [16]. Similarly, under four different exposure conditions (wet/dry cycles, humidity chamber, water immersion with/without refreshment, and air exposure), the healing effect of CA in terms of strength recovery has been studied in [57]. In contrast to previous study by Ferrara *et al*. [16], CA showed a better SH capacity under wet/dry exposure.

Using a different technique, a similar study by Roig-Flores *et al*. [17] investigated the effects of CA only on the SH of concrete in four types of environmental exposure conditions. Based on the measure of the global permeability of the specimen and different geometrical characteristics of the crack before and after the SH period, they developed a method that can evaluate the SH properties of cracked samples. In the experimental program, CA with a dosage of 4% (by the weight of cement) were considered and the crack width below 0.3 mm was induced into cylindrical specimens ($\Phi 150 \times 150$ mm) at 2 days of age. Afterward, a method based on standard water permeability test was employed to measure the water flow and the test was performed by applying a head water pressure equal to 2.00 ± 0.05 bars. Additionally, crack's geometrical parameters were measured in this study based on the composed panorama pictures showing the cracks along their length. Water Immersion (WI), Water Contact (WC), Humidity Chamber (HC), and Air Exposure (AE) were the different environmental conditions considered with the objective of simulating practical circumstances. It was reported that neither control specimens nor those with CA healed when

exposed to moist conditions. In their findings, the four exposures in order of decreasing permeability healing ratio were: WI (around 0.9) > WC (around 0.8) > HC (around 0.5) > AE (around -0.15) [17].

Following the previous study, Roig-Flores *et al*.'s [18] work analyzed the SH properties of early-age concretes, engineered using CA, by measuring the permeability of cracked samples and their crack width. Under three different exposure conditions, they also studied the SH behavior in two typically used concrete classes, one common for precast concrete elements (C45/55) and one standard class broadly used for building constructions (C30/37) [18]. In the experimental program, CA added into the matrix, in powder form, at a dosage equal to 4% by weight of cement and in addition, and steel fibers were also used to control crack width during the pre-cracking and healing stages. The range of studied crack widths was 0.1–0.4 mm. Like the pervious study by Roig-Flores *et al*. [17], in order to evaluate the SH capacity of treated concrete specimens, water permeability was analyzed using a test method based on the standard procedure in EN 12390-8 [58] to measure water depth penetration. Under water at 15 °C and especially at 30 °C, it was concluded that healing ratio was higher for CA treated specimens compared to those for control; however, the high-scattered results were observed for both treated and un-treated concrete under the wet/dry cycles exposure. The obtained results were slightly better when using CA in the high-performance concrete, mainly due to the lower scattering of results.

In a recent study by Ferrara *et al*. [19], the influences of CA on the self-healing capacity of the cementitious composites with reference to both a Normal Strength Concrete (NSC) and a High Performance Fiber Reinforced Cementitious Composite (HPFRCC) have been evaluated. In the treated mixture, a dosage of 3% CA was added and more details of their experimental program was reported similarly in [16]. The case of both NSC and HPFRCC, the CA enhances and makes more reliable the autogenous healing capacity of cementitious composites. In NSC, CA could promote up to 60% of crack sealing even under air exposure condition. In the case of HPFRCCs, which would already feature autogenous healing capacity because of their peculiar mix compositions, the synergy between the dispersed fibre reinforcement and the action of the CA has resulted in a likely 'chemical pre-stressing' of the same reinforcement, from which the recovery

of mechanical performance of the material has greatly benefited, up to levels even higher than the performance of the virgin un-cracked material.

No well-standardized self-healing testing procedure can be found to measure self-healing efficiency of concrete (e.g. modified with CA). Also, in general, quantification of healing efficiency appears to be of great significance. There is a lack of significant studies focused on the assessment approaches available for assessing the efficiency of different self-healing mechanisms. Hence, a new challenge in the area of self-healing concrete technology can be introduced as setting common grounds toward a standardized evaluation of self-healing mechanisms in concrete. Utilizing current healing agents such as SAP or bacteria is still not enough to be able to close surface crack width more than 1000 µm.

Previous research works largely focused on self-healing concepts of CA-treated concrete whereas to author's knowledge, no research work has been conducted in this area to address durability characteristics of this material (i.e. electrical resistivity or chloride diffusivity) especially when combined with Supplementary Cementitious Materials (SCM) or PLC. Since the resistance of concrete against ions' penetration is a function of its permeability (i.e. the volume fraction of pores and their structures (tortuosity), and pore solution conductivity), it is a good indicator to non-destructively assess concrete durability during its service life. Hence, electrical resistivity measurement, providing some information about the interconnected pore network, can be considered a reliable tool to investigate the crystalline admixtures' efficiency as it modifies the concrete's microstructure by crystals' deposition and improves its permeability. In the following section, a comprehensive published literature review was conducted to address current gaps between research and industry state of knowledge. To also identify the influencing parameters on resistivity measurements, this review was done.

2.2 Electrical Resistivity of Concrete for Durability Evaluation

This paper was published in the journal of Advances in Materials Science and Engineering [22].

The citation is: Pejman Azarsa and Rishi Gupta, "*Electrical Resistivity of Concrete for Durability Evaluation: A Review*," Advances in Materials Science and Engineering, vol. 2017, Article ID 8453095, 30 pages, 2017 [https://doi.org/10.1155/2017/8453095].

Author Contributions: Pejman Azarsa conducted the literature review; Rishi Gupta shared knowledge on the subject, contributed materials and funding; Pejman Azarsa wrote the paper and Rishi Gupta revised as needed.

This paper highlights the correlation between electrical resistivity and other durability parameters of concrete. Different techniques in the measurement of concrete resistivity including bulk and surface resistivity measurements are presented. Furthermore, this paper reviews the influence of several parameters such as external environment (e.g. temperature or water saturation degree) and concrete mixture on the electrical resistivity which is one of the main focuses in the thesis. This review helped a lot in identifying current issues related to resistivity measurement technique and implementing them in this study.

2.2.1 Abstract

Degradation processes in reinforced concrete structures that affect durability are partially controlled by transport of aggressive ions through the concrete microstructure. Ions are charged and the ability of concrete to hold out against transfer of ions is greatly reliant on its electrical resistivity. Hence, a connection could be expected between electrical resistivity of concrete and the deterioration processes such as increase in permeability and corrosion of embedded steel. Through this paper, an extensive literature review has been done to address relationship between concrete electrical resistivity and its certain durability characteristics. These durability characteristics include chloride diffusivity and corrosion of reinforcement as these have major influence on concrete degradation process. Overall, there exists an inverse or direct proportional correlation between these parameters. Evaluated results, from measuring the concrete electrical resistivity, can also be used as a great indicator to identify early age characteristics of fresh concrete, evaluation of its

properties, determination of moisture content, connectivity of the micro-pores, and even for condition assessment of in-service structures. This paper also reviews and assesses research concerning the influential parameters such as environmental conditions and presence of steel rebar and cracks on measuring electrical resistivity of concrete. Moreover, concrete resistivity concept, application, and its various measurement techniques are introduced.

Keywords:
Concrete electrical resistivity, Reinforcement corrosion, Chloride diffusivity, Concrete durability, Non-destructive testing

2.2.2 Introduction

The durability of concrete is defined as its ability to resist weathering action, chemical attack, abrasion, or any other deterioration process to retain its original form, quality, and serviceability when exposed to harsh environment [59]. To a large extent, it is commonly accepted that concrete durability is governed by concrete's resistance to the penetration of aggressive media. This media may be present in a liquid or gaseous state and that may be transported by various mechanisms such as permeation, diffusion, absorption, capillary suction, and combinations of the items just mentioned. Hence, for concrete in service, a combined action of various media may prevail, and mixed modes of transport processes occur. Moreover, there are correlations between transport parameters of concrete and the following durability characteristics: carbonation, sulphate attack, alkali-aggregate reaction, frost resistance, leaching, soft water attack, acid attack, abrasion, chloride ingress, and reinforcement corrosion. Consequently, the transport of ions through microstructure of concrete plays an important role in the control of concrete durability. When ions are charged, then it is the concrete's ability to withstand transfer of charged ions which is highly dependent upon its electrical resistivity. In this study, since chloride ingress and reinforcement corrosion are reported as major concrete deterioration processes, one of the main concentration is on these durability characteristics and their relationship with concrete electrical resistivity.

Over the last few decades, a great deal of attention has been paid to research and development of electrical resistivity measurement techniques as a Non-Destructive Technique (NDT) to evaluate the durability of concrete structures. This method is becoming more popular especially for field evaluations due to its simplicity, rapidness, and cost during test conduction. However, the inclusion of these methods into the standards and guidelines are quite slow. Electrical resistivity has been standardized in 2012 by ASTM C1760 [60] to measure the concrete bulk resistivity and also by AASHTO TP 95-11 [61] to quantify the surface resistivity of concrete. However, there is a gap that still exists between the current knowledge and industry practice.

Electrical resistivity is a material property that can be used for various purposes, one of which is to identify early age characteristics of fresh concrete. When the fresh concrete sets and hardens, de-percolation (discontinuity) of the capillary pore space leads to an increase in its electrical resistivity. Since electrical current is conveyed by dissolved charged ions flowing into the concrete pore solution, it is a good indicator of concrete pore structures [62]. This pore structure formation at early-ages can define the long-term durability of concrete. In addition, the tensile strength of cementitious materials at early-ages is low and the material is prone to cracking. This initial cracking also serves as a pathway for deleterious materials to ingress into the matrix. This cracking can also be captured by resistivity measurements and thus helps predict the long-term durability of concrete. In addition, electrical resistivity can be used as an index to determine the moisture content and the connectivity of the micro-pores in the concrete [63].

Several researchers attempted to characterize the effects of various parameters on electrical resistivity measurements. One of the important factors affecting the measurements is environmental conditions such as temperature, rainfall and relative humidity. During testing, good electrical connection between concrete and electrodes as well as specimen geometry also play a key role in having a reliable measurement. The electrical resistivity measurements are highly influenced by the moisture content of concrete. For instance, when the moisture content is reduced, the resistivity is increased noticeably. Therefore, considering all these

influencing parameters for on-site resistivity measurements and to make meaningful conclusions is not a simple task.

In this paper, the correlation between electrical resistivity and certain durability characteristics of concrete are discussed. These concrete characteristics include chloride permeability, corrosion rate, and compressive strength. Also, different approaches in the measurement of concrete resistivity including bulk and surface resistivity measurements are presented. This paper reviews the effect of several influencing parameters such as external environment (e.g. temperature) and concrete mixture on the electrical resistivity. In addition, some of bulk and surface resistivity test setups (both of laboratory and field tests) conducted by authors are also presented.

2.2.3 Theoretical background

2.2.3.1 Concept

Electrical resistivity (ρ) of a material is defined as its capability to withstand the transfer of ions subjected to an electrical field. It is largely dependent on the microstructure properties of concrete such as pore size and shape of the interconnections (that is, tortuosity) [64]. Specimens with similar degree of water saturation and temperature should be used as both of these factors affect resistivity. Lower permeability results from a finer pore network with less connectivity and eventually leads to higher electrical resistivity. The range spanned by resistivity is one of the greatest of any material property [65]. For concrete, it varies from $10^6\ \Omega.m$ for oven dried samples to $10\ \Omega.m$ for saturated concrete [66]. Electrical resistivity is the ratio between applied voltage (V) and resulting current (I) multiplied by a cell constant and the electrical current is carried by ions dissolved in the pore liquid [67], [68]. Thus, it is a geometry independent property and an inherent characteristic of a material, as described in Equation 2.1 [64], [67].

$$\rho = k.R = k.\left(\frac{V}{I}\right) \qquad \text{Equation 2.1}$$

where R is the resistance of concrete; and k is a geometrical factor which depends on the size and shape of the sample as well as the distance between the probes on the testing device [64]. There are several factors

that may affect electrical resistivity of concrete, and they can be divided into two groups: (1) intrinsic factors affecting the electrical resistivity of concrete, such *w/c* ratio, aging, pore structure, etc. (2) factors affecting the resistivity measurements, including specimen geometry, moisture content, temperature, electrode spacing, presence of rebar, etc. For instance, more pore water as well as wider pores results in lower concrete resistivity and environmental factors such as higher temperature decreases the resistivity values [68]. Furthermore, adding reactive supplementary cementitious materials such as blast furnace slag, fly ash lead to lower permeability and higher electrical resistivity due to reduction in capillary porosity and hydroxyl ions (OH^-). Both carbonation and chloride penetration also individually cause an increase in concrete resistivity in particular in Portland cement concrete but penetrated chloride impact is relatively small [68]. The effects of above-mentioned parameters will be discussed in detail later in this paper.

2.2.3.2 Measurement techniques

Electrical resistivity measurements can be performed in several ways non-destructively: using electrodes positioned on a specimen surface or placing an electrode-disc or linear array or a four-probe square array on the concrete's surface. Types of device techniques that can be used typically to measure resistivity physically include (1) bulk electrical resistivity test (2) surface disc test (3) Wenner four-point line array test (4) four-probe square array test.

2.2.3.2.1 Bulk electrical resistivity test

In the bulk resistivity method (or uniaxial method), two electrodes are placed on the concrete surface (usually two parallel metal plates) with moist sponge in between (Figure 2.1.a). Generally, only standard cylinders/prismatic specimens or cores taken from existing structures are used in this method. The geometrical factor in this method can be obtained by following equation:

$$k = \frac{A}{L} \qquad \text{Equation 2.2}$$

where A is the cross-sectional area perpendicular to the current and L is the height of sample. Although, this non-destructive test takes only few seconds, its application is limited for field evaluation because

electrodes access to opposite sides of the concrete element is not possible all the time; while, other above-mentioned resistivity measurement (surface disc test, Wenner four-point line array test, and four-probe square array test) methods may use probes placed on only one side surface of specimen.

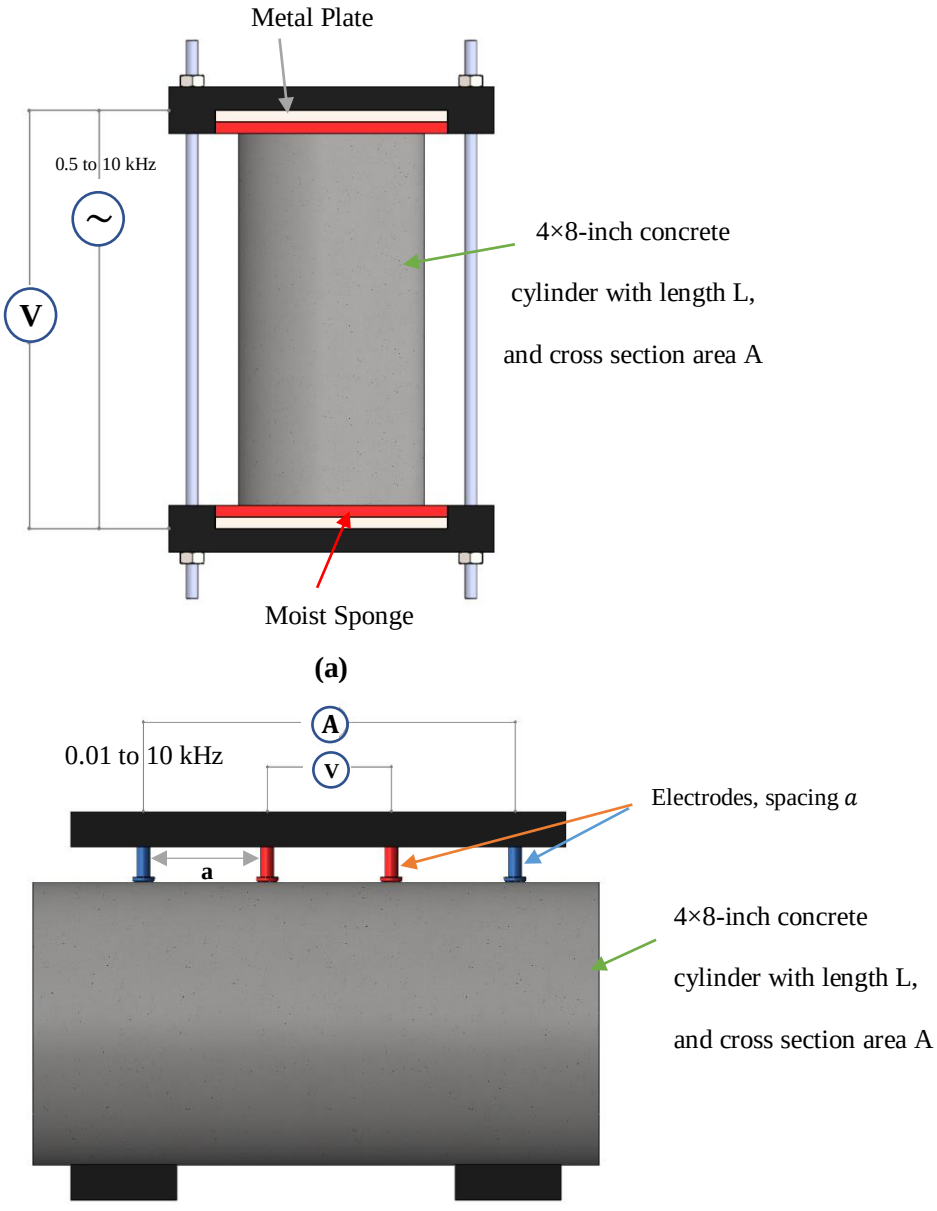

Figure 2.1. Electrical resistivity measuring techniques: **(a)** two-point uniaxial method; and **(b)** four-point (Wenner probe) method (Reproduced from [64]).

2.2.3.2.2 Surface disc test

The electrode-disc test method includes an electrode (disc) placed over a rebar and measuring the resistance between the disc and the rebar, as shown in Figure 2.2 [68]. One disadvantage of this method is a connection requirement to the steel reinforcement and full rebar continuity. In this technique, a cell constant is dependent on cover depth (which varies over the surface) and the rebar diameter in which precise measurements is impossible due to lack of exact current flow prediction [68]. For cover depth, disc and bar diameters being 10-50 mm, the cell constant is approximately 0.1 m. Hence, the resistivity can be derived using Equation 2.3:

$$\rho(disc) = 0.1 \times R(disc - bar) \qquad \text{Equation 2.3}$$

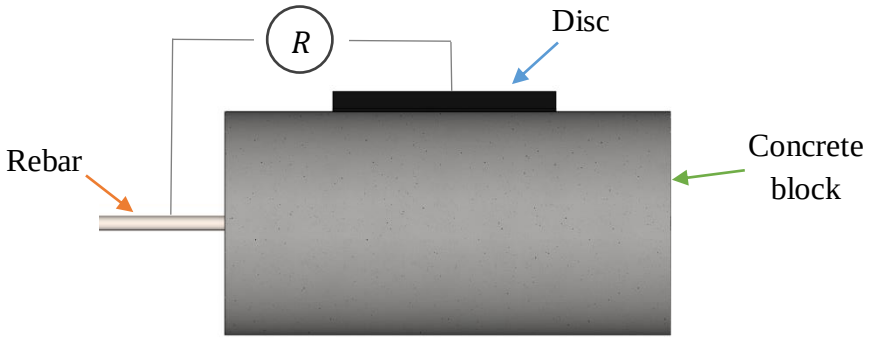

Figure 2.2. Setup of one electrode-disc: measurement of concrete resistivity (Reproduced from [68]).

2.2.3.2.3 Wenner four-point line array test

The Wenner probe technique was first introduced for the geologist's field in order to determine soil strata by Frank Wenner at the National Bureau of Standards in the 1910s and then modified through time for concrete application [69]. In this technique, four equally spaced linear electrodes are used to measure the surface electrical resistivity of concrete (Figure 2.1.b). The two exterior electrodes apply an AC current to the concrete surface while the electrical potential is measured from the interior probes. It should be noted that DC current is not desirable as it may result in inaccurate readings because of polarization effects. The effect of current frequencies on measurements is discussed in section 2.2.6.2.6 (Studies on electrical signal shape and frequency). The constant cell is defined as Equation 2.4 for semi-infinite homogenous material [64]:

$$k = \gamma . a$$ Equation 2.4

where a is the distance between the equally spaced electrodes and γ is the dimensionless geometry factor which is equal to 2π for semi-infinite concrete elements such as concrete slabs [64]. However, the geometry factor is different for tests conducted in a laboratory condition on small cylinders or cubic specimens. To measure the surface electrical resistivity, AASTHO TP 95 is the only specified standard which requires an electrode spacing of 1.5 inch (or 38 mm) with an AC frequency of 13 Hz [61]. Due to its configuration, this method is reliable for on-site measurement however many factors that will be discussed in section 2.2.6 can affect the results such as rebar and cracks presence, surface conditions, concrete mixture, and environmental conditions.

2.2.3.2.4 Four-probe square array test

The four-probe square array consists of the four probes that are arranged in square position with spacing of 50 to 100 mm [70].

2.2.3.3 Applications

Electrical resistivity can be related with certain performance characteristics of concrete and can be used as a promising quality assurance tool for fresh or hardened concrete [64]. Some of these correlations will be discussed in the following sections. It can be used as a measure of concrete resistance to chloride ingress as well as corrosion initiation and rate measurements. The concrete diffusion coefficient as an important factor in the service life estimation of structures also can be obtained by electrical resistivity technique. In addition, it is a reliable test method to detect and monitor the initiation and propagation of cracks in concrete since they change the connectivity of concrete pore structure, and thus its electrical conductivity [71]. Cement mortars and concrete setting time can be determined through the concept of electrical resistivity. However, the correlation between setting time and concrete durability is not fully understood. Another potential application of the electrical resistivity method is to compute the moisture content of concrete, although, reliability of this method is still under question [63]. However, electrical resistivity method is a simple and reliable non-destructive test method, the application and reliability of this method in determining

certain characteristics of concrete has yet to be widely evaluated. This is more due to the limited knowledge in this area especially for on-site evaluation.

2.2.4 Objective and methodology

The primary objective of this paper is to review the existing state of practice on the electrical resistivity measurements technique. This paper also identifies the applicability and limitation of electrical resistivity method and reviews the correlation between resistivity and certain durability properties of concrete. Correlation between surface and bulk electrical resistivity and their applications are also discussed. Finally, key parameters affecting the electrical resistivity readings are identified for future research in the area.

An extensive literature search was undertaken from most relevant publications in the area. A comparison was made of the experimental setup (Section 2.2.5), and the way in which the correlated data was obtained between resistivity and durability properties of concrete (Sections 2.2.7-2.2.7.4). Several parameters influencing the concrete resistivity were identified and compared (Section 2.2.6). The information observed from the literatures was based on experimental and numerical studies. The reviewed data was compiled in tables and later compared. Detailed information on the experimental setups is presented in Table 2.1-Table 2.5. The literature search covered both laboratory and field investigations.

2.2.5 Comparison of the experimental investigations

In this section, experimental setups developed by other researchers have been summarized in Table 2.2-Table 2.5. These tables consist of specimens' configuration, materials type, resistivity measurement techniques, and specimen curing/exposure conditions. The data in the tables is arranged in the order in which the citations appear in sections 2.2.6 to 2.2.7.4. An additional row that contains authors' data on measuring electrical resistivity of simulated field circular hollow-section columns is also included. The extent to which differences in the setups can influence electrical resistivity measurements are discussed later in sections 2.2.6-2.2.7.4 using data presented in this section. A comparison of the experimental setups is given in the sections 2.2.5.1-2.2.5.3. Abbreviations and symbols are defined in Table 2.1.

Table 2.1. List of symbols and abbreviations.	
Symbols	Explanation
CON	Concrete
CEM	Cement paste
MOR	Mortar
MK	Meta-kaolin
SF	Silica Fume
RHA	Rice Husk Ash
OPC	Ordinary Portland Cement
SLG	Slag
FA	Fly Ash
NP	Natural Pozzolan
UPV	Ultrasonic Pulse Velocity
WPC	White Portland Cement
PFA	Pulverized-Fuel Ash
MS	Micro-silica
LPR	Linear Polarization Resistance technique
TNVM	Total Number of Various Mixtures
w/b	Water/binder ratio
NR	Not Reported
CR	Counter Electrode
RE	Reference Electrode
SC	Slag Cement
CA	Crystalline Admixtures
PLC	Portland Limestone Cement

2.2.5.1 Specimen geometry and setup

Frequently, in the electrical resistivity studies, samples with dimensions between 100 and 400 mm were used (Table 2.2). Specimens with dimensions over 1000 mm to simulate real-world condition were more seldom used. According to Table 2.3, the steel rebar diameter varied from 4 to 25 mm. In most cases, no detailed information was provided about the type of steel embedded, both smooth and ribbed steel was used. Cover depth ranging from 10 to 80 mm was considered for steel reinforcement bars in the majority of the experimental investigations. For those studies investigating the relationship between steel reinforcement corrosion and concrete resistivity, chloride ingress was the major cause of corrosion. However, no information provided on the size of the anode and the ratio between anode and cathode in the reviewed articles. Only one study concentrated solely on carbonation-induced corrosion.

2.2.5.2 Materials and exposure conditions

According to data in Table 2.2, concrete or mortar samples were cast with a *w/b* ratio between 0.4 and 0.65 by mass in most reviewed experimental programs. The mixture proportions and cement content varied and blended cements such as fly ash or slag cements were used in parts of the studies. In a couple of studies, no detailed information was provided about the cement type. However, ASTM Type I and CEM I/II cements were used in most of the articles. Only one reported study used White Portland Cement (WPC) [72]. Also, Rice Husk Ash (RHA) as a cementitious supplementary material was only studied by Gastaldini *et al*. [73]. Work done by authors of this paper seems to be the only one that considered crystalline admixture as a healing agent to investigate its effect on electrical resistivity of concrete.

The specimens were cured and exposed to various and/or changing conditions over the testing period (Table 2.4). In most studies, samples were cured in the lime-saturated water tank with controlled temperature to eliminate the temperature effect on resistivity measurements. The temperature was kept constant between 20 °C to 25 °C in most experiments. To achieve a wide range of concrete resistivity, drier climates were considered occasionally. In most experiments, specimens were kept in a water tank during resistivity measurements or exposed to a high relative humidity (RH). For those studies focused in accelerating corrosion process, RH between 90% to 95% was chosen as an exposure regime. In parts of studies, samples were exposed to outside climates, in particular marine conditions (similar to authors' experimental setup). In general, laboratory experiments were undertaken over a period between 28 and 365 days. Only a few studies measured electrical resistivity for period over one year [74]–[77].

2.2.5.3 Measurement methods

Either two-electrode or four-point electrode (Wenner probe setup) techniques were employed to record concrete electrical resistance, which is then converted into resistivity by multiplying it with an appropriate geometrical factor. The limitations of 2-electrode method resulted in using Wenner probe configurations in most studies specially for field investigations. In experimental studies that attempted to find correlation between concrete electrical resistivity and its durability parameters, other destructive and non-destructive

testing techniques from standardized measuring protocol including Rapid Chloride Permeability (RCP) test, Rapid Chloride Migration (RCM) test, Bulk Diffusion (BD) test, Ultrasonic Pulse Velocity (UPV) were employed. Authors on-going work also employs use of both 2-electorde and 4-electorde techniques as well as UPV technique.

Table 2.2. Details of the specimen geometry (in terms of specimen size), material type and number of specimens.

Refs	Specimen configuration			Materials Type							w/b Ratio	Rebar Presence
	Type	Size (mm)	TNVM	Mix Type	OPC	SLG	FA	MK	SF	Others		
[62]	Disk	Φ100×50	44	CON/CEM	×	×	×	-	× (5% & 10%	NP (30% and 50%)	0.35,0.4, 0.45	N
[71]	Slab	254×76×12.7	18	CON	× Type I	-	×	-	-	-	0.26	N
[78]	Cylinder	Φ 47×95	30	CEM	× Type I	-	× (Class C & F)	-	-	$CaCO_3$ (10% & 15%)	0.35	N
[79]	Slab	250×200×120	1	CON	×	-	-	-	-	-	0.5	Y
[80]	Slab, cube, cylinder	300×300×135, 300×300×200, 100×100×100, Φ100×200	6	CON	× (blended)	-	× (20% blended)	-	-	-	0.4	Y
[81]	Prism	300×300×150	7	CON	× Type I	-	×	-	-	-	0.42	Y
[82]	Cylinder, prism	Φ100×200, Φ150×300, 200×200×175, 160×160×140, 120×120×110	NR	CON	× Type I	-	-	-	-	-	0.4, 0.6	Y
[83]	Cylinder, prism	Φ150×300, 40×40×160	NR	MOR	×	-	-	-	-	-	0.5	Y
[84]	Prism	400×400×100	6	MOR	×	-	-	-	-	-	0.6	Y
[85]	Cylinder	Φ150×220	4	CON	×	-	-	-	-	-	0.4, 0.6	Y
[86]	Slab, cube	650×650×100, 150×150×150	1	CON	×	-	-	-	-	-	0.5	N
[87]	Slab	600×600×120	9	CON	×	-	-	-	-	-	0.36, 0.48, 0.61	Y
[88]	Beam	1500×200×100	2	CON	×	-	-	-	-	×	0.7	N
[89]	Cylinder	Φ100×200	21	CON	× Type I/II	× (Grade 100 & 120, 50%)	× (Class C & F, 20%)	-	× (5% & 10%)	-	0.35, 0.5, 0.65	N
[90]	Cylinder	Φ100×200	33	CON	× Type I/II	-	×	-	×	-	0.41	N
[91]	Cube	150×150×150	47	CON	×	×	-	-	-	-	0.4-0.55	N
[72]	Prism	100×100×170	12	CON	×	× (50% and 70%)	-	-	-	WPC	0.3,0.42,0.55	N
[92]	Cylinder	Φ150×300	3	CON	× Type I	-	-	-	-	-	0.45,0.55,0.65	N
[93]	Cylinder	Φ75×150	NR	CON	× Type V	-	-	-	-	-	0.45	N

Table 2.2. Details of the specimen geometry (in terms of specimen size), material type and number of specimens.

[94]	Cube, Cylinder, Block	100×100×100, Φ100×200, Φ150×300, 300×300×200	NR	CON	× (Blended)	-	× (18% blended)	-	-	-	0.4	N
[95]	Cube	150×150×150	NR	CON	×	×	-	-	×	PFA	0.59-0.7	N
[96]	Cylinder	Φ100×200	12	CON	×	×	×	×	×	Micro-FA	0.3-0.4	N
[97]	Cube	150×150×150	33	CON	× Type I & Type V	×	-	-	-	-	NR	N
[98]	Cylinder	Φ100×200	19	CON	×	×	×	-	×	-	0.41	N
[75]	Slab, cylinder	280×280×102, Φ102×204	NR	CON	×	×	×	×	-	MS	0.35-0.45	N
[99]	NR	NR	NR	MOR/CEM	× Type I	-	-	-	-	-	0.42	N
[100]	Cylinder	Φ100×200	12	CON	×	×	×	-	-	-	0.41	N
[101]	Block	300×300×200	3	CON	×	×	-	-	-	PFA	0.39, 0.4, 0.44	Y
[102]	Slab, cylinder	610×610×152, Φ100×200, Φ150×300	10	CON	×	×	× (Class F)	-	-	MS	0.43	Y
[103]	Prism	1000×1000×300, 150×270×150	NR	CON	×	-	×	-	-	-	0.35-0.65	Y
[104]	Cylinder	Φ100×200	NR	CON	× Type I/II	-	× (20%)	-	× (8%)	-	0.4	N
[105]	Cylinder	Φ100×200	10	CON	×	× (SC)	-	-	-	-	0.45, 0.65	Y
[76]	Prism	100×100×300	12	CON	×	×	×	-	-	-	0.4,0.45,0.5	Y
[106]	Cylinder, cube	Φ100×200, 100×100×100	12	CON	×	×	-	-	×	-	0.25, 0.28, 0.35	N
[107]	Cylinder	Φ100×200	12	CON	×	×	×	×	×	(Super fine fly ash)	0.28-0.49	N
[108]	Cylinder	Φ100×200	11	CON	×	×	×	-	-	-	0.37-0.45	N
[109]	Cylinder	Φ100×200	343	CON	× Type I/II	-	× (Class C, 25%)	-	-	-	0.42	N
[110]	Cylinder	Φ100×200	514	CON	×	×	× (Class F)	-	-	-	0.41	N
[111]	Cylinder	Φ100×200	57	CON	× Type I	-	-	×	×	RHA, NP	0.4-0.6	N
[112]	Cube, slab	100×100×100, 250×250×100	10	CON	×	×	-	(5%, 10%, and 20%)	-	MS (5% and 10%) &	0.52	N

Table 2.2. Details of the specimen geometry (in terms of specimen size), material type and number of specimens.

										PFA (30%)		
[113]	Disk	Φ100×50	6	CON	×	× (30%)	-	-	× (10%)	-	0.25, 0.28, 0.35	N
[114]	Cylinder	Φ150×300	24	CON	×	× (50%)	-	-	8%	NP (12%, 25%)	0.28-0.6	N
[115]	Cylinder	Φ150×200	4	CON	×	-	-	-	-	-	0.4, 0.6	Y
[116]	Cylinder, prism	Φ102×178, 406×76×102	NR	MOR	×	-	-	-	-	WPC	0.42	N
[117]	Cylinder	Φ100×200	33	CON	× Type II-V	(Grade 100 & 120)	(Class C & F)	×	×	-	0.44	N
[118]	Cylinder	Φ100×200, Φ150×300	23	CON	× Type II-V	× (Grade 120)	(Class F, 20%)	×	×	-	0.44	N
Authors	Hollow section, cylinder	Inner dia. 152 and external dia. 304, Φ100×200	18	CON	×	×	-	×	-	CA (2%), PLC	0.5	Y

In summary, the experimental setup can have a significant effect on the electrical resistivity measurements. Specifically, the measurement methods and environmental conditions comprise a variety of parameters affecting the obtained data. The geometry of specimen and the general setup have a minor influence on the recorded resistivity values. To investigate electrical resistivity, the material, curing condition, and exposure condition should be carefully selected. Simulating the real-world conditions are in any case desirable since the recorded data can be used later as input in prediction models. As field survey data is rarely reported in the reviewed studies, it seems critical to identify possible deviations between laboratory investigations and field conditions. Also, authors' focus currently is to find these deviations to fill this knowledge gap by measuring concrete resistivity on both laboratory-size and field-size specimens.

Table 2.3. Details of the reinforcements and measurement methods used to record corrosion rate.

Refs	Reinforcement			Cause of corrosion	Corrosion rate		
	Φ (mm)	Length (mm)	Cover depth (mm)		Technique	Details	Correction for ohmic drop
[79]	10	200	1,10, 20	Carbonation	-	-	-
[80]	10	300	50 & 75	Not Studied (NS) (only effect of rebar presence on resistivity measurement were considered)	-	-	-
[81]	16	300	50	Cyclic ponding with sea water	-	-	-
[82]	4	110, 160, 200	Various (53.5-100)	NS	-	-	-
[83]	8	40	80	NS	-	-	-
[84]	13,19, 25	410	20, 30, 40	NS	-	-	-
[85]	10	250	150	NaCl Solution/marine exposure	LPR	Embedded steel rebar	N
[87]	10	-	25	NS	-	-	-
[101]	16	200	50	NaCl Solution/marine exposure	-	-	-
[102]	NR	NR	NR	NaCl Solution	LPR	NR	NR
[103]	NR	NR	70	NaCl Solution	-	-	-
[105]	16	NR	42	NaCl Solution	NR	Embedded steel rebar	NR

Table 2.3. Details of the reinforcements and measurement methods used to record corrosion rate.

[76]	8	150	10 or 30	NaCl Solution	LPR	Embedded CE & RE on the surface	N
[115]	10	200	15	NaCl Solution	-	-	-
Authors	10	914	19-38	NaCl Solution	LPR	Embedded steel rebar	Y

Table 2.4. Details of the curing conditions, exposure conditions, and measurement period.

Refs	Curing Conditions	Temperature (°C)	Exposure Conditions	Measurement Period (days)
[62]	Lime-saturated water tank	20 (except one type mixture kept in water having 5, 20 & 35 temperature)	Lime-saturated water tank/ Lab condition and oven dry state (only one type mixture)	90 (except ten of the mixture tested at age 365 days)
[71]	Lime-saturated water tank	23±1	Lime-saturated water tank	28
[78]	NR	15, 26, 40	Plastic wrapped	1
[79]	NR	20	Laboratory (Air dry)	1000
[80]	Water tank	20	Water tank (except two slabs were kept in air after 7 days)	30
[81]	NR	NR	Various	120
[82]	Lime-saturated water tank	23	Various	28
[83]	100% relative humidity in a chamber	20 ± 2	100% relative humidity in a chamber	28
[84]	Water tank	20	Water tank	45
[85]	NR	NR	Seashore Exposure/immersed in saline solution	1000
[86]	Plastic wrap	20	Room temperature	90
[87]	NR	NR	NR	28
[88]	Room temperature	25 ± 2	Room temperature	28
[89]	Lime-saturated water tank	Laboratory	Lime-saturated water tank	56
[90]	NR	10-45	Room condition with RH>95%	2,190
[91]	Water tank	20	Water tank	181
[72]	Wet chamber with RH>95%	23±2	Wet chamber with RH>95%	91
[92]	Water tank	23±0.5, 105±2	Various	28
[93]	Wet burlap	20	Oven dried and then water bath	31
[94]	Water tank	20 & 5	Water tank (After 7 days, some cylinders subjected to air condition)	30
[95]	Water tank	20±2	Water bath	720
[96]	Lime-saturated water tank	23 ± 2	Lime-saturated water tank	91
[97]	Water tank	NR	Water tank	365

Table 2.4. Details of the curing conditions, exposure conditions, and measurement period.				
[98]	Various	21-45	Various	1,100-2,200
[75]	Lime-saturated water tank/wet burlap	NR	Lime-saturated water tank/wet burlap for 3 or 7 days	91
[99]	Lime-saturated water tank	Various (10-45)	Various	65
[100]	Various	Various	Various	500
[101]	Wrapped in damp hessian and stored under poly-thenetentage	15-20	Maine exposure	140
[102]	Various	18-32	Salt ponding	90
[103]	Water tank and laboratory air	20±2	Actual tidal zone, wet and dry cycle	NR
[104]	Five various curing regimes (tap water, NaCl solution, Fog room)	Room	Various	1500
[105]	Various	20 ± 2/ Uncontrolled	Various	90
[76]	Six days in fog room/three weeks in room condition	20	26 weekly cycles of 24 h 3% NaCl solution penetration and drying for 6 days/After 30 weeks, various conditions	52
[106]	Water tank	25	Water tank	90
[107]	Moist room with a sustained 100% humidity	23	NaCl solution	1,092
[108]	Lime-saturated water tank	22	Lime-saturated water tank	56
[109]	Changing exposure	23±2	Changing exposure	90
[110]	Lime-saturated water tank	21 or 36	Various	1000
[111]	Lime-saturated water tank	23±2	Lime-saturated water tank	28
[112]	Water tank for 14 days/14 days in drying cabinet at 40°C	20±1 & 40±1	Salt ponding (wet & dry cycle)	270
[113]	Lime-saturated water tank	25	Lime-saturated water tank	90
[114]	Chamber with RH>95%	21	Chamber with RH>95%	28
[115]	Laboratory environment (kept in plastic bag)	14-27, 3-13	Seashore condition	1,000
[116]	Water tank	21 ± 3	Water tank	7
[117]	Lime-saturated water tank	NR	Lime-saturated water tank	1
[118]	Lime-saturated water tank	NR	Lime-saturated water tank	730
Authors	14 days wet burlap and 14 days air dry	Uncontrolled	Natural environment and simulated seashore condition	720

Table 2.5. Details of the different measurement methods used in the literature.

Refs	Measurement Technique			
	Concrete Resistivity		Rapid Chloride Permeability Test	Others
	Two Electrode	Four Point Method		
[62]	×	-	-	Rapid chloride migration test (NT Build 492) & ASTM C1760
[71]	×	-	-	-
[78]	×	-	-	-
[79]	×	×	-	Multi-Ring Electrodes
[80]	×	×	-	NT Build 492
[81]	-	×	-	-
[82]	-	×	-	-
[83]	×	×	-	-
[84]	-	×	-	-
[85]	-	×	-	Steel potential
[86]	×	×	-	-
[87]	-	×	-	Ultrasonic Pulse Velocity
[88]	-	×	-	Electric imaging
[89]	-	×	×	-
[90]	-	×	-	-
[91]	×	-	-	NT Build 492
[72]	-	×	-	-
[92]	-	×	-	-
[93]	×	-	-	-
[94]	×	×	-	NT Build 492
[95]	×	-	-	-
[96]	×	×	-	-
[97]	×	×	-	-
[98]	-	×	-	-
[75]	×	×	× (ASTM C1202)	-
[99]	×	×	-	-
[100]	-	×	-	-
[101]	×	-	-	-
[102]	×	×	× (AASHTO T227)	Half Cell Potential
[103]	×	×	-	-
[104]	-	×	-	-
[105]	-	×	-	-
[76]	×	-	-	Steel corrosion potential
[106]	×	-	-	NT BUILD 492
[107]	-	×	-	ASTM C1556-04
[108]	×	×	× (ASTM C1202)	-

Table 2.5. Details of the different measurement methods used in the literature.				
[109]	-	×	×	KDOT Boil Testing
[110]	-	×	-	Bulk Diffusion test (NT Build 443), NT Build 492
[111]	-	×	×	Water Penetration Depth
[112]	-	-	-	Resistivity using disc method (one external electrode)
[113]	×	×	-	NT Build 492
[114]	-	×	-	Natural diffusion test (90 days)
[115]	-	×	-	Half-cell potential method
[116]	×	×	-	-
[117]	×	×	-	-
[118]	×	×	-	-
Authors	×	×	×	UPV, Half-cell potential, Infrared camera

2.2.6 Influencing parameters on electrical resistivity measurements

In the following sections, investigated parameters in published literature that influences the electrical resistivity readings have been discussed. For simplicity, they have been divided into two sub-groups: (1) factors affecting the intrinsic electrical resistivity of concrete (2) factors affecting the electrical resistivity measurements.

2.2.6.1 Intrinsic factors affecting electrical resistivity of concrete

2.2.6.1.1 Effect of water to cement (w/c) ratio

Generally, water to cement (*w/c*) ratio is one of the main factors contributing in permeability of concrete and its properties. Higher *w/c* ratio results in a high percentage of porosity (more voids) and leads to a lower electrical resistivity value indicating a more permeable concrete [89]. However, concrete containing supplementary cementitious materials such as slag showed an irregular behavior for various *w/c* ratio [89]. For instance, an increase in *w/c* ratio from 0.35 to 0.65 caused an increase in electrical resistivity values, which means a less permeable concrete. Additionally, the electrical resistivity measurements are affected by the degree of hydration as further hydration typically reduces the concrete porosity and how these pores are interconnected [90]. The results from experimental study conducted by Noort *et al*. [91] on different concrete compositions with various *w/c* ratio ranges also indicated that concrete's electrical conductivity increased as *w/c* ratio increased. Within a hardened concrete matrix, electrical conduction flows through

the fluid contained in the pores, therefore the relative volume of interconnected pores controls the concrete's electrical resistivity. Increasing the *w/c* ratio (at fixed cement content) leads to a higher volume fraction of hydrated cement paste in the concrete mix and results in higher concrete electrical conductivity. Similar tendency has been observed [72] even for concrete containing White Portland Cement. When *w/c* ratio was reduced, conductivity of pore solution was increased due to the greater ionic concentration of the solution. Su *et al*. [92] studied the effect of moisture content on concrete resistivity measurements. It was found that the electrical resistivity difference for mixes with 0.55 and 0.65 *w/c* ratios was not noticeable, although, it became significant for specimens with a *w/c* ratio of 0.45. It seems that both the capillary pore size effect and inter-connectivity effect improve resistivity for saturated concrete with a higher *w/c* ratio. Long term experimental study also showed the reduction in concrete resistivity with the increase of *w/c* ratio until approximately 500 days. However, after 500 days, the resistivity results revealed a contrary behavior because the concrete specimens kept in unsaturated condition (in a laboratory environment) with higher *w/c* ratio favored the carbonation process that led to larger resistivity values for more advanced ages. Saleem *et al*. [93] also found similar trend for concrete samples contaminated with sulphate/chloride. About 15-20% reduction in electrical resistivity values was reported when the water/cement ratio increased from 0.4 to 0.6 [82].

2.2.6.1.2 Effect of aggregate size and type

In general, aggregates depending on their location and size have a higher electrical resistivity compared to hardened cementitious paste because they have less porosity, thus electrical current can easily flow through the pore system of the paste. Hence, a few researchers attempted to investigate aggregates' effect on electrical resistivity measurements. The experimental study performed by Sengul [62] indicated that increasing aggregate content resulted in higher electrical resistivity. He also observed the resistivity of the mixture containing 60% aggregate with the size of 16-32 mm was approximately 3 times higher than that of the hardened cementitious paste [62]. Increase in aggregate content and reduction in cement paste for a given volume resulted in higher resistivity values because of replacing the porous hardened cement paste

with denser aggregates. The investigation on comparing effect of two different aggregate sizes (0-4 mm and 16-32mm) on electrical resistivity showed that larger aggregate size resulted in higher electrical resistivity values. Morris *et al.* [119] also reported that the variability was greater on the specimens with larger maximum aggregate size. Two possible causes of this variability originate from the tortuosity effect and formation of more Interfacial Transition Zone (ITZ) which exists between large particles of aggregate and the hydrated cement paste (more porous structure compared to bulk cement paste) for smaller aggregate/particle size. ITZ zone is less dense and more porous than the other phases in concrete which makes current to flow easier inside as compared to aggregate. Therefore, variation in aggregate content and size should be taken into account when comparing the resistivity values of different concretes.

As reported in the Sengul study [62], aggregate type also affected the electrical resistivity of concrete. For electrical resistivity measurements, comparison between the crushed limestone aggregate and gravel showed higher values when crushed limestone were used [62]. Gravel were rounded shaped aggregates with smooth surface whereas the limestone aggregates have rough surface texture. Therefore, using rounded aggregates such as gravel results in poor bonding between gravel and cement paste which may also be a reason behind the variations in resistivity readings. In addition, tortuosity can be higher for crushed stone aggregates due to the rough surface texture and irregular particle shape, which in turn, may reduce the rate of electrical flow and affect resistivity [62]. Comparable standard deviation values were also observed when different aggregate type were used with the same maximum aggregate size [119]. Furthermore, using granite as coarse aggregate with fly ash also resulted in higher resistivity measurements than the mixture containing limestone aggregate type [100]. Hence, the effects of aggregate type should not be ignored during resistivity measurements.

2.2.6.1.3 Effect of curing conditions

The resistivity evolution of concrete is affected by the curing regimes [104]. Two key elements influence this variation in resistivity: the degree of hydration of the cementitious material and the degree of saturation of the specimen. The numerical study performed by Weiss [120] attempted to simulate a mortar with a

water-to-cement ratio of 0.42 with three curing conditions: (a) sealed during curing and testing, (b) sealed during curing and saturated during testing, and (c) saturated during curing and testing. It was concluded the specimen that was sealed both during curing and testing had the highest resistivity whereas the sample that was sealed during curing and saturated at the time of testing had the lower most resistivity [120]. This difference can be explained by the saturation degree of the sample. The results recommend that storing a sample underwater in the lab may cause a remarkably different degree of hydration than what may occur in a field structure. The sample that was continually saturated and the sample that was sealed and saturated at the time of testing had a similar resistivity for the same degree of hydration; however, the continually saturated sample had a higher degree of hydration at the same age [120]. For specimens cured under saturated lime water, it has also been hypothesized that the volume of solution in which samples are stored can affect resistivity measurements due to possible pore solution concentration or dilution via leaching [120], [99]. According to AASHTO TP 95 [61], for the samples cured in a lime-water tank, the average resistivity value needs to be multiplied by 1.1 while this coefficient is 1 for the specimens stored in a 100% relative humidity moist room. For a given water-cement ratio, it was observed that better curing procedure yielded higher electrical resistivity since curing plays an important role in enhancing higher hydration rate and decreasing the overall matrix porosity due to furtherer usage of cement during hydration process especially at early age [105]. For both wet and dry curing conditions experimented in the study [80], the resistivity distinctly increased with increasing age. Sample storage and curing conditions are important, as they can influence the degree of hydration, the degree of saturation, the pore structure, and changes in ionic concentration in solution if leaching occurs [99]. Differences in resistivity can develop as a result of sample storage conditions and wetting the specimens prior to the resistivity measurements is recommended.

2.2.6.2 Factors affecting the electrical resistivity measurements

2.2.6.2.1 Presence of rebar

Several researchers have been exploring the effect of embedded rebar presence on concrete electrical resistivity through experimental and numerical investigation. Theoretically, electrical current fluxes take

pathways having the least amount of resistivity and when there is embedded rebar in concrete, the current field is distorted. However, the alternation in current field is dependent on many factors such as orientation of rebar with respect to the probe, rebar diameter and spacing, and depth at which it is located [79], [121], [122].

Millard [121] and Gower & Millard [122] utilized an experimental setup with steel rebar in the tanks filled with conductive medium solution and its finite element modeling in order to study the effects of concrete cover thickness as well as rebar diameter and spacing on concrete resistivity using four-point Wenner probe. According to this study, distance between the probe and embedded rebar was found to be the main influential parameter when measurements were taken on top of the bar. It was also reported that rebar diameter is not impactful in its disturbance. Moreover, it was found measurement errors were increased by reducing rebar spacing while measurements taken between two parallel rebars. However, it should be noted that results were obtained from measurements on the conductive solution tank and not from a concrete block. Similar study of resistivity measurements utilizing Wenner probe on concrete block with embedded steel reinforcement showed that orienting the probe perpendicular to reinforcements significantly reduced their influence on resistivity measurements [79]. It is more common in reinforced concrete structures that rebars are available in both directions and electrically linked together but, in the tested concrete block, no lateral rebars were present which then may have different effects on measured resistivity.

Practical general guidelines were developed by Polder's work [68] from summarizing literature for the RILEM TC 154 [67] technical recommendation for taking resistivity measurement on concrete. It was identified that placing all four electrodes over an embedded rebar at 10 or 20 mm depth can result in errors by a magnitude of two to six-times that of true resistivity and even if one of the four electrodes was near a rebar, results will lead to errors. Because of lack of research on resistivity measurements over rebar meshes, it was recommended that resistivity measurement with Wenner probe are taken in diagonal alignments on the concrete surface (Figure 2.3). Five measurements, each a few millimeters in distance from one another, and taken the median of them are also suggested for collecting the resistivity value of the interested area.

However, no recommendations were made for the case where it is not possible to fit all four electrodes inside the mesh unit created by the rebars. In addition, the recommended scheme in this study was not supported by any experimental and numerical works.

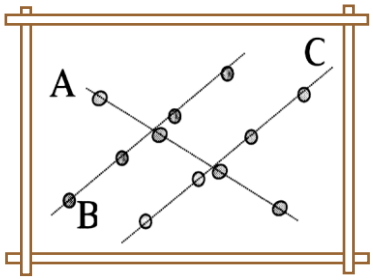

Figure 2.3. Resistivity using four electrodes at various spots in the same area to minimize influence of rebars [68].

Another similar experimental investigation, done by Sengul and Gjorv [80], studied the effects of different parameters on concrete resistivity measurement using Wenner probe setup due to rebar presence. The study included the effective parameters: cover thickness, probe measurement directions relative to embedded rebar, electrode spacing, and probe measurement distance away from the embedded rebar. In total, five different probe positions with respect to the location of embedded steel reinforcement were considered, where four of these configurations were parallel to the rebar and the last one was perpendicular (Figure 2.4). Similar to Weydet *et al.*'s study [79], only a single rebar was positioned in the slab and two different thicknesses of 50 mm and 70 mm were studied. Their findings similar to the previous works stated that placing the probe orthogonally to the rebar did not influence the resistivity measurements, although, significant errors were obtained once measurements taken directly above and parallel to the rebar. It was also suggested that all measurements should be captured as far away as possible from embedded steel to reduce errors and if not possible due to dense reinforcement configuration, then space between electrodes should be kept relatively small. As only one rebar was placed in the tested concrete block as well as a small slab size was used, this possibly contributed to errors due to edge effect. Hence, it may be difficult to extrapolate these conclusions to real cases.

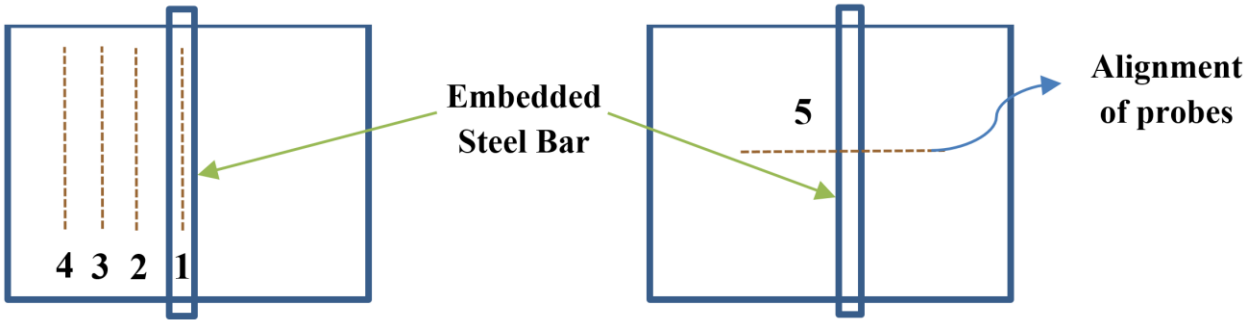

Figure 2.4. Five Wenner probe configurations with respect to embedded rebar tested by Sengul and Gjorv [80].

Moreno [81], [123] has recently attempted to numerically and experimentally understand the influences of the number and configuration of embedded steel reinforcement along with the location and angle of the Wenner probe with respect to rebar alignment on concrete resistivity measurements. One of the few studies considered the effect of rebar mesh as well as orientation of the Wenner probe and demonstrated the difference between data achieved once there is a rebar mesh rather than a single rebar. Overall, six and five different orientations were investigated for the presence of a single rebar and rebar mesh, respectively. Like previous studies, it is also recommended to take the measurements perpendicular to the rebar location. However, the performance of Wenner probe due to variation in rebar spacing, cover thickness or location and orientation of the probe with respect to the rebar mesh was not considered in this study.

Salehi *et al*. [124], [125] numerically characterized the effects of different concrete and slab thicknesses, rebar diameter, probe arrangements with respect to the rebar mesh and rebar mesh densities on concrete electrical resistivity measurements with rebar presence using the four-point Wenner probe technique. It was concluded that the smallest error will result while setting up the probe parallel to the top rebar within the rebar mesh and perpendicular to bottommost rebar during measurements taken, as illustrated in Figure 2.5. It was also found that the observed resistivity decreased once the rebar mesh densities increased and the rebar diameter effect on concrete resistivity measurements can be neglected, although, the numerical study results were not validated by experimental investigation.

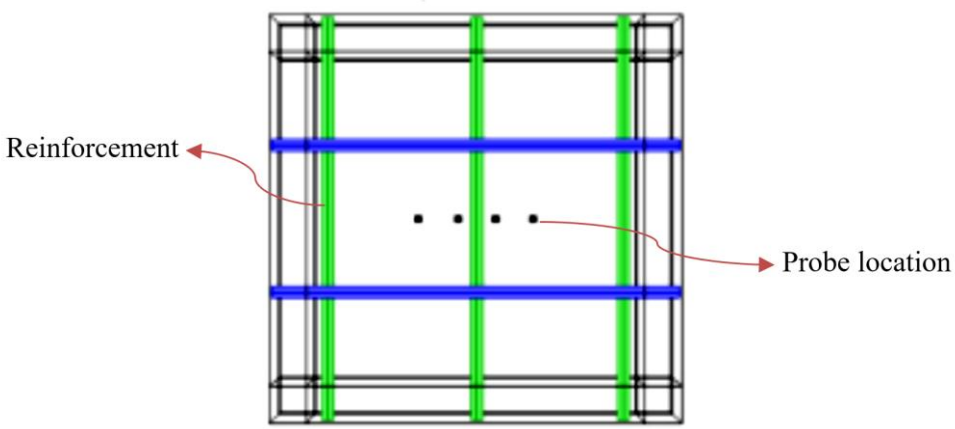

Figure 2.5. Probe configuration with respect to rebar mesh suggested to reduce electrical resistivity measurement error [124].

For cylindrical concrete specimens with a single embedded steel rebar, study conducted by Chen *et al.* [82], suggests a correction factor to be applied to resistivity measurements corresponding with the ratio of specimen length to electrode spacing as well as the ratio of specimen diameter to electrode spacing. It was stated that no correction factor for prismatic specimens was necessary with the possibility that the applied current did not pass through the reinforcement. This study also lacked in embedding more than a single rebar and considering larger concrete specimens.

The effect of rebar presence on mortar electrical resistivity conducted by the four-point Wenner method was also investigated numerically and experimentally by Garzon *et al*. [83] and Lim *et al*. [84]. In Garzon's experimental study, small scaled cylindrical and prismatic specimens were cast. As polarization will happen due to double layer at the steel and concrete interface acting as a resistance-capacitor, resistivity measurements taken directly above rebar will result in errors. Hence, a rebar factor was suggested to apply to the obtained resistivity results. In addition, modified Wenner equations are recommended for various geometric parameters [83]. Only reinforced cylindrical and prismatic specimens were included in the experimental setup without considering a reinforced slab. However, in a numerical study, a slab with embedded rebar was considered [83]. The experimental investigation lacked in using concrete mixture instead of a mortar mixture which is not exactly representative of real-world cases and may lead to more errors. Furthermore, the proposed rebar factor may not be applicable to a large concrete slab with multiple

rebar because their experimental conclusions are based on laboratory testing. Lim *et al*. [84] also studied the effects of cover depth, electrode spacing, rebar diameter and the resistivity of concrete and reinforcement in the numerical model. However, only one probe configuration taken right above and parallel to rebar was considered. It was suggested to apply a geometric effect rate that ranges from 0 to 1 in order to estimate the reinforcement geometry impact and this rate is derived utilizing a resistivity estimation model. The geometric effect rate was also validated through the experimental investigation for on-site measurements. Based on experimental findings, it was stated that the geometric effect rate decreased with increasing concrete cover thickness and increased with increasing rebar diameter and increasing electrode spacing. Again, using mortar mixture, only one single rebar, and a single probe configuration with respect to rebar is not completely representative of real-world conditions. An error to resistivity measurements may also be introduced while the epoxy coating on the mortar specimens were used in this study due to a barrier between the electrodes and mortar surface.

The last and recent study in this category belongs to Sanchez *et al.* [126] who numerically proposed a modified 4-point Wenner method based on the experimental data, deployed on a bridge over the River Danube in Romania. In this study, a "rebar factor", f_b, was introduced through the modified version of Wenner method to measure the resistivity in reinforced concrete structures with thin concrete covers. Effect of rebar presence on concrete electrical resistivity measurements also can be found in details in similar studies by [122], [127], [77], [85], [86].

2.2.6.2.2 Presence of cracks in the concrete cover

Due to the presence of cracks, apart from embedded rebar, the electrical resistivity measurements may vary using Wenner probe technique because it is initially assumed that concrete is homogeneous and isotropic with semi-infinite geometry. In this section, some researchers' investigations in order to characterize cracks in concrete conducted by electrical resistivity measurements are summarized.

Lataste *et al*. [70] attempts to identify and locate cracks and spalling in concrete by means of electrical resistivity. For this a utilized instrument was built to measure the electrical resistivity through the use of four electrodes in a square configuration, rather than linearly conventional Wenner probe arrangement (Figure 2.6). The specified built probe allows taking the measurements in two orthogonal directions without having to rotate the probe between measurements. To change the function of electrodes from current imposing to potential measurement, the use of an electrical switch was considered. Both on-site measurements on a reinforced concrete slab and laboratory measurements on a cracked reinforced concrete beam were experimentally studied. To observe the effects of crack characteristics, such as crack opening, bridging degree between crack lips and depth of crack, a numerical model was developed as well and validated experimentally. It was reported that when a conductive crack was present, depending on the direction of imposed electrical current, resistivity readings could overestimate or underestimate the true resistivity. Once current was orthogonally imposed to the crack, no impact was detected, however, reduction in electrical resistivity measurements was observed while the crack was parallel to the imposed electrical current. For an insulated crack, perpendicular readings overestimated resistivity, and parallel measurements underestimated it. It was also concluded that crack depth has a direct relation to the electrical resistivity measurements (increase in crack depth leads to increase in the resistivity measurements).

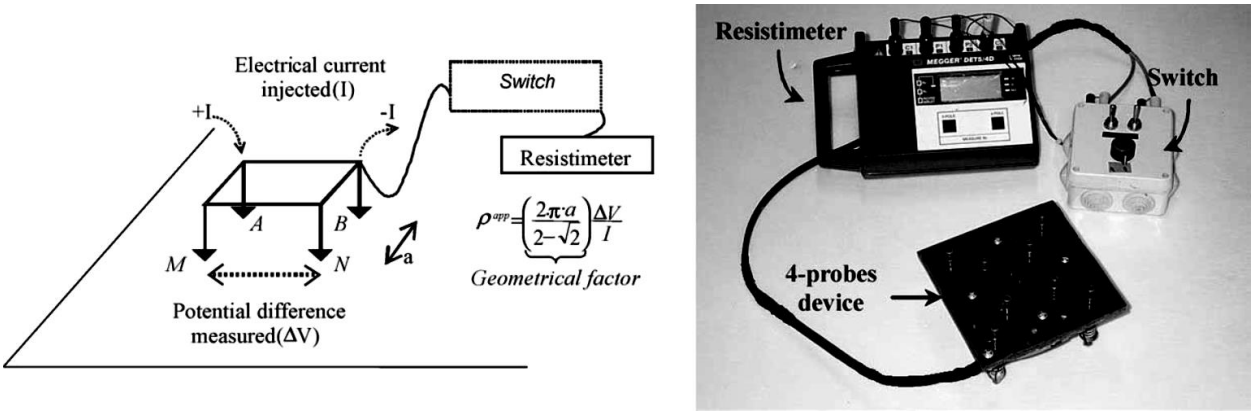

Figure 2.6. Four-probe square array principle [70].

A couple of assumptions and conclusions in Lataste's work [70] may not be adaptable with reality. First, it was assumed that the rebar effect on the resistivity measurements is independent of crack depth or type

which might not be true for the cases that rebar mesh or conductive crack present. Second, simulations on limited size concrete block can possibly exaggerate the crack impact. Finally, the four electrodes square configuration, which is a less common electrode setup compared to the Wenner probe array, may generate different measurement errors.

Goueygou *et al*. [87] used the same square probe configuration proposed in Lataste's work [70] to compare electrical resistivity measurements with transmission of ultrasonic waves for characterizing, detecting, and localizing the surface cracks. For taking measurements in both directions (parallel and perpendicular), concrete beam specimens bent via three-point loading to induce one main crack were constructed. Both non-destructive techniques were capable of identifying the main simple crack inside the concrete specimens; however, complexity rose when the number of cracks increased and, in most cases, became impossible to detect cracks depth and patterns. Similarly, experimental and numerical investigations in detecting and characterizing cracks using electrical resistivity measurements with a square probe were done by Shah *et al*. [128]. In their study, two experimental setups including a set of five cubic laboratory concrete specimens and a small area on a 40-year-old reinforced concrete slab as well as numerical model to identify the crack depth and differentiating insulated and conductive cracks were involved. Overall, it was showed that lower resistivity readings obtained from insulative cracks and larger resistivity measurements from conductive ones. From field data and numerical work, variations on electrical resistivity measurements were observed for different crack depth and opening [128].

Experimental study conducted by Wiwattanachang *et al*. [88] also investigated the capability of concrete electrical resistivity measurements with Wenner probe method in detecting a crack development in the concrete beams. Artificial cracks made up of plastic sheet inside a concrete beam to simulate insulated cracks as well as cracks being induced in a beam by a four-step loading test on its tension face were studied in this work. After correcting resistivity readings for the specimens' geometry, it was concluded that obtained data were increased for both crack types, although, only insulated cracks were examined, conductive cracks were not. Simulated images of electrical resistivity were plotted from obtained results,

as demonstrated in Figure 2.7. Although, using electrical resistivity measurements for detecting cracks inside concrete were explored in the study, investigations on different type of cracks and their orientations toward the probe were ignored.

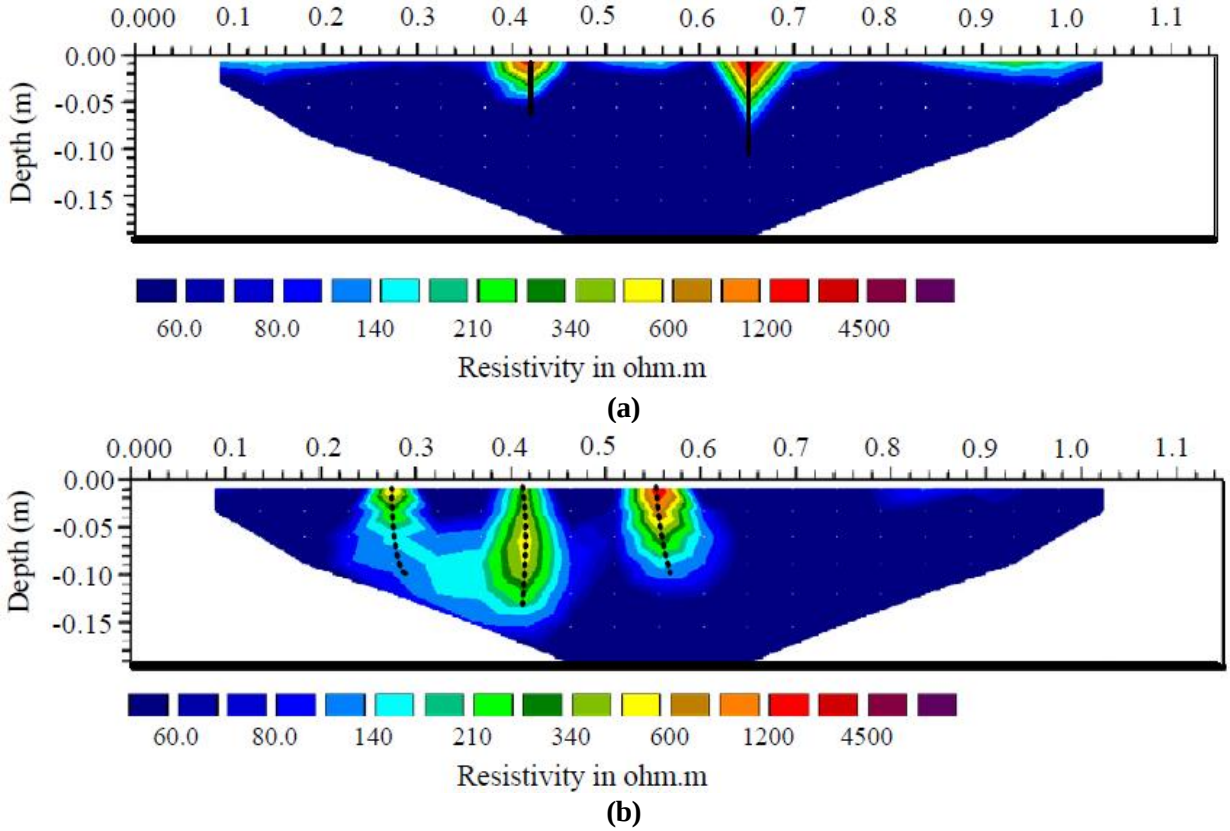

Figure 2.7. Electrical resistivity image of a concrete beam with cracks [88]: **(a)** concrete beam with artificial plastic sheets as crack; **(b)** concrete with cracks being developed from a four-point loading.

It was also numerically found that when cracking and delamination were present in reinforced concrete structures, electrical resistivity measurements were different from when they were not present [129]. Similar to previous studies, this finding gave rise to the conclusion that delamination at early stages can be detected using resistivity measurements with 21 linearly aligned electrodes instead of four-point Wenner method. However, proposed model in Chouteau *et al*. [129] only identified the effect on resistivity measurements as being different when cracking was present. In addition, to evaluate and detect cracks and discontinuities, such as joints, in massive concrete structures within pre-existing boreholes, electrical resistivity measurements with a DC current was stated to be a good quality assessment indicator [130];

however, using a DC current rather than AC current may result in unfavorable results due to polarization effect which was not considered in Taillet *et al*. [130].

A comprehensive numerical study by Salehi *et al*. [131] on the effect of different cracks types, depths, and widths incorporating both the presence of cracks and rebar mesh indicated that measurements on conductive cracks result in lower electrical resistivity values. For conductive cracks, numerical results showed that decreasing crack depth did not significantly disturb the electrical resistivity measurements. Furthermore, for an insulated crack between two inner electrodes, electrical resistivity readings led to a maximum error of about 200% higher than actual concrete resistivity. Conductive crack in here represents as a crack filled with water and insulated one denotes a crack without bridging and filled with air. It was also concluded that once the crack depth decreased, lower errors were observed. Also, the rebar and crack were found to act independently of one another while rebar mesh was present. Salehi's work lacked from validating numerical investigation with an experimental study. Following to this study, Morales [127] experimentally investigated the effect of rebar, chloride ingress, corrosion, and various crack types on concrete electrical resistivity measurements. For all moisture conditions, it was suggested that discrete cracks of all depth and conductivity properties should be avoided in order to minimize potential errors when performing resistivity measurements. Although, it was observed that electrical resistivity measurements were not significantly affected by surficial micro-cracking, it may be able to identify delamination as the difference observed between measured resistivity of in-tact and delaminated concrete covers. Still, investigations on the effects of cracking induced by corrosion, and insulated and conductive cracks with bridging conducting electrical resistivity measurements lacked in this study.

2.2.6.2.3 Probe spacing

Concrete is considered to be a heterogenous material and this is one of the assumptions behind the Wenner probe method. However, this assumption appears to be a likely source of error since aggregates inside concrete typically have greater resistivity and they propagated widely in different locations with various sizes. Hence, this inconsistency in the initial assumption of concrete homogeneity may affect resistivity

measurements. To mitigate this issue, some researchers recommended considering enough wide space between electrodes (usually between 20 mm and 70 mm) in order to reduce the influence of non-homogeneity due to the aggregates presence [80], [119], [121]. It was suggested to take several readings at various locations and then these measurements should be averaged. Many commercial instruments are also equipped with a variable probe spacing as well to allow the device to measure concrete resistivity involving larger aggregate size.

One recommendation to help reduce variance in resistivity measurements is to consider probe spacing 1.5 times higher than the maximum aggregate size [122]. It was observed that when probe spacing became smaller than the maximum aggregate size, standard deviation in the measurements increased to around 10% (Figure 2.8) [122]. For various probe spacing (16 mm, 25 mm, and 50 mm), Millard [121] experimentally found that as the maximum aggregate size became closer to the probe spacing, the scattering in the observed results increased. Therefore, to compensate the local effect of aggregates, larger electrode spacing should be considered for practical purposes. For concrete cubes (100×100×100 mm), while the electrode spacing was changed in different steps from 20 to 35 mm, the relative resistivity measurements increased by approximately 70% [94]. Increasing electrode spacing also resulted in increasing resistivity values to even a greater extent than that in the cubes for concrete cylinders [94]. Increase in resistivity observed due to wider spacing are in part also due to finite geometry and not just the aggregate size. The results of the resistivity measurements preformed on 28-day water-cured concrete slabs with and without embedded steel rebar indicated only a small difference for probe spacing less than 30 mm [80]. For larger electrode spacing, however, both the steel rebar and the probe spacing showed significant impact on the electrical resistivity measurements, and the larger the electrode spacing, the larger the effect of the steel rebar. For instance, increase in electrode spacing from 20 to 70 mm led to increase in resistivity by approximately 26% for the slab without any steel reinforcement whereas the resistivity values either increased by 33% or decreased by 25% depending on the orientation of taken measurements (perpendicular or parallel) for the slab with rebar [80].

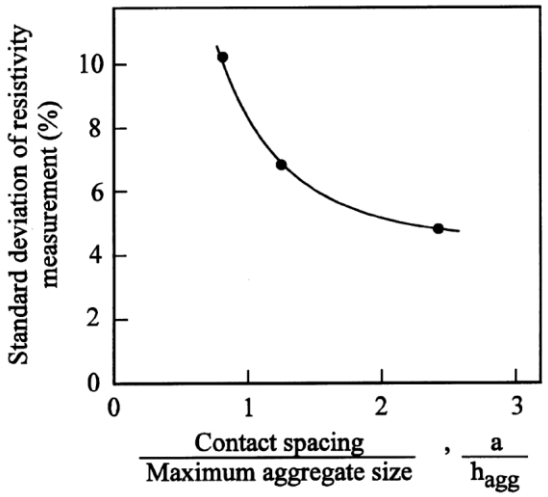

Figure 2.8. Effect of contact spacing on resistivity measurement [122].

According to Polder [68], the electrical current may travel through the concrete volume with approximately the same depth as of the electrode spacing. Hence, as the probe spacing increases, the current flows deeper inside the concrete volume and when the electrical current reaches to the surface of the rebar, the current is transported through the reinforcement and, thus results in lower resistivity observation [80]. For prismatic specimens, it was also suggested by Chen *et al.* [82] that the effects by the probe spacing can be ignored when the spacing is larger than 40 mm, however, the resistivity values increased with less electrode spacing. For application of Wenner probe method, the important role of electrode spacing should be definitely considered during electrical resistivity measurements as it will affect the obtained results.

2.2.6.2.4 Electrode contact

The contact area between the electrodes and concrete surface may alter the electrical resistivity measurements using four-point Wenner probe. The experimental investigation in electrolytic tanks and finite element modeling resulted in that the contact between the concrete surface and the probes has no significant influence on Wenner probe resistivity measurements [121], [122]. It was also reported a maximum error of 6% in resistivity (without stating lower or higher readings) when the diameter of electrode contact area varied from 1 mm to 40 mm [121]. According to Gowers work [122], misleading values can be lessened by use of a fairly low frequency and alternating current (AC). Practically, electrode

contact area becomes vital for both external current imposing and internal potential measurement electrodes. It was observed by Ewins [132] that contact resistance between electrodes and concrete surface can lead to significant increase in electrical resistivity values. Both symmetry of the system and the probe performance as it was also confirmed in Gowers work [122] may be affected by the contact resistance [132].

In two-electrode method (bulk resistivity measurements), poor contact between the plate electrode and the test cylinder surface is main responsible for electrode resistance. One solution to minimize the contact resistance effect is to use flexible electrodes [119]. Also, to mitigate this issue in laboratory testing, using an aid that allows for a good electrical contact such as an electrically conductive gel were recommended [133], [134]. Other alternative solutions included the use of soft conductive medium, saturated sponges, chamois cloth, and paper towels [95], [135]. By using a saturated sponge, only an average of 2% difference in resistance was reported for contact resistance between the sponge and concrete surface [96]. The sponge resistance is largely dependent on the moisture content of the sponges and the conductivity of the solution in which they are saturated. It was shown that in the two-point measurement procedure, a sponge contacting system can give a higher resistivity than those obtained using four-point techniques, and careful consideration must be given to the electrode-sample contacting system when trying to evaluate concrete resistivity [97]. According to McCarter's work [97], the sponge contacting method introduced a misleading resistance originating from the sponge-sample interface that was in series with the bulk resistance of the sample. Therefore, an operator using an electrical resistivity device needs to ensure proper contact between the electrodes and concrete surface as poor contact may affect the electrical resistivity readings. The influence of electrode-contact is less governing in the Wenner probe method than in the uniaxial method and hence, measurements can be performed in a wider frequency range (10 Hz to 10 kHz) [64].

2.2.6.2.5 Specimen geometry

In the four-point Wenner method, the electrical resistivity measurements are initially presumed to be performed on the domain of semi-infinite medium which is not a practically accurate assumption. This assumption leads to deviation from the ideal condition of having infinitely large geometry which can

possibly occur in different electrode orientations. For relatively small size concrete elements (e.g. cylinder or prism specimens), constriction of current to flow into a different field pattern is one of the major reason for this deviation. Even though, several researchers have realized the effect of specimens' geometry, only very limited information is available on this topic.

To account for interference between current flow and coarse aggregates in a small size sample, a suggested correction coefficient factor (or geometry correction factor) has been established in Spragg's work [136], using the simulations developed by Morris *et al*. [119]. The correction coefficient factor proposed formula is outlined below (Equation 2.5) and only needs to be used when $^{d}/_{a} \leq 6$ or $^{L}/_{a} \leq 6$ (where a and d are parameters related to electrode spacing and specimen diameter, respectively) [136].

$$k = 1.10 - \frac{0.730}{^{d}/_{a}} + \frac{7.34}{(^{d}/_{a})^{2}} \qquad \text{Equation 2.5}$$

For a standard cylinder size (φ100 mm × 200 mm), the correction coefficient value ranges from 1.8 to 1.9 while using the probe spacing of 38 mm [136], [98]. Also, for the correction factor (k), Morris *et al.* [119] plotted a graph based on the finite element modeling data to study a wide range of geometrical variations in concrete cylinders (Figure 2.9). However, this study provides wide-ranging values for correction factor; different electrode spacing and configuration as well as various geometrical concrete element types were not investigated (only 25.4 mm electrode spacing for concrete cylinders was considered).

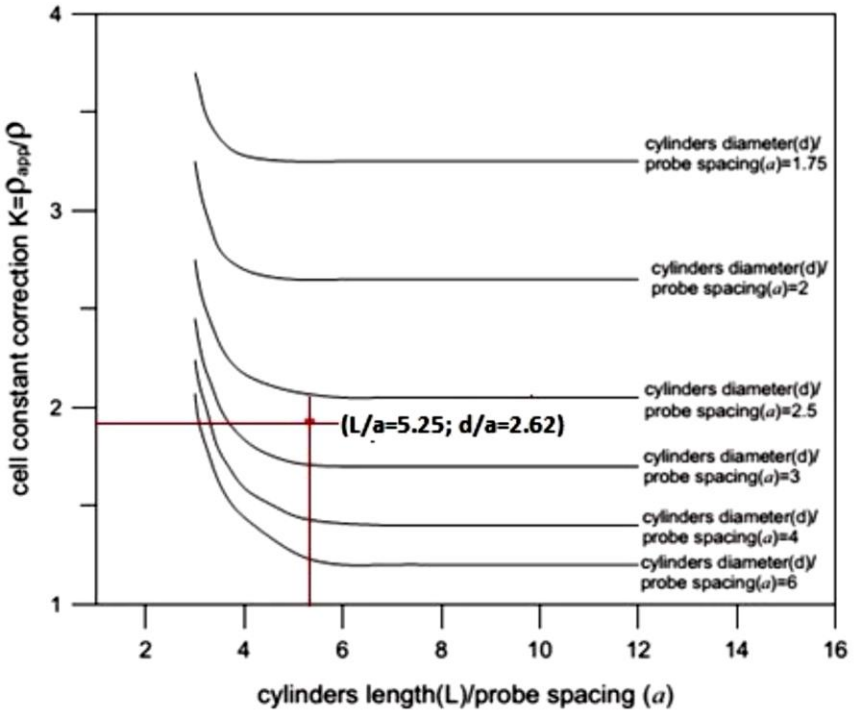

Figure 2.9. Cell constant correction to determine the concrete resistivity [119].

According to Millard [121] and Gowers *et al*. [122] through experimental findings, electrode spacing should be $^1/_4$ times smaller than concrete section dimensions and half the distance of the contact area from any element edge due to the three-dimensional current flow restriction closer to the edge. It was also observed that when the domain of the medium becomes smaller than the ideal semi-infinite condition, overestimated resistivity values were resulted. Study performed by Bryant *et al*. [75] found an average of 24% higher electrical resistivity values for cylindrical samples in comparison with concrete slab specimens for various ages even when the geometry correction factor was used; however, Shahroodi [137] reported an average 25.8% lower resistivity value. The differences in the mentioned values could possibly originate from variation in geometry correction coefficient, surface texture, device, operator, material, production and curing process [138]. Measured resistivity values can also change by the geometry of the measuring plane. The variation in resistivity values observed experimentally by Chen *et al.* [82] on the curved surface and the cutting flat surface showed an increased with the volume of cutting portion. Therefore, correction factor should be applied accordingly, especially for large size specimen. They also confirmed that the resistivity

of the cylindrical samples varied with the specimens' size even though the electrode spacing remains the same [82]. Furthermore, for the two-electrode method, since electrical current passes through the entire specimen volume, this measurement method is independent of specimen geometry while for the four-point method, the depth of the electrical current passing through the concrete volume is related to both the geometry of the sample and the distance between the electrodes. This independency was also reported in Sengul's work [94] when the electrical resistivity values using both two and four electrode methods for concrete block of size 300 mm × 300 mm × 200 mm (semi-infinite geometry) and standard cylinder samples were almost the same.

2.2.6.2.6 Electrical signal shape and frequency

Due to resistor-capacitor circuits' behavior in saturated cementitious system, it introduces a phase difference between electrical current imposing and the measured potential (impedance) [99]. At different frequencies, there is a significant difference in impedance and it follows that the real component of the impedance at zero phase angle is the true uniaxial resistance. Since the phase is almost never zero, the meters record the total impedance: the real and imaginary components added in quadrature. The impedance spectrum consists of two arcs in high and low frequency ranges is illustrated in Figure 2.10 [64]. At higher frequencies, the impedance spectrum characteristics are featured by the concrete microstructure, but these characteristics are mainly attributed to the conditions at the electrode-concrete interface for low frequency domain. Generally, the frequency range in between 0.5 to 10 kHz is used for uniaxial electrical resistivity measurements method, however, no general statement can be found on the optimum frequency since it varies with moisture contents and mixture proportions. At lower frequencies (below 500 Hz), it was stated that electrical resistivity measurement can result in overestimated data because of electrode-concrete contact interface impact [64]. As it is described in section 2.2.6.2.4, this effect is less dominant in the four-point probe method, and a wide-ranging frequency (10Hz to 10kHz) can be conducted [64].

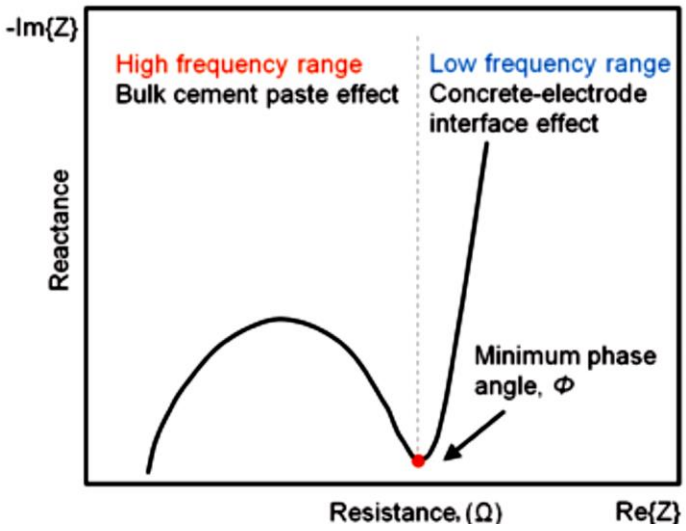

Figure 2.10. Schematic representation of the AC Impedance response of concrete [64].

Two signal shapes used usually for electrical resistivity measurements are sine-wave and square-wave AC current. Ewins [132] reported 800% error in results when high frequency (600 Hz) sinusoidal signals with poor contact were used for taking the resistivity measurements. Presence of parasitic capacitors and uneven contact resistance were the two major error sources affected the accuracy of the measurements. However, impact from parasitic capacitors was larger. To avoid unwanted effects, using low frequency square wave signal, instead of sine wave, was recommended in Ewins work [132]. Similarly, it was found that sine wave Wenner probe with 300 Hz frequency was adversely affected by the addition of external resistors compared to the case for which square wave Wenner probe was used or frequency of the sine wave signal was reduced [121]. The external resistors used to mimic the unbalanced contact area resistance. Having unbalanced contact resistor in the voltage measurement circuit has the most significant effect on the accuracy of four-point probe method while high frequency sinusoidal AC signal is being used.

2.2.6.2.7 Effect of temperature

Temperature variation has been reported to have a significant influence on electrical resistivity of concrete, and an increase in temperature results in a decrease in resistivity. Electrical current generally flows through the ions dissolved in the pore solution and can be affected by temperature which causes changing the ion (Na^+, K^+, Ca^{2+}, SO_4^{2-} and OH^-) mobility, ion-ion and ion-solid interactions, as well as the ion concentration

in porous media [68], [139], [140]. It was reported that the effect of temperature on bulk pore solution resistivity was noticeably different from that of cement paste or mortar with the same ion concentration, which was most likely because of strong ion-solid interactions in cement paste or mortar and less internal ionic frictions [122]. Increase in temperature has an impact on concrete isotherm curves and also tends to reduce the moisture content of concrete which indirectly affects the resistivity readings [141]. So, temperature plays an important role in concrete electrical resistivity and a number of researchers attempted to correlate its effect with true concrete resistivity values. It should be noted that not all studies performed the resistivity measurements for the different temperatures at the same moisture content. If not saturated (i.e. immersed), the concrete needs to be left for a long enough time at a given temperature and moisture. Castellote *et al*. [139] as well as Liu *et al*. [98] have attempted to produce equations to convert from one temperature to a normalized temperature.

Studies conducted by Millard [142] and Gowers *et al*. [122] found that decrease in ambient temperature led to increase in resistivity values and suggested a correction factor of 0.33 KΩ-cm/˚C in order to compensate the variation in temperature; however, the range of temperatures used in their studies was limited. For simplicity, a change of 3% to 5% on resistivity measurements at per ˚C has been recommended for temperature range of 0 ˚C to 40 ˚C [68], [143]. A linear relationship has been developed on temperature dependency of resistivity [140], [144], [101]:

$$\rho = \rho_0(1 + \alpha.\Delta T) \qquad \text{Equation 2.6}$$

where

ρ: resistivity at temperature T (˚C)
ρ_0: resistivity at reference temperature T_0
ΔT: temperature difference between T and T_0
α: temperature coefficient (between 0.022-0.035/˚C)

It was found that above equation is only applicable over a limited interval of ±5 ˚C to the reference temperature [140], [144], [101]. A model developed in DuraCrete [145] also describes the correlation between ρ_T at temperature T (˚C) and resistivity ρ_{20} at 20 ˚C:

$$\rho_T = K_T.\rho_{20} \qquad \text{Equation 2.7}$$

where K_T is characteristic value of the temperature factor for resistivity and K_T is defined as:

$$K_T = \frac{1}{1 + K(T - 20)} \quad \text{Equation 2.8}$$

K=0.025 when $T < 20$ ℃ K=0.073 when $T > 20$ ℃

Several researchers also defined a wide agreement for this correlation using Arrhenius law [139], [144], [146], [101], [140], [98]:

$$\rho_T = \rho_0 . \exp\left[\frac{E_{a,\rho}}{R}\left(\frac{1}{T} - \frac{1}{T_0}\right)\right] \quad \text{Equation 2.9}$$

where

ρ: resistivity at temperature T (K)
ρ_0: resistivity at reference temperature T_0(K)
R: gas constant (8.314 $kJ^{-1}mol^{-1}$)
$E_{a,\rho}$: activation energy for resistivity (J/mol) (ranges from 16.9 J/mol to 42.77 J/mol)

The activation energy of conduction ($E_{a,\rho}$) can be determined using the slope of a plot of the natural logarithm of resistivity and the inverse of temperature [99]. The slope of the best-fit line is multiplied by the negative of the universal gas constant [8.314 $kJ^{-1}mol^{-1}$] to determine the activation energy of conduction. The above-mentioned correlation is published using only standard cylinder samples (φ100×200mm) and additional work is still needed for real-world resistivity measurements and also to consider the influence generated by moisture content as an additional factor. For standard curing conditions in water at 20 ℃, it was suggested the effect of temperature can be eliminated [62]. Spragg *et al*. [99] stated that the resistivity measured using the same mature sample can differ by as much as 80% when the temperature of the sample fluctuates between 10 ℃ and 45 ℃. Additionally, several other studies showed in details a prominent effect on resistivity results due to temperature variation [102], [103], [106], [107]. In summary, when the temperature increases, electrons move faster causing higher electrical conductivity, thus lowering resistivity.

2.2.6.2.8 Effect of moisture content

Moisture content is one of the influencing factors that can inversely affect the concrete electrical resistivity measurements. Essentially, electrical conductivity increases with an increase in moisture content due to

change in the ion mobility [98], [147]; however, there could be a difference in resistivity between samples immersed (either water or lime water) and those in high humidity. Larsen *et al.* [147] found that when moisture degree decreases from 88% to 77%, the resistivity increases by an average of two times and from 88% to 66%, increases by an average of 6 time. In the air-dry state, it was also reported that concrete had approximately 50% higher resistivity than that in saturated condition [62]. As the electrical current is carried by ion flowing through the pore solution in concrete, higher moisture content leads to easier electrical flow and thus, the electrical resistivity reduced. However, at low resistivity values, moisture content has less effect on the accuracy of the resistivity measurements [102]. For quality control purposes, it is essential to ensure the same moisture degree in different mixtures and also the resistivity measurements of the specimens with low moisture content are inappropriate [82]. Furthermore, it was experimentally found that poor surface saturation using pressurized water and static ponding can lead to misinterpretation of resistivity of over 30% compared to full laboratory saturation [138]. So, additional research is still required to simulate the onsite saturation by different systems and to understand how much time is required for water to penetrate through concrete surface in order to obtain constant moisture level through the bulk specimen.

2.2.7 Correlation between concrete resistivity and its durability characteristics

Through following sections, relationship between electrical resistivity and the two main concrete durability characteristics including chloride ingress and corrosion of embedded reinforcements will be presented.

2.2.7.1 Correlation between electrical resistivity and chloride diffusivity

Diffusivity is the controlling parameter which determines the time it takes for chloride ions to diffuse into concrete and reach the critical chloride threshold for corrosion initiation. Typically, this can be measured through Rapid Chloride Migration (RCM) test, Rapid Chloride Permeability Test (RCPT) or Bulk Diffusion (BD) method [148]. However, such test methods are either time consuming or expensive for evaluating the concrete permeability properties. Hence, electrical resistivity was found experimentally and theoretically to be an efficient method that can be applied indirectly to determine concrete chloride permeability.

In theory, the relationship between diffusivity of ion species i and its partial conductivity can be described by Nernst-Einstein equation (Equation 2.10) [149]:

$$D_i = \frac{RT\sigma_i}{Z_i^2 F^2 C_i} \quad \text{Equation 2.10}$$

where D_i is the diffusivity of ion i (m^2/s); σ_i is the partial conductivity of ion i (s/m); R is the gas constant (8,314 J/mol); T is absolute temperature (K); Z_i is the charge of ion i ; F is the Faraday's constant (96500 Coulombs/mole) and C_i is the concentration of ion i (mol/m^2). By applying Archie's law, the correlation between the bulk resistivity, pore solution resistivity, and porosity can be expressed by Equation 2.11 [94], [150]:

$$F = \frac{\rho}{\rho_0} = \frac{\sigma_0}{\sigma} = a.\varphi^{-m} \quad \text{Equation 2.11}$$

where F is formation factor; a and m are constants; and φ is porosity of concrete. m is dependent on tortuosity of concrete and have been found to be 1.5 to 3.2 [94], [150]. Combining the above equations gives the formation factor as a function of effective chloride diffusion coefficient of concrete (D_{eff}) and chloride ion diffusion coefficient in the pore solution (D_0) (Equation 2.12).

$$F = \frac{D_0}{D_{eff}} \quad \text{Equation 2.12}$$

Several researchers have also conducted various experiments to investigate the relationship between concrete resistivity and chloride diffusivity. A strong correlation between these two parameters has been reported for various concrete mixtures at different ages [62], [76], [75], [103], [106], [107]. Due to presence of chloride, experimental results showed that the electrical resistivity of mortar was reduced [122]. The concrete resistivity inversely related to chloride ingress, where lower resistivity indicated the area that chloride penetration will be faster [68]; however, its effect on electrical resistivity readings is relatively small compared to carbonation process [68], [76]. Recent field experience indicated that the relationship between surface resistivity at 28 days and 56-days with RCPT data was moderate [108]. Experimental investigation by Florida Department of Transportation (FDOT) on wet cured concrete specimens in a controlled environment or cured samples in lime water, using RCP test and 4-point Wenner method in

conjunction, confirmed the inverse correlation of chloride resistivity [151], [152]. The summary of FDOT proposed relationship between resistivity and chloride can be found in the Table 2.6. The table also shows an indication of the risk of chloride penetrability with regards to charge passed based on ASTM C1202 standard [153]. In RCP test, a 60V potential is applied across the sample of 95 mm diameter and 50 mm thickness for 6 hours. Current readings are taken every 30 minutes, at minimum, and then the total charge passed in Coulombs is calculated by integrating the Current vs. Time graph developed from the readings taken.

Similar experimental investigation conducted by the Louisiana Transportation Research Center (LTRC) also found a good correlation between resistivity and RCP test while the classified concrete permeability to surface resistivity values equal to those proposed by FDOT as shown in Table 2.6 [89]. Following these experimental investigations, AASHTO published a provisional method TP 95-11 for indicating the concrete's ability to resist chloride ion penetration using surface resistivity measurement method [61]. However, Kansas Department of Transportation (KDOT) reported different value range for surface resistivity [109]. For instance, it is considered that chloride penetration is high when surface resistivity value is less than 7.0 kΩ-cm for 4×8 cylinder with 1.5 inch probe spacing which is a relatively small value compared to two other experimental results (Table 2.6) [109].

Table 2.6. Classification of concrete permeability to surface resistivity values.

RCP Test versus Surface Resistivity					
		Surface Resistivity Test			
Chloride Ion Permeability	RCP Test Charged Passed (Coulombs)	4×8 Cylinder (kΩ-cm) a=1.5 k=1.8 (measured)	6×12 Cylinder (kΩ-cm) a=1.5 k=1.8 (measured)	Semi-infinite Slab (Real)	KDOT 4×8 Cylinder (kΩ-cm) a=1.5 k=1.8 (measured)
High	> 4000	< 12	< 9.5	< 6.7	< 7.0
Moderate	$2000 - 4000$	$12 - 21$	$9.5 - 16.5$	$6.7 - 11.7$	$7.0 - 13.0$
Low	$1000 - 2000$	$21 - 37$	$16.5 - 29$	$11.7 - 20.6$	$13.0 - 24.3$
Very Low	$100 - 1000$	$37 - 254$	$29 - 199$	$20.6 - 141.1$	$24.3 - 191$
Negligible	< 100	> 254	> 199	> 141.1	> 191

In addition to the experimental study on laboratory specimens, the correlation between electrical resistivity and apparent diffusivity coefficients (D_{app}) is reported by researchers for field specimens [108], [110]. Due to complexity of the exposure environments such as humidity difference, temperature and the elevation from water level, results are scattered. However, a recent investigation on Florida bridges showed a better correlation between resistivity and apparent diffusivity once resistivity was measured under saturated condition [77]. The authors of this paper are currently involved in a study where the effect of full or partial saturation is being studied. To predict chloride threshold (Cl_{TH}) values, the electrical resistivity method was used periodically during 1000 days monitoring of reinforced concrete element exposure to marine environment [85]. After applying the geometrical factor, the relationship between chloride content, in terms of chlorides relative to the weight of cement, and resistivity (ρ) can be expressed as shown in Equation 2.13 [85]:

$$Cl_{TH}(\%) = 0.019\rho + 0.401 \qquad \text{Equation 2.13}$$

A good correlation between RCM coefficients and electrical resistivity measured by two-electrode method was reported in European Union-Brite EuRam III experimental investigation [145]. Similarly, this correlation for resistivity measured by Wenner method is reported in Dhir's work [154]. Although, resistivity measurements can be possibly a good alternative or replacement for the RCM test, more experiments need to be conducted to validate this correlation. The electrical resistivity test was suggested to be used as a quality control predictor of the chloride ingress resistance, but not as a predictor of diffusion behavior of all kind of concretes or as replacement of the long term diffusion tests [111]. FDOT long-term monitoring of various concretes concluded that correlation between the RCM and the long-term tests were equal or slightly better than those obtained by the RCPT and surface resistivity due to less sensitivity of RCM test to presence of supplementary cementitious materials [155]. A linear trend exists between chloride diffusion coefficient (D_{RCM}) derived by RCM test and concrete electrical conductivity using two electrode resistivity measurements [91], [102], [112], [113]. Additionally, to account for the retardation of chloride penetration due to the chloride reaction or binding with the cement phases, a factor needs to be applied to

electrical resistivity measurements [114]. A reaction factor (r_{cl}) is defined as the ratio between the diffusion coefficients D_{app} and D_{eff} assuming lineal chloride binding as shown in Equation 2.14 where ρ_{app} and ρ_{eff} are apparent and effective electrical resistivity [114]:

$$r_{cl} = \frac{D_{eff}}{D_{app}.\varphi} = \frac{\rho_{app}}{\rho_{eff}} \qquad \text{Equation 2.14}$$

2.2.7.2 Correlation between electrical resistivity and reinforcement corrosion

Once rebar is de-passivated and corrosion is initiated by chloride ions or carbonation, corrosion rate will be the most influential parameter that determines how fast the reinforced concrete structure is deteriorating. It is dependent on many parameters including oxygen availability, ratio of anodic/cathodic area, relative humidity (RH), concrete electrical resistivity, and so on (Figure 2.11) [156]. When enough oxygen is available to supply the anodic current especially under aerated state (such as the splashing area zone), cathodic control no longer exists. In this condition, the corrosion rate can be limited by controlling the flow of ionic current through concrete which is directly related to electrical resistivity of concrete [156]. Therefore, several researchers have attempted to correlate the corrosion probability and corrosion rate to concrete electrical resistivity [115], [157]–[162].

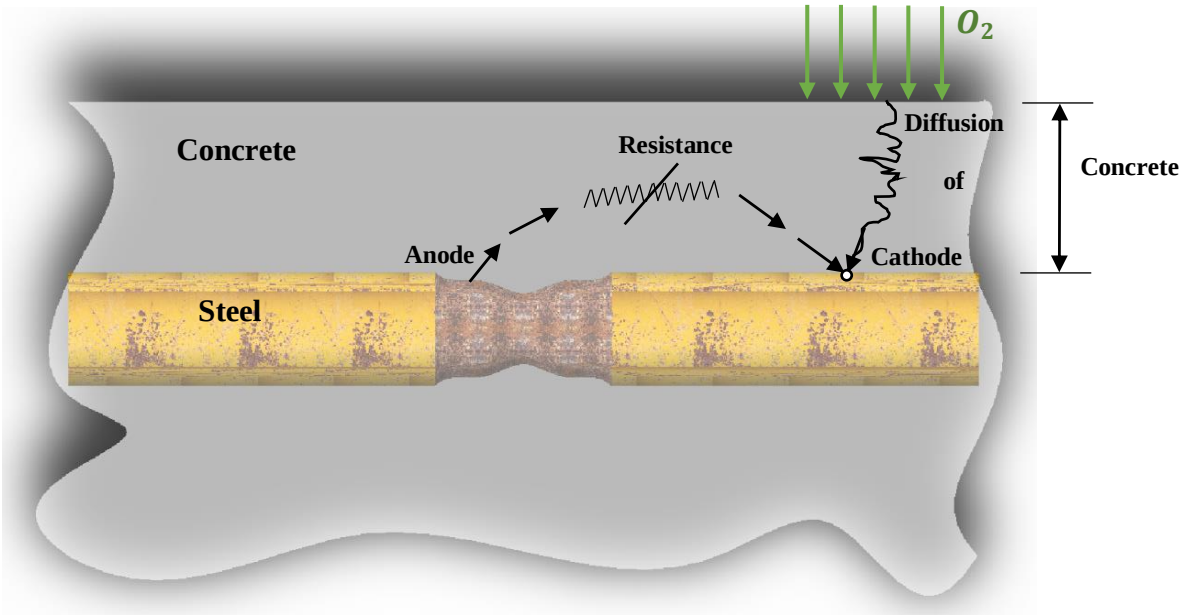

Figure 2.11. Schematic descriptions of factors which may affect corrosion rate of steel in concrete: i) O_2 availability and ii) electrical resistance of concrete (Reproduced from [156]).

Among all the studies conducted so far, there is an agreement that corrosive environment in reinforced concrete and electrical resistivity of concrete have an inverse relationship. As the electrical resistivity of concrete decreases, the rate of steel reinforcement corrosion increases. A theory by Glass *et al*. [157] stated that the corrosion rate of reinforced concrete is under anodic control with the anodic reaction being limited by the mortar resistivity. Glass's anodic resistance theory is also supported by studies conducted by Morris *et al* [115] and Bertolini *et al* [158]. In their investigations, it has been found that concrete resistivity not only affected corrosion rate, but also the corrosion potential [115], [158]. The only standardized test method for corrosion monitoring is the ASTM C876 half-cell potential mapping technique [159]. Hence, electrical resistivity measurements can be an effective standard indicator of steel reinforcement corrosion potential and rate.

Combining both half-cell potential and electrical resistivity measurements techniques makes it possible to examine corrosion probability and corrosion rate once it is initiated [160]. For high resistivity values, Carino [160] stated that even if the embedded rebar in concrete is actively corroding detected by half-cell potential technique, the corrosion rate may be slow when steel rebar de-passivates; thus the concrete electrical

resistivity has better correlation with corrosion rate than half-cell potential. Experimental investigation on reinforced concrete specimens immersed in saline solution came to the conclusion that steel rebar is likely to reach a corrosion state while resistivity readings are lower than 10 kΩ.cm, and reach a passive state when resistivity measurements are higher than 30 kΩ.cm [115]. The results also showed that the risk for chloride-induced corrosion and the chloride threshold value that will initiate the corrosion process can be estimated via a straightforward and non-destructive technique like concrete resistivity [85]. For various concrete mixture types, Polder and Peelen [76] indicated the corrosion initiation with respect to electrical resistivity under simulated de-icing salt, but no relationship or effect was established. Similarly, Basheer *et al*. [112] and Smith *et al*. [102] used both electrical resistivity measurements and half-cell potential to evaluate the probability of corrosion in embedded steel rebar but then again, no correlation was developed. It was also confirmed that corrosion potential can be detected by means of electrical resistivity but it was not specifically indicated how this can be done [161]. In addition, using the electrical resistivity or half-cell potential measurements was suggested to evaluate the deterioration caused by corrosion in the experimental study preformed on a concrete bridge deck [162]. In this study, it was stated that no need of electrical connection to embedded rebar is the main advantage of electrical resistivity over half-cell potential technique. The effect of concrete cover as an influential parameter on corrosion detection using both electrical resistivity and half-cell potential measurements has been studied experimentally [127]. For small concrete cover thickness, it was observed that both measurement corresponded well together, but more discrepancy in measurements values was obtained when concrete cover became thicker [127]. From few published papers in this area that examined the possibility of corrosion by applying both electrical resistivity and half-cell potential technique, it was difficult to find a systematic methodology. As a rule of thumb, methodology proposed in the Figure 2.12 by Sadowski [163] can be used when possible corrosion areas are identified by both half-cell potential and a four-point Wenner probe. Only identifying the probability of corrosion was suggested when conducting a corrosion assessment [163].

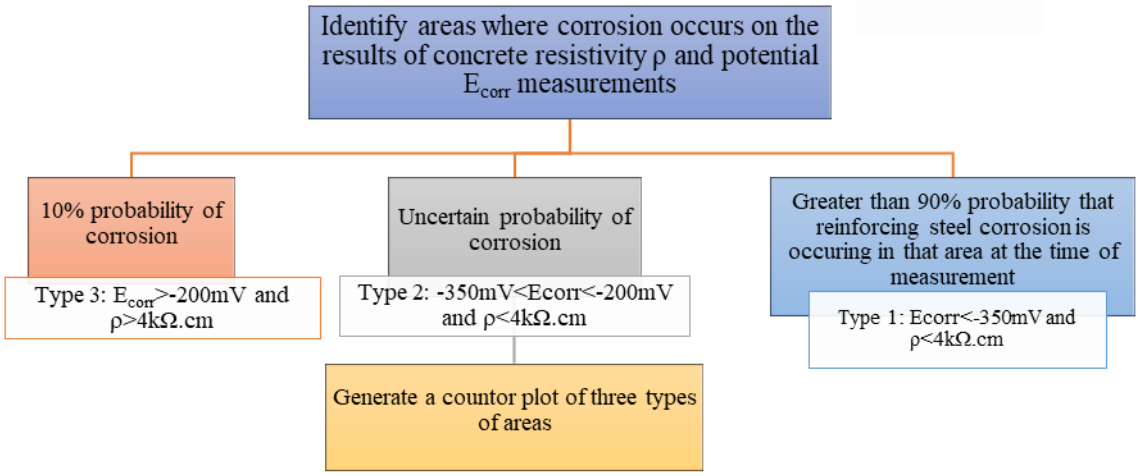

Figure 2.12. Assessment of corrosion probability in concrete slabs through half-cell potential and resistivity measurements [163].

A number of researchers as well as commercial Wenner probe instrument manuals (Proceq and Giatec Scientific Inc. [164], [165]) provided a general guideline in terms of corrosion risk when interpreting electrical resistivity measurements, as seen in Table 2.7. The difference between provided resistivity values originates in the various experimental setup, concrete quality, concrete composition, and initial chloride concentration. For example, the corrosion state resistivity for passivation value reported in Polder's [68] review is higher than the one recorded in Morris's work [115] due to different experimental setup and test conditions.

Table 2.7. Concrete resistivity and risk of corrosion of steel reinforcement.

Corrosion Risk	Resistivity values (kΩ.cm)		
	Polder [68]	Song and Sarawath [166], Elkey and Sellevold [143]	Commercial Wenner probe instrument manuals [164], [165]
High	< 10	< 5	≤ 10
Moderate	$10 - 50$	$5 - 10$	$10 - 50$
Low	$50 - 100$	$10 - 20$	$50 - 100$
Negligible	> 100	> 20	≥ 100

A linear relationship between concrete electrical conductivity and corrosion rate has been found in several articles [158], [160], [167]–[169]. Experimental study on carbonated mortars also confirmed this linear trend and showed a different slope in case of chloride presence as the corrosion rate was affected by $Cl^-/_{OH^-}$ratio [168]. Variation in concrete cover depth as well as concrete composition also showed an

effect on the slope of linear trend between resistivity and corrosion rate [158]. Andrade *et al.* [170] proposed an empirical equation describing relationship between resistivity and corrosion rate.

$$I_{corr} \cong \frac{3 \times 10^3}{\rho} \qquad \text{Equation 2.15}$$

Two other similar models have been proposed by DuraCrete [145] and LIFECON [171], as illustrated below:

$$I_{corr} = \frac{k_0}{\rho(t)} \times F_{cl} \times F_{Galv} \times F_{O_2} \qquad \text{Equation 2.16}$$

where

I_{corr}: corrosion rate in $^{\mu A}/_{cm^2}$
k_0 : constant regression parameter in $^{\mu m.\Omega.m}/_{a}$
$\rho(t)$: actual resistivity at time t in $\Omega.m$
F_{cl}: accounting for the influence of the chloride content
F_{Galv}: influence of galvanic effect
F_{O_2}: availability of oxygen

In most cases, F_{cl} is dependent on the chloride concentration at the location that corrosion occurs and F_{Galv} and F_{O_2} equals to 1. Due to microcell geometric arrangements of anodic and cathodic sites, concrete electrical resistivity plays an important role in controlling corrosion rates [169]. Similar to Glass's study [157], it was stated by Guliker [169] that overall corrosion cell resistance is not inherently controlled by concrete electrical resistivity, but rather cathodic activation controls mostly. It should always be considered that the interpretation of electrical resistivity measurements is a challenging task due to many variables affecting the results such as moisture condition, salt content, etc.

In summary, it can be concluded that still large range and scatter exists for correlation between corrosion rate and concrete resistivity. Also, effect of moisture state and temperature as well as corrections to corrosion rate measurements should be considered during an investigation on finding correlation between resistivity and corrosion rate. Knowledge is still lacked in the literature to understand which mechanism dominates the corrosion process and how resistivity measurements are impacted. To practically determine the corrosion and resistivity relationship, more field data should be collected and analyzed. In order to address some of these issues, authors of this paper initiated a project with field specimens as shown in

Figure 2.13. In this study, influence of various parameters (noted below) on resistivity are being studied (Parameters: cover thickness, crystalline water-proofing admixtures effect, cement type). In addition, authors are also studying the effect of self-sealing on resistivity of concrete. Previous work done in this area (self-sealing) is reported elsewhere [1], [20].

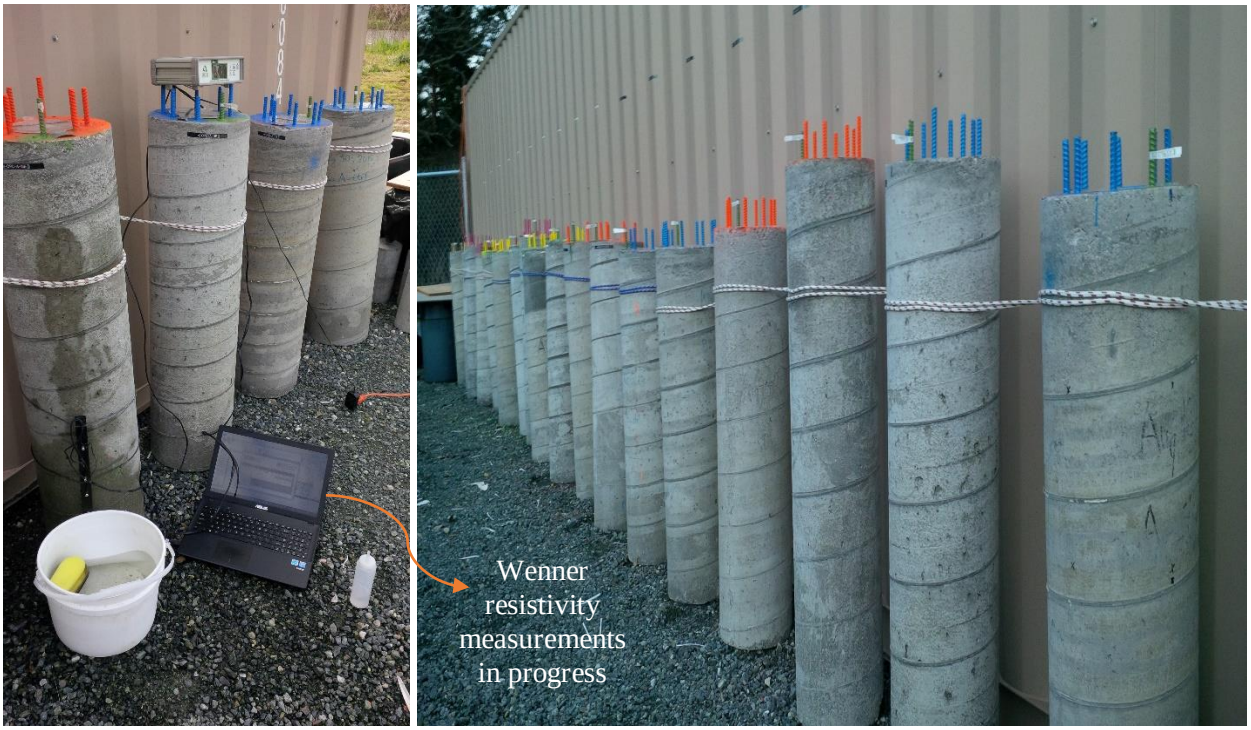

Figure 2.13. Instrumented circular hollow columns being studied by authors to establish the relationship between electrical resistivity and durability characteristics.

2.2.7.3 Correlation between electrical resistivity and compressive strength

One of the most important mechanical properties of concrete is compressive strength. It can be simply measured by compression testing machine, as load at the failure divided by area of specimen gives the compressive strength of concrete [111]. Thus, a number of researchers performed different experiments to understand the relation between compressive strength and electrical responses in cementitious materials. In the compressive strength, one of the key factors is the strength of Interfacial Transition Zone (ITZ) that has no remarkable impact on concrete electrical resistivity. It was observed when different cementitious materials were used in concrete mixture, there was no sensible relationship between concrete resistivity and

compressive strength ($R^2 = 0.413$) [111]. This is mainly linked to the fact that chemical compound of pore solution has not a great impact on compressive strength while affecting the concrete resistivity significantly. On the other hand, for the case of similar cementitious materials, better correlations can be achieved between compressive strength and concrete resistivity due to relationship between permeability and compressive strength [111]. As the strength increases, the electrical resistivity increases correspondingly for the same concrete mixture design. The study on the electrical properties of concrete with White Portland Cement also found an approximately linear trend between these two properties as both directly depend on the porosity of the matrix at early age. As concrete matured, this relationship was affected by other properties such as the conductivity of the pore solution and the degree of concrete saturation [72]. Also, as the density and compactness of the concrete structure increases, its compressive strength and the electrical resistivity will both increase. It was reported that at the same *w/c* ratio, the changes of the specimens' resistivities with different sizes (φ100 mm × 200 mm & φ150 mm × 300 mm) were close to those changes of the compressive strengths. For example, the differences between the resistivities or compressive strengths of the specimens were both around 93% at *w/c* of 0.6 and 95% at *w/c* of 0.4 [82]. No direct relationship between 56-days concrete electrical resistivity and 28-days compressive strength was found in Gudimettla's work [108] due to variety of samples taken from different field projects. In terms of activation energy, the investigation done by Liu and Presuel-Moreno [100] showed that resistivity is noticeably higher than the reported activation energy for compressive strength. In conclusion, there is no practical correlation between electrical resistivity and compressive strength for various cementitious materials; however, for the same mixture design, electrical resistivity is linearly related to compressive strength. Generally, as concrete permeability decreases, both electrical resistivity and compressive strength increases.

2.2.7.4 Correlation between surface and bulk electrical resistivity

As it is discussed in previous sections, every electrical resistivity (ρ) measurement is composed of a resistance (R) and a geometry correction factor (k) that converts the resistance to a resistivity which is a geometry independent intrinsic material property [116]. The correction factor (k) depends on the geometry

and size of the sample and the electrodes location. Hence, for the same concrete material, variation in electrode geometries and sample size may result in different resistance values but eventually will yield the same resistivity using Equation 2.17. Four common measurement electrode geometries that have been employed in several studies to conduct electrical test on cementitious cylinders are included: (1) uniaxial resistance (or bulk resistance), (2) surface resistance, (3) embedded sensors, (4) disc method (one external electrode). In this section, researchers' review on correlation between the first two common (bulk and surface) resistivity measurement methods are summarized.

$$\rho = R.k \qquad \text{Equation 2.17}$$

Theoretically, the ratio of surface and bulk resistance for standard size cylinder specimen (100 mm × 200 mm) and probe spacing of $a = 50$ mm can be computed in Equation 2.18 [119]:

$$\frac{R_1}{R_2} = \left(\frac{\rho_1}{\rho_2}\right)\left({}^{1}/_{8}\right) \qquad \text{Equation 2.18}$$

where

R_1 : resistance measured by 4-point Wenner method (surface resistance)
R_2 : resistance measured by uniaxial method (bulk resistance)
ρ_1 : resistivity measured by 4-point Wenner method (surface resistivity)
ρ_2 : resistivity measured by uniaxial method (bulk resistivity)

The ratio of two different resistivity types (ρ_1 and ρ_2) is equal to 2.63 [119]. Therefore, the theoretical ratio of surface and bulk resistance can be computed as:

$$\frac{R_1}{R_2} = {}^{2.63}/_{8} = 0.33 \qquad \text{Equation 2.19}$$

Also, a number of researchers experimentally attempted to study this correlation between bulk and surface resistivity data. Studies performed by Ghosh *et al.* [117], [118] showed the correlation between bulk and surface resistivity for different groups of binary and ternary mixtures. It was observed that for most groups of mixtures, the coefficient of determination (R^2) values for linear trend line were higher than 0.8 and sometimes close to 1 except some silica fume mixtures at early ages where the coefficient became less than 0.80. The linear trend line varied from 0.29 to 0.47 at different concrete age of 7, 14, 28, 56, 91, and 161 days. For probe spacing a = 38.1 mm, Spragg *et al.* [96] also reported a strong linear correlation with an

$R^2 = 0.9986$, with surface resistivity measurements tending to be 1.86 times higher than bulk resistivity which supports previous work done by Morris *et al*. [119]. Several Department of Transportation (DOT) and other agencies participated in a round robin program (summarized by Indiana DOT). A recent study on specimens cast during actual concrete production in the field through different US states proved that the surface and bulk measurements correlate extremely well with each other at 28 and 56 days age [108]. It was observed that the surface resistivity results were typically 1.9 times higher than the bulk resistivity obtained data. Authors have found a similar correlation between bulk and surface resistivity ($R^2 = 0.979$).

Both surface and bulk resistivity measurement methods have been used to determine the presence of a heterogeneity problem [116]. To investigate the heterogeneous systems, the surface and uniaxial resistivity tests were performed on the cylindrical specimen with a 10–mm thick white cement paste on outer layer and the prismatic specimens with two separate layers of white and grey cement pastes setup in parallel and series configurations, as illustrated in Figure 2.14 [116]. For the uniaxial case, the total resistivity (ρ_c) can be calculated through the proposed Equation 2.20 and Equation 2.21 for parallel and series configurations, respectively. a correction factor (Γ) has been developed for heterogeneity which depends on the material of interest and proposed an approach to compare the resistivities measured from a surface test and a bulk test. In this approach, if there is heterogeneity, the values from the two tests will be different. This difference can give an indication as to whether the surface layer is more or less resistive [116]. Similarly, correlation between surface and bulk resistivity found in other studies indicated a strong relationship between the resistivity values when the appropriate geometry factor was applied [80], [94].

$$\frac{1}{\rho_c} = \sum_{i=1}^{n} \frac{A_i}{\rho_i} \quad \text{(Parallel configuration)} \quad \text{Equation 2.20}$$

$$\rho_c = \sum_{i=1}^{n} \rho_i . L_i \quad \text{(Series configuration)} \quad \text{Equation 2.21}$$

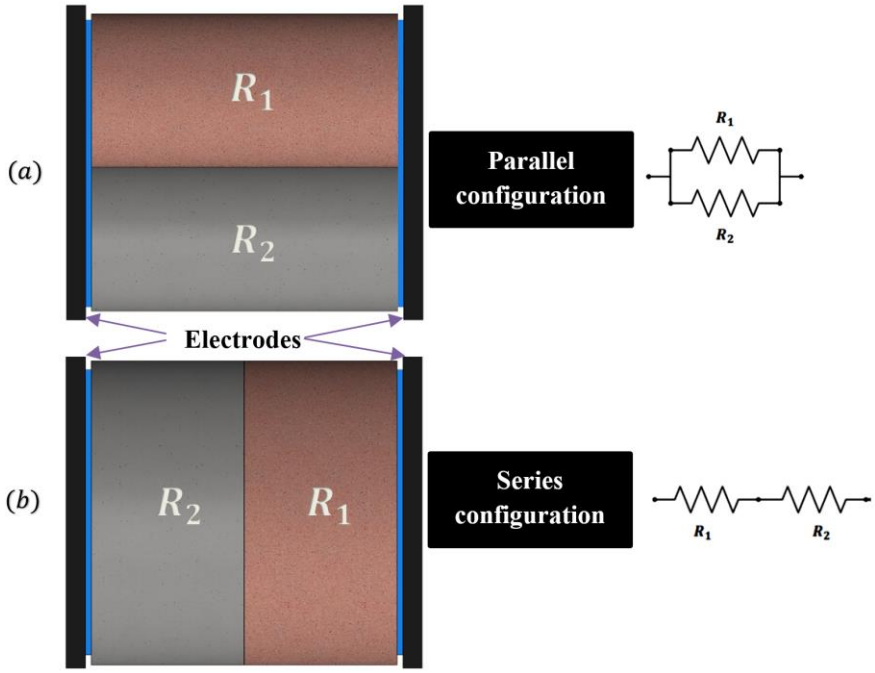

Figure 2.14. Schematic of the **(a)** parallel and **(b)** series models of heterogeneous systems (Reproduced from [116]).

In summary, the coefficient of determination value (R^2) for linear trend between bulk and surface resistivity in different literatures for various ages are shown in Table 2.8. Based on the reported data, it can be concluded that a strong relationship exists between resistivity measured by surface and bulk tests. However, in practical cases, caution is needed for multilayered cementitious composite systems as electrical current flows differently in these two techniques and for the types of layered electrical properties that can occur due to moisture gradients, chemical changes, and ionic gradients [116]. More complicated situations for resistivity measurement that arise during field measurements where seasonal and wet/drying that might take place at the tidal section on partially immersed structures has been studied by Presuel-Moreno [77].

Table 2.8. Coefficient of determination (COD) value for linear trend between bulk and surface resistivity in the literatures.

Reference	Coefficient of determination value (R^2)
Sengul *et al*. [94] (2008)	0.99
Sengul *et al*. [80] (2009)	0.99
Spragg *et al*. [96] (2011)	0.9986
Ghosh *et al*. [117] (2015)	0.82-0.95
Gudimettla *et al*. [108] (2016)	0.98
Authors work (2016)	0.979

2.2.8 Summary and conclusions

Through an extensive literature review, this paper identifies several factors which might have potential influence on the electrical resistivity of concrete. Effect of each parameter is briefly summarized in blow:

- In agreement with most studies, when there is an embedded rebar in the concrete, the electrical current field is distorted, and thus errors can result in the electrical resistivity measurements. To minimize this effect, it is suggested to place all electrodes perpendicular to the embedded rebar on the concrete surface and take at least five measurements, each a few millimeters in distance from one another. Also, a correction factor should be applied to resistivity measurements once rebar is presents in concrete. However, effect of rebar presence on the resistivity measurements is well-understood, just a few studies could be found to identify the rebar presence effect and more field investigations are still needed in this area.
- Presence of cracks in concrete was also identified as an influential parameter on electrical resistivity since it is initially presumed that concrete is homogenous, isotropic, and un-cracked. Depth of crack, orientation of probes on crack, and type of crack (conductive or isolated) can individually affect the resistivity readings. As suggested for embedded rebar in the concrete, all electrode should be placed in perpendicular direction to cracks. It was reported that higher resistivity readings were obtained from conductive cracks whereas lower resistivity values were gained for insulated cracks. However, no information is provided to show how much cracking induced by corrosion influences concrete resistivity. In addition, when both insulated and conductive cracks are bridged together, their integrated influence on electrical resistivity is not well-understood.
- The moisture state and temperature of concrete during resistivity measurements were also found to be of major influence on recorded data. As temperature increases, the ions mobility become faster; consequently, electrical conductivity of concrete also increases. To lessen the temperature effect on resistivity results, no practical correlation is still published for real-world conditions.

Essentially, electrical resistivity reduces with an increase in moisture content as a result of changing in the ion movement. It is strongly recommended to take resistivity measurements when concrete is in Saturated Surface Dry (SSD) condition. Yet, more investigations are required to understand how much time is needed for water to infiltrate into the concrete to obtain constant moisture level through the bulk sample.

- The studies related to resistivity measurement test device confirmed that electrical signal shape and frequency, electrode contact with concrete surface, and probe spacing of surface resistivity measurement device can affect the resistivity results. To minimize the effect of signal shape and frequency, using low frequency range square wave signal for surface resistivity and high frequency range for bulk resistivity is recommended. Proper contact should also be provided to not mislead resistivity readings. Using a saturated sponge between electrodes and concrete surface can reduce this effect. In 4-point Wenner probe method, as it is assumed that concrete is homogenous material, aggregates inside concrete also affect its homogeneity due to their higher resistivity. Therefore, providing enough wide space between electrodes is essential to diminish aggregates effect. As a rule of thumb, probe spacing 1.5 times higher than the maximum aggregate size should be considered.
- Aggregate content and type was identified to have an influence on concrete resistivity. Increase in aggregate content results in higher resistivity values due to their less porosity and lower electrical conductivity. Also, aggregates with rough surface texture was found to have higher resistivity as their tortuosity is higher. Therefore, the effect of aggregates content and type should be accounted in resistivity measurements.
- Carbonation process in aged concrete forms a multilayered system that results in various resistivity values through the concrete depth. So, its effect should be mitigated during resistivity measurements. Lower resistivity is also generated when *w/b* ratio is high due to higher percentage of porosity.

Correlation between concrete electrical resistivity and its certain durability characteristics such as chloride diffusivity, compressive strength, and corrosion potential/rate were discussed in this paper and are summarized below.

- Concrete resistivity is inversely related to chloride ingress, where lower resistivity indicated the area where chloride diffusion will be faster. A retardation of chloride can be taken into account through the introduced reaction factor (r_{cl}). More research is still required to better simulate sea site conditions.
- Furthermore, a strong correlation can be found between increasing electrical resistivity of concrete and the corrosion rate. The relationship can be seen when corrosion has initiated (active conditions). It will not be valid in the case of saturated concrete, where although the resistivity is low, yet the corrosion rate will be small because of lack of oxygen. Field data was considered in just a few investigations and thus, it is of high interest to gather more field experience.
- In addition, concrete compressive strength and its electrical resistivity have a direct relationship with each other as both directly depend on the porosity of the matrix at early age. However, at a later age, the conductivity of the pore solution and the degree of concrete saturation both influence this relationship. No practical relationship was identified in the literatures between compressive strength and electrical resistivity.
- Four common measurement electrode geometries that have been employed in several studies to conduct electrical test on cementitious cylinders were introduced in this article. Among them, a strong direct linear correlation between two common method of resistivity measurements (concrete surface and bulk resistivity) were presented. However, more attention should be paid to multilayered cementitious composite systems in the field as electrical current flows differently in these two techniques and for the types of layered electrical properties that can happen because of moisture gradients, chemical changes, and ionic gradients.

2.2.9 Conflict of interest

The authors declare that there are no conflicts of interest regarding the publication of this paper.

Chapter 3 Electron Imaging and Microstructure Investigation of Cement-based Materials Containing Crystalline Admixtures

The objective of this chapter is to (1) develop a unique technique for specimen preparation and nano-scale investigation of cement-based materials using FIB and STEHM (2) study needle-shaped crystals formation and quantify reduction in void volume using SEM when crystalline admixtures (CA) is used; (3) identify various hydration phases and chemical compositions of CA- and un-treated concrete by means of EDX spectroscopy. To fulfil these objectives, this chapter is divided into two sections: (1) this sub-chapter summarizes a developed technique that can be used to manufacture nano-size particles and investigate nanostructure of cement-based materials (in this case waterproofing admixtures) using Scanning Electron Microscope (SEM), Focused Ion Beam (FIB), and Scanning Transmission Electron Holography Microscopy (STEHM); (2) this section presents quantitative analysis and morphological aspects of mortars treated with CA, investigated by means of SEM micrographs and EDX spectra. To conduct multiscale investigation, first a preliminary study was conducted to study nano-scale features of CA particle and possibly to develop a nano-structure model that can quantify certain parameters such Ca/Si ration in C-S-H gel. Next, micro-size specimens treated with CA was studied using SEM to characterize morphology, topography and identify cement hydration products.

3.1 Specimen Preparation for Nano-scale Investigation of Cementitious Repair Material

This paper was published at Micron Journal [23].

Pejman Azarsa and Rishi Gupta. "*Specimen Preparation for Nano-scale Investigation of Cementitious Repair Material*", Micron Journal, vol. 107, (2018) 43-54 [https://doi.org/10.1016/j.micron.2018.01.007].

Author Contributions: Pejman Azarsa and Rishi Gupta conceived and designed the experiments; Pejman Azarsa performed the experiments and analyzed the data; Rishi Gupta contributed materials and experimental equipment; Pejman Azarsa and Rishi Gupta wrote the paper.

3.1.1 Abstract

Cementitious Repair Materials (CRMs) in the construction industry have been used for many decades now and has become a very important part of activities in cement world. The performance of some of these CRMs when applied to retrofitting concrete structural elements is also well documented. However, the characterization of some of the CRMs at the micro- and nano level is not fully documented. The first step to studying materials at the microscopic level is to be able to fabricate proper specimens for microscopy. In this study, a special and newly developed class of CRM was selected and fabricated by Focused Ion Beam (FIB) using well-known "Lift-out" technique. The prepared specimen was later examined using various analytical techniques such as energy dispersive x-ray analysis using one of the highest and most stable Scanning Transmission Electron Holography Microscopy (STEHM) around the world. This process enabled understanding of the composition, morphology, and spatial distribution of various phases of the CRM. It was observed that the microstructure consisted of a very fine, compact, and homogenous amorphous structure. X-ray analysis indicated that there was considerable deviation between the Si/Ca ratios for the hydrated product.

Keywords:

Specimen Preparation, Focused Ion Beam, Cementitious Materials, Scanning Transmission Electron Holography Microscopy (STEHM), Electron Diffraction Pattern.

3.1.2 Introduction

Understanding the material structure of new materials at sub-micro scale, can lead to improved development of such materials for the construction and building industries. In order to examine properties of these materials at micro (or Nano) scale, it is essential to observe their morphology, particle size, chemical compositions, and physical characteristics [172]. Nowadays, nano characterization of novel construction materials has become a significant field of research [172]. In particular, the nanoscopy techniques utilizing electron microscopes are the most commonly used methods for cement-based materials.

The electron microscope is a microscope that uses a beam of high voltage electron to create an image of the sample. Electron microscopes are typically used to examine the micro-structure of a wide range of

biological, inorganic, metallic, crystals, polymers, or cementitious materials. By utilizing electromagnetic and/or electrostatic lenses to control path of the electrons, they enable the observation of much smaller objects in finer details. For research related to cement-based building materials, currently, SEM has been heavily used instrument for better understanding of the materials' composition, morphology, topography, and also for obtaining crystallographic information. Despite the fact that combination of higher magnification, larger depth of field, and greater resolution makes SEM one of the most powerful tools in research areas and industries dealing with construction materials [172], yet there are certain limitations in using SEM for investigating materials' properties especially at the atomic level when compared to TEM, which allows an evaluation of the internal structure and spatial distribution of the various phases. In high resolution, the TEM imaging capability allows the instrument's operator to observe fine details [172]. The current TEM systems can inspect in atomic level, which is in the range of 1nm or less as compared to the resolution of SEM which is about tens of nm for common materials. Also, TEM can identify many characteristics of the sample, such as morphology, crystallization, stress, or even magnetic domains (holography) but common SEM only scan a specimen surface which mainly provides information about its morphology.

In contrast to TEM, the specimen preparation of SEM is much simpler. Many materials can be directly loaded in SEM for inspection and some insulating materials require an additional coating. On the other hand, TEM sample preparation is a challenging task as specimens need to be thinned to thickness of 100 nm or less. However, the complex multiphase nature of hydration products in cementitious materials makes the preparation of specimens thin enough, for electron penetration and TEM examination, far from trivial [173]. The thinning procedure is very time consuming and it can be done by mechanical breakup and dispersion of the solid [174]–[177], replication of fracture surface [178], mechanical thinning [179], [180] or abrasive and ion-beam milling [181]–[187]. In the past few years, there has been an upward trend in the use of the Focused Ion Beam (FIB) system which is also adopted in the present work to fabricate a specimen with consistent thickness for TEM examination. By utilizing ion-beam thinning, among other techniques,

Jennings *et al.* [183] could obtain information on the morphology of hydrated Tri-calcium Silicate (C_3S) pastes. Dalgleish and Ibe [185] also performed some qualitative analyses of Portland cement pastes thinned by ion-beam milling tool. Groves and co-workers [186], [187] have obtained the thinning procedure of hardened cement pastes using ion-beam milling. Through ion-beam thinning process, the possibility of developing artificial defects during the specimen preparation stage must be wisely considered. The drying impact of the vacuum of the ion-beam thinning apparatus and carbon evaporation chamber is inevitable, as the microscope also operates at high vacuum, it must be realized that any observed morphologies relate to a dry state [173].

In previous studies, TEM has been used to observe structures of Di-calcium Silicate (C_2S) and Tri-calcium Silicate (C_3S) at sub-micro scale and examine cement hydration products in the form of dispersed particles or crushed specimens [174]–[176], [184], [188]. TEM has also been operated to identify both inner and outer product regions of the C-S-H phase. The hydration of dispersed cement fragments has been imaged in an environmental cell by high-voltage TEM [189], but all these previous studies have not considered the fact that the cement particle is typically too thick to enable its internal structures to be fully observed under TEM. As mentioned by Jennings *et al.* [183], the abovementioned techniques have limitations in terms of loss of spatial relationships and limitation to a fracture path, respectively. This drawback was overcome with ion-beam milling by Javelas *et al.* [190] on mature mortars and later by Dalgeish *et al.* [185] on mature cement pastes. Furthermore, TEM has been extensively used by Groves [186], [191], Henderson [192], Rodger [193] and Richardson [173], [194]–[197]. These studies have generally focused on both fresh and mature cementitious materials, hydrated for 2 hours or more. Many of the main features and hydration products in a mature ordinary Portland cement (OPC) paste were identified by Rodger and Groves using TEM with microanalysis [193]. Over a range of Ground Granulated Blast-furnace Slag (GGBS) incorporated with OPCGGBS/OPC, a linear relationship has been observed between an increase in the R/Ca ratio (where R is a trivalent cation, mainly Al_3) and an increase in the Si/Ca ratio [173], [194]. Through TEM, early age hydration product shells around cement grains were also studied by Gallucci *et al.* [198].

In their results, the Ca/Si ratio of C-S-H gel was determined to be 2.8-3.5, which is contrary to findings of other previous studies. Plank *et al*. [199] investigated the intercalation product, composed of AFt and AFm with organic polycarboxylate (PC) polymers using TEM. Its raw material was pure mineral and the intercalation product was synthesized in specified condition.

The size distributions, as a factor to be considered for nanomaterials, can be envisaged with TEM [200]–[204]. Hou *et al*. [205] studied the effects of colloidal nano-SiO_2 (CNS) with a mean particle size of 20 nm and its precursor, tetraethoxysilane (TEOS), on the transport properties of hardened cement pastes with various *w/c* ratios. TEM morphology micrograph in this study indicated that CNS particles are generally round in shape and well-dispersed, however, agglomeration are also observed. Monitoring the interaction between various components of a mixture can be also clearly achieved by TEM. For instance, the microstructure of fly ash binders incorporated by Cement Kiln Dust (CKD), a by-product of the cement industry, was investigated under a TEM [206]. Through TEM work, the morphology of calcium alumino-silicate hydrate (C-A-S-H) gel present in the CKD-based fly ash binders, was evidently observed to be fibrillar type. To identify crystalline phases for cement paste at an age of 90 days, Ramezanianpour *et al*. [207] used TEM in bright field mode. In their TEM micrographs, hexagonal portlandite ($Ca(OH)_2$) crystalline cubes and aragonite ($CaCO_3$) was observed. Recently, there is an upward trend among physical and biological science disciplines to use TEM for real-time observations of materials interactions in their native fluid environment [208]. For the in-situ transformation observation, Xin *et al*. [208] embedded their sample inside a micro-fabricated cell with electron transparent membranes in order to contain the fluid in the high vacuum environment of the microscope.

With the development of SEM and TEM, the associate technique of Scanning Transmission Electron Microscopy (STEM) was first described in 1938 by Manfred von Ardenne and later re-investigated at University of Chicago by Crewe *et al*. [209] with advancement of the field emission gun and adding a high-quality objective lens. Using annular dark-field imaging, Crewe was able to image single heavy atoms on thin carbon substrates [210]. Later, the first attempt on cementitious materials at early age was made using

STEM to observe the formation of separated shells around reacting cement grains in samples as young as 5h [211], [212]. Mixtures of mono-phased grains of C_3S, C_3A and hemi-hydrate were also studied using STEM in Scrivener and Pratt's work [213]. At 1-day of hydration, they noticed gaps of up to 10 μm between C_3A grains and their hydration shells while there was a close contact between the C_3S grains and hydration products. This difference in behavior between cement and mixtures of pure phases indicates that the hydration process is influenced by the anhydrous phases within the cement grains [213]. Although, STEM and SEM have been widely used to examine and review the micro-level structure of cement-based materials for building and construction industries, the manufacturing procedures and quantitative techniques for microscopic level investigation using STEM have not been reported in detail in any present-day literature. Hence, the authors have attempted to investigate the microstructure of CRM that contribute to bond cracks together to identify its morphology, chemical compositions, and obtain crystallographic information of this material.

The objectives of the current study are to provide better understanding about fabrication and examination of a cement-based repair material at sub-micro scale as well as detailed characterization of its morphology, composition and structure using one of the highest resolution STEHM in the world as the main tool of investigation. Through this paper, the fabrication process and STEHM analyses of ion-thinned CRM sample, cured and activated for 7-days by spraying water, are also explained in Section 3.1.3, followed by obtained results and discussion presented in Section 3.1.4. This study is expected to be of significant value in the investigation of the CRMs' nanostructure and the composition of hydration product, and thus may provide a valuable tool in understanding and further development of these construction materials.

3.1.3 Experimental Program

3.1.3.1 Materials

A Cementitious Repair Material (CRM) has been selected in this study for STEHM examination. This is referred to as a modified synthetic CRM which contains Portland cement, reactive silica, calcium and

aluminum salts of organic acids and bases, and some crystalline catalysts [214]; a special category of repair material commercially produced and used for waterproofing cementitious materials. However, the chemistry of this product is proprietary and available. The chemical compositions and IR spectra of similar product have been reported in [15], [214]. Some of the physical properties of the material, reported by its manufacturer and used in this study, are given in Table 3.1. It should be noted that the focus of this paper is to further develop the specimen fabrication technique and not so much to characterize one particular type of CRM.

Table 3.1. Physical properties of CRM.

Color	Gray
Texture	Powder
Particle size	40-150 μm
Bulk density	1.2~1.5 g/cm^3
pH	13 (when mixed with water)
Solids	100%

3.1.3.2 Specimen preparation

Any specimen for STEHM analysis must be of an appropriate size with thickness less than 50-100 nm in order to allow passage of electrons for imaging sample's internal structure. As noted in Table 3.1, the average particle size of anhydrous CRM powder is reported by its supplier to be about 40-150 μm. Hence, the main obstacle was to prepare an appropriate size specimen that can easily fit inside the STEHM chamber. This requires CRM particles to be cut and thinned. Prior to the thinning procedure, anhydrous particles were dispersed and mounted on aluminum stub covered with carbon paste (Figure 3.1). Although the anhydrous particles' size reported by its supplier is about 40-150 μm, it should be noted that the particles' size measured from SEM images turned out to be above 20 μm and less than 1.5 mm. Hence, picking a suitable particle size for thinning procedure was quite a challenging task. The SEM and X-ray analyses of dispersed particles were later performed on raw material using Hitachi S-4800 SEM equipped with Burker Quantax EDS system for X-ray spectroscopy.

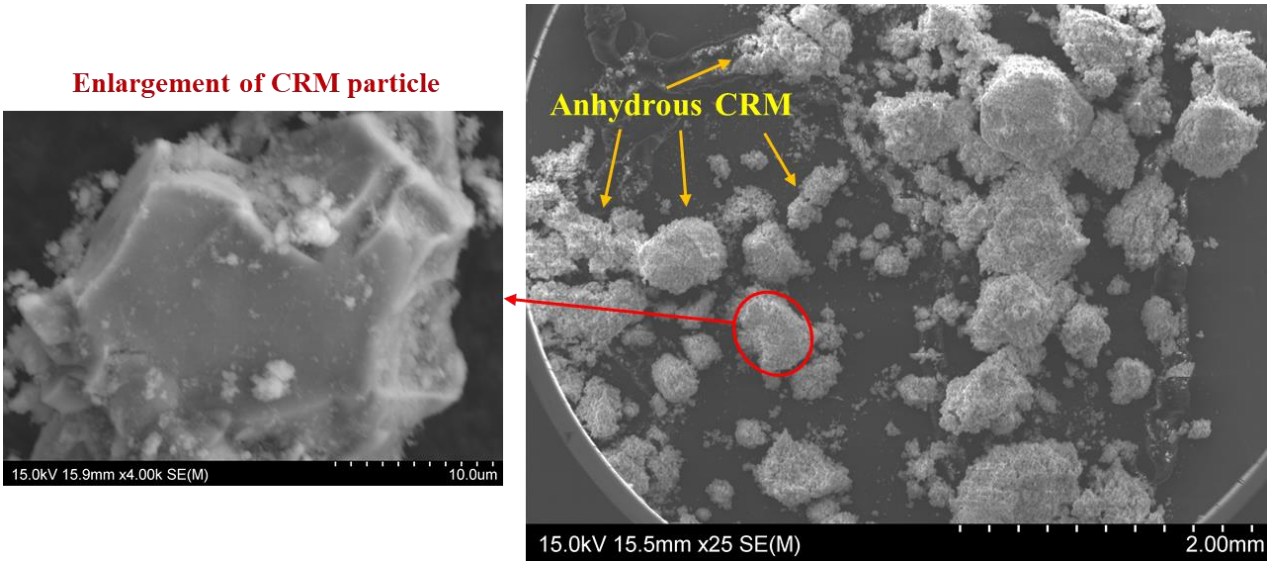

Figure 3.1. SEM micrograph of anhydrous CRM particles (Magnification: x25).

For investigation of hydration products, the specimen was prepared by spraying with tap water for a period of 7 days (three times per day) to activate the hydration of the CRM crystals. It is reported that there can be some negative effects of using tap water instead of distilled water. Negative effects reported include: decrease in initial and final setting time mainly due to flocculation process on setting and reduction in pH level of the paste due to presence of bicarbonate (HCO_3^-) and carbonate (CO_3^-) ions in the tap water which cause an increase in the solubility of CO_2 and acidity of water [215]. Also, according to this study, more portlandite [$Ca(OH)_2$] content may be observed in hydrated pastes having tap water than those mixed with pure water. However, to simulate casting of practical concrete mixtures used in construction and in accordance with ASTM and Canadian Standards, tap water was chosen as the type of mixing water in this study. Authors also suggest that future research could focus on studying the effect of tap water vs. pure (distilled) water on carbonation and resulting hydration products. The specimen was kept in a clean room inside pin stub storage box during 7-day curing period to remove chance of contamination and exposure to carbon dioxide in the air; thus, eliminate the risk of carbonation in the ambient conditions. The hydrated particles were again imaged by SEM to identify morphology and various phases after 7-days hydration, shown in Figure 3.2. The enlargement of particles and formation of needle-shape crystals were observed through SEM investigation.

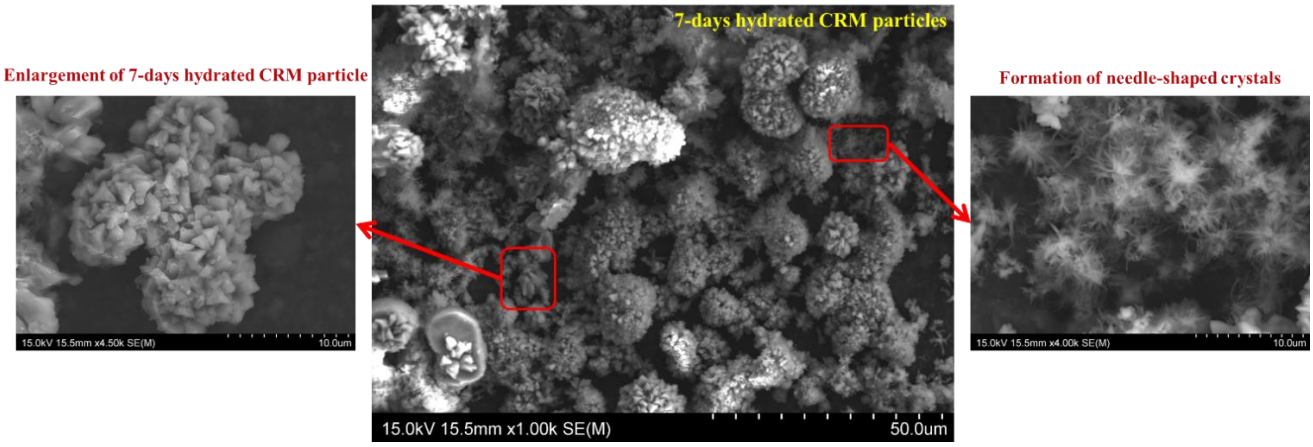

Figure 3.2. SEM micrograph of 7-days hydrated CRM (Magnification on the image in the center: x1.00k).

Thinning processes were conducted by Hitachi FB-2100 FIB system for making micrometer- and nanometer-sized cut in the CRM powder. A well-known sample preparation technique called "lift-out" technique was used to fabricate proper sample size for STEHM imaging. The only requirement for the lift-out technique is that the bulk sample must fit inside the FIB specimen chamber, this condition could easily be satisfied with obtained hydration products. After platinum deposition on sample surface was completed (Figure 3.3-(a)), a large stair-step FIB trench was cut on one side of the Region of Interest (ROI) and a rectangular FIB trench was cut on the other side of ROI (Figure 3.3-(b) & -(c)), following similar procedures as reported in [216], [217]. Before final thinning, the specimen was tilted to >45° and then the bottom, left side, and a portion of the right side of the specimen was cut free. A solid glass rod pulled to a sharp tip (~20–30 µm) was inserted into the arm of a hydraulic micromanipulator. Using the micromanipulator, the membrane was "lift-out" of the bulk sample and was then positioned onto a coated copper (Cu) FIB lift-out TEM grid which is designed for in-situ lift to attach the TEM lamellae milled out by FIB systems. Electrostatic forces allow the membrane to be lifted out by means of the glass rod. TEM grids, with typical thickness of 35 µm/-5 µm, fit all standards TEM holders and provide a full view of the thin section attached to the posts. A grid with three narrow flat posts has been used with identification letters (A-C) were etched into it as schematically shown in Figure 3.3-(e) & (f). Later, sample was tilted back to its starting position

and thinned to electron transparency. A final FIB cut was performed ~1-2° with respect to the plane of the specimen surface. In this manner, the thinnest portion of the specimen lies in the ROI. The remaining right side of the specimen was milled free leaving the electron transparent membrane lying in the cut trenches. After completing the above-mentioned steps, the specimen was ready for STEHM analysis. It should be mentioned that two individual particles were initially attempted to be mounted on the grid; however, the second attempt for picking and welding the particle to the grid failed. So, only one particle could successfully be welded to the Cu grid. This indicates some of the challenges still encountered during this process.

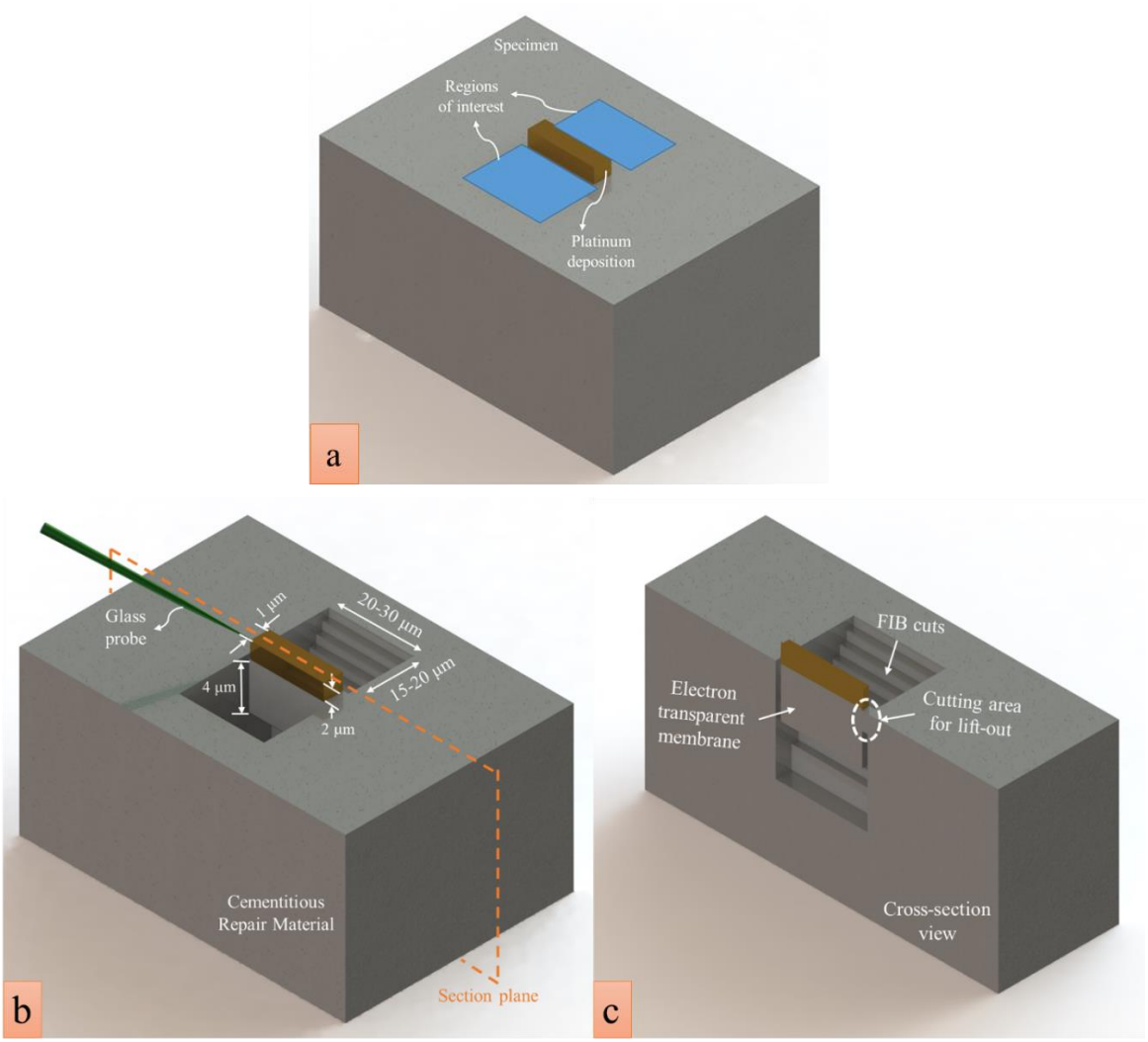

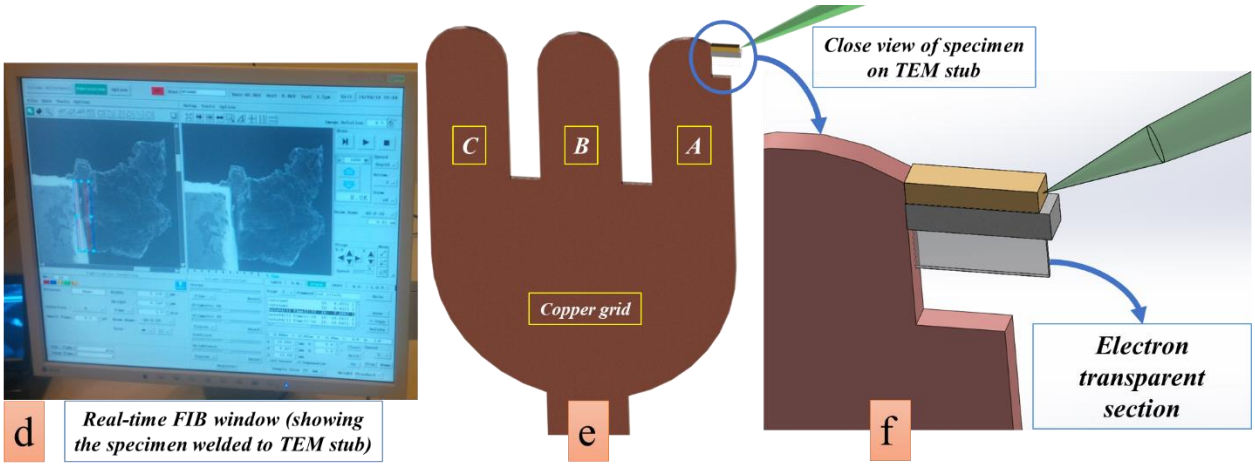

Figure 3.3. Schematic and real view of "lifted-out" technique used to manufacture CRM sample.

3.1.3.3 Scanning Transmission Electron Holography Microscopy (STEHM)

Structure of the CRM was examined by imaging and diffraction techniques using Hitachi HF-3300v STEHM having spherical + Coma correction of its TEM mode. The STEHM, used through this work, has proven to be the most stable microscope in the world as well as one of the highest resolution microscopes. The operating voltage was 200 kV and the current at the sample surface was estimated to be about 1 nA. STEHM makes it easier to obtain high magnification images without beam damage. Some images were acquired in the dark-field mode, with a high angle annular detector fitted in the microscope; this improves contrast for low atomic weight materials such as cement-based materials. For elemental analysis, STEHM is also equipped with Bruker EDS analyzer at a high take off angle for efficient collection of the X-rays. This enabled analysis to be made without tilting the specimen.

3.1.4 Results and Discussion

3.1.4.1 EDS analysis using SEM

Prior to FIB fabrication process and imaging with STEHM, the CRM (before and after 7-days hydration) were analyzed using SEM/EDS to identify its morphology, elements inside and hydration products. The x-rays generated can be collected using Energy Dispersive X-ray Spectroscopy (EDS) detector and used to form high spatial resolution elemental maps. Through this study, EDS analysis spots were chosen carefully

depending on the morphology of the un- and hydrated phases probed, so that results could be attributed as accurately as possible to pure phases. In this paper, the distribution of different elements of CRM using both SEM and STEHM were identified.

EDS analysis of CRM in selected regions indicated mostly typical elements of cement (calcium, oxygen, and silicon in major amounts, in addition to iron, aluminum, magnesium). SEM photograph and EDS elemental mapping were acquired for anhydrous CRM, shown in Figure 3.4. The figure provides direct visualization (Figure 3.4-(a)), elemental mapping (Figure 3.4-(c) & -(d)) and quantification of elements in raw specimen (Figure 3.4-(b)). Multi-elemental mapping performed by raster scanning of area marked in SEM image and taking a spectrum at each point to build up an areal distribution of the elements, indicates very high concentration of Calcium (Ca), Silicon (Si) and relatively high Magnesium (Mg) content, revealing that there is a considerable amount of Mg present in the examined sample. This observation was also confirmed from spectrum in Figure 3.4-(b) which provides information about what elements are present and the quantities of each. The obtained information from EDS was later used to identify hydration products and attain atomic ratio of the elements. Similar micrograph was obtained for the CRM, hydrated for 7-days (Figure 3.5).

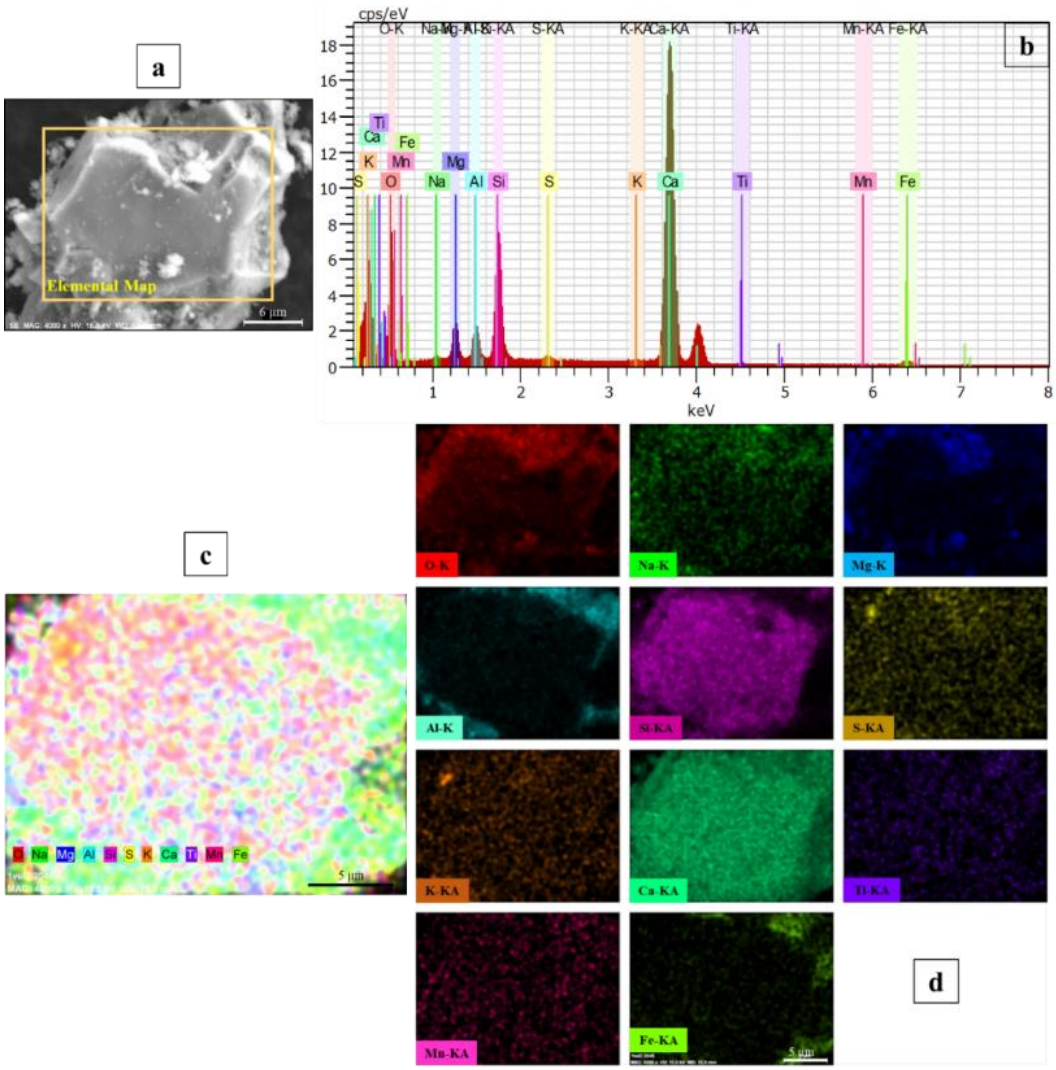

Figure 3.4. EDS spectrum, multiple and individual elemental mapping of anhydrous CRM.

After spraying water for 7 days, it was observed with naked-eye that particles swelled on the stub and expanded in size due to the reaction process. Three selected locations in SEM image (Figure 3.5), where needle-shape crystals were formed, indicate that high amount of Ca exists predominantly compare to other elements. Elemental mapping also reaffirmed these crystals were consisted of mostly Ca. The EDS analysis of hydration product did not show any significant elemental differences with that of un-hydrated one in Figure 3.4 except only high content of Ca and less amount of Si or Mg; this suggests that in spite of the different morphology of hydrated CRM (e.g. formation of needle-shaped crystals, shown in Figure 3.5), the reaction products are the results of growth in particle size. As one of the preparation steps, the x-ray analysis has only been done to select proper location for thinning procedure as well as STEHM investigation and

not to draw any conclusions about CRM chemical compositions. Authors also believe that spraying water for 7-days period might not be enough time and good curing method to get fully hydration product. Hence, authors recommend that CRM needs to be cautiously hydrated by suitable wet-curing method before its intended application since curing is a critical step and plays an important role in obtaining fully performance of cement-based materials. Further investigation on this material is required to understand the effect of various curing methods on morphology and hydration products.

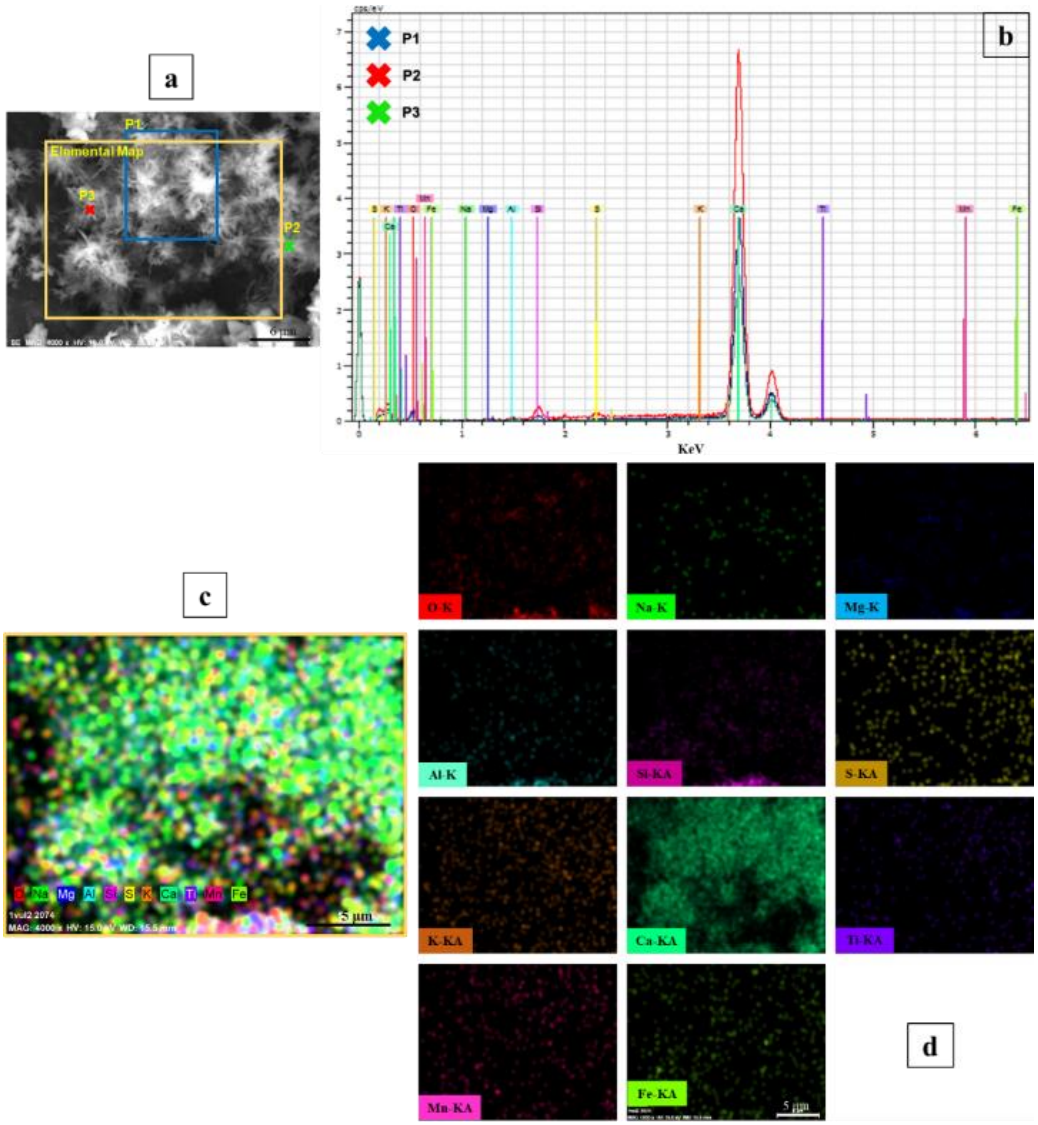

Figure 3.5. EDS spectrum, multiple and individual elemental mapping of 7-days hydrated CRM.

One of the ways to present and further analyze the data, and thus hydrated compositions, is graphically, in the form of atomic ratio plot. The plots in Figure 3.6-(a) & -(b) were obtained from EDS spectra of hydration

products by calculating each element's atomic percent from its mass percent for all selected spots, and then presented in the form of a graph after deriving atomic ratios for particular elements. To derive comprehensive analysis, more than 10 different spots were selected and all data points, collected from EDS analysis spectrums, represent a point for Si/Ca vs Al/Ca in one plot Figure 3.6-(a) and Al/Ca vs S/Ca in Figure 3.6-(b). It is important to appreciate that the plots quantify the compositions of the hydration product; however, the proportion of each composition present in the paste cannot be quantified.

Although more sampling from the CRM and its chemical compositions are needed for comprehensive conclusions, the plot of Si/Ca vs Al/Ca in Figure 3.6-(a) shows that calcium hydroxide ($Ca(OH)_2$) was the main product of selected regions in 7-days hydrated CRM. It also indicates that Si/Ca ratio of the sample is approximately between 0.01~0.1 while the Al/Ca ratio is 0.02~0.04. The typical Si/Ca ratio of the inner product C-S-H in neat Portland cement have been widely reported from several characterization techniques, with values ranging from approximately 0.45 to 0.6 while the Al/Ca ratio is 0.04~0.06. Hence, the cluster near origin in Figure 3.6-(a) & -(b) corresponds to largely CH crystals and rarely C-S-H gel. The plot demonstrates that no AFt (a group of calcium sulfoaluminate hydrates) and AFm (a group of calcium aluminate hydrates) phases were detected. As the most common and important member of AFt group, ettringite also forms needle-shape crystals similar to the ones imaged in CRM; however, through authors analyses, the CRM crystals have not been identified to be ettringite. Figure 3.6-(b) clarifies the picture considerably. No pure gypsum, a hydrated calcium sulfate in chemical form that helps in compensating the rate of hardening of the cement, is identified.

It is hypothesized that dominant presence of pure CH in hydration products can be rooted in random data collection from various locations. Hence, it is strongly recommended to not collect data from random locations before seeking out visually different hydration phases from SEM micrograph. Furthermore, more spectra for hydrated compositions is required to be collected in order to systematically identify single or more than one phases of hydration product since different forms of these phases can intergrow on a scale

smaller than the X-ray excitation volume. However, the goal of this work was to establish an experimental methodology as opposed to determining the absolute proportions of various elements.

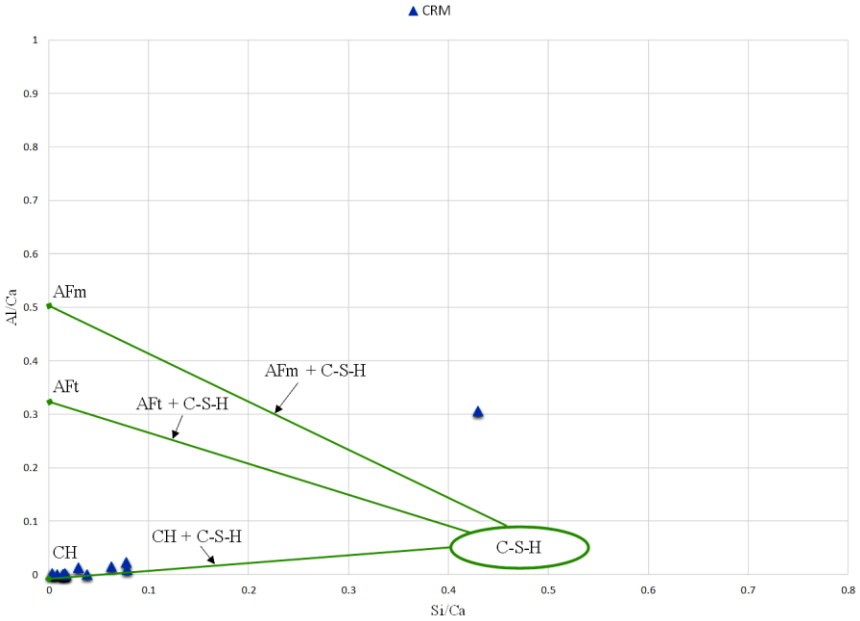

(a)

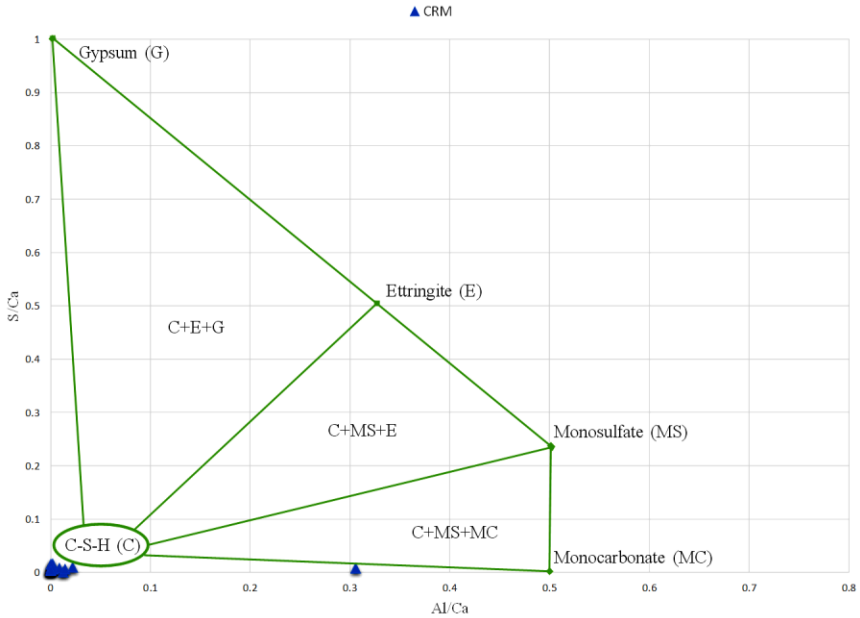

(b)

Figure 3.6. 7-days hydrated CRM atomic ratio plot of **(a)** Si/Ca vs Al/Ca **(b)** Al/Ca vs S/Ca.

Moreover, EDS analyses for un- and hydrated CRM for 7-days are plotted as atomic percentage, another way of data representation, normalized to 100%, in Ca-Si-(Al+Mg) ternary diagram in Figure 3.7. The analyses of hydration product resulted in identification of dominant phase of CH, similar to data represented

in Figure 3.6. While most data points of hydration products in Figure 3.7-(b) are located close to the cluster of analyses plotted in Figure 3.6, the un-hydrated CRM collected spots in Figure 3.7-(a) are scattered in random directions which makes the conclusion about its phases difficult, and thus requires more data to be collected. For comparison purposes, Portland cement hydration product range is also plotted on the graph.

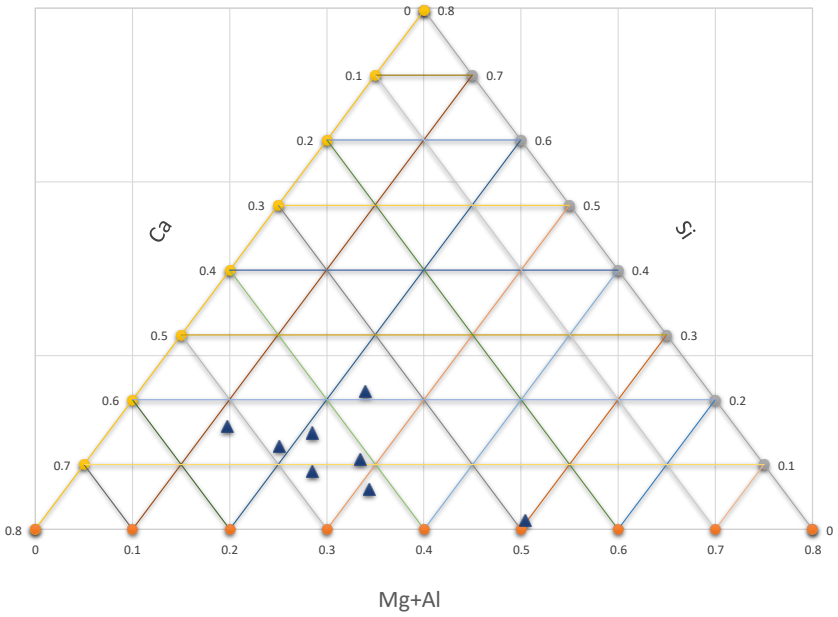

(a)

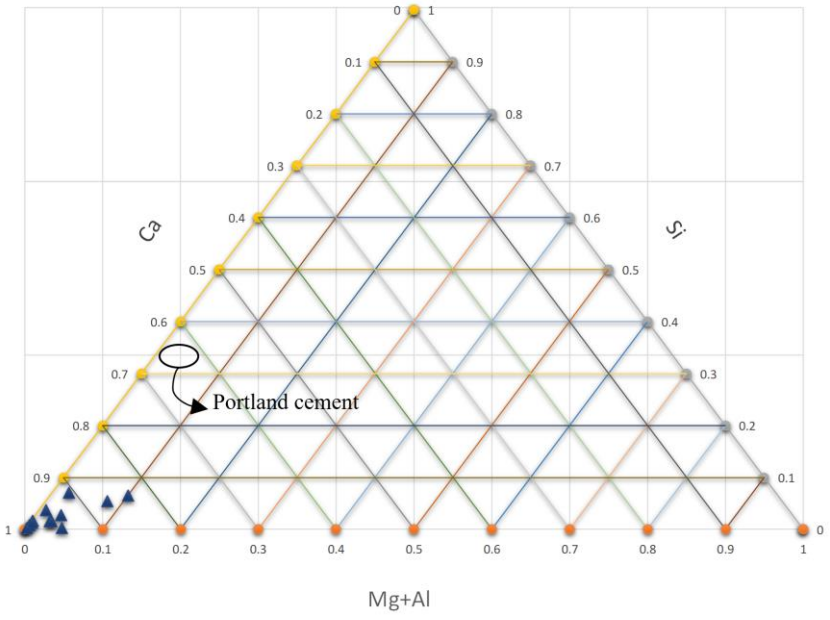

(b)

Figure 3.7. (a) Un- and **(b)** hydrated CRM Ca-Si-(Mg+Al) ternary diagrams.

3.1.4.2 STEHM Micrographs

A CRM with a mean particle size of 80 μm was thinned down into 1~2 μm size using FIB and further magnified in STEHM in order to investigate morphology, element distribution, and structural order of its nano structure. Using STEHM, a highly-focused electron probe was raster-scanned across the prepared specimen to acquire various types of scattering. Figure 3.8-(a) exhibits a bright-field micrograph, taken in TEM mode from 7-day hydrated CRM specimen, indicating compact, fine-scale, homogenous morphology. Many regions are free of obvious defects and dislocation (dislocation will of course be introduced when the bulk sample is ground to make powder). For further investigation of sample's morphology, it was divided into 5 different color-coded regions (ROI: A-E in Figure 3.8-(a)) where TEM micrographs were obtained and are explained in section 3.1.4.4. In addition, mapping the intensity of high-angle scattered electrons of the CRM using STEHM resulted in formation of Z-contrast micrograph which is incoherent (Figure 3.8-(b)). Since the image was formed from high-angle scattering of atomic nuclei, the scattering cross section relates to atomic number (Z^2). In Figure 3.8-(b), areas that appear bright in the specimen correspond to higher atomic weight elements. For example, on the right brighter region of the specimen (illustrated in Figure 3.8-(b) by yellow boundary), there are more elements with higher atomic weight like Fe or Al, although, for further element identification, EDS examination was required. Later, EDS analysis on thinned particle using STEHM have been performed to identify elements inside and acquire X-ray spectrum (Section 3.1.4.6). Thickness map and crystallographic information were additionally obtained as characterization techniques for further investigation of the CRM structure, and reported in the sections 3.1.4.3 and 3.1.4.5. It should be noted even though one sample was mounted on the stub, the sample was divided into five areas, thus increasing the reliability of the results.

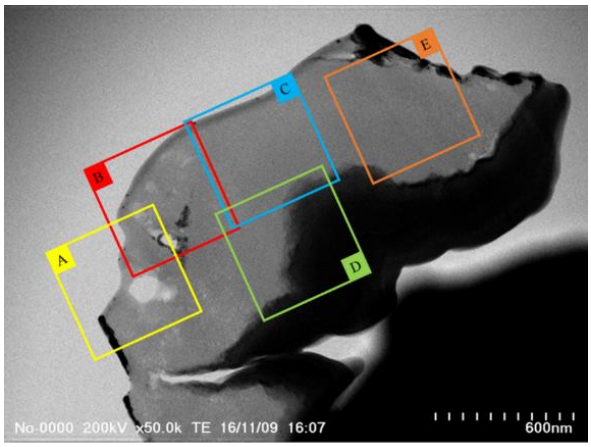

(a)

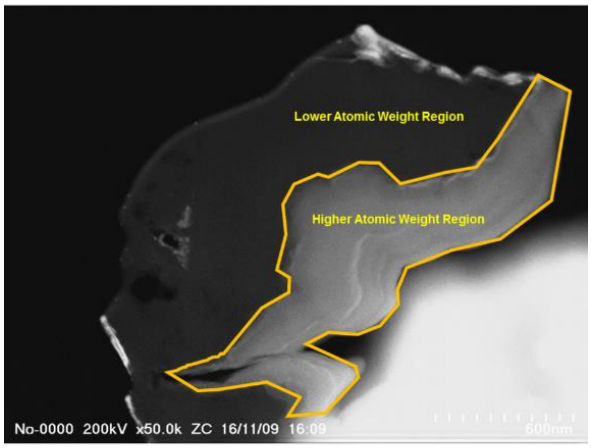

(b)

Figure 3.8. Seven-days hydrated CRM **(a)** TEM micrograph (bright-field image) **(b)** Z-contrast micrograph.

3.1.4.3 Relative thickness map

It is necessary to check the thickness of fabricated specimen to ensure passage of electrons through the sample. A reliable indicator to overlook is the Mean Free Path (MFP) value, λ, which represents the average distance a beam electron will travel inside the samples between electron energy loss scattering events for inelastic scattering which contributes to significant details at the atomic level to high resolution images particularly in high voltage instruments. For a specimen of thickness *t*, the average number of times, an electron beam will scatter in-elastically, is t/λ.

To obtain thickness map for the CRM particle, two images, one unfiltered image without introducing an energy-selection slit that is inserted into the energy dispersive plane of an energy filter, which selects

electrons having specific energies and another filtered (zero-loss) image by introducing the energy selecting slit around the zero-loss energy (with slit width 10 eV) were acquired. Then, the relative thickness map obtained from these two images using the log-ratio method in Gatan Digital Micrograph provided the local sample thickness in units of inelastic mean free path (λ). The relative thickness map and corresponding average intensity profile were obtained for ROIs (A-E) of the particle at 200 keV incident energy, shown in Figure 3.9. The MFP values for most of ROIs A-C and E are in the range between 0.4-0.7. Knowing the λ values for 7-days hydrated CRM, the sample thickness, *t*, was measured to be 50-80 nm. The obtained t/λ value indicates the suitability for the ROI area for transmitting electrons through specimen and performing Electron Energy Loss Spectroscopy (EELS) studies since its value provides a direct indication of the degree of signal degradation by plural scattering independent of the sample composition. Similar approach can be performed in Energy Filtered TEM (EFTEM) to generate a two-dimensional t/λ map.

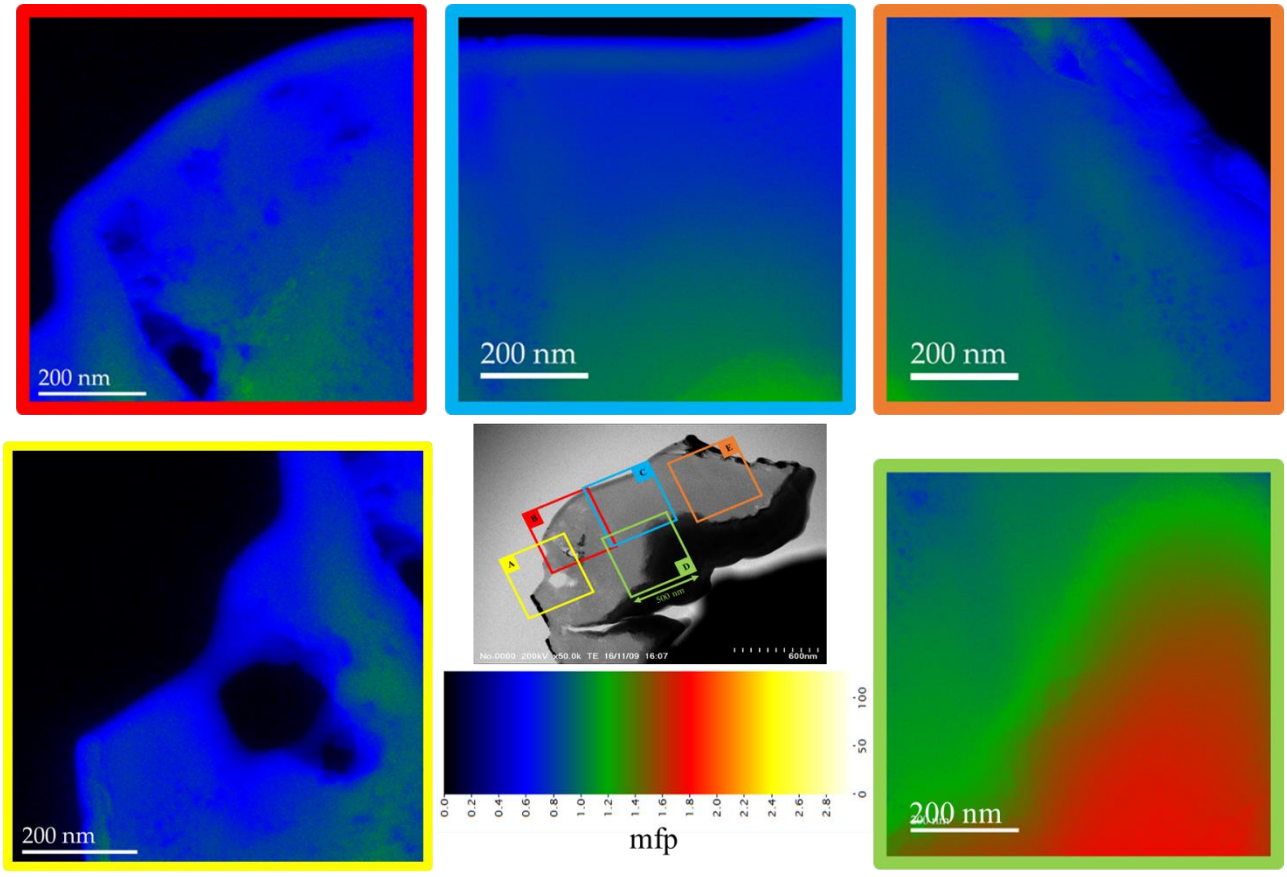

Figure 3.9. Relative thickness map of selected CRM particle regions.

3.1.4.4 Morphological aspects of hydration products

The morphological characteristics of hydrated CRM were acquired for five color-coded (500×500 nm^2 square) ROIs (Regions: A-E) under STEHM. All ROIs were nearly devoid in the TEM micrograph except ROI-A that has double holes with 150-200 nm size. No quantitative significance can be attached to the hole sizes seen on the micrograph since the holes' structure were initially observed to exist and coarsen as a result of electron beam damage. The amount of damage suffered in a very short time, due to electron beam, was sharply evident in the ROI-B micrograph, appearing brighter in Figure 3.10; however, we were still able to get clear satisfactory images. Also, no morphology other than a fine structure is seen within ROI-C of TEM micrograph. It is hypothesized that large quantities of crystals, observed in Figure 3.2, which were highly hydrated, might have readily decomposed during FIB fabrication and specimen preparation. In the region D, evidence of contamination from electron beam was observed as well. It must be noted that the morphology of prepared specimen just brought into field of view may have sustained preventable damage, not only from sample preparation technique, but how the beam had been manipulated over the sample. For instance, if the beam current is initially turned up at low magnification with a large spot size and poorly defocused electron beam, then an extensive area can be damaged [173]. Hence, an operator who implements the proposed sample preparation technique and nano-scale investigation, needs to consider sufficient cautious in all steps to avoid any damages to the sample.

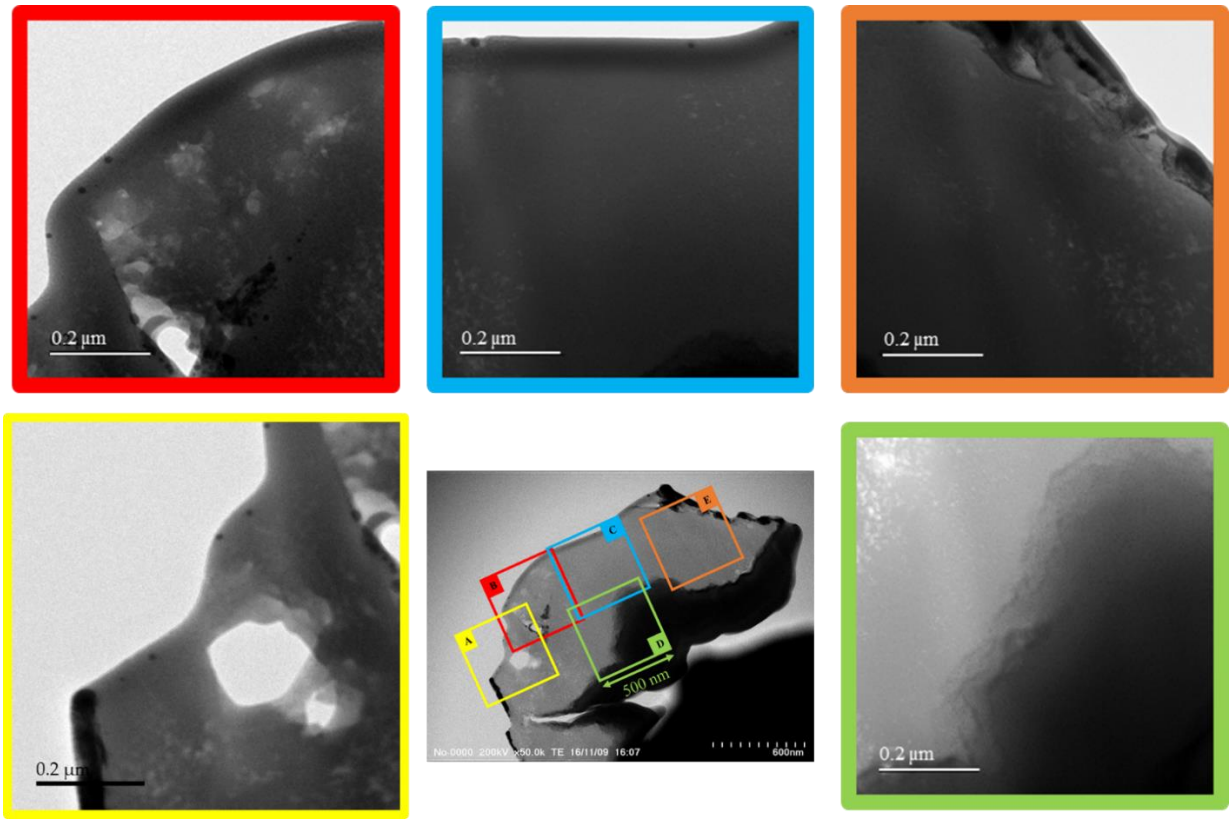

Figure 3.10. TEM micrograph of color-coded selected regions of CRM specimen.

3.1.4.5 Selected Area Electron Diffraction (SAED) pattern

Selected Area Electron Diffraction (SAED) patterns can be obtained from localized regions of the sample by inserting a selected area diffraction aperture into the image plane of the objective lenses. SAED patterns help to determine whether a specimen is single crystal, polycrystalline, or amorphous. The sampled 7-days hydrated particle was studied using SAED to ensure the presence or absence of crystalline phases. SAED patterns were obtained from five various selected regions (ROI: I-V) within the boundary and inner-body of the particle, shown in Figure 3.11. The area covered by a SAED aperture was 100-120 nm in diameter. Inspection of these patterns led to some very interesting findings. In spite of the complex appearance of this microstructure, SAED patterns of all regions show that most of the diffracting material has amorphous structures. This observation is also confirmed by intensity profile of SAED patterns, as illustrated in Figure 3.11. As an additional characterization technique, a simple XRD examination can be also performed to identify non-crystalinity of the hydrated CRM particle. Part of difficulty in the reliability of the SAED

investigations may relate to amorphization of the specimen by the ion beam milling process and/or beam damage in the microscope [218]. Groves *et al*. [186] successfully achieved the thinning of Hardened Cement Paste (HCP) specimens by ion-beam methods, using a liquid-nitrogen-cooled stage-to minimize thermal damage- and a slow thinning rate. They were able to obtain reproducible results in their investigations. They also noted that the possibility of thermal damage during preparation is more serious than beam damage in the microscope, because the damage accumulated in the microscope can be monitored *in situ.*

Diffuse rings, evidence for short-range structural order and sub-crystalline region in specimen were observed in region I, IV and V using SAED (indicated by yellow arrows); however, further investigation of the hydration product, as also performed by Viehland *et al*. [218] for the C-S-H gel phase, require to be conducted to better understand the midscale structural units that result in short-range ordering, seen in the marked areas with arrows in the SAED patterns. Presence of nanocrystallinity region can be indicated in sample's structure through High Resolution Electron Microscope (HREM) studies and its development inside specimen may occur very rapidly at short times, slowing down, as sample ages. Similar results have been reported for C-S-H gels for freshly cured and aged gels [218]. Their results supported the arguments that system becomes metastably trapped in a sequence of near-degenerate states because of the inability to undergo long-term diffusion. Overall, the safe statement that can be made at this point is that SAED patterns of observed CRM particle show amorphous structure; however, more samples are required to be prepared for comprehensive conclusion.

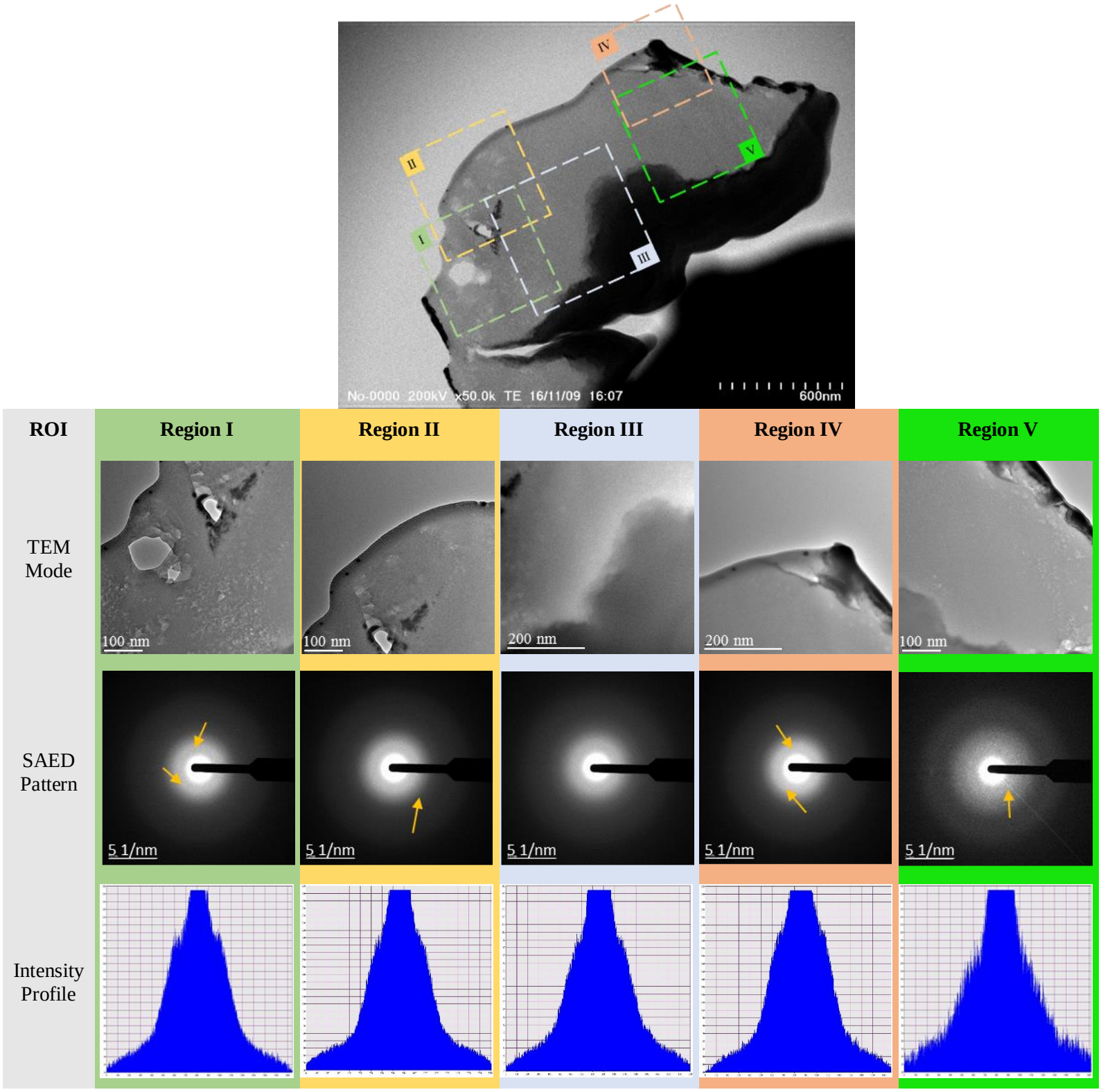

Figure 3.11. Selected Area Electron Diffraction (SAED) pattern of CRM particle and its intensity profile.

3.1.4.6 EDS analysis using STEHM

EDS analysis was performed by STEHM on fabricated specimen to investigate the elemental distribution, confirm observations from SEM/EDS analysis and calculate Ca/Si ratio of examined particle. The size of the mapping area was chosen to be about 2×2 μm^2 (Figure 3.12-(a)) and the X-ray mapping involved the simultaneous analysis of eight elements (O, Ca, Si, Mg, Fe, Al, Ga, W) (Figure 3.12-(c)). EDS elemental maps show that the specified region of the specimen mainly contains silicon and calcium together with small amounts of aluminum and iron, shown in Figure 3.12-(d). It should be mentioned that calcium was not detected by EDS on the right side of specimen area. Iron (Fe) was also present throughout the selected region but did not appear to be particularly associated with either aluminum or magnesium. Iron contents occurred in the right area were higher. Additionally, the amount of magnesium, originally presents in the anhydrous sample, was not significant in EDS elemental map. In Figure 3.12-b, the spectra, acquired from the investigated particle, shows high peak for Si and Ca. Evidence of Gallium (Ga), most likely sputtered from electron beam, was also observed in different spots which cautiously needs to be prevented during sample preparation as it makes EDS analysis of investigated sample less appealing. The Ca/Si ratio of the particle was calculated to be about 0.4–0.6. In reviewing previous TEM work by the authors (unpublished), it was noted that no similar cement hydration products contain substantial silicon content. The low Ca/Si ratio measured was interpreted as being due to one or more of the following: (a) the fine intermixing of Wollastonite ($CaSiO_3$), Quartz (SiO_4), or Silica (SiO_2), (b) residual undissolved silicon calcium particles, or (c) the less coexistence of tobermorite (T2) and jennite (J2) like structures [198]. Also, the Ca/Si ratio has been reported previously to depend on the beam acceleration voltage, indicating the influence of beam-spreading effects [219]. Generally, preliminary experiments have shown that determination of specimen's composition by EDS combined with STEHM is feasible, however, the variability of Ca and Si was too severe to allow fully quantitative results to be presented from these initial experiments.

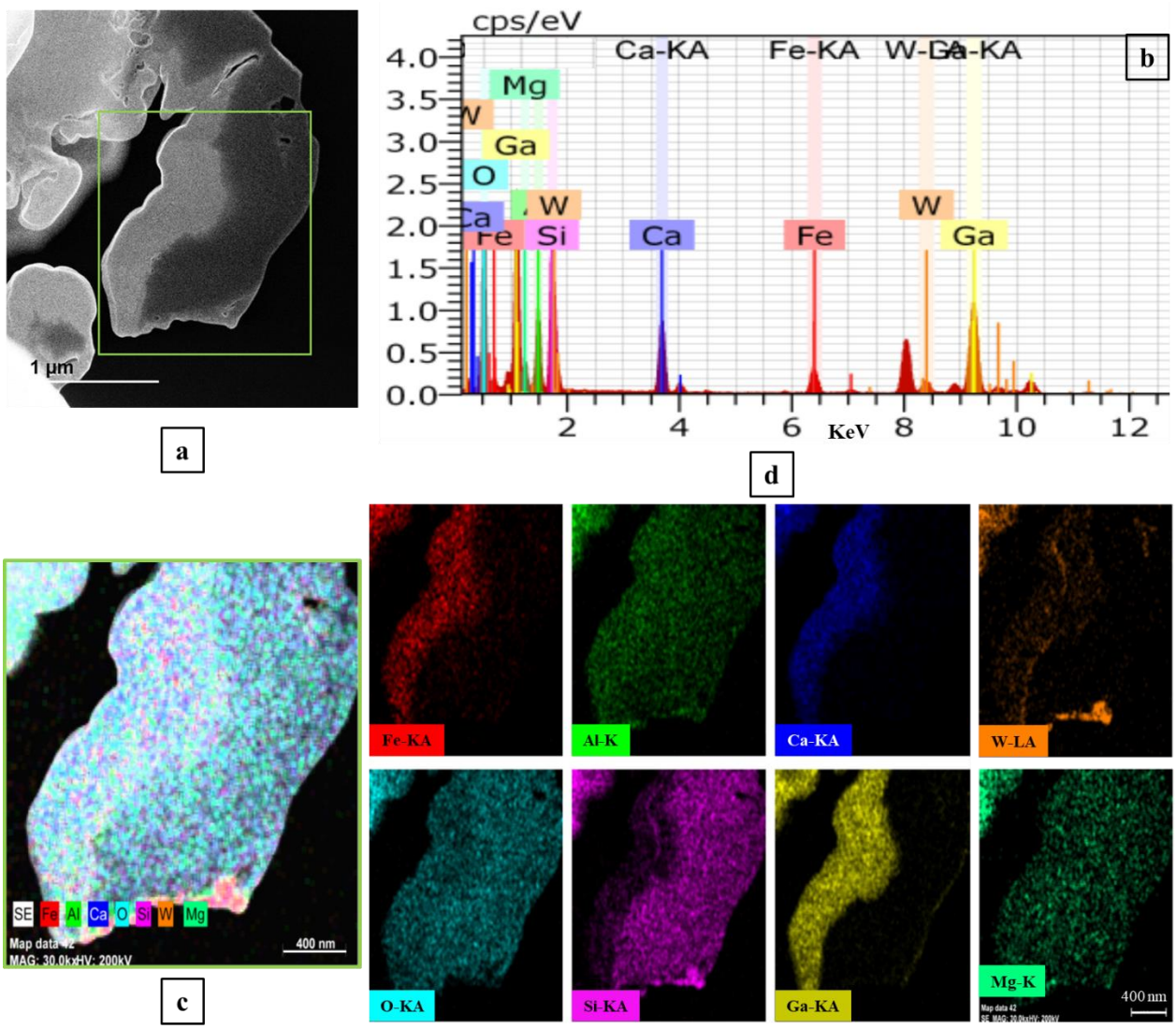

Figure 3.12. EDS analysis and elemental mapping of CRM particle.

3.1.5 Conclusions

Through this study, a cementitious repair material has been fabricated by FIB system and studied analytically by STEHM. No previous studies documenting the nanostructure of this material when studied using STEHM (one of the highest resolution in the world) have been reported. After activating the CRM by water-spray, lift-out technique has been used in FIB system to manufacture appropriate size specimen (50~100 nm thickness) for STEHM analyses. Hydrated specimen revealed fine, compact, homogenous morphology and its diffraction pattern after water-activation indicated nearly amorphous structure, however, evidence of short-range structural was observed which requires further investigation. The relative

thickness map, attained from hydrated particle under STEHM, indicated that measured specimen thickness, thinned through FIB processing, was about 40-70 nm which allows sufficient electrons to transfer inside sample. This preliminary investigation leaves many questions unanswered but demonstrates the feasibility of a powerful technique for examining the nanostructure of the cement-based material, and the effects of its microstructure and solution compositions on the stage of hydration. Great care should be exercised when manipulating ion-thinned specimens in the STEHM because it is quite possible for an operator to be unaware about the damage that has occurred. This report provides new insights in the fabrication and examination of the microstructural development of cement-based products at the nano-scale.

3.1.6 Conflict of interest

The authors declare that there is no conflict of interest regarding the publication of this paper.

3.1.7 Acknowledgment

Thanks are due to the Natural Sciences and Engineering Research Council of Canada (NSERC) for financial support. The authors are grateful to Drs. Rodney Herring, Elaine Humphrey, Arthur Buckham, and Mana Norouzpour for first engaging their interest in the subject of cement, and for continued valuable discussion.

3.2 Quantitative Characterization of The Microstructure of Mortars Containing Crystalline Admixtures Using SEM

Although the microstructure of cementitious materials have been studied by many researchers [220]–[226], there is limited information available to quantify the reduction in void volume when CA is used in combination with PLC and also to compare microstructural performance of different CAs. This section aims to provide clear understanding about crystal formation at micro scale in cement-based composites treated with CA as well as detailed characterization of their morphology, chemical compositions and structures using Scanning Electron Microscopy (SEM) as the main tool of investigation. Microstructure features, porosity and hydration products of CA treated mortars will be quantitatively explained in sections 3.2.2.1 and 3.2.2.3.

3.2.1 Experimental Program

3.2.1.1 Materials and mixture proportions

Two different experimental setups were developed to study the effect of CA on the mortar microstructure. To investigate the morphology of the hydration products or the shapes of the formed needle-shaped crystals, first experiment in this study included four CA types, called K, P, X-C, and X-NF admixtures. These are commercially available products using crystalline waterproofing technology and their chemical compositions are proprietary of their manufacturers which is not accessible. The dosage of CA used was 25 times higher than recommended one by manufacture in experiment I. Higher dosage than those recommended by manufacture was used to accelerate observation of needle-like crystals in the matrix under SEM and obtain their morphological and chemical compositions information since SEM examination is relatively costly process. After spending couple of hours, there was also a chance to not quickly distinguish these crystals when low dosage was used. In this experiment fracture surface of mortars with and without CAs were characterized by SEM and EDX analysis. In the second experiment, polished and flat surface of mortar specimens were used to systematically analyze different hydration phases and porosity of the treated

system. Only one type of CA (K admixture) was used in this experiment. Typical dosage (2% weight of cement) was used in this experiment to understand actual behavior of CA in blocking pores or cracks. Table 3.2 summarizes the mix designs, used for this phase with a water/binder (*w/b*) ratio of 0.5.

Table 3.2. Mortar mix design and proportions.

Experiment type	Mix ID	Materials				Curing age (days)
		Mix proportions (kg/m^3)			Crystalline admixtures	
		Cement Type	Fine Aggregate	Water	Dosage (% cement weight)	Water tank
Experiment I (Fracture surface analysis)	Control	OPC	736	2207	368	-	56
	CA-I					50%	
	CA-II					20%	
	CA-III					25%	
	CA-IV					50%	
Experiment II (Polished section analysis)	OPC	OPC				-	28
	OPC-CA					2 %	
	PLC	PLC				-	
	PLC-CA					2 %	

3.2.1.2 Specimen preparation and curing regime

The sample preparation for SEM was much simpler than abovementioned proposed technique for STEHM investigation (section 3.1.3.2). Many materials could be directly loaded without coating in SEM for inspection and some materials need an additional coating. For the purpose of this study, cement, sand and water, with an addition of four different CA types in experiment I and only one type with two cement types (OPC and PLC) in experiment II, were mixed manually together to make various mixtures of mortar cubic samples (50×50×50 mm). A dosage of 50%, 20%, 25%, and 50% percent K, P, X-C, and X-NF were used in experiment I. The main reason behind using such high dosage was mentioned in previous section. After casting, cubes were plastic wrapped for a period of 24 h and later, cured in the water tank. After 56 days of immersion in the water to perform experiment I, specimens were broken into the small pieces with fresh fracture surface for further investigations using SEM. The specimens with approximate dimensions of 2 cm × 2 cm were randomly selected and were left at ambient temperature for 7 days and later placed into a vacuum desiccator to dry. Next, surface of three samples from each mix were coated with carbon to dissipate excess charge from the specimen.

To prepare polished sections for experiment II, three mortar cubes from each mix were cut into thin slices. These 10 mm thick slices were then embedded in low viscosity epoxy resin using vacuum impregnation in a vacuum desiccator. Once the resin was hardened, a few millimeters from the surface were removed using wet-and-dry abrasive sheet to reveal surface to be examined. Later, the specimen surface was ground to a flat surface using a polishing/lapping machine. The time spent on each grinding and polishing stage was about 10-15 min. The flat surface was cleaned in acetone, dried, and ready for carbon coating. After applying carbon-coating by an evaporative coater, the polished sections were ready to be studied by Hitachi S-4800 SEM with a backscatter electron detector and EDX analyzer. The microscope was operated at an accelerating voltage of 15 kV and working distance 15 mm. The EDX system had been calibrated with oxide standards suitable for cement analyses. X-ray spectrums and elemental mappings were collected for elements O, Na, Mg, Al, Si, S, K, Ca, Ti, Mn, and Fe.

3.2.1.3 Image analysis of polished sections

The images were taken from random locations on the specimen while attempts were made to not capture them from the cast finished surface or edges since carbonation might be taken place near these areas. Image analysis was performed using ImageJ software developed by the National Institutes of Health [227]. Ten images were collected per sample at a magnification of 800x, which is a common magnification used to study concrete pore structures. A representative SEM image is shown in Figure 3.13-(a). Firstly, these images typically contain some fraction of sand particles which need to be removed from original BSEM image using segmentation algorithm [222] before thresholding and segmentation of the pore phase due to overlap with hydrated cement paste grayscale. An initial step was to use filtering operations to reduce noise in SEM micrograph (Figure 3.13-(b)). For mortar specimens, where there was a pore peak in the histogram, the minimum point between the pore peak and the hardened paste peak was considered as the porosity threshold which this process was done by referring to the first derivation curve of the brightness histogram. In the ImageJ software, auto-threshold utility, which calculates based on the overall histogram of the image, was also used for thresholding purpose. Adjustment of contrast and brightness was also performed to

balance grayscale level (Figure 3.13-(c)). When the pore thresholds had been determined, binary segmentation was conducted on the BSEM images to distinguish pores from other phases (Figure 3.13-(d)). Based on a percentage of the segmented pore area to the total paste area, porosity of hardened paste was later calculated. Also, since EDS spectra is collected simultaneously with the backscatter electron image, the image set can be combined to determine the mineral phase present at each location.

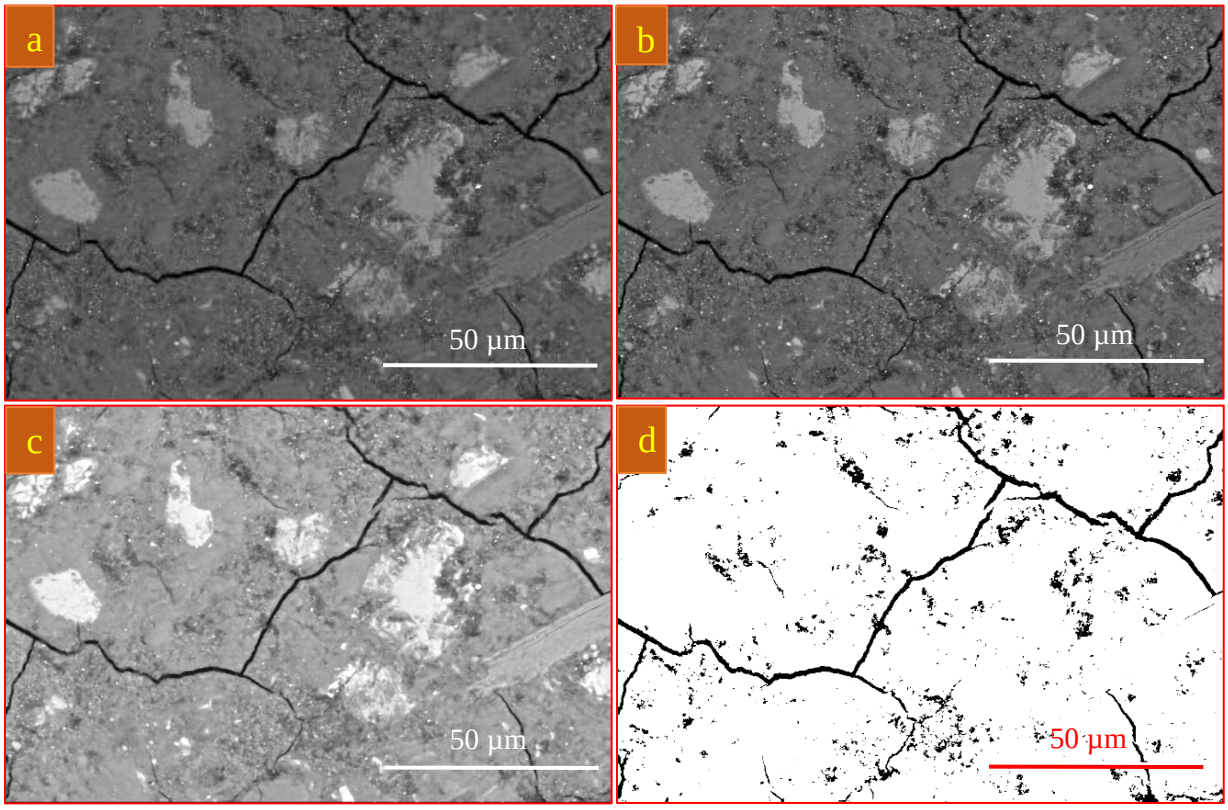

Figure 3.13. (a) A representative SEM micrograph, **(b)** the noise reduced image, **(c)** the adjusted grayscale image and **(d)** the binary image.

3.2.2 Results and Discussion

3.2.2.1 Experiment I results

SEM micrographs and morphological aspects

In the first experiment, SEM analyses were carried out on fragments collected from mortar specimens treated with four CA admixtures in order to obtain useful morphological information and identify formation

of any needle-like crystals. SEM micrographs of both admixture treated and control samples, taken from different random locations on the specimen surface, are shown in Figure 3.14. The following figures show the needle-like crystals growing in treated samples and filling cracks/voids while in the control specimens, the cracks/voids were left uncovered. These images can be good indicators of admixtures' performance in filling voids and cracks with crystals. These crystals are up to 3-5 μm in length and some of them are less needle-like perhaps signifying either different compositions or geometry development. Considering different admixture types (P, K, X-C, and X-NF), there were no detectable differences in the shape and geometry of formed crystals. It should be mentioned that ettringite crystals are also known for having a "needle-like" (i.e. acicular) shape. Ettringite's chemical formula is $3CaO{\cdot}Al_2O_3{\cdot}3CaSO_4{\cdot}32(H_2O)$, and is composed of 19.16% Ca, 4.3% Al, 7.66% S and 63% O in atomic percent [228]. To differentiate between discovered crystals in treated specimens and ettringite, the specimens were considered for further analyses using EDX analyzer to obtain the chemical elements and EDX spectra of the formed crystals.

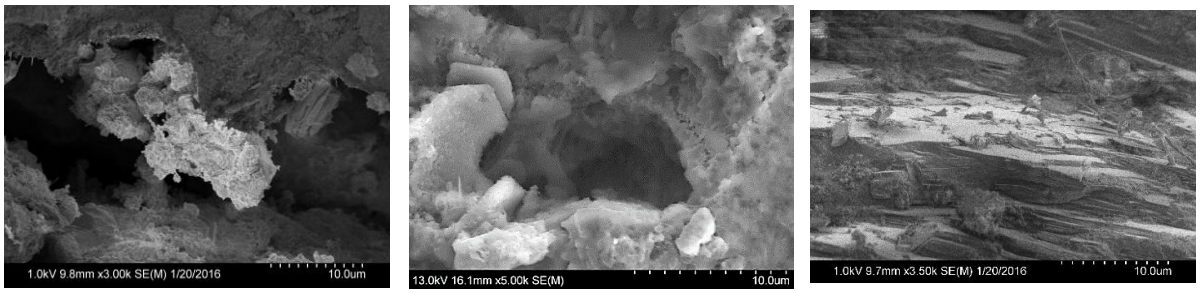

(a) Control mix

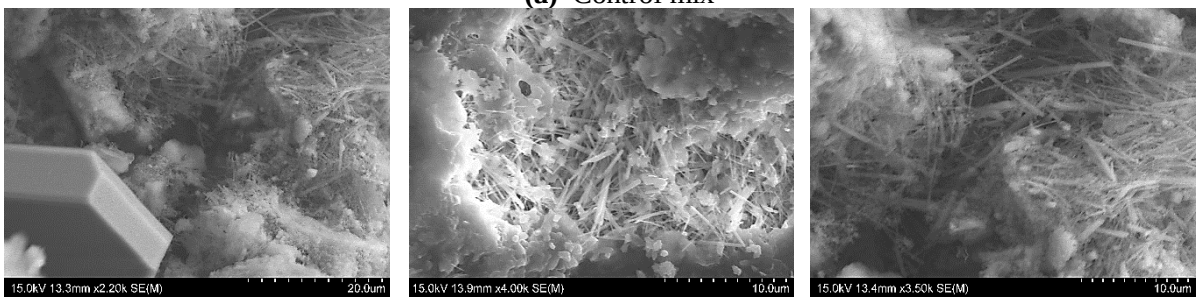

(b) K admixture

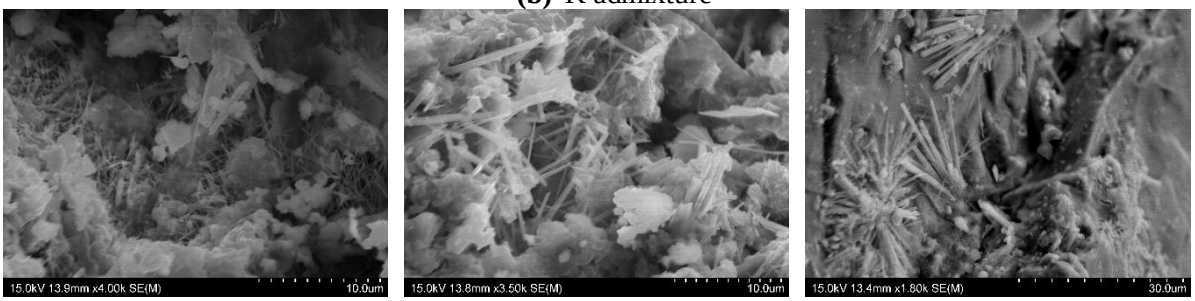

(c) P admixture

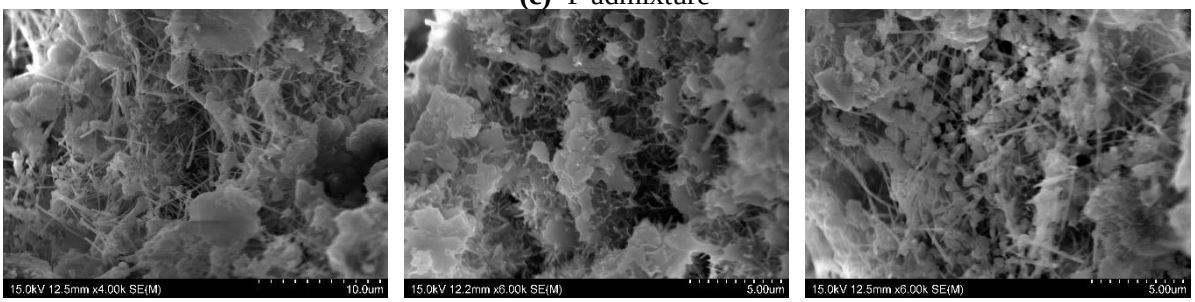

(d) X-C admixture

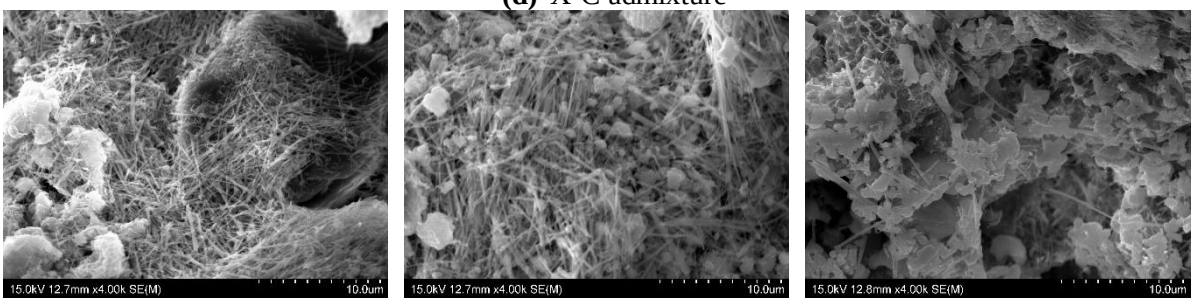

(e) X-NF admixture

Figure 3.14. SEM micrographs of mortars with and without CA (taken from different locations).

3.2.2.2 EDX results

Through this study, spots for EDX analysis were chosen based on the morphology of the formed crystals and hydrated phases. EDX analysis of CA treated specimens (K admixture in this case) showed mostly typical elements of hydrated control mix (Ca, O, and Si in major amounts, in addition to Al, Fe, and Mg), illustrated in Figure 3.15. In this figure, direct visualization, quantification of elements in raw specimen and elemental mapping are plotted. High calcium distribution at bottom left corner of Ca elemental mapping indicated that hexagonal structure, observed in the SEM micrograph. is a CH crystal. X-ray analysis of needle-shaped crystals' regions showed no significant element concentration in the elemental map. It was a combination of different elements in these areas. The results of EDX analysis showed that the matrix of CA treated specimens is relatively homogenous in chemical compositions. Additionally, from the preliminary analysis, it appears that the composition of the "needle-like" crystals in the CA specimens with K admixture are different from the ettringite due to low peak of sulphur (S) in the EDX graph which is one of the major elements in the ettringite chemical composition. Other mortars with different admixture types were also investigated to understand exact chemical compositions of these crystals (ettringite or not). To identify what the hydration products are and whether needle-like crystals are ettringite or not, EDX analysis were performed.

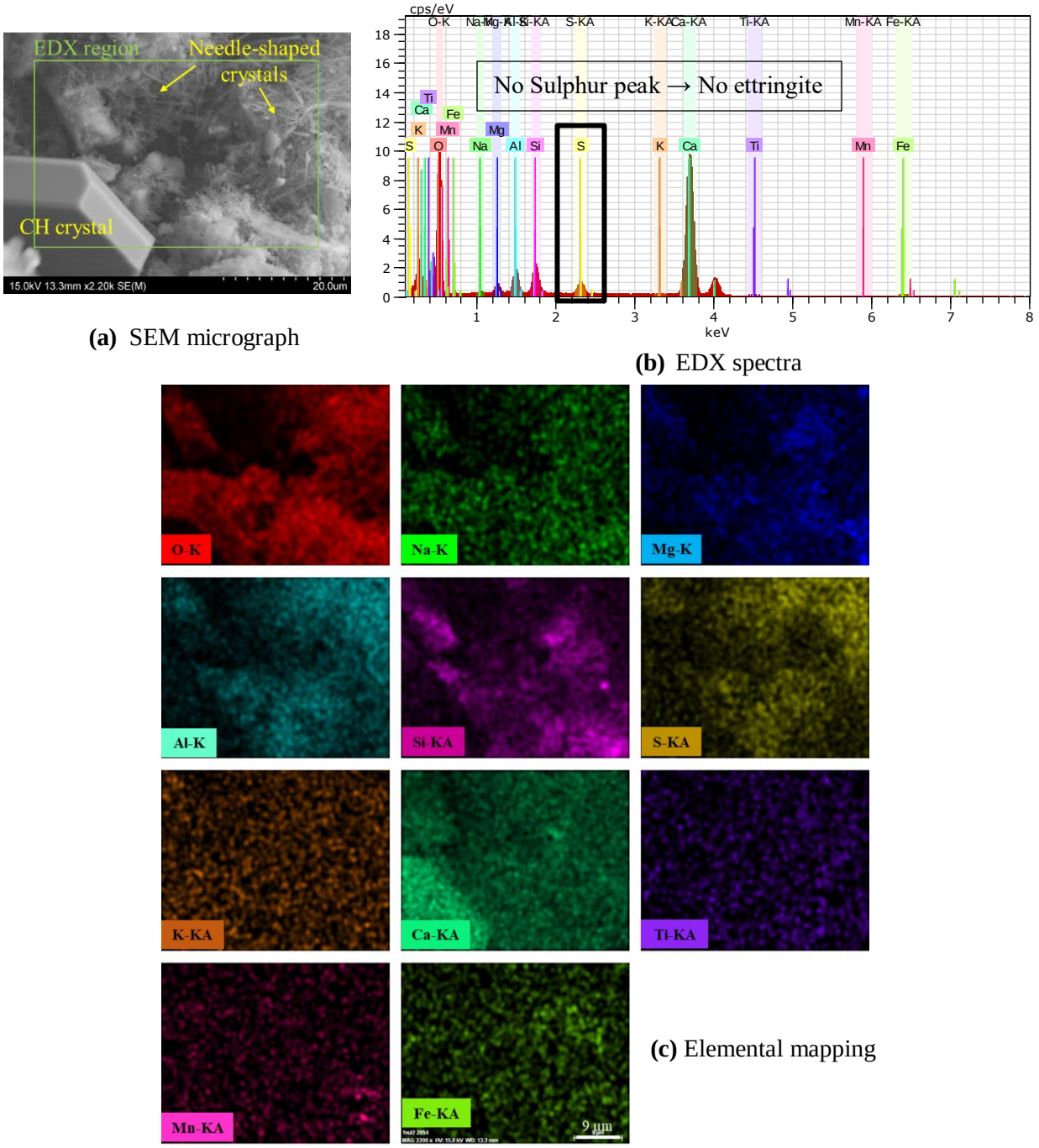

(a) SEM micrograph

(b) EDX spectra

(c) Elemental mapping

Figure 3.15. EDS spectrum and multiple elemental mapping of CA treated mortar mix.

The results obtained from EDX spectrums for other admixtures indicated that not all admixtures can possibly develop needle-like crystals which have different compositions from ettringite. Ettringite's X-ray spectrum typically has the strongest peaks due to calcium, sulfur and aluminium according to spectrum shown in Figure 1.6 in Winter's book [229] (section 1.1.2). In admixtures P and X, similar signs of ettringite

were spotted in different locations as illustrated in Figure 3.16 spectrums. The ettringite crystal holds a lot of water and once it forms, a large increase in solid volume will occur in available pore spaces which leads to expansion of the paste and cracks formation particularly around aggregate particles [230]. Hence, the delayed formation of ettringite needs to be prevented inside the cement matrix.

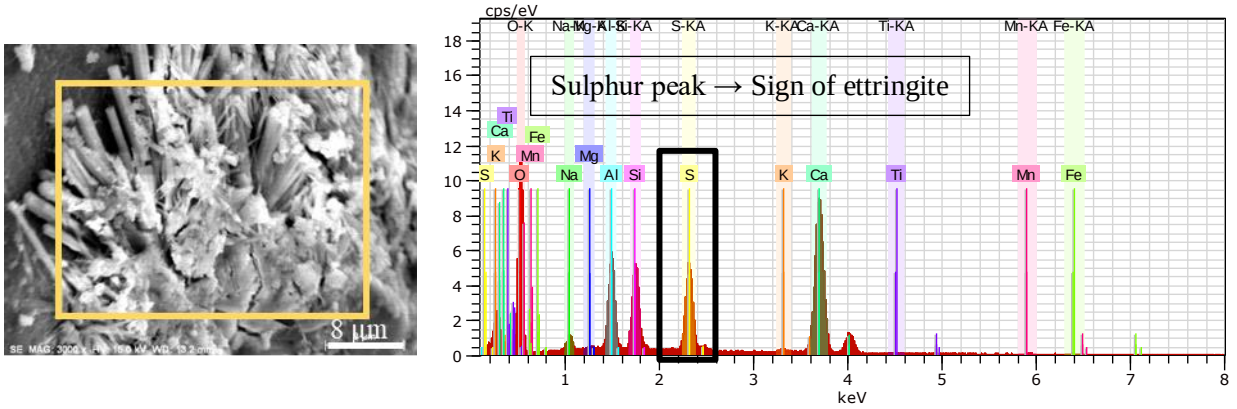

(a) P admixture

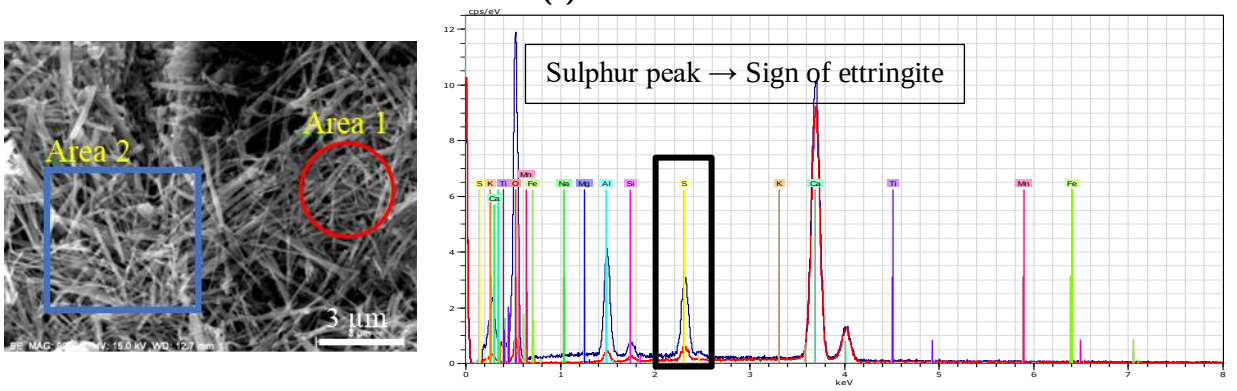

(b) X-C admixture

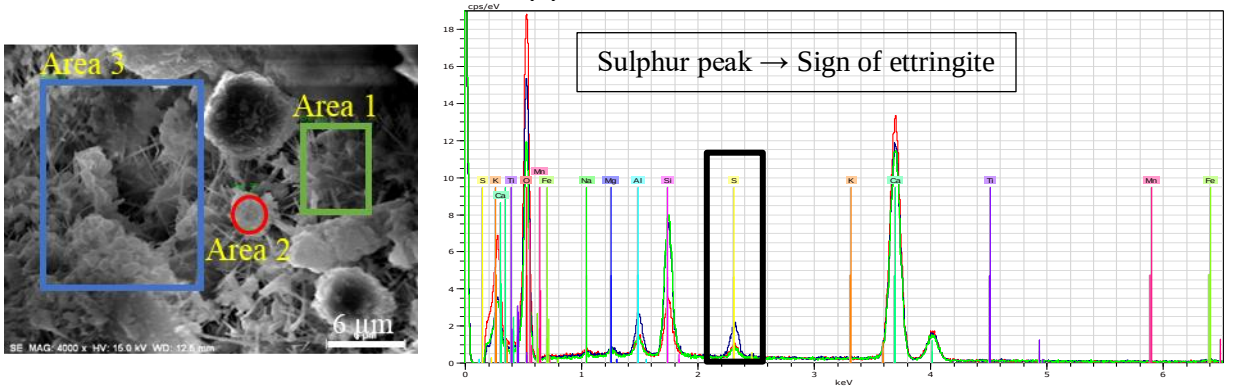

(c) X-NF admixture

Figure 3.16. EDX spectrums of regions containing needle-shaped crystals, investigated for ettringite.

As mentioned in section 3.1.4.1, atomic ratio plot is one of the methods to analyze the EDX data and understand more about the hydrated compositions. Similar procedures, reported in section 3.1.4.1, were followed to calculate atomic ratios for particular elements, illustrated in Figure 3.17. For each mortar type, more than 10 different locations were selected on the specimen and analyzed from their EDX spectrums; then each point was plotted in the following figures. Among these admixture types, P admixture showed irregular distribution and contained some spots located totally outside the specified hydration products regions. X and K admixtures treated specimens indicated Si/Ca and Al/Ca ratios approximately between 0.01-0.45 and 0.01-0.23, respectively. These ratios are within typical range of cement hydration phases. They also showed intermix compositions of CH, CSH and AFt phases while X-NF is mostly located near the line connecting CH to CSH phase. Mono-sulfate and mono-carbonate phases presented in K and P admixtures, indicating intergrow of these phases in the hydration products. No pure gypsum or AFm phase was detected in the hydration products. Overall, no substantial differences were observed between hydration products forming in the presence of CA.

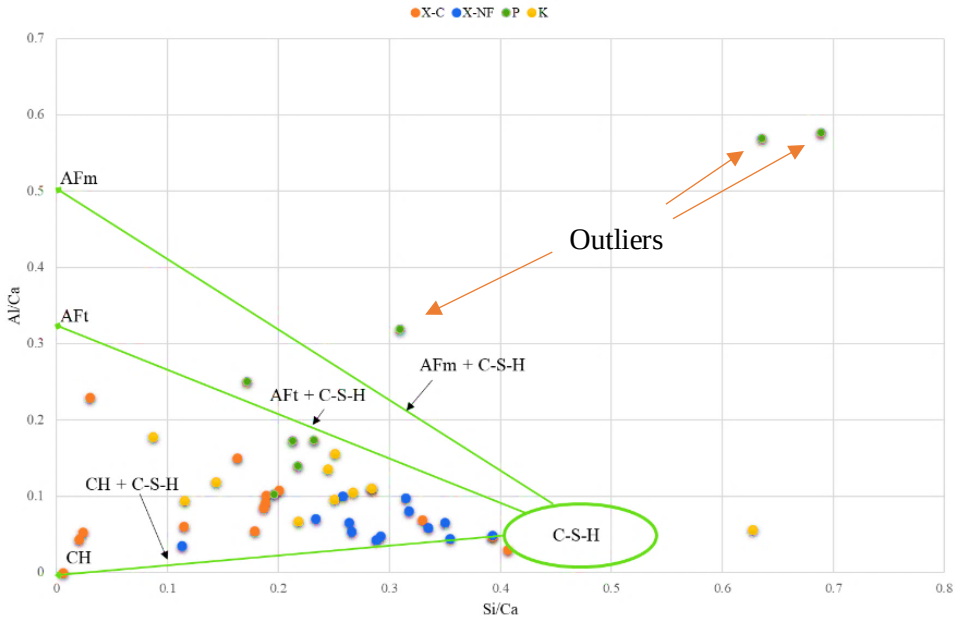

(a)

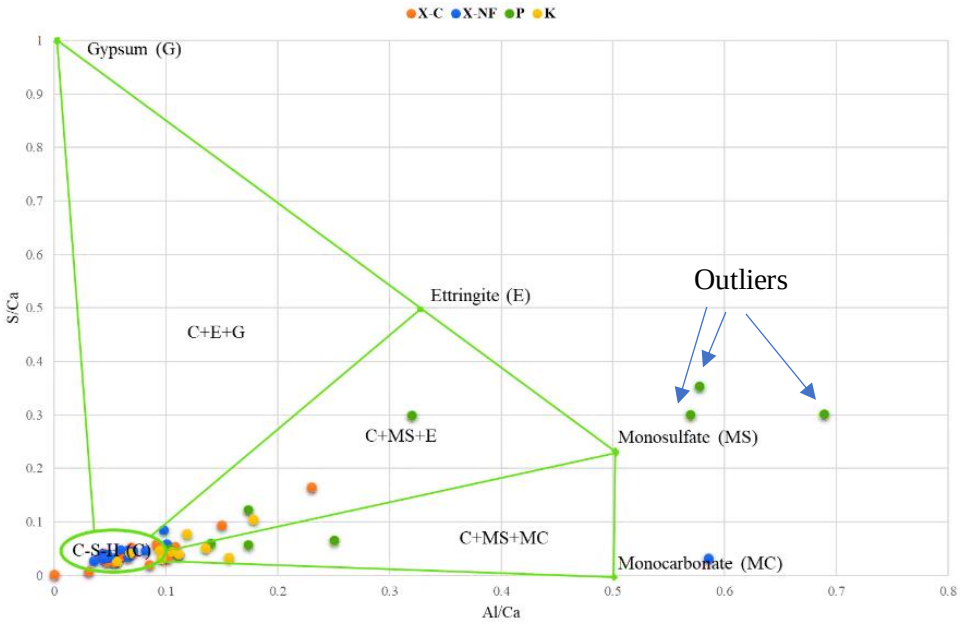

(b)

Figure 3.17. Different CA treated mortars atomic ratio plot of **(a)** Si/Ca vs Al/Ca **(b)** Al/Ca vs S/Ca.

3.2.2.3 Experiment II results

To study morphological aspects and hydration products of polished mortar sections, backscatter mode of SEM along with x-ray detector was used. Fracture surfaces from specimen are typically useful to study morphology of the hydration products or the shapes of the clinker mineral crystals while polished sections are generally much more beneficial in evaluating concrete issues compared with fracture surfaces. From a BSEM image of a polished section of concrete can get an approximate idea of the concrete porosity, degree of cement hydration and cement type used in the mix, all by looking at SEM image [229]. With less reliability and longer analysis time, this information can be also obtained from a fracture surface SEM image. The path length of X-rays generated at depth, which is dependent on the X-ray take-off angle, plays an important role in X-ray travelling time and eventually element peaks in EDX spectrum. To eliminate the role of electron travelling time, polished sections are typically used for SEM analysis to get identical flat surfaces on different spots. Figure 3.18 is a comparison of BSEM images of mortars made with two different cement types and also CA addition. In these images, various hydration phases were identified by using chemical element maps, taken from EDX analysis, and degree of image brightness as marked by different

colours in the micrograph. The difference in image grey levels is mostly attributed to chemical changes since elements with higher atomic number appear brighter in BSEM image. In this examination, most of typical cement hydration products including CSH and CH were identified. The mortars represent CA treated system that did not also indicate any noticeably different morphology than those without admixture and showed similar hydration phases. In some locations, cracks were evidently observed which might be developed at specimen preparation stage because of elevated temperature required for such treatment. As clearly visible, some partially hydrated cement particles could be detected as a grey rim of inner hydration products formed around a white core of anhydrous cement (Figure 3.18).

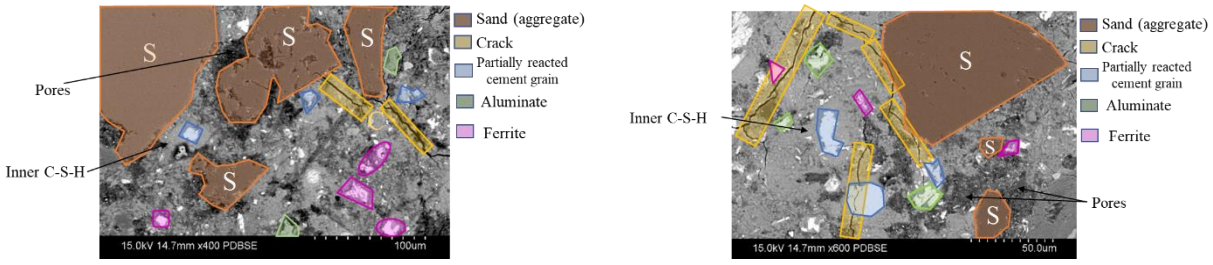

(a) OPC mortar mix

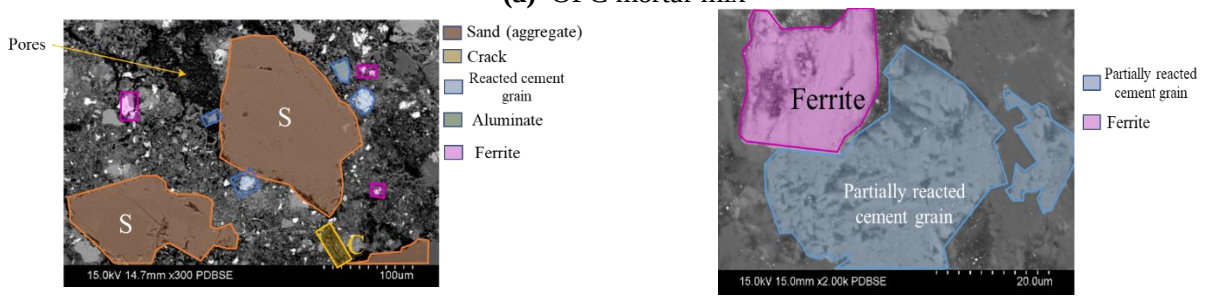

(b) OPC-CA mortar mix

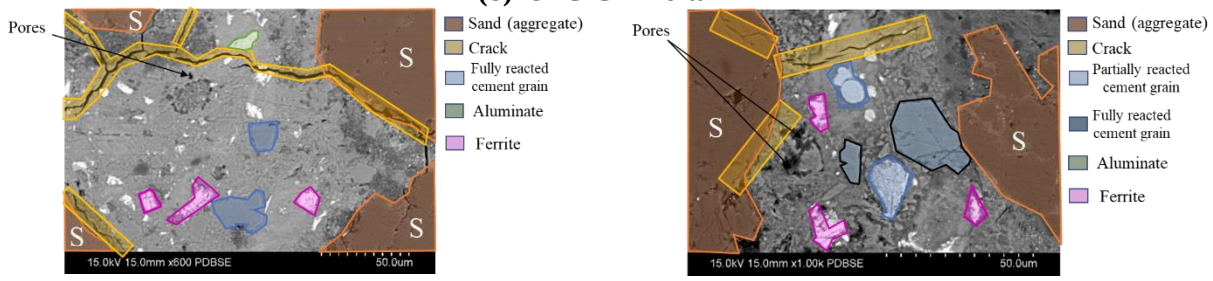

(c) PLC mortar mix

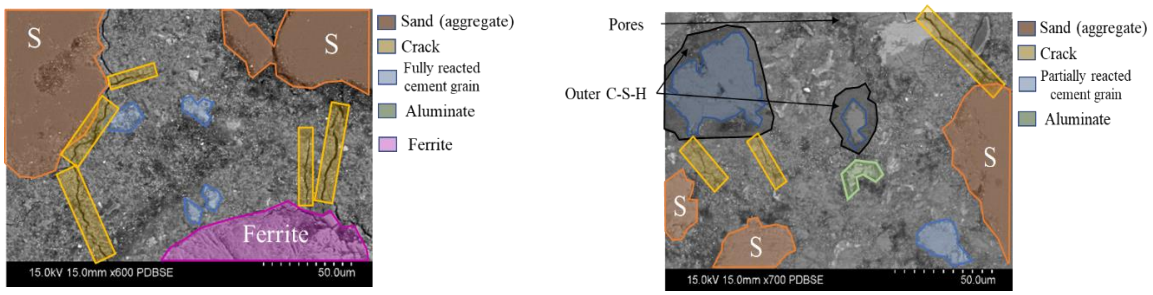

(d) PLC-CA mortar mix

Figure 3.18. BSEM images of polished mortar sections with and without CA.

To examine hydration products of the polished sections, Figure 3.19 shows atomic ratio plots of Si/Ca vs Al/Ca and Al/Ca vs S/Ca for more than 20 different spots in each mix. It was observed that examined spots in PLC mix mostly clustered near CH and CSH regions, suggesting formation of these main hydration products in examined locations while PLC treated mix showed intermix formation of different hydration products. Similarly, the OPC-CA group showed the same trend as PLC mix with most points clustered near CH and CSH. Similar to the PLC-CA mix, combination of hydration phases was observed for OPC mix. These observations can be also confirmed by Figure 3.19-(b). PLC and OPC-CA mixes show mostly CSH gel as their hydration product while intermix of mono-carbonate and CSH phases were observed for OPC and PLC-CA mixes. Presence of CA in the mix did not indicate any differences in major hydration products than those in control samples.

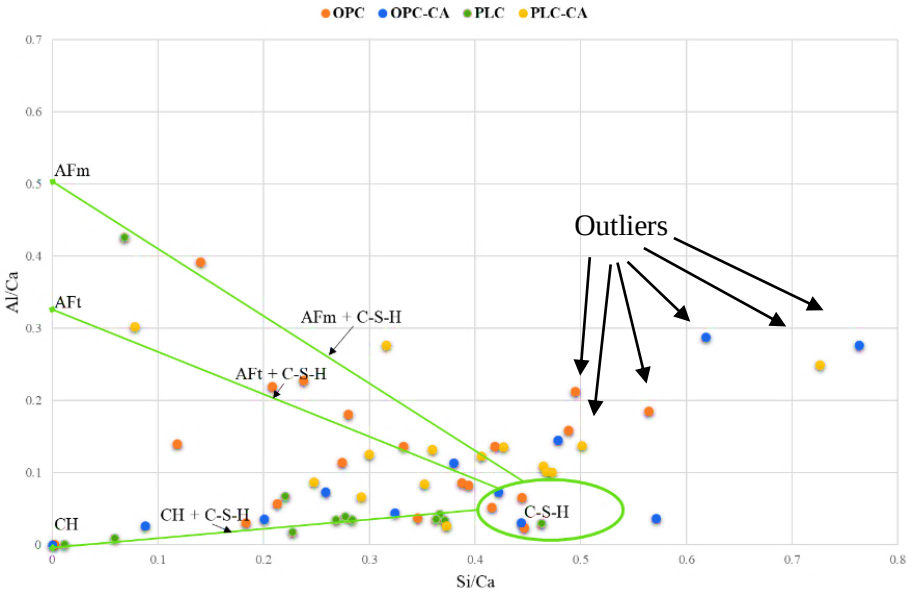

(a)

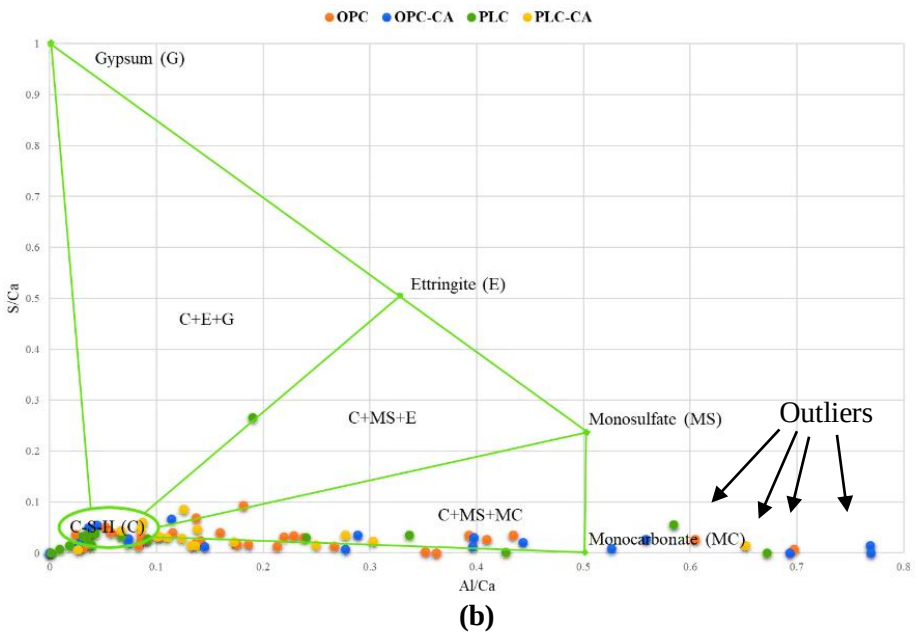

(b)

Figure 3.19. CA un-/treated mortars atomic ratio plot of **(a)** Si/Ca vs Al/Ca **(b)** Al/Ca vs S/Ca.

Figure 3.20 illustrates the change in the average porosity of hardened cement paste with the number of frames analyzed for mortar specimens with and without CA. The average porosity was determined as percentage of the segmented pore area (black spots) to the total paste area in the generated binary image (described in section 3.2.1.3). The average values for paste porosity range from 8.5% to 29.3% for all mixes. As can be seen, addition of CA into the mix resulted in slightly lower paste porosity, indicating possible effect of this admixture in blocking pores/cracks and reducing the matrix's overall porosity. It should be noted that reduction in porosity does not necessarily mean that permeability is reduced since pore size and its connectivity are also influential parameters to be considered. Using PLC instead of OPC did not also show a substantial reduction in paste porosity. No similar study found to report such microstructure features of crystalline admixtures treated system at micro level using SEM and EDX analyses.

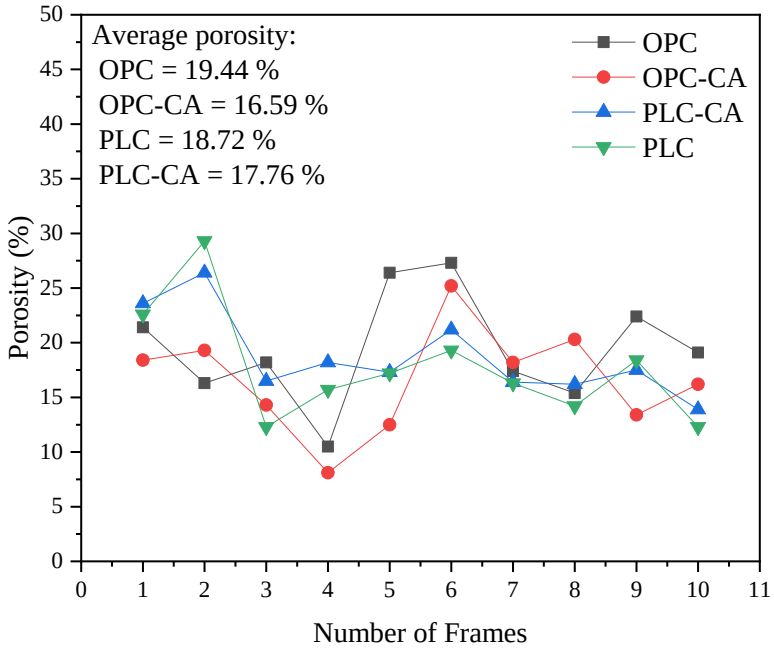

Figure 3.20. Variation of average porosity with the number of images analyzed for mortars with and without CA.

3.2.3 Concluding remarks

This section aimed to draw some insights about the microstructural features of cementitious composites modified by CA addition. In the first batch, four CA types from different manufacturers were individually added into the cement matrix and their effects on modifying microstructure, forming needle-like crystals, and hydration phases were examined using SEM and EDX analysis. The SEM micrographs taken from specimen's fracture surface showed formation of pore-blocking crystals for all treated mixes while similar spots in un-treated sections left uncovered. Although needle-shaped crystals were observed in the treated mortar specimens, not all of them had different shapes and chemical compositions than ettringite (well-known to form needle-like crystals). Care should be taken in choosing and applying different CA systems into new or existing structures since different hydration products and type of needle-like crystals were observed to be formed in each system. Using backscatter SEM images and EDX spectrums, examination of polished mortar sections with and without CA also showed typical hydration phases, forming in the

control system. Image processing using ImageJ software indicated a slight decrease in porosity of CA treated mortars than those with only OPC or PLC cement.

Chapter 4 Assessment of self-healing and durability parameters of concretes incorporating crystalline admixtures and PLC

This paper has been submitted to the Journal of Cement and Concrete Composites on July 30, 2018.

Pejman Azarsa, Rishi Gupta, Alireza Biparva. "*Assessment of self-healing and durability parameters of concretes incorporating crystalline admixtures and PLC.*' Submitted to Journal of Cement and Concrete Composites (2018).

Author Contributions: Pejman Azarsa, Rishi Gupta and Alireza Biparva conceived and designed the experiments; Pejman Azarsa performed the experiments, collected the data, and analyzed them; Rishi Gupta and Alireza Biparva contributed materials and experimental equipment; Pejman Azarsa wrote the paper and Rishi Gupta revised it as needed.

Highlights

- Chloride and water permeability tests are compared/correlated for concretes containing crystalline admixtures (CA).
- Influences of CA on the crack self-healing of concrete have been studied using an innovative technique.
- PLC is slightly more effective than OPC in improving concrete's durability and strength.
- Influencing parameters on electrical resistivity of concrete treated with CA have been investigated.

4.1 Abstract

Infrastructure is in need of cementitious materials that are both durable and sustainable for use in new and repair applications. The repair of concrete structures damaged by water or water borne chemicals is estimated to cost billions of dollars every year worldwide. However, the solutions that can make concrete structures more sustainable and durable, are limited. The use of crystalline admixtures has a potential of improving the durability and permeability of concrete structures especially those exposed to corrosive coastal environments. This paper presents various investigations on the influence of crystalline admixtures on the strength, self-healing, and durability characteristics of concretes with two different cement types (Ordinary Portland Cement (OPC) & Portland Limestone Cement (PLC)). This study also reviews the

previous work that has been done on crystalline admixtures. Test methods include the rapid chloride permeability (RCP) test per ASTM C1202, surface and bulk electrical resistivity, water permeability test per DIN 1048, self-healing test, compressive strength test and salt ponding test per ASTM C1556. The results indicate that the water permeability coefficient decreased by 3 times whereas the self-healing ratio increased by higher rate by adding crystalline admixtures into the concrete mix. It was also found that the electrical charge passed in Coulombs reduced for treated samples during RCP test when compared to reference samples as temperature increases. Based on experimental results and regression analyses, empirical equations are established to correlate the concrete durability characteristics such as resistivity, total charge passed, or water permeability with each other. It is hypothesized that electrical methods, as indirect methods, may not be able to estimate chloride permeability in CA-treated concrete due to differences in pore solution chemistry or porosity. To asses this hypothesis, results from electrical tests were compared with diffusion coefficient from bulk diffusion in salt solution and also water permeability coefficient obtained by water penetration test. Total charge passed, and resistivity measurements showed poor correlation with diffusion coefficients from salt ponding test and underestimated the resistance to chloride ion and water penetration for concretes containing CA. The correlation between the outcome of the surface and bulk resistivity is strong, revealing interchangeable application of these methods in construction industry. Finally, evidence from self-healing test of CA treated specimens suggests faster water flow stoppage through average surface crack widths up to 250 µm, measured by an optical microscope.

Keywords:

Crystalline Admixtures, Self-healing, Chloride Diffusivity, Electrical Resistivity, Water Permeability

4.2 Introduction

Self-healing (SH) materials are innate in the human body from the day we are born and can be identified by blood clotting mechanisms, repairing of fractured bones and even the continuous rebirth of the skeleton cells which typically results in a full renovation of the skeleton [19]. Interestingly, concrete, the most widely used construction material, is also not exempt from this phenomenon. It can naturally heal itself to a certain

degree. When a crack occurs inside the matrix, concrete can autogenously seal the crack through four mechanisms including (1) formation of calcium carbonate ($CaCO_3$) (2) continued hydration upon moisture contact (3) swelling of cement matrix (4) sedimentation of debris which eventually results in gaining its certain mechanical or durability properties (Figure 4.1 [231]). In young concrete, continued hydration is the dominant healing mechanism because of its fairly high content of un-hydrated cement particles whereas calcite formation becomes the main mechanism at later age [232]–[234]. Different SH mechanisms which can initiate simultaneously are highly dependent upon the concrete age at the time of cracking. Starting to appear in the past two decades, great research studies have been conducted to understand various aspects of intrinsic SH in concrete [30], [35], [48], [54], [232]–[241]. Due to limited crack width closure (~200-300 μm) and uncertainty of natural healing [48], [239], [242]–[244], the concept of Engineered Self-healing Concrete (EShC), by artificially triggering healing agents such as microencapsulation of bacteria or use of crystalline admixtures, has been introduced and has recently become a weighty topic of interest in the concrete world. Use of EShC in structures could lead to a decreased deterioration rate, less repair demands, minimized costs and eventually extended ultimate service life [245]. Additionally, it allows *in-situ* self-repair with no external human involvement for inaccessible structures. Considering EShC's benefits, influences on structural serviceability and sustainably, several smart methodologies have been employed to design this concrete type, including chemical encapsulation [7], [27], [246], expansive agents and mineral admixtures [15], [40], shape memory materials [247], [248], bacteria-based concrete [6], [10], [12], [13], hollow fibers [25], [26], [29], [249]–[255], and self-healing triggered by self-controlled tight microcracking [48], [49], [231], [256]–[261].

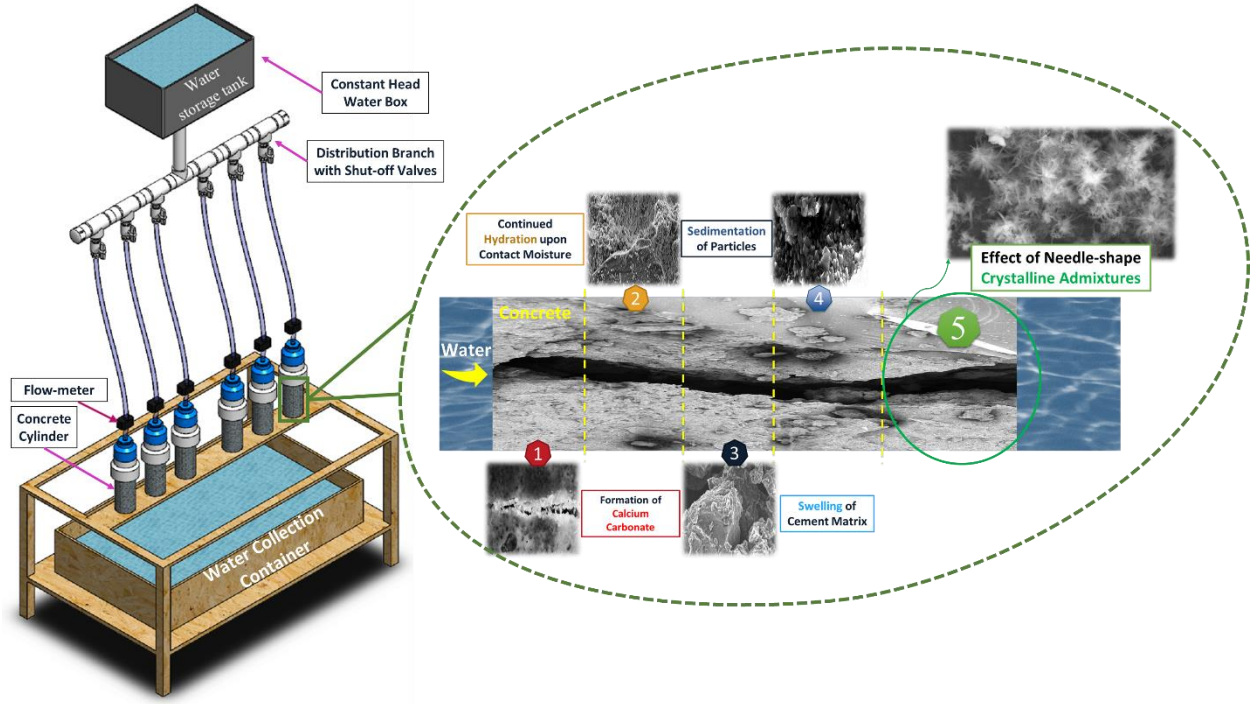

Figure 4.1. Self-healing mechanisms and testing setup [231].

One of the smart materials for fabrication of EShC is Crystalline Admixtures (CA) which is one of the Permeability-Reducing Admixture (PRA) types with hydrophilic nature that can react easily with water. Typically, CA consist of a proprietary mix of active chemicals, implanted in a carrier of cement and sand, reacting with tricalcium silicates (C_3S) in the concrete compounds as described by the American Concrete Institute (ACI) Committee 212 [21]; however, in Sisomphon *et al.* [15] study, it is stated that calcium hydroxide ($Ca(OH)_2$) is the reactive component. As a result of the chemical reaction described in Equation 4.1 and deposition of integrally bonded crystals into the hardened cement paste, pressure resistance of modified matrix increases as high as 14 bars [21].

$$3CaO - SiO_2 + M_xR_x + H_2O \rightarrow Ca_xSi_xO_xR - (H_2O)_x + M_xCaR_x - (H_2O)_x$$

(Calcium silicate + crystalline promoter + water⟶ modified calcium silicate hydrate + pore-blocking precipitate) Equation 4.1

There are relatively a few recent studies that address the influence of CA as a promoter of self-healing. Jaroenratanapirom and Sahamitmongkol [55], [56] studied the visual closing of cracks in mortar samples which were treated with crystalline and expansive admixtures and were immersed in water for the healing period. Their results indicated that CA performed better than control mortars in healing small (under 50

μm) and early age cracks (at 3 and 28 days) although showed ineffective behavior for larger cracks (300 μm). In a similar study, Sisomphon *et al*. [15] reported that only crack up to 150 μm were completely sealed when pre-cracked cement-based materials treated with Calcium Sulfo-Aluminate (CSA) based expansive additive and CA were immersed under water for 28 days. From water permeability test results, they observed rapid healing for mortars with CA during first 5 days, but only limited reaction from control mixes. Later, Sisomphon *et al*. [57] examined the recovery of mechanical properties of CA treated strain-hardening cementitious composites subjected to wet/dry cycles, humidity chamber, water immersion, and air exposure. Although, their results showed slight benefit of using CA as compared to control mixes, the reaction was observed for both CA- and un-treated samples when exposed to wet/dry regime. Ferrara *et al*. [16] investigated the self-sealing capability and recovery of stiffness and load-bearing capacity by means of 3-point bending (3pb) test, in normal strength concrete containing CA at a dosage of 1% by the cement weight. In addition to that, Ultrasonic Pulse Velocity (UPV) test and microstructural observations were performed. Three exposure conditions examined in this study included water immersion, air exposure, and accelerated temperature cycles. For water immersion condition, they reported that the presence of CA sped up the crack healing process and recovered the bending stiffness as well as load-bearing capacity of concrete. However, for specimens in accelerated exposure condition, no definite conclusion was stated due to high dispersion of obtained results. It was also found that a crack closure above 70-80% is necessary to start recovery of stiffness and load bearing capacity [16]. CA influences on the concrete self-healing, measured by standard water permeability test after being subjected to four healing conditions, were tested in Roig-Flores *et al*. [17]. Crack geometrical parameters were also measured in this study based on the composed panorama pictures showing the cracks along their length. Water Immersion (WI), Water Contact (WC), Humidity Chamber (HC), and Air Exposure (AE) were different environmental conditions with the objective of simulating practical circumstances. They stated that neither control specimens nor those with CA healed when exposed to moist conditions. In their findings, the four exposures in order of decreasing permeability healing ratio were: WI (around 0.9) > WC (around 0.8) > HC (around 0.5) > AE (around -0.15) [17]. Afterwards, Roig-Flores *et al*. [18] studied the self-healing capability of early-age concretes

containing 4% CA using water permeability test based on the standard procedure in EN 12390-8 [58]. Under water at 15 ºC and especially at 30 ºC, they concluded that healing ratio was higher for CA treated specimens as compared to those for control. However, the high-scattered results were seen for both treated and un-treated concrete under the wet/dry cycles exposure. The obtained results were slightly better when using CA in the high-performance concrete, mainly due to the lower scattering of results. In a recent study by Ferrara *et al.* [19], the effects of CA on the self-healing capacity of the cementitious composites with reference to both a Normal Strength Concrete (NSC) and a High Performance Fiber Reinforced Cementitious Composite (HPFRCC) were examined. In the treated mixture, a dosage of 3% CA was added and more details of their experimental program was reported similarly in [16]. Both in the case of NSC and HPFRCC, the CA enhances and makes more reliable the autogenous healing capacity of cementitious composites. In NSC, CA could promote up to 60% of crack sealing even under exposure to open air. In the case of HPFRCCs, which would already feature autogenous healing capacity because of their peculiar mix compositions, the synergy between the dispersed fiber reinforcement and the action of the CA has resulted in a likely 'chemical pre-stressing' of the same reinforcement, from which the recovery of mechanical performance of the material has greatly benefited, up to levels even higher than the performance of the virgin un-cracked material.

Although, CA efficacy as self-healing agent has been already documented and fairly well-understood, some discrepancies have been noted when reviewing the healing capability of concrete containing CA which motivates specific analysis on this topic to enlarge the database available in the literature. Besides that, self-healing has been observed frequently in the field, but an appropriate lab test method is required to enhance supporting laboratory data. For instance, in the above-mentioned studies where they used standard water permeability test to measure water penetration depth in pre-cracked concrete, the main requirement is to continuously subject the specimen to hydrostatic pressure which may not happen in practice and interfere with the results. However, an experimental methodology, schematically shown in Figure 4.1 and developed in authors' previous publication [1], can analyze real-life conditions of the self-healing process and directly

quantify this mechanism. The innovative test technique involves three stages: (1) inducing repeatable cracks (2) subjecting the cracked specimens to controlled hydrostatic pressure to measure flow (3) quantifying the self-healing property of cement-based materials. Also, influence of CA on water permeability and durability properties such as chloride penetration resistance and electrical resistivity in virgin concrete especially when combined with Portland Limestone Cement (PLC) has yet to be confirmed and is still under question. Through deposition of crystalline and densification of concrete matrix, it is expected that porosity reduces, resulting in reduced permeability and enhanced ion diffusion resistance (e.g. chloride). However, no studies have discussed the chloride permeability and electrical resistivity of concrete with CA which to the authors' knowledge is herein investigated for the first time. Hence, research is required to recognize the potential physical/chemical mechanisms affected by adding CA into concrete, contributing to the design of durable and sustainable CA treated concretes for construction industry. Limited experimental studies have been performed to find relationships between aforementioned test results of concrete which will be explored in this study as well.

The objective of the present study was to experimentally investigate the effectiveness of CA in enhancing self-healing mechanisms and improving the water and chloride penetration characteristics of concrete. The penetration properties were measured using rapid chloride permeability (RCP) test following procedures documented in ASTM C1202 [153], surface/bulk electrical resistivity test in accordance with AASHTO TP95 [61], bulk diffusion test according to ASTM C1556 [262], and DIN 1048 [263] test that determines the water permeability under hydrostatic pressure. Correlation and systematic comparison between these test methods were also established for concretes with CA. The well-standardized methodology employed from authors' pervious work [1] to evaluate the self-healing properties of cracked specimens based on measure of the flow rate through the crack. The results of this study were instrumental in quantifying self-healing and certain durability related parameters for concretes containing CA which could be used into a durability design framework.

4.3 Experimental Program

This study investigated the effect of CA on concrete durability properties and its self-healing. This section comprises of a description of the materials, mixture proportions, casting, curing conditions and preparation of specimens including the testing procedures performed in this study to determine the mechanical and certain durability properties of CA treated concrete.

4.3.1 Materials and mixture proportions

Two different cement classes, Ordinary Portland Cement (OPC) - Type I in accordance with ASTM C150 (referred as type GU in CSA A23.1-14 [264]) and Portland Limestone Cement (PLC) (also referred as Type GUL in CSA A23.1-14 [264]), were investigated in this study, featuring the same water/cement (*w/c*) ratio and cement contents. The concrete compositions of these two cement types were further modified by adding CA, in powder form, at a dosage equal to 2% by the weight of cement whose behavior was being compared with control specimens (without CA). A commercially available hydrophilic permeability reducing admixture (PRA) commercially produced was used as the waterproofing cementitious material (or CA). However, the chemistry of this product is proprietary and not available. The *w/c* ratio used was 0.532 in all types of concrete mixes and the mix design, which represents a typical mix used in the field with target strength of about 35 MPa, is given in Table 4.1.

Table 4.1. Mixture proportions of concrete.

Mix ID	Mix proportions (kg/m^3)					*w/c* ratio
	Cement	Aggregates		Water	CA (2%)	
		Coarse (5-14mm)	Fine			
OPC	358	990	862	190	-	0.532
OPC-CA					7.16	
PLC					-	
PLC-CA					7.16	

4.3.2 Specimen preparation

For each mixture, in total, twenty cylinders of both Φ100×200 mm and Φ100×150 mm, and also three conical frustum of Φ150(top)×175 mm for water permeability test were prepared in accordance to recommendations by ASTM C192 [265] practice. In accordance with ASTM C143 [266], slump flow test were performed within 15 minutes after preparing the mixes to avoid any loss of workability with time. For all mixtures, air content was also determined by following the procedure in ASTM C231 [267]. The density of a fresh concrete batch was measured in accordance with ASTM C138 [268]; it is theoretically defined as the mass to volume ratio [268]. For measuring the fresh mixture density, a container of known volume and weight is filled to the brim with the freshly prepared concrete mixture. Temperature of fresh concrete mixture was measured in accordance with ASTM C1064 [269]. A thermometer was placed in different locations of the mixture after the mixing process was complete and average reading of the temperature was recorded. After measuring fresh concrete properties, the specimen molds were placed on a vibrating table, filled with fresh concrete in two approximately equal layers, and then compacted by an external vibration for a duration of 60-90 seconds. After consolidation, each mold was labeled; then covered with a plastic sheet to prevent the evaporation of water from the concrete surface and kept for 24±2 h in the laboratory. After removal from molds, all Φ100×200 mm cylinders were continuously cured in a water bath before testing while other samples were air-cured. Table 4.2 summarizes the specimens' type and quantity as well as curing conditions used in different test methods.

Table 4.2. Type, number, and curing conditions of specimens used in different test methods.

Test method	Number of specimen	Type of specimen	Curing condition	Standard
Compressive strength	3	Cylinder (Φ100×200mm)	28 days (water-cured)	ASTM C39
Water permeability test	3	Conical frustum (Φ150(top)×175mm)	28 days (air-cured)	DIN 1048
Electrical resistivity measurement test	3	Cylinder (Φ100×200mm)	210 days (water-cured)	AASHTO TP95
Rapid chloride permeability test	4	Cylinder (Φ100×50mm)	28 & 56 days (water-cured)	ASTM C1202
Apparent diffusion coefficient test	3	Cylinder (Φ100×75mm)	28 & 56 days (water-cured)	ASTM C1556

Table 4.2. Type, number, and curing conditions of specimens used in different test methods.				
Self-healing test	10	Cylinder (Φ100×150mm)	28 days (air-cured)	-

4.3.3 Items of investigation

4.3.3.1 Compressive strength

At 28 days from casting, three cylindrical specimens (Φ100×200 mm) from each mixture were tested in Saturated Surface Dry (SSD) condition, following the procedure reported in ASTM C39 [270] in order to determine each mix's compressive strength. Prior to testing, each cylinder end was surface ground to ensure even distribution of the load applied on the cylinder surface.

4.3.3.2 Water permeability coefficient

The water permeability of mixtures was determined using DIN-1048-Part 5 standard [263]. Prior to testing, specimens' top surface was wire brushed, following the DIN 1048 standard, and then three specimens from each mixture were subjected to 0.5 MPa (5 bar) of hydrostatic pressure for three days (72 h). Each specimen was mounted into a cell consisting of a rubber gasket with a 100-mm diameter to avoid leakage while applying water pressure. After the testing was completed, the specimens were then split into two halves (perpendicular to the injected face) using a compression machine and the depth of water penetration was marked for each half and measured immediately.

Assuming that the flow of water through the concrete pores is stationary and laminar [271], coefficient of water permeability (k_w) can be determined using measured water depth according to modified Darcy's Law [271] as follows:

$$\frac{dx}{dt} = k_w \frac{h}{x} \qquad \text{Equation 4.2}$$

where x is the penetration depth (m), t represents the experiment time (s), k_w indicates the permeability coefficient (m/s), and h is the water head (m). Permeability coefficient can be simply derived by integrating Equation 4.2 to obtain Equation 4.3:

$$k_w = \frac{x_t^2}{2ht} \qquad \text{Equation 4.3}$$

where x_t is the penetration depth at time *t*. Since the water flow is unsteady and associated with sorptivity, it is more reasonable to consider average depth of water penetration instead of maximum one to calculate k_w [271]. Using AutoCAD software, the x_{avg} for divided specimens was determined by measuring the wetted area (A_w) and maximum width (w_{max}) of this region as illustrated in Figure 4.2. Then, x_{avg} was calculated as the average of the A_w divided by w_{max} for each half.

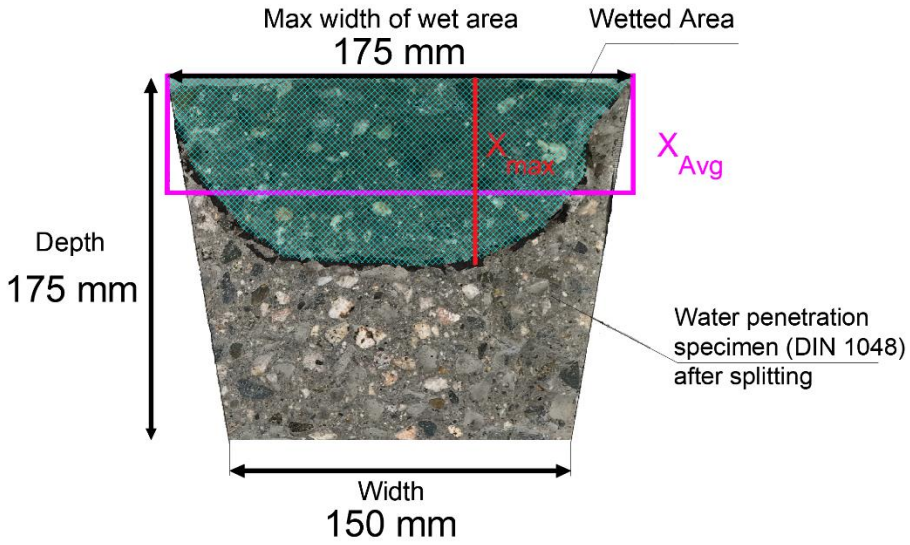

Figure 4.2. Method for calculating the average depth (x_{avg}) in the wetted region.

4.3.3.3 Rapid Chloride Permeability (RCP) test

Following procedure reported in ASTM C1202 [153], the RCP test was performed on four concrete slices with 50-mm thickness, cut from four Φ100×200 mm cylinders. To ensure one-directional Cl^- ions penetration, the side surfaces around the circumference of concrete slices were epoxy-coated. Afterward, the disks were vacuum saturated (for 3 hours period), deaerated, and then submerged in water for 18±2 h before testing (Figure 4.3). Specimens were then mounted into test cells of Giatec Perma2^{TM} device containing two reservoirs, where one reservoir was filled with 0.3 Normal NaOH solution (anode), and the

other with 3% wt. NaCl solution (cathode). 60 V potential difference was applied during test to allow the transfer of chloride ions through concrete from cathode (NaCl solution) to anode (NaOH solution). The test was conducted for a six-hour period, during which the current and temperature were measured every minute. The total charge passing was measured by integrating the area under current vs time curve, presented in Coulombs and the average value of four samples was reported.

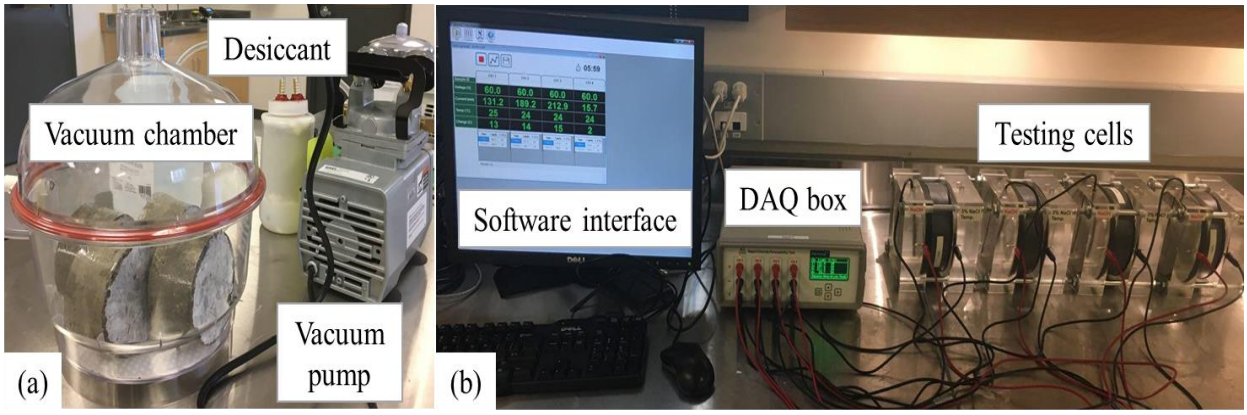

Figure 4.3. (a) Water saturation setup **(b)** RCP test apparatus.

4.3.3.4 Electrical resistivity (surface and bulk resistivity)

Non-destructive electrical resistivity measurement was performed on three Φ100×200 mm cylinders at ages of 7, 14, 28, 56, 90, 160, 210 days. The surface electrical resistivity measurement, following both AASHTO TP95 [61] and ASTM working document (WK37880) methodologies, was performed by two commercially available non-destructive four-probe Wenner SR meter - 38 mm equally spaced - manufactured by Proceq and Giatec Scientific Inc. The equipment, shown in Figure 4.4-(a), works on low fixed frequency alternating current (AC) which is flowing between the outer electrodes and measures the potential difference between two inner electrodes. This study also investigates the influence of different frequencies (13, 40, 100 Hz) and two commercial SR meters. All cylinders were removed one by one from the water curing tank before testing in the specified days and tested at Saturated Surface Dry (SSD) condition at 23±3 °C. Readings were taken for a total of eight measurements with the four set of probes centered every 90° along the longitudinal direction of cylinder.

RCON meter was used to measure the Bulk Resistivity (BR) of the same Φ100×200 mm concrete cylinders. It is another non-destructive instrument, manufactured by Giatec Scientific Inc (Figure 4.4-(b)). Since resistance measurement with a DC signal is not recommended due to electrodes' polarization effect, an Alternating Current (AC) was used to apply the current at a fixed frequency of 1 kHz through the specimen. The electrodes consist of circular stainless-steel plates, on which a contact sponge wetted with a dilute solution of soap, was inserted in between two electrodes to ensure that the entire surface is in electrolytic contact with the electrode. Figure 4.4 also shows a schematic diagram of fundamental physics involved for the measurement of the SR and BR. For each test, three specimens were tested, and average of these readings were taken.

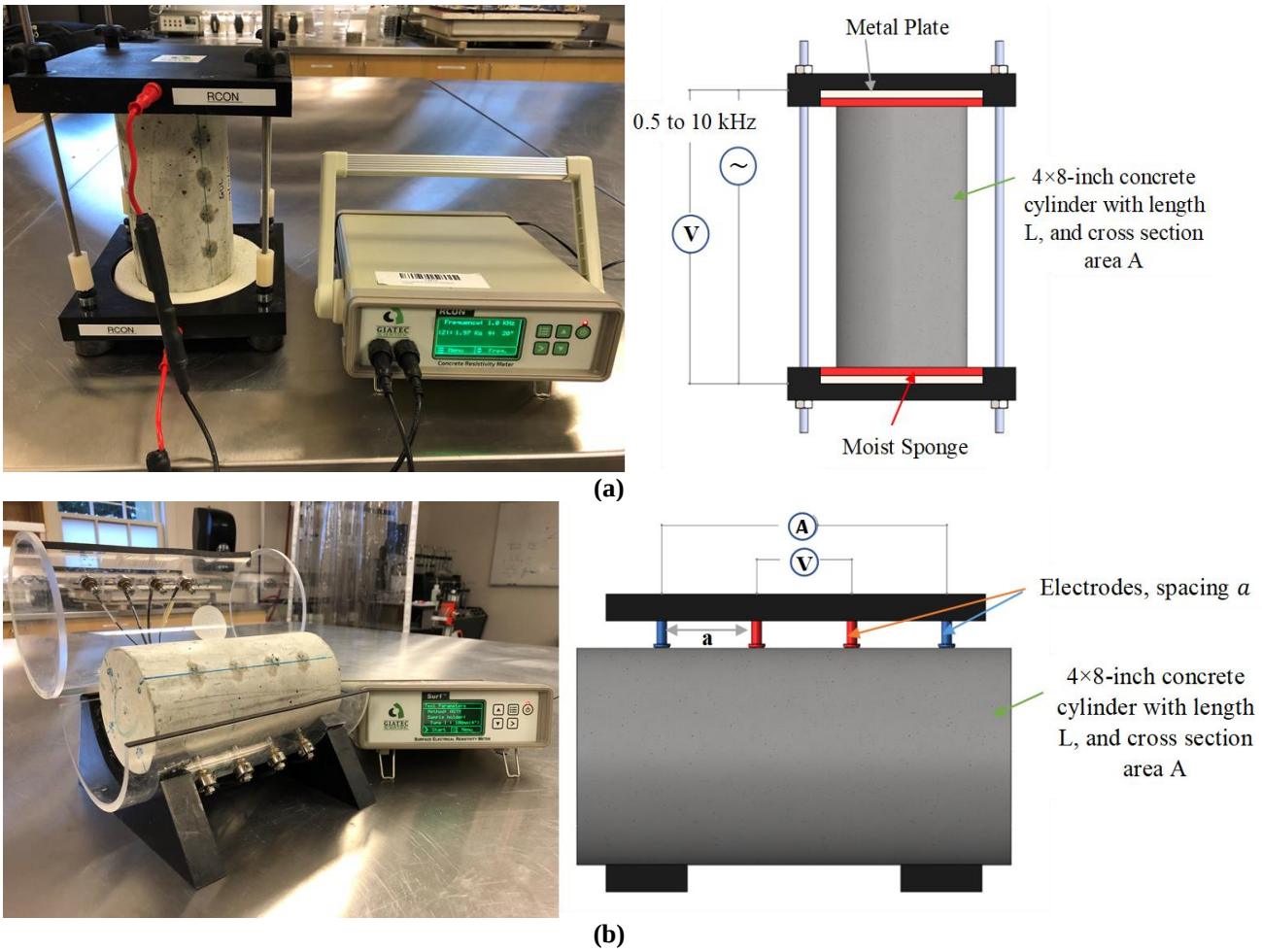

Figure 4.4. Testing concrete specimen & schematic diagram of **(a)** RCON meter **(b)** SR testing instrument.

4.3.3.5 Apparent chloride diffusion coefficient

To determine values of surface chloride concentration and apparent chloride diffusion coefficient for each mixture, Φ100×200 mm cylinders were sliced into 75 and 20 mm thick disks cured inside the water curing tank for 28 and 56 days. After the curing period, specimens were air-dried, sealed from all sides except the finished surface, immersed in a saturated calcium hydroxide (3 gr/L) water tank until the mass did not change by more than 0.1 % in 24 h; later ponded in 165 g/L aqueous NaCl solution according to ASTM C1556 [262] for 6 months at 23±3 °C. The specimens' weight prior and after ponding were measured. After ponding, samples were removed from the solution and stored for 24 h in the laboratory at 23±3 °C and 50±4% RH. Using a rotatory hammer drill, 10 grams of powder sample were obtained from each layer by grinding off material parallel to the exposed surface. To determine acid-soluble chloride-ion content of powder mass, C_x (mass %), Rapid Chloride Test (RCT) kit from Germann instruments was used.

4.3.3.6 Self-healing test

As mentioned earlier, ten cylinders of Φ100×150 mm for each mixture were prepared. These were later cracked using an innovative technique reported by authors in [1] in order to examine self-healing capability of cracked cylinders. In this method, one of the major benefits of this method, is to use simple and readily available specimens that are commonly prepared for determining resistivity and compressive strength of concrete. All cylinders were kept in laboratory room and cured in ambient temperature prior cracking. After curing, each sample was placed in a Standard Crack-Inducing Jig (SCIJ) to induce a crack width ranging from 0.1 to 0.4 mm using MTS Universal Testing Machine. Surface crack width for each cylinder (top and bottom ends) was measured by an optical crack-detection microscope at 14 equidistant points along the crack: seven along the top face, and seven along the bottom face. The measurements were then averaged and recorded as the cylinder average. The cracked specimens were later inserted into special rubber sleeves, sealed using silicon sealant; then one end of cylinder sample was exposed to a constant water head (~ 1.7 m). The flow of water through specimens was collected in water containers and measured over a period of time. It should be noted that depending on the water head chosen for the test and the crack width, the initial

flow through the specimens could be large. This may need fairly large size containers and it may require frequent readings and emptying the containers. Details of the self-healing test setup is illustrated in Figure 4.5.

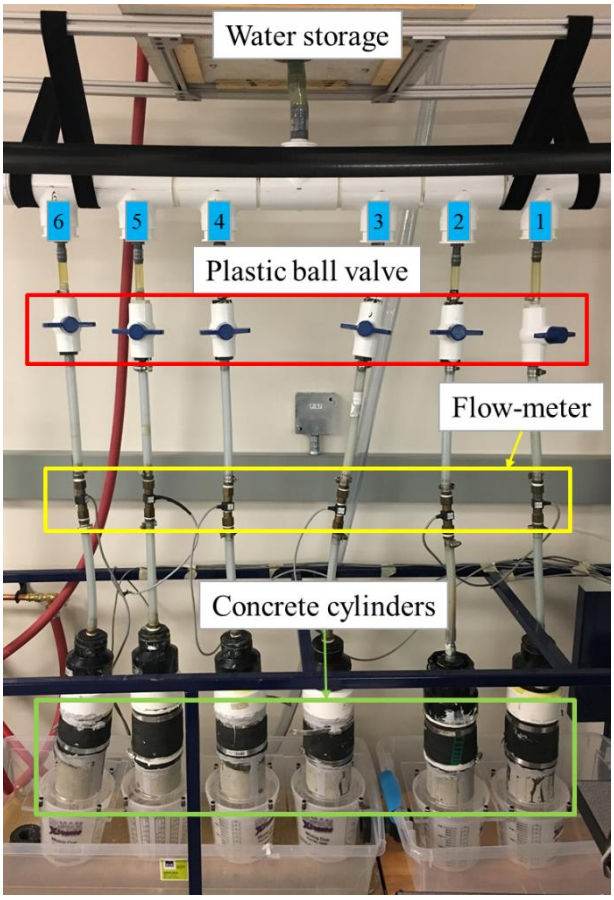

Figure 4.5. Self-healing apparatus in UVic's Facility for Innovative Materials and Infrastructure Monitoring (FIMIM).

4.4 Results and discussion

This section is aimed to show the influence of CA addition into concrete with two different cement types on the strength, electrical resistivity, water permeability, electrical charge passed based on RCP test, chloride diffusivity. In addition, several correlations of these durability parameters were established. Self-healing efficiency of all mixtures was also demonstrated using an innovative technique developed by the authors.

4.4.1 Fresh concrete properties and compressive strength results

The experimental results of the concretes with and without CA including fresh properties (slump, air content, and plastic density), compressive strength, and electrical resistivity is summarized in Table 4.3. Compressive strength and electrical resistivity results, determined at 28 days, are the average from three cylinders (Φ100×200). As indicated by the results in Table 4.3, the addition of CA increased the compressive strength by 11% for OPC mixture and by 8% for PLC mixture, while not much remarkable increase has been observed for electrical resistivity data (both SR and BR). In addition, presence of CA in the mix indicated a reduction in slump values whereas a slight increase in the air content was observed. Moreover, plastic density and temperature of all mixes were very close to each other.

Table 4.3. Fresh and hardened concrete properties.

Mix ID	Fresh properties				Compressive strength (MPa) at 28 days	Electrical resistivity (kΩ.cm) at 28 days	
	Slump (mm)	Air content (%)	Plastic density (kg/m^3)	Temp. (°C)		Surface	Bulk
OPC	130	2.0	2400	21.0	41.54	6.75	4.01
OPC-CA	110	2.2	2394	21.0	46.35	6.47	4.06
PLC	130	1.9	2394	20.5	42.07	6.12	3.91
PLC-CA	85	2.2	2396	21.0	45.62	6.61	4.03

4.4.2 Electrical resistivity results

The surface and bulk electrical resistivity of concrete with and without CA at 7, 14, 28, 56, 90, 160, 210 days are illustrated in Figure 4.6. Generally, as concrete aged, resistivity increased due to further cement hydration. Other studies also reported similar trend [102], [112], [117], [118] although none of them studied the effect of CA addition or PLC in the mixture. Dependency of resistivity of concrete on its microstructure properties as well as conductivity of its pore solution, proves increase in resistivity over time since concrete's interconnected pore network reduces and OH^- ions in the pore solution is consumed, attributing to decrease in its conductivity. Table 4.4 summarizes the chloride permeability classifications for electrical resistivity and RCP test methods. According to the classifications given in this table, electrical resistivity

results correspond to high chloride permeability. It is evident that addition of CA helped concrete to slightly enhance its SR over time; showed greater resistivity values (especially for PLC mixtures) than that of control mixes. Comparing the cylinders containing only Portland cement (reference ones), the SR and BR of mixtures with limestone was lower (less than 10%) than that of ordinary ones for all ages tested. Concrete resistivity typically increases with time and can be expressed by:

$$\rho(t) = \rho_0 \left(\frac{t_0}{t}\right)^{-m} \quad \text{Equation 4.4}$$

where $\rho(t)$ and ρ_0 is the concrete resistivity at time (t) and reference time (t_0), respectively; m is the ageing factor ($0 \leq m \leq 1$) which depends on concrete composition and environmental conditions. The ageing factor, (m), determined using Equation 4.4 with a reference age of 7 days (t_0) and the concrete resistivity measured at that age ρ_0, are dependent on microstructure changes with time. As illustrated in Figure 4.6, the fitting curves are plotted by dash-lines and the growth of SR and BR have a common rate of development trend while SR measurement represented better correlation than that of BR method according to its coefficient of determination (R^2), suggesting less dependency of this method on the testing and concrete parameters. Considering only SR measurements, a strong correlation between SR and curing age has been established ($R^2 > 0.93$), indicating reliability of proposed equations to predict SR evolution over time. A fair correlation ($R^2 = 0.53$ and 0.74) was also observed for PLC mixtures measured using bulk resistivity method while the correlation for OPC mixtures was poor. For OPC mix, BR data was randomly distributed over time that m value could not be obtained after several iterations in regression analysis. All fitted curves in BR graph could not cover all data points due to larger scattering in the results. This could not be fulfilled by adjusting the data into Equation 4.4. Generally, concretes containing crystalline admixtures did not show any considerable differences in enhancing electrical resistivity when compared to control mixes. It should be noted that measuring concrete electrical resistivity is an indirect testing technique to obtain information about its permeability which might not be appropriate way to understand CA behavior under permeation or diffusion. Hence, this study also investigates other durability evaluation techniques to draw some

comprehensive conclusions about the aspects of using CA or to determine which technique can truly represent real behavior of CA in a concrete system.

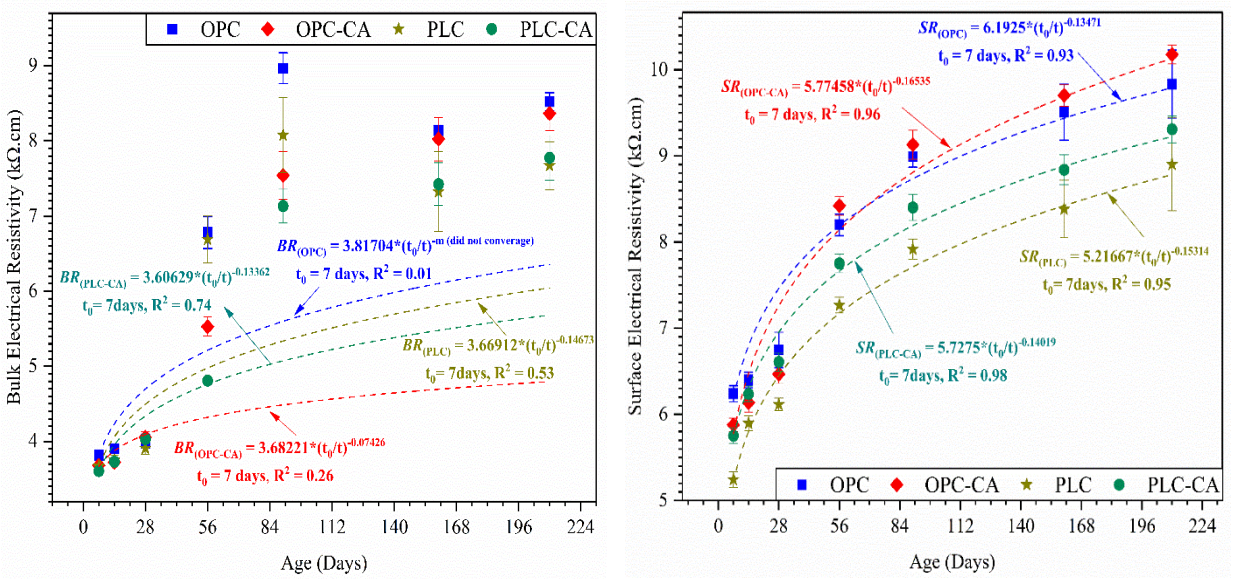

(a) BR data **(b)** SR data

Figure 4.6. (a) Surface & **(b)** Bulk electrical resistivity variation over time.

Table 4.4. Chloride permeability classifications.

Chloride permeability	RCPT [153] (Coulomb)	Electrical resistivity (kΩ.cm)		Diffusion coefficient (10^{-12} m^2/s)
		Surface [61]	Bulk [118]	
High	> 4000	> 12	> 5	> 15
Moderate	2000 – 4000	12 – 21	5 – 10	10 – 15
Low	1000 – 2000	21 – 37	10 – 21	5 – 10
Very Low	100 – 1000	37 – 254	21 – 207	2 – 5
Negligible	< 100	< 254	< 207	< 2

4.4.2.1 Influencing parameters

Due to the resistor-capacitor circuits' behavior in saturated cementitious system, it introduces a phase difference between electrical current imposing and the measured potential (impedance) [22]. At different frequencies, there is a significant difference in impedance and it follows that the real component of the impedance at zero phase angle is the true uniaxial resistance. Since the phase is almost never zero, the meters record the total impedance: the real and imaginary components added in quadrature [64]. At higher frequencies, the impedance spectrum characteristics are featured by the concrete microstructure, but these

characteristics are mainly attributed to the conditions at the electrode-concrete interface for low frequency domain [64]. At lower frequencies (below 500 Hz), it was stated that electrical resistivity measurement can result in overestimated data because of electrode-concrete contact interface impact [64]. To investigate the influence of signal frequencies on SR data, Figure 4.7-(a) shows a relationship between resistivity measurements using three different signal frequencies (13, 40, and 100 Hz) in the 4-point Wenner method. No notable difference in SR results between different signal frequencies was observed and as frequency increased, less than 5% reduction in the SR values was detected. Strong linear correlation between three different frequencies verifies such experimental observation. In this study, two different SR meters (Giatec Surf and Proceq Resipod) were used to compare and validate the SR measurements taken each time and also two different technical standards (AASHTO TP 95 [61] and ASTM WK37880) were followed to identify any variation in the results. As illustrated in Figure 4.7-(b) & (c), following different technical standards and using different SR meters led to similar results since they were very well-correlated (R^2 = 0.99).

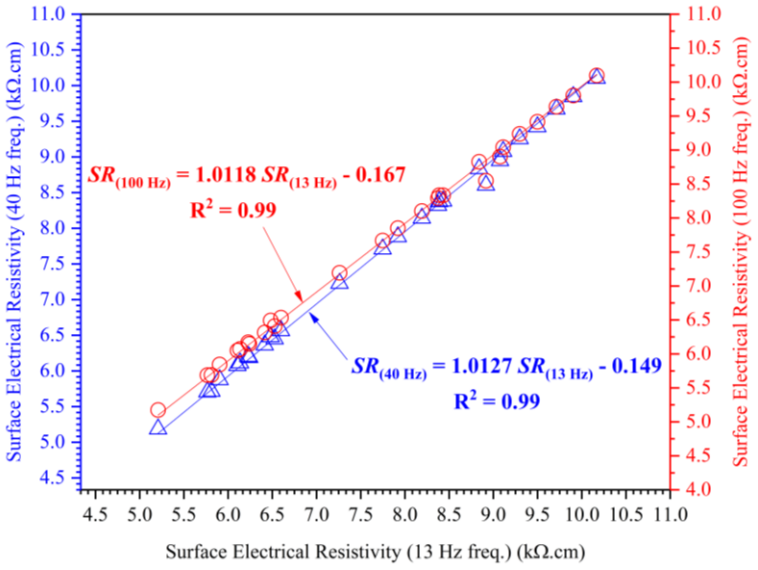

(a)

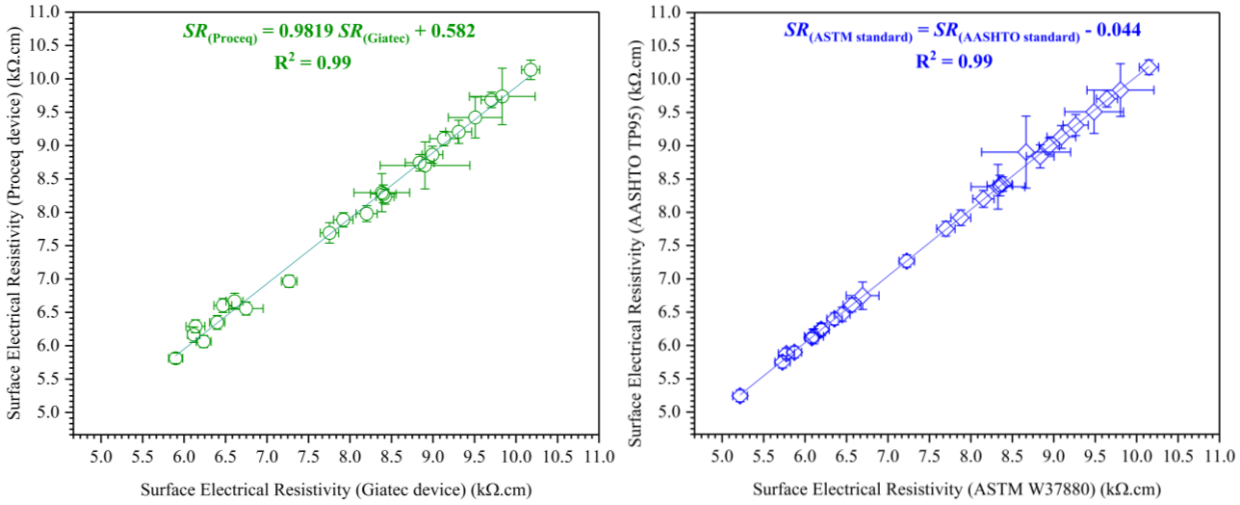

(b) **(c)**

Figure 4.7. (a) influence of signal frequencies on SR measurement **(b)** SR correlation b/w two resistivity meters **(c)** SR correlation b/w two standard methods.

4.4.3 Rapid Chloride Permeability (RCP) test results

The chloride permeability was measured by RCPT as acid-soluble chloride (total chloride), in accordance with ASTM C1202 [153]. Figure 4.8 presents the results of RCP test for individual specimens in each mixture as well as their average values taken from four samples. The average cumulative charge after 6 h was 5538C for OPC at 28 days, and was approximately 25%, 35%, and 30% higher for OPC-CA, PLC, and PLC-CA, respectively. This was 2315C for OPC at 56 days, roughly 5% higher than OPC-CA, and was ~11% and 19% lower for PLC and PLC-CA mixes, respectively. Based on these results, the charge passed reduction in all mixes over time (28 to 56 days) can be attributed to the reduction of the pore volume as well as pore solution chemistry. Similar findings have been reported in other studies [111], [271]–[277] for OPC mixes although none of these studies examined the crystalline admixtures' effect. It should be noted that one of criticism of the RCPT is that an increase in temperature is resulted from the high voltage applied across the sample, especially for low quality concretes, which is known to lead to an increase in charge passed, resulting in poor quality concrete looking worse than it actually is [278]. Addition of CA into OPC mixture induced a considerable decrease in the charge passed at 28 days and relatively the same value at 56 days while in contrast the inclusion of CA into PLC mixture indicated slightly higher value than control

one (PLC mix), representing the uncertainties inherent in the test method. The enhancement of the resistance to chloride penetration in OPC-CA mix can be related to the capillarity and pore volume reduction as well as microstructural characteristics of this mix, formed by the deposition of pore blocking crystals inside the matrix. Comparing only OPC and PLC mixes, it is evident that cement composition can affect the electrical conductivity of the pore solution and matrix, resulting in lower value for PLC mix at 28 days (Figure 4.8). At the age of 28 and 56 days, RCPT results indicate high and moderate chloride permeability for all mixes based on the classification in ASTM C1202 [153], presented in Table 4.4. Based on the obtained RCPT data, only definite conclusion is that the total charge dropped in all mixes from high to moderate range from 28 to 56 days.

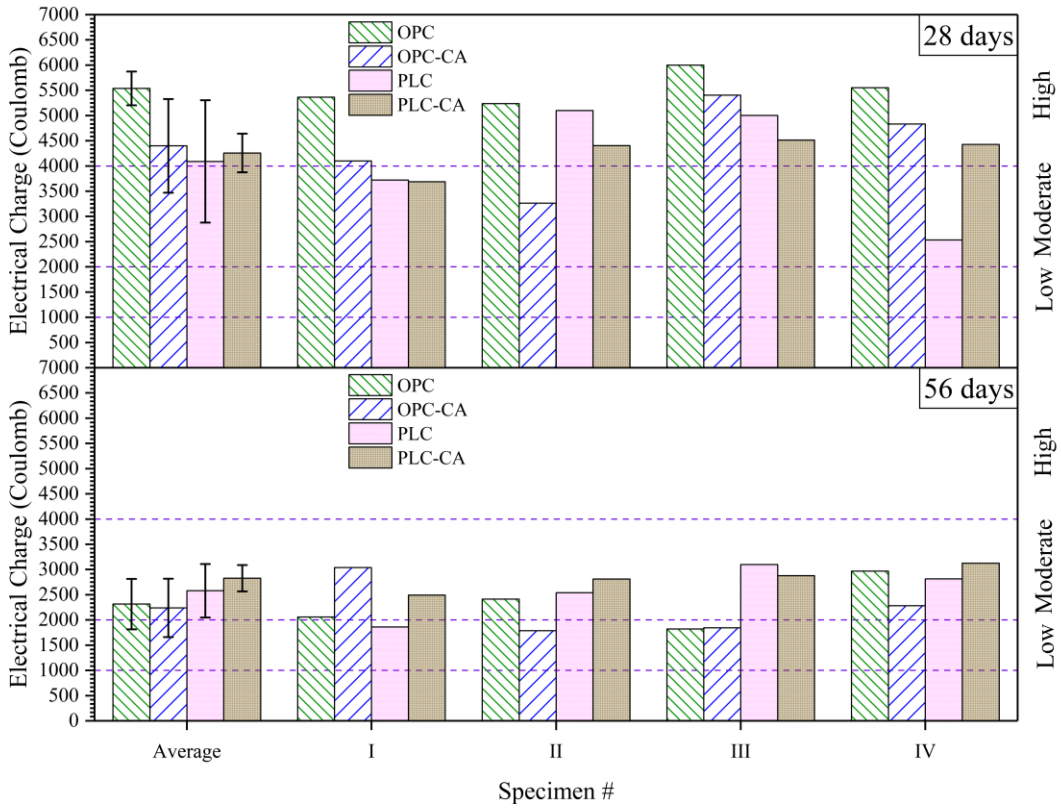

Figure 4.8. RCPT results (Electrical charge passed (Q) in Coulomb) at 28 and 56 days.

4.4.4 Water permeability test results

The ease of water penetration into the concrete usually determines its deterioration rate while affects its durability [59]. Generally, the lower the concrete permeability, the higher its durability. To evaluate the

concrete permeation, water penetration test in accordance with DIN 1048-Part 5 [263] has been utilized in this study. After performing the water penetration test for period of 72 h and splitting the specimens into two halves, average and maximum depth of water penetration (x_{avg} and x_{max}) were measured as illustrated in Figure 4.9. It can be simply observed that incorporation of CA into concrete reduced water penetration depth. For all concrete mixes, Figure 4.10 exhibits the average and maximum depth of water penetration as well as their permeability coefficients ($k_{w(avg)}$ and $k_{w(max)}$, calculated from Equation 4.3) based on DIN 1048 test results. As can be seen in the graph, the penetration depth reduced considerably (40-50%) for concretes treated with CA, indicating the effectiveness of these admixtures for waterproofing purposes. According to Hedegaard and Hansen's study [279], concrete can be considered as watertight for all practical purposes when max penetration depth is less than 50 mm. Only CA treated mixes satisfy this statement by having the average values of 40 mm for OPC-CA and 25.7 mm for PLC-CA. Comparing the water penetration depth based on maximum or average values, it was observed that standard errors of results were lower for average penetration depth, suggesting reliability of using average depth instead of maximum one. OPC mixture (control one) showed the highest penetration depth, as result the highest permeability coefficient (k_w), followed by PLC, OPC-CA, and PLC-CA. According to obtained results, the mixture of PLC-CA indicates the best behavior to the water penetration among other mixtures. Considering only reference mixes, Portland limestone cement showed noticeable water tightness than that of ordinary Portland cement (~25% improvement). It should be noted that no similar study has been found to investigate the role of PLC on concrete waterproofing.

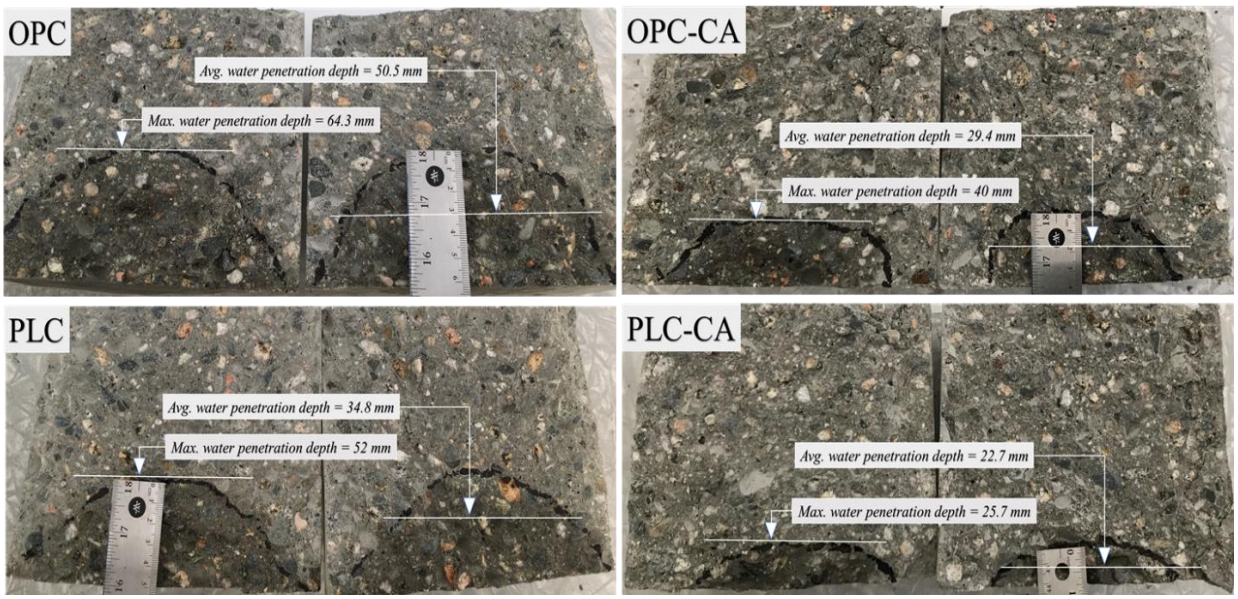

Figure 4.9. Water penetration depth of concretes with and without CA.

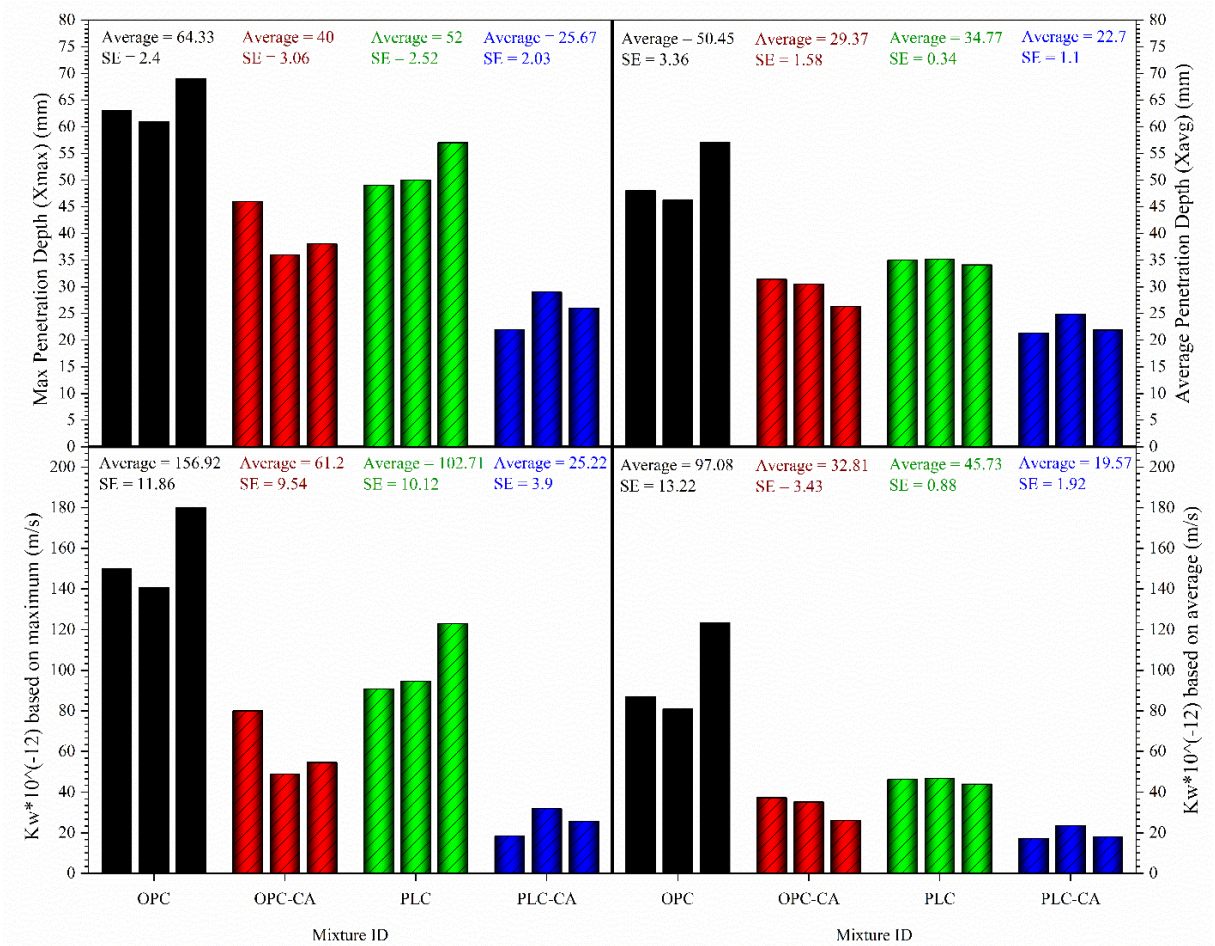

Figure 4.10. Mixtures' water penetration depth and coefficient of permeability based on DIN 1048 test results.

The main motivation of using average water penetration depth is to have a better prediction for the permeability coefficient (k_w). The correlation between water penetration depth and permeability coefficient for all mixes is shown in Figure 4.11. The figure reveals that there is a strong linear correlation ($R^2 = 0.88$) between the x_{avg} and x_{max} while average penetration depth showed less variation in the results. According to the best fitting trendline, the ratio of the x_{max} and x_{avg} is approximately 1.3 which is in well agreement with findings in Ibrahim and Issa study [271]. Both average and maximum penetration depth were later used to predict the water permeability coefficient of concrete (k_w) from Equation 4.3. Similar linear trend between average penetration depth and coefficient of permeability based on max. and avg. penetration depth was also observed (Figure 4.11). Further investigation is needed to understand the influence of the mixture properties (e.g. *w/c* ratio, presence of SCM, and the inclusion of aggregates) and curing regime on water permeability of concretes containing CA.

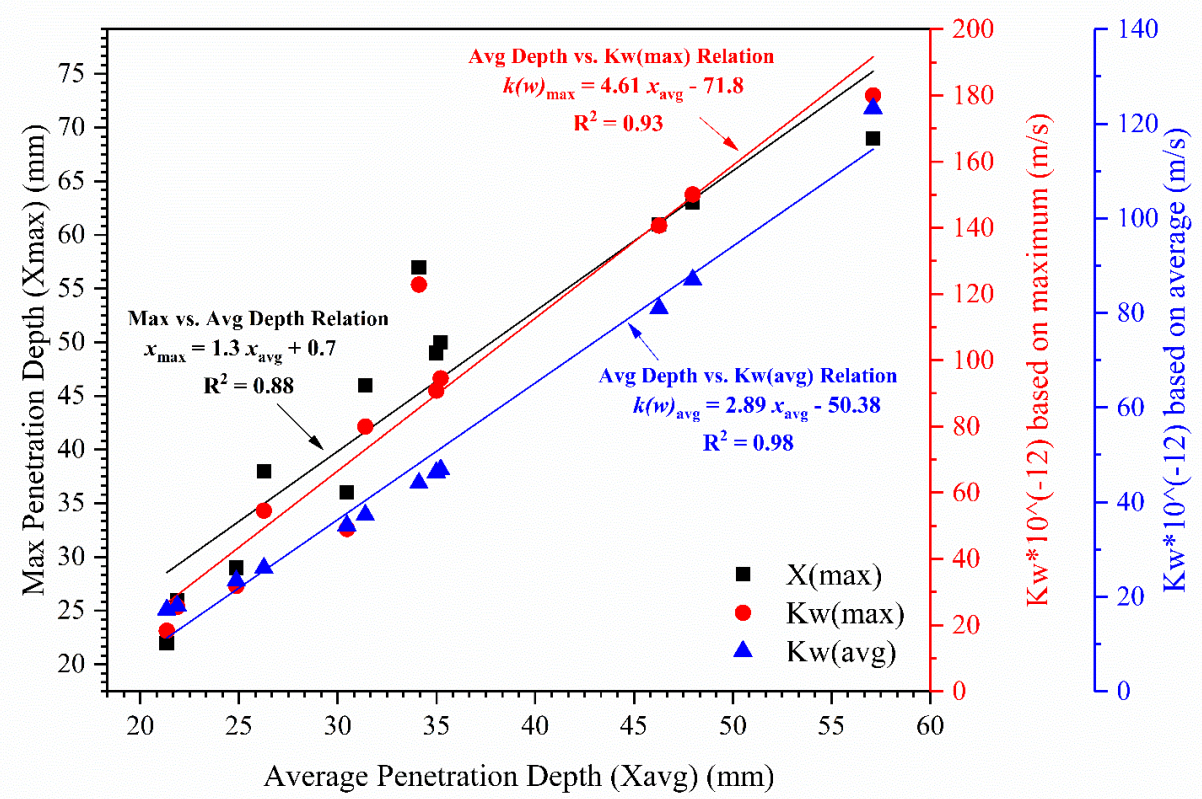

Figure 4.11. Average versus maximum water penetration depth and permeability coefficient per DIN 1048 standard.

4.4.5 Chloride diffusion coefficient

For all mixtures exposed to bulk diffusion in NaCl solution for 180 days, the values of chloride content (Cl^- % of concrete weight) vs layer depth (mm), measured at 2.5, 8, 14.5, and 21.5 mm depth from concrete surface, is plotted in Figure 4.12-(a) where specimens, shown on the right side, were cured for 28 days in water and on the left side for 56 days prior to exposing to NaCl solution. The best-fit curves are also shown by dash-lines in the same plot and their slopes decrease as concrete ages. It was observed that specimen curing time can affect the penetration of chloride ions into different depth, mostly due to gradual improvement in the extent of the concrete hydration, density and inner pore structures with time. Besides that, different diffusing ions clogged the pores inside concrete, not allowing further diffusion of chloride ions and resulting in concrete's higher capacity to withstand chloride diffusion; thus, leading to a low chloride concentration. Hence, the more concrete cures with moisture in a marine environment, it will be less prone to chloride attack. Overall, for both curing ages, the chloride content values were lower for specimens treated with CA than that of control mixes, suggesting formation of crystalline structures inside pores acts as physical barrier which can increase chloride binding capacity of matrix; also, can decrease penetration depth of water carrying chloride ions into concrete. As shown earlier, water penetration depth was lower in concrete containing CA. Comparing two cement types showed ~15-20 % higher chloride content at all depth for PLC mixes.

The service life of concrete in a chloride environment can be explained by Fick's second law. Using chloride ions' content profile and the method of least square, the values of surface concentration and apparent diffusion coefficient were determined by fitting the following equation (solution of Fick's second law when $C_0 = C_s$ for $x = 0$ at time t) [262]:

$$C(x,t) = C_s - (C_s - C_i) \cdot \mathrm{erf}\left(\frac{x}{\sqrt{4 \cdot D_a \cdot t}}\right) \qquad \text{Equation 4.5}$$

where $C(x,t)$ is chloride concentration measured at depth x and exposure time (t = 6 months) in mass % of concrete; C_i is initial chloride-ion concentration of the cementitious mix before salt solution submersion;

C_s is projected chloride concentration at the interface between the exposure liquid and cylinder finished surface and D_a is apparent chloride diffusion coefficient in m^2/s which both parameters are determined by nonlinear regression analysis. The resulting chloride surface contents and diffusion coefficients are illustrated in Figure 4.12 for all mixes at 28 and 56 days. The calculated surface contents range from 0.8% to 2% which higher contents belongs to specimens cured for 28 days and not treated with CA. Those of OPC and PLC (1.6-1.8%) are higher than for OPC-CA and PLC-CA. It was observed that C_s of all mixtures decrease with an extension in the curing age. The chloride typically penetrates into concrete through capillary absorption and diffusion [280], [281]. The C_s mainly depends on capillary absorption of chloride [282] and until saturation happens into capillaries, concrete absorbs saltwater. The calculated apparent diffusion coefficients range from 4 to 14×10^{-12} m^2/s. These values correspond to moderate/low chloride permeability according to classifications given in Table 4.4. Without any exception, the results indicate that OPC/PLC-CA have the lowest diffusion coefficient at both 28 and 56 days while value difference in OPC control and treated mixes are relatively small at 56 days. It is interesting that specimens containing crystalline admixtures exhibited lower diffusion coefficient, indicating lower rate of chloride ingress into matrix. As more hydration happens, the modified CSH gel and needle-shape crystals were produced in the pores of the capillary, which in turn increased the amount of hydration products and reduced the porosity and pore diameter in CA treated system. Hence, the concrete enhances its binding capacity with chloride ions and also its diffusion coefficient increases. This result suggests noticeable differences in chloride binding between CA treated and control concretes. These preliminary data cannot be taken as conclusive evidence to support this theory, but definitely shows the need for further exploration. The following equations can be used to estimate chloride profile and diffusion coefficient of concretes incorporating CA or PLC after t = 6 months salt solution exposure:

$$C(x,t)_{OPC-28D} = 1.786 - 1.781 \cdot \mathrm{erf}\left(\frac{x}{2 \cdot \sqrt{13.4t}}\right)$$ OPC (28-day curing) Equation 4.6

$$C(x,t)_{OPC-56D} = 0.918 - 0.913 \cdot \mathrm{erf}\left(\frac{x}{2 \cdot \sqrt{5.25t}}\right)$$ OPC (56-day curing) Equation 4.7

$C(x,t)_{OPC-CA-28D} = 1.292 - 1.287 \cdot \text{erf}\left(\frac{x}{2 \cdot \sqrt{6.28t}}\right)$	OPC-CA (28-day curing)	Equation 4.8
$C(x,t)_{OPC-CA-56D} = 0.843 - 0.838 \cdot \text{erf}\left(\frac{x}{2 \cdot \sqrt{4.83t}}\right)$	OPC-CA (56-day curing)	Equation 4.9
$C(x,t)_{PLC-28D} = 1.903 - 1.898 \cdot \text{erf}\left(\frac{x}{2 \cdot \sqrt{11.2t}}\right)$	PLC (28-day curing)	Equation 4.10
$C(x,t)_{PLC-56D} = 1.796 - 1.791 \cdot \text{erf}\left(\frac{x}{2 \cdot \sqrt{8.66t}}\right)$	PLC (56-day curing)	Equation 4.11
$C(x,t)_{PLC-CA-28D} = 1.216 - 1.211 \cdot \text{erf}\left(\frac{x}{2 \cdot \sqrt{9.77t}}\right)$	PLC-CA (28-day curing)	Equation 4.12
$C(x,t)_{PLC-CA-56D} = 1.203 - 1.198 \cdot \text{erf}\left(\frac{x}{2 \cdot \sqrt{6.51t}}\right)$	PLC-CA (56-day curing)	Equation 4.13

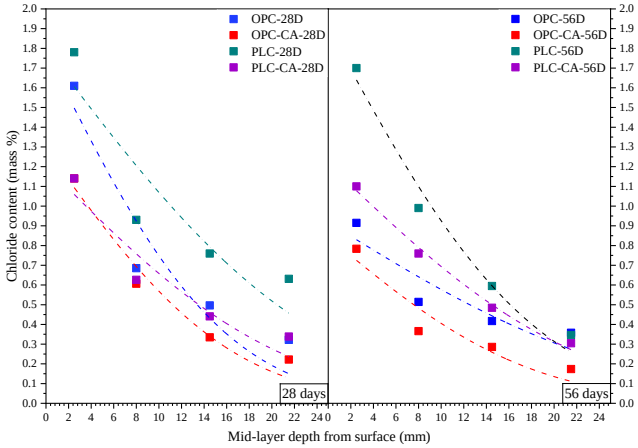

(a)

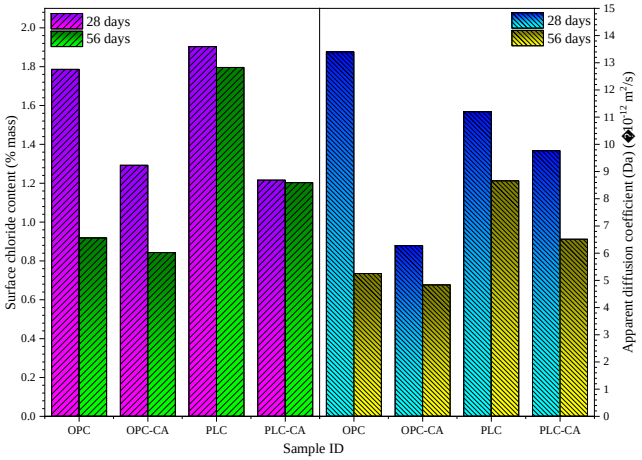

(b)

Figure 4.12. (a) Chloride content profiles & **(b)** Surface chloride concentration and diffusion coefficient for different concrete mixes.

4.4.6 Inter-relationship between permeation properties and durability of concrete

In this section, an attempt is made to demonstrate any possible correlation between different durability indicator parameters such as ER and RCPT.

4.4.6.1 Correlation between surface and bulk electrical resistivity

Considering all curing ages, Figure 4.13 shows the relationship between SR and BR data for all mixes. Linear equation was the best regression fit to correlate the SR and BR data. As can be seen, two measurement techniques correlate fairly well (R^2 = 0.84) with each other for all cylinders. This finding agrees with the results reported in other studies [117], [118]. Ignoring the limited application of BR testing technique for field evaluation, it worth to mention that two test methods can be used interchangeably to measure concrete resistivity in the laboratory. From statistical tests, it was also observed that there were variations in the BR and SR results as concrete aged, shown by error bars in Figure 4.13.

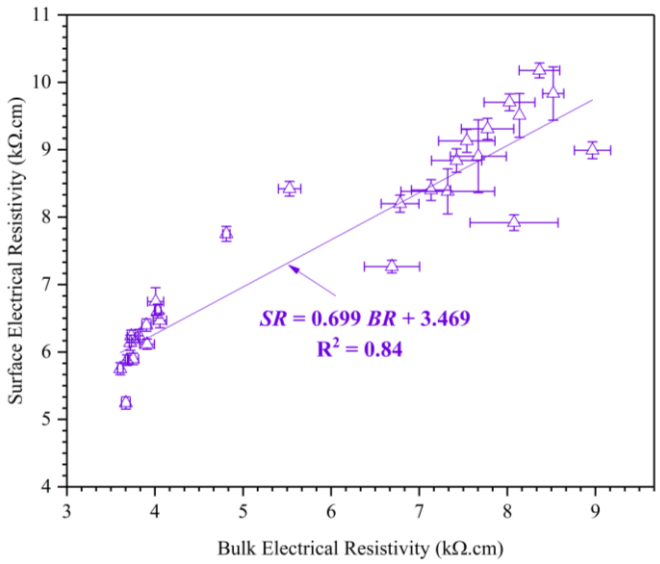

Figure 4.13. Relationship between surface and bulk resistivity of concrete with and without CA.

4.4.6.2 Correlation between surface/bulk resistivity and RCPT

Figure 4.14 shows the overall relationship between the charge passed and SR (or BR) measurements for CA-treated and control mixes at 28 and 56 days. Each data point on the figure represents test results from a single specimen. Correlating 28 days SR/BR and RCPT results, CA group showed fairly strong linear

relationship between these test methods while poor correlation was observed for control samples. There was also a very good relationship between the SR measurements for CA-treated concretes at 56 days. Comparing different testing age, control samples only indicated an acceptable coefficient of determination at 56 days. There was almost no correlation between RCPT and resistivity methods at 28vs56 and 56vs28 days, suggesting comparing these values only at the same age. The present research is among few studies investigating the correlation between RCPT and resistivity values [111], [275], [283]. Other studies suggest the use of power function to fit the data although it happened not to be a suitable fitting curve for this data set. This might be due to the not enough sample size or due to high *w/c* ratio and small variations in RCPT and SR/BR values at certain age, not having wider range of data set. Generally, SR measurement indicated better correlation with RCPT than that of BR measurement.

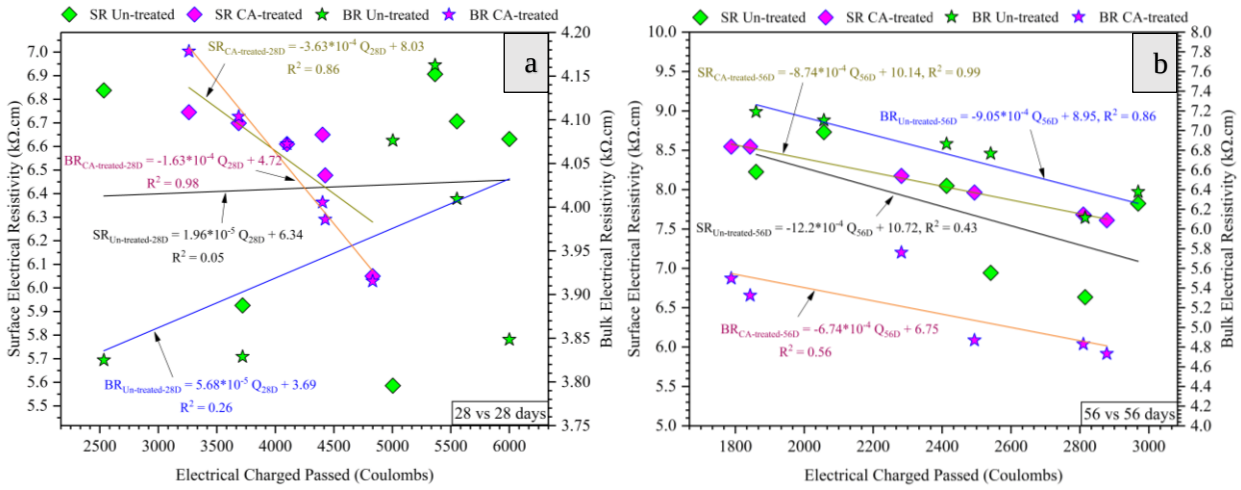

Figure 4.14. Relationship between RCPT and surface (or bulk) electrical resistivity for CA-treated and control mixes **(a)** 28 vs 28 days **(b)** 56 vs 56 days.

4.4.6.3 Correlation between surface/bulk resistivity and water permeability

For all mixtures, Figure 4.15 exhibits the relationship between concrete resistivity obtained at 7, 28, and 56 days age and its water permeability coefficient measured based on maximum penetration depth. As seen, there is literally no linear relation between these parameters. No linear relationship was also found between resistivity and k_w measured based on average penetration depth. Fair correlation was observed only at 7

days and specifically for BR data. This is mostly due to air curing of water permeability test samples after casting. Previous studies showed the proposed relationship between these parameters [111], [275]. Concretes containing CA showed no correlation between resistivity and water permeability when compared to control mixes. As reported earlier, presence of CA in concrete led to considerable reduction in water permeability but no notworthy difference in resistivity values which is a possible root to not find any meaningful correlation between these techniques. This also suggests that practitioners who frequently deal with these test methods should be cautious enough to not implement these techniques interchangeably for different cement-based mixes because permeability test is a direct method to physically estimate the water penetration depth and permeability coefficient while resistivity method is an indirect technique to obtain information on permeability based on electrical resistivity of porous medium.

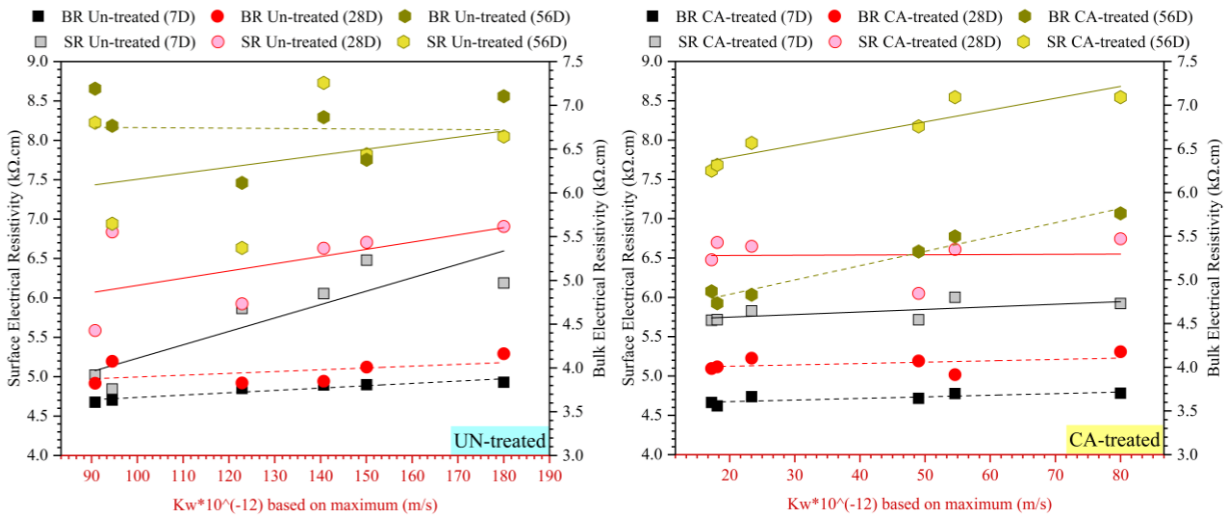

(a) **(b)**

Figure 4.15. Relationship between SR/BR and water penetration coefficient for **(a)** control & **(b)** CA-treated mixes.

4.4.6.4 Correlation between RCPT and water permeability

The charge passed based on the RCPT results at 28 and 56 days were correlated with the k_w, calculated based on the x_{avg} and x_{max} measured from DIN 1048 test, as illustrated in Figure 4.16. Moderate linear relationship between Q and k_w can be observed for both CA-treated and control concretes at 28 days; however, there is almost no correlation between these parameters at 56 days (R^2 < 15). The similar

conclusion can be found in the literatures [111], [271], [275]. Even though, CA-treated concretes showed better performance in water penetration test and RCPT, they did not establish any relation between two parameters as compared with control samples. Further investigation is required to validate this relationship with wider range of testing specimens including different *w/c* ratio, curing age/regimes, and cementitious combinations.

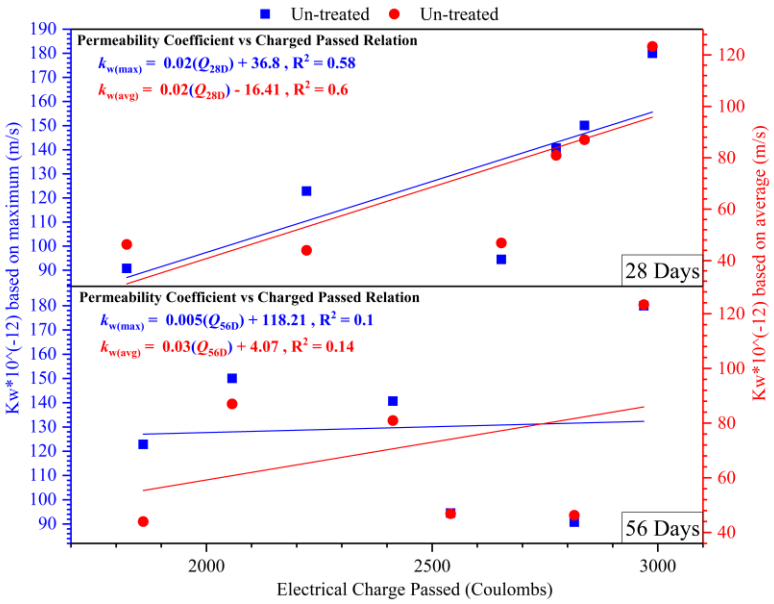

(a) Un-treated

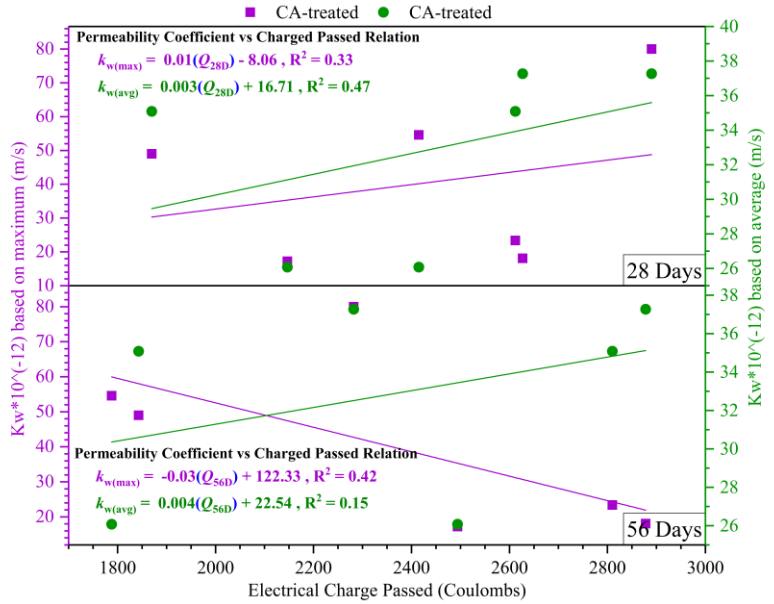

(b) CA-treated

Figure 4.16. Relationship between charge passed in RCP test and water permeability coefficient (k_w) obtained from DIN 1048 test.

4.4.6.5 Correlation between apparent diffusion coefficient and other durability parameters

To analyze the interdependence between concrete rapid chloride penetration, resistivity and chloride diffusion coefficient, the correlation between them was studied with assumption that data follow a normal distribution. Figure 4.17 shows the relationship between chloride diffusion coefficient and other parameters measured through RCP, WP, ER, and compressive strength tests. Linear equation in the form of $y = ax \pm b$ was used for regression analysis in all cases as the best correlation. All parameters indicated poor correlation with D_a (R^2 <0.6).

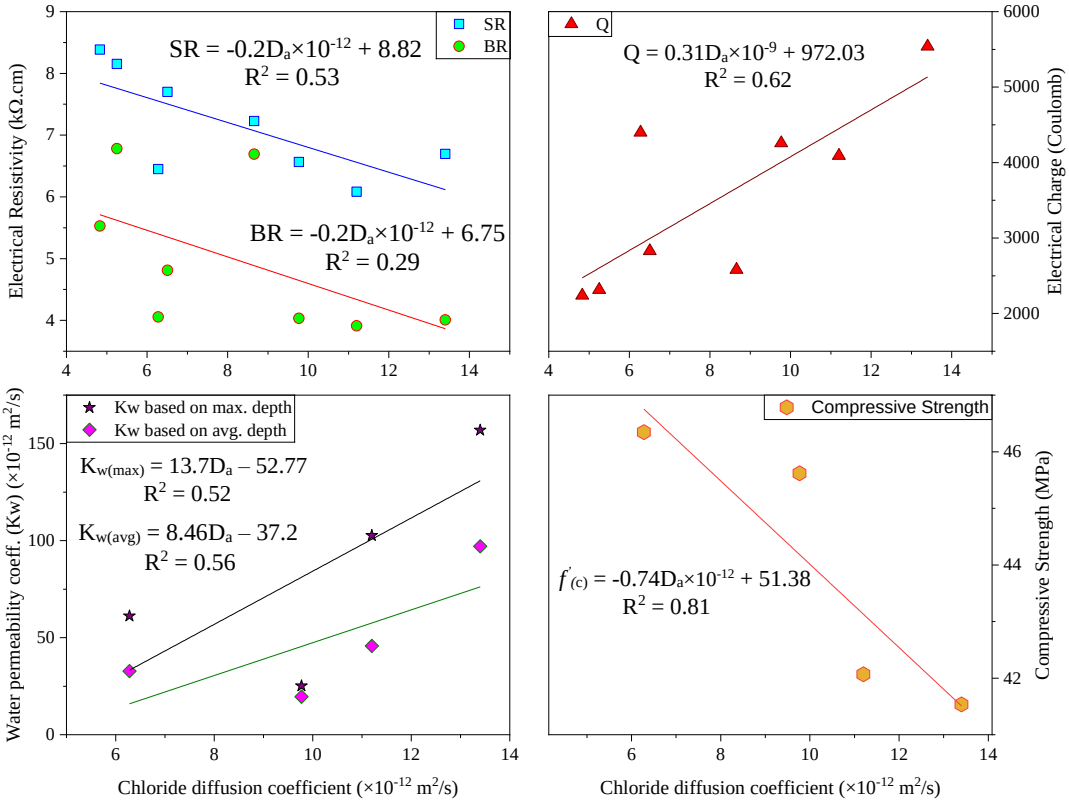

Figure 4.17. Variation of apparent chloride diffusion coefficient with ER, WP, electrical charge, and strength of concrete.

4.4.6.6 Correlation between durability properties and compressive strength

Due to the mutual influence of pore structure on mechanical and durability properties, there is a great interest to relate transport properties and compressive strength of concrete. Hence, in order to investigate the interdependence between the properties of the concrete mixes, Figure 4.18, which compares

compressive strength with certain durability parameters such as ER and *Q*, illustrates this correlation. As it is shown in the plot there is no considerable linear relationship between the resistivity/RCPT and compressive strength; however, it is noteworthy that the correlation coefficient of the correlation between water permeability and strength results is relatively high. The relationships between physical and chemical effects of CA in improving concrete durability could play a vital key in performance-based design of concrete materials and structures.

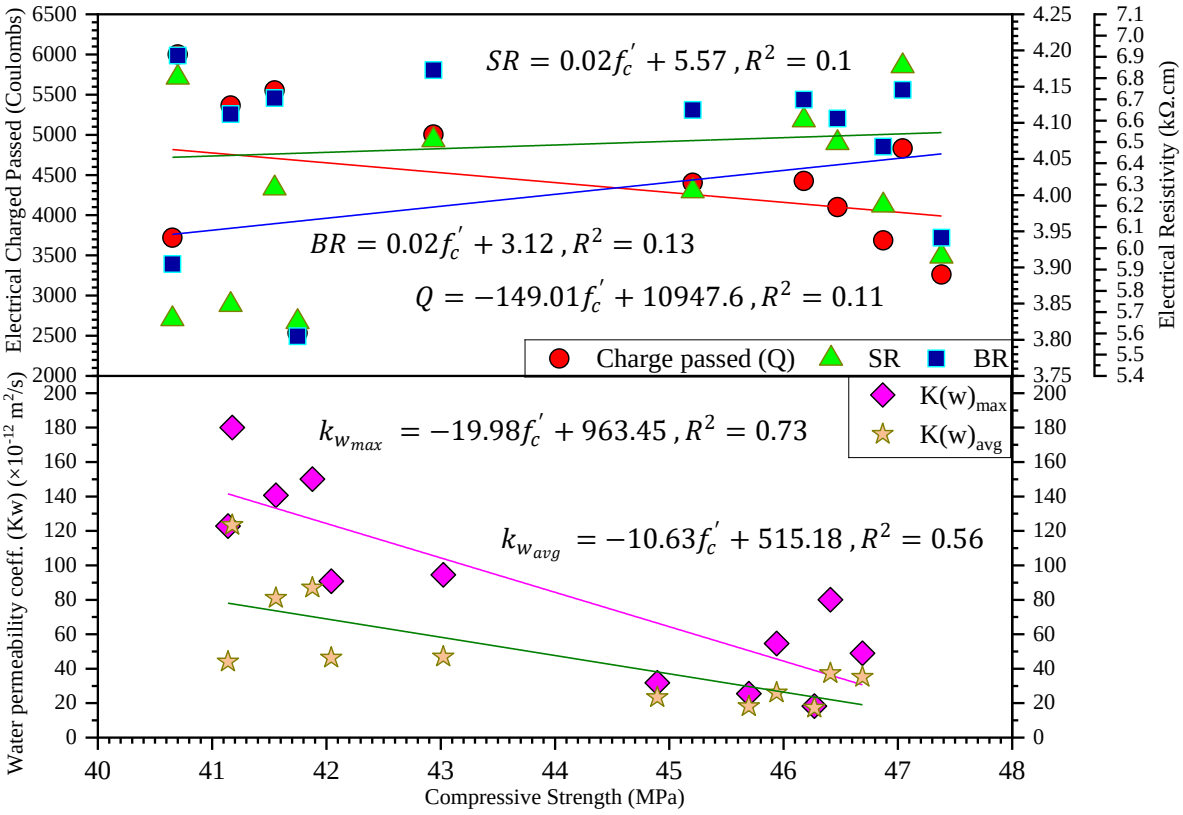

Figure 4.18. Correlation between concrete compressive strength and its durability properties.

To sum up all results collected from different test methods, Table 4.5 is presented for concretes with and without CA/PLC which included standardized penetration classification. Use of CA indicated better performance in improving water permeability and chloride diffusivity. According to concrete resistivity results, no much development was observed when using CA which opens up a need for further investigation of this parameter. As concrete ages, its durability properties also improve as can be seen in Table 4.5.

Table 4.5. Summary of conducted durability indicator test results.

Mix ID			OPC	OPC-CA	PLC	PLC-CA
Compressive strength (MPa)		28D	41.54	46.35	42.07	45.62
Electrical resistivity (kΩ.cm)	SR	28D	6.69 (High)	6.45 (High)	6.08 (High)	6.57 (High)
		56D	8.15 (High)	8.38 (High)	7.23 (High)	7.7 (High)
	BR	28D	4.01 (High)	4.06 (High)	3.91 (High)	4.03 (High)
		56D	6.78 (Moderate)	5.53 (Moderate)	6.69 (Moderate)	4.81 (High)
Electrical charge (Coulombs)		28D	5538 (High)	4399.25 (High)	4089.25 (High)	4257.75 (High)
		56D	2314.75 (Moderate)	2238 (Moderate)	2578.75 (Moderate)	2827 (Moderate)
Water permeability coefficient ($\times 10^{-12}$ m^2/s)	Based on max. depth		156.92	61.2	102.71	25.2
	Based on avg. depth		97.08	32.81	45.73	19.57
Apparent chloride diffusion coefficient ($\times 10^{-12}$ m^2/s)		28D	13.4 (Moderate)	6.28 (Low)	11.2 (Moderate)	9.77 (Low)
		56D	5.25 (Low)	4.83 (very low)	8.66 (Low)	6.51 (Low)

4.4.7 Investigation of self-healing efficiency

4.4.7.1 Visualization of crack-filling

Visualization of crack filling was performed under an optical crack-detection microscope at multiple fixed locations along the crack length. As a first immediate view of specimen's cracked surface, it was observed that white precipitates were formed on the crack surface; however, chemical analysis of the formations was required to identify its compositions which was beyond the scope of this work. Figure 4.19 shows the cracks at the end of its testing period, where it can be seen that both control and CA-treated cylindrical specimens showed signs of crack sealing. Apparently, in some locations at the surface, cracks were completely filled with healing products. It should be noted that these visual images deliver some understanding whether crack sealing has taken place whiles they are of little use in identifying chemical compositions of healing products or quantifying performance. It is worth to note that if the calculated crack widths for specimens are not

similar, then either these specimens should not be compared, or a note of dissimilar crack widths should be mentioned.

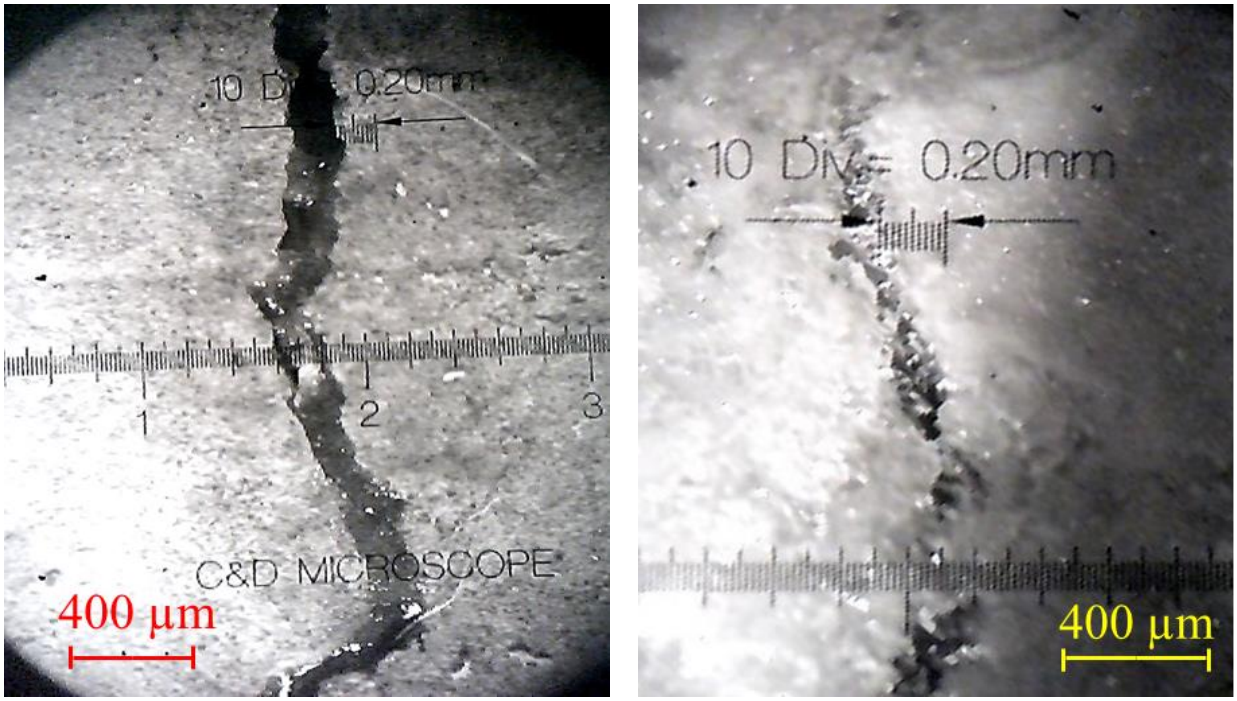

(a) Un-treated **(b) CA-treated**

Figure 4.19. Representative sealed cracks of randomly selected specimens with and without CA.

4.4.7.2 Self-healing results

The surface crack width (mm), measured initial flow, percent flow-reduction rate, and Healing Ratio (HR) of three cylinders for each mix are summarized in Table 4.6. From the analyzed data in Table 4.6, it is clear that the samples being compared had almost similar average surface crack width. The OPC samples had an average measured crack width of 0.244 mm as compared to 0.245 mm for OPC-CA, 0.251 mm for PLC, and 0.247 mm for PLC-CA. As expected, the higher the crack width, the higher the initial flow. The effect of healing was examined by calculating a HR parameter as follows (Equation 4.14) [18]:

$$Healing\ Ratio = 1 - \frac{Final\ Flow}{Initial\ Flow} = 1 - \frac{q_F}{q_0} > 0 \qquad \text{Equation 4.14}$$

where q_0 is the initial water flow (lit/5 min), measured after running self-healing apparatus; q_F is the final water flow (lit/5 min), measured after a healing period of 100 h. Presence of CA show slightly higher HR compared to control concretes; however, the average HR values were generally very close to each other.

Table 4.6. Measured crack width and intial flow.

Sample ID		Surface crack width (mm)				Real initial flow q_0 (lit/5 min)	Percent flow-reduction rate q_F/q_0	Healing ratio
		Top	Bottom	Average				
OPC	I	0.226	0.290	0.258	0.2443	0.0696	99.1%	0.991
	II	0.292	0.268	0.28		0.1891	93.8%	0.938
	III	0.184	0.206	0.195		0.0248	94.1%	0.941
OPC-CA	I	0.230	0.254	0.242	0.2453	0.0575	99.6%	0.996
	II	0.332	0.275	0.304		0.1926	98.5%	0.985
	III	0.176	0.205	0.191		0.0290	99.7%	0.997
PLC	I	0.185	0.226	0.206	0.2510	0.0226	98.8%	0.988
	II	0.325	0.25	0.288		0.1826	98.2%	0.982
	III	0.244	0.273	0.259		0.0796	99.5%	0.995
PLC-CA	I	0.203	0.263	0.233	0.2467	0.0915	97.5%	0.975
	II	0.248	0.192	0.22		0.0378	99.0%	0.99
	III	0.33	0.243	0.287		0.2294	99.2%	0.992

The results of reduction in water flow and healing ratio over time is presented in Figure 4.20. One can observe that the specimens experienced a rapid initial flow during the first day of exposure to water pressure; however, the flow reached a constant rate and a fairly steady curve within days. As can be seen, the flow through the specimens reduced over time, indicating "self-healing" of concrete. The addition of the CA yielded positive results with regards to self-healing as slope of flow rate line dropped noticeably within few hours after testing for CA treated samples, not the case for control ones. It is hypothesized that the deposition of crystals into the crack which acts as membrane and hydrophilic nature of these admixtures can contribute to further fill the pores and create enough time for concrete to improve its natural healing process; thus, seal the cracks. By adding 3-4 % into the matrix, the enhancement of CA effectiveness under water pressure has been also confirmed by other studies [15]–[19], reporting 7-10% increase in the healing capability with respect to control samples, similar to those observed in this work. From this data, the time required for flow to reduce to a certain threshold value can be determined or the time required for completing sealing of cracks can also be found. As seem from Figure 4.20-(c), with the increase of healing time, the HR ratio (especially for CA treated samples) were increased. Among all mixes, OPC showed the

lowest healing rate over time while CA group indicated ~90% healing within first 30 h of testing. A clear tendency of better healing rates can be seen when increasing the time and available water.

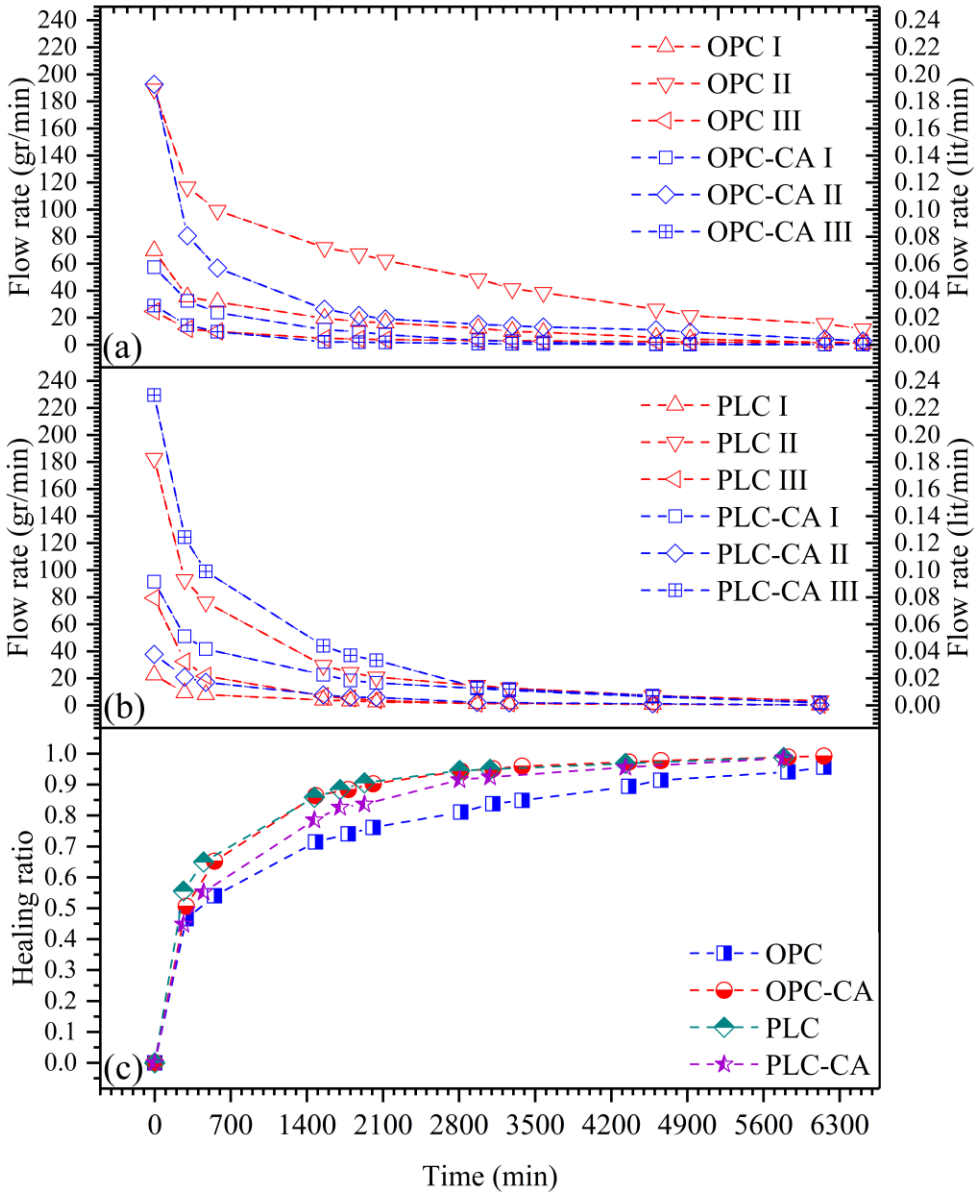

Figure 4.20. Relationship between water flow and time for **(a)** OPC and OPC-CA specimens & **(b)** PLC and PLC-CA samples **(c)** healing ratio vs. time for all mixtures.

Poiseuille's Law is defined as $q_r = \Delta p.b.\frac{w^3}{12.\eta.l}$, where q_r is real flow of water (m^3/s), Δp is differential water pressure between inlet and outlet of the crack (Pa), b is surface crack length (m), w is surface crack width (m), η is dynamic viscosity of water (Ns/m^2), and l is length of flow path (m). Based on Poiseuille's

law, Edvardsen proposed a model that determines the relation between the water flow passing through a crack and the crack width which is a third-order polynomial with only the cubic term [244]. The model is expressed in Equation 4.15:

$$q_o\left(\frac{liters}{h}\right) = 740 \times I \times CW_{avg}^3 \times k_t \qquad \text{Equation 4.15}$$

where q_o is the initial water leakage per meter visible crack length (lit/h); I is hydraulic gradient, m of water head/m; CW_{avg} is average crack width at the surface (mm); k_t is factor comprising different water temperature (k_t = 1 for water at 20 °C with viscosity $\nu = \frac{\eta}{\rho} = 1.00$ mm^2/s). This expression can be adjusted to the parameters of this study by changing units and the crack length (considered 75 mm), resulting in the expression:

$$q_o\left(\frac{liters}{h}\right) = 740 \times \frac{1.5}{0.15} \times CW_{avg}^3 \times 1 \times 0.075 \qquad \text{Equation 4.16}$$

Figure 4.21 shows the experimental values of initial water flow measured at beginning of self-healing test versus the corresponding initial average crack width of all specimens. The best fitting curve was set to be a cubic function as shown in Figure 4.21. The results show that there is an acceptable correlation between q_0 and crack width with determination coefficient of 0.76. The obtained fitting curve from experimental results of water flow and averaged crack width fit reasonably well in the theoretical predictions given by Equation 4.16, illustrated also in Figure 4.21. The lower experimental values might be due to the inclusion of CA which could help blocking water flow inside the crack or difference in crack profile/structure inside the specimen. As self-healing could also be happening inside the sample, not only on the surface crack, this correlation can only be utilized to compare the parameters of healing, rather than to draw an exact relationship between both parameters. It was also attempted to use the minimum and maximum crack width instead of average values and find a correlation between these values and initial water flow. No stable trend was observed between theses parameters. This finding is in agreement with Roig-Flores *et al*. study [17].

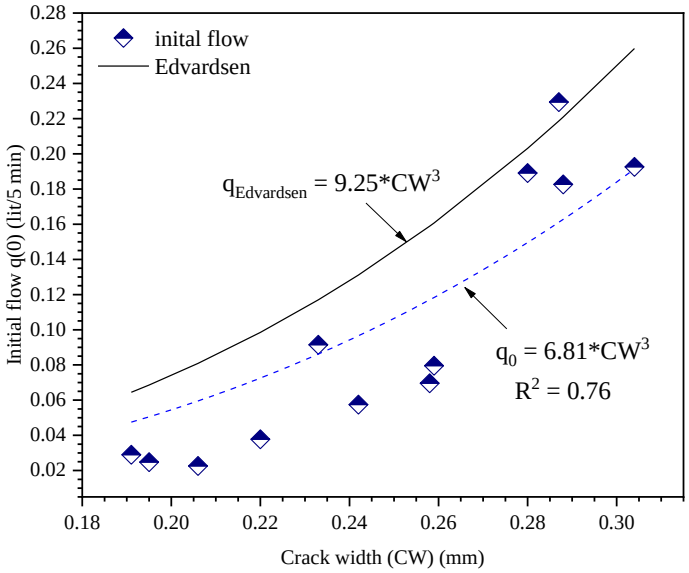

Figure 4.21. Comparison between experimental and theoretical water flow and averaged crack width results.

4.5 Conclusions

In this study, the influence of the crystalline admixtures (CA) as permeability reducing admixtures on the durability and self-healing of concrete was investigated. The following conclusion can be drawn based on the results obtained in this study:

- Concretes treated with CA had almost 50% lower water penetration depth and thus smaller permeability coefficient when compared with the virgin OPC or PLC concretes. Generally, the average water penetration depth appeared to be a better indicator to determine the water permeability coefficient than those obtained from maximum water penetration depth.
- The difference in the total charge passed (coulombs) in RCP test between concrete mixes with and without CA was inconsistent although reduction in electrical charge was observed when specimens cured for 56 days instead of 28 days. At 28 days, treated specimens showed a significant decrease in coulomb values for both PLC and OPC group while this trend was not resumed in samples cured for 56 days.

- The presence of CA did not reveal any significant effect on the surface or bulk electrical resistivity of concrete in comparison to the control mix. A nonlinear relationship between concrete SR (or BR) and its curing age was established, showing dependency of resistivity on sample's age.
- The self-healing test results showed that addition of CA into mix led to higher rate of healing and fully crack closure when compared to reference concrete. An empirical equation that relates water flow to the crack width was also proposed in this study.
- According to bulk salt diffusion test, results showed that use of CA helps in enhancing the resistance to chloride penetration compared to control concrete. This improvement increases with increasing in concrete age.
- No practical relationship between chloride permeability, RCPT results, water permeability, compressive strength, and electrical resistivity of concretes with and without CA was exhibited. Only strong linear relationship between SR and BR data was observed which indicates that these test methods can be used interchangeably.

4.6 Acknowledgment

The authors acknowledge financial support of National Sciences and Engineering Research Council (NSERC) of Canada for this project. The authors would also like to thank Kryton International for the engagement and material donation.

Chapter 5 Long-term resistivity modeling of concrete structures treated with crystalline admixtures

This chapter investigates the long-term durability performance of concretes treated with CA in both laboratory and field using electrical resistivity method. In the laboratory conditions, the effects of CA addition into concretes incorporating supplementary cementitious materials (SCM) and PLC detected by means of electrical resistivity technique is discussed in detail in section 5.1. Considering the effects of temperature variation and water content in concrete pores, an empirical model is developed that can predict the long-term variation in the electrical resistivity of CA treated concretes incorporating PLC, slag and metakaolin when compared to reference concretes. In section 5.2, the influence of CA presence on reinforcement corrosion and durability parameters in steel reinforced hollow-section concrete columns exposed to both natural and 3.5% wt. NaCl solution is studied using electrical resistivity method, chloride diffusivity, and half-cell potential technique.

5.1 Long-term change in electrical resistivity of concrete containing crystalline admixtures

This paper has been submitted to the Journal of Cement and Concrete Composites on July 30, 2018.

Pejman Azarsa, Rishi Gupta. "*Long-term change in electrical resistivity of concrete containing crystalline admixtures*." Submitted to Journal of Cement and Concrete Composites (2018).

Author Contributions: Pejman Azarsa and Rishi Gupta conceived and designed the experiments; Pejman Azarsa performed the experiments; Pejman Azarsa and Rishi Gupta analyzed the data; Rishi Gupta contributed materials and experimental equipment; Pejman Azarsa and Rishi Gupta wrote the paper.

5.1.1 Abstract

Electrical resistivity is an important durability property of concrete since it enables assessment of the accessibility of aggressive ions such as chloride before steel reinforcement corrosion initiates and after it

propagates. It is also more suitable and rapid method for concrete quality control and durability evaluation than those time-consuming diffusivity testing which are widely being used in performance-based specifications. This study investigated the long-term change in electrical resistivity of concrete mixes containing crystalline admixtures (CA), and slag or metakaolin from 7 to 700 days. Test techniques included compressive strength, surface resistivity (SR) and bulk resistivity (BR). Influence of environmental conditions such as temperature and water content on the SR and BR of concrete were also evaluated. Electrical resistivity evolution as well as correlation between SR and BR after several days was established for all concrete mixtures. The resistivity values were used to predict the aging factor of concrete. Inclusion of both slag and metakaolin resulted in significant increase in concrete electrical resistivity. Results also showed that environmental conditions and addition of CA affected the concrete resistivity to some degree. Finally, a model was developed to predict the resistivity of concrete over time when exposed to various temperature and water content. Overall, this study will contribute to the current state of knowledge practitioners of implementing non-destructive SR and BR measurement technique as a potential tool for researchers and industry agencies to evaluate binary and ternary mixtures and estimate corrosion rate.

Keywords:

Concrete electrical resistivity, Crystalline admixtures (CA), Supplementary cementitious materials (SCM), Durability indicator, Non-destructive technique (NDT)

5.1.2 Introduction

Chemical admixtures are predominantly water-soluble ingredients used to improve concrete's properties in the fresh state, its mechanical properties in the hardened state, or both [21]. Typically, their effects on concrete properties in the plastic stage include increased workability, improved pumpability, setting time, or finishability; on the other hand, when concrete hardens, chemical admixtures contribute in improving durability, increasing compressive and flexural strength at all ages, reducing shrinkage phenomena, or decreasing permeability of concrete. Chemical admixtures also act as agents which allow the manufacture and construction of special sustainable concrete types such as self-healing concrete, high-strength concrete, self-consolidating concrete [284]. Among these special concrete types, Engineered Self-healing Concrete

(EShC) is a type of concrete which has the capability to autonomously heal cracks inside its matrix to a certain level, by incorporating various substances such as crystalline products; help in reducing concrete permeability; thus, increasing its service-life. In recent years, more attention has been paid to EShC which is associated with artificially triggered healing mechanisms into the cementitious matrix and presented mainly by some chemical or biological agents such as the use of microencapsulated healing agents, bacterial concrete, or the use of crystalline admixtures.

Among these aforementioned chemical admixtures, Crystalline Admixtures (CA) are one of the Permeability-Reducing Admixtures (PRA) types, consisting of a proprietary mix of active chemicals, implanted in a carrier of cement and sand, as described by the American Concrete Institute (ACI) Committee 212 [1]. Contrary to hydrophobic or water-repellent materials, these products are hydrophilic which makes them react easily with water and cement particles when moisture enters the pores/cracks of concrete. After taking this reaction in place, CA forms water insoluble pore blocking precipitates, reducing concrete porosity and permeability, enhancing its durability; thus, making the material more sustainable. Also, CA increases the density of Calcium Silicate Hydrate (C-S-H, main cement hydration product) and consequently, makes concrete more resistant to penetration of aggressive ions [21]. Preliminary Scanning Electron Microscopy (SEM) study performed by authors indicated the development of crystals in the voids of mortar specimen, as illustrated in Figure 5.1 (magnification: x3.0 k times) [23].

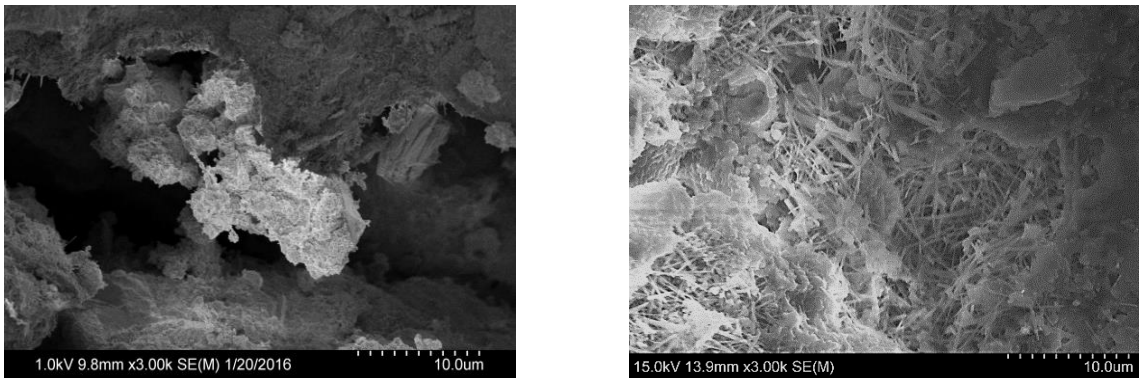

(a) Un-treated **(b)** CA-treated

Figure 5.1. SEM micrographs of **(a)** control mortar sample without CA addition **(b)** CA-treated mortar specimen.

As a smart construction material, crystalline products have been used for over two decades in the construction industry while their effects on concrete self-healing and shrinkage behavior have been investigated in some aspects by researchers [14]–[19], [22], [23], [55]–[57], [285]. The visual closure of cracks in mortar specimens incorporating fly ash, expansive admixtures, silica fume, CA and limestone powder under water immersion conditions were investigated by Jaroenratanapirom and Sahamitmongkol [55], [56]. Self-healing (SH) potential and water tightness of pre-cracked cement-based materials treated with Calcium Sulfo-Aluminate (CSA) based expansive additive and CA were also explored in Sisomphon *et al.*'s study [15]. They also examined the healing effects of CA on strength recovery under four different exposure conditions (wet/dry cycles, humidity chamber, water immersion with/without renovation, and air exposure) [57]. Ferrara *et al.* [16] studied the CA effects on the concrete SH and their healing capability on the recovery of mechanical properties; evaluated the influences of the SH phenomena on the recovery of stiffness and load-bearing capacity by means of 3-point bending (3pb) test before and after conditioning [16]. Using a different technique, a similar study by Roig-Flores *et al.* [17] investigated the effects of CA only on the SH of concrete in four various types of environmental exposure conditions. Based on the measure of the global permeability of the specimen and different geometrical characteristics of the crack before and after the SH period, they developed a method that can evaluate the SH properties of cracked samples. Following the previous study, Roig-Flores *et al.*'s [18] work analyzed the SH properties of early-age concretes, engineered using CA, by measuring the permeability of cracked samples and their crack width. Under three different exposure conditions, they considered the SH behavior in two typically used concrete classes, one common for precast concrete elements (C45/55) and one standard class broadly used for building constructions (C30/37) [18]. In a recent study by Ferrara *et al.* [19], the influences of CA on the self-healing capacity of the cementitious composites with reference to both a Normal Strength Concrete (NSC) and a High-Performance Fiber Reinforced Cementitious Composite (HPFRCC) have been evaluated. It is evident that previous research works mainly focused on self-healing concepts of CA-treated concrete whereas to the best of authors' knowledge, no research work has been conducted in this area to understand and address certain durability characteristics of this material (i.e. electrical resistivity or chloride

diffusivity) especially when combined with Supplementary Cementitious Materials (SCM). Since the resistance of concrete against ions' penetration is a function of its permeability (i.e. the volume fraction of pores and their structures (tortuosity), and pore solution conductivity), it is a reliable parameter to non-destructively assess concrete durability during its intended service life. Hence, electrical resistivity measurement, providing some information about the interconnected pore network, can be considered a reliable tool to investigate the crystalline admixtures' efficiency as it modifies the concrete's microstructure by crystals' deposition and improves its permeability.

Electrical resistivity of concrete is a geometry-independent material property defined as the difficulty of dissolved ions movement through its medium or the resistance against the flow of electrical charges. At certain ages, electrical resistivity measurement can indicate the performance parameters – strength, maturity, and permeability- to identify the progress of standard specimens fabricated during construction [22]. Dependency of all these parameters on concrete microstructure is the possible origin of their correlations with concrete resistivity. In general, presence of more interconnected pores in concrete microstructure results in higher permeability; thus, lower resistivity and strength. Considering substantial cost savings for both agencies as well as a contractor associated with fast and non-invasive resistivity measurement technique leads to implementation of this method in most specifications. Due to its dependence on the matrix's microstructure and conductivity of the pore solution, concrete resistivity is highly influenced by several parameters such as *w/b* ratio, cement type, presence of cracks and rebar, binder composition, addition of minerals/pozzolans, moisture content, etc. The effects of some of these parameters on electrical resistivity have been reviewed in authors' pervious work [22]. In this study, the interactions of CA with some of these parameters, not being reported elsewhere, are investigated. The analyzed parameters include the cement type, moisture content, presence of SCMs, chemical admixtures, temperature and curing age, determined by using resistivity data collected at different times. Additionally, there is a significant number of studies addressing the electrical resistivity of concrete with slags or metakaolin [102], [106], [108], [112], [117], [118], none related to the effect of CA addition in the mixture when other

minerals are added. Further investigations are also required to study the evolution of concrete resistivity over time especially regarding the inclusion of concrete with CA additions and long-term data.

The aim of this paper is to study the effect of crystalline admixtures on the surface and bulk electrical resistivity of concrete over a period of 2 years when SCMs are present. Results were compared with a control mix with 100% ordinary Portland cement (OPC), 100% Portland-limestone cement (PLC) (launched in Canada in 2011), and two binary mixes, one with 20% Ground Granulated Blast-furnace Slag (GGBS) and the other with 10% Metakaolin (MK). This makes this work one of the first to report such information. Some of the environmental factors such as moisture content and temperature, affecting the resistivity, were also discussed to provide further information. Correlation between bulk and surface resistivity was established and the aging factor was calculated from the resistivity measurements over time on concrete specimens with mineral additives. Eventually, a predictive model to estimate concrete resistivity evolution considering temperature and water content effects was also developed.

5.1.3 Experimental Program

This study explored the effect of crystalline admixtures on the long-term resistivity of concrete incorporating slags and metakaolin. In this section, the applied methods for the preparation and storage of the concrete samples, as well as the methods used for determining the compressive strength and electrical resistivity are explained.

5.1.3.1 Materials and mixture proportions

This study was quite extensive and included a total of 100 samples of ternary and binary cementitious mixtures including the control mixture of 100% ordinary Portland cement with a constant water/binder (*w/b*) ratio of 0.45; containing 340 kg/m^3 of cementitious materials in all mixtures. This water/binder ratio is typical for concrete exposed to severe rain or alternate wetting and drying; concrete entirely immersed in sea water or exposed to coastal environment. Table 5.1 represents the masses of materials used per m^3 for each of the cementitious mixtures. The basic mixture parameters were coded into the label names of the

mixtures with each supplementary cementitious material and crystalline admixtures, e.g. OPMK-CA means ordinary Portland (OP) cement, metakaolin (MK) and 2% crystalline admixtures (CA) (Table 5.1).

Table 5.1. Mixture proportions of concrete.

No.	Mixtures ID	Cement Content (kg/m^3)	*w/b* ratio	Coarse Aggregate (kg/m^3)	Fine Aggregate (kg/m^3)	SCM		
						GGBS (kg/m^3)	MK (kg/m^3)	CA (kg/m^3)
1	OPC	340	0.45	1120	820	×	×	×
2	OPC-CA	340				×	×	6.8
3	OPGGBS	272				68 (20%)	×	×
4	OPGGBS-CA	272				68 (20%)	×	6.8
5	OPMK	306				×	34 (10%)	×
6	OPMK-CA	306				×	34 (10%)	6.8
7	PLC	340				×	×	×
8	PLC-CA	340				×	×	6.8
9	PLGGBS	272				68 (20%)	×	×
10	PLGGBS-CA	272				68 (20%)	×	6.8

All SCMs were replaced on a one-to-one basis by mass of cement in a mixture whereas CA were added in powder form at a dosage of 2% by the weight of total cementitious material. A special category of hydrophilic permeability reducing admixtures (PRAs) commercially produced was used as waterproofing cementitious materials (or CA). However, the chemistry of this product is proprietary and not available. The binders used in this study include (a) *Ordinary Portland Cement (OPC) – ASTM C150 Type I cement* (b) *Portland Limestone Cement (PLC)* (c) *Ground Granulated Blast-Furnace Slag (GGBS)* (d) *Metakaolin (MK)*.

A mid-range water reducing admixtures (BASF Canada Master Pozzolith 210) and an air entraining agent (Grace Canada DAREX® AEA ED) were used to meet better workability and durability performance specifications. Meeting ASTM C33 [286] requirement, the coarse aggregate used was natural gravel and mostly of siliceous origin, fine aggregate was river sand. The physical properties of aggregates used in this study are summarized in Table 5.2.

Table 5.2. Coarse and fine aggregate properties.		
Aggregate	Coarse	Fine
Maximum Size (mm)	12.5	4.75
Specific Gravity	2.8	2.7
Water Absorption (%)	0.45	1.2
Fineness	-	2.61

5.1.3.2 Specimen Preparation

For each mixture, cylinders of Φ100 × 200 mm were prepared for non-destructively testing the SR and BR resistivity at ages of 7, 14, 28, 42, 56, 84, 96, 112, 640, 670, 700 days. All mixtures were cast in accordance to recommendations by ASTM C192 [265] practice. In accordance with ASTM C143 [266], slump test was performed within 15 minutes after preparing the mixes to avoid any loss of workability with time. For all mixtures, air content was also determined by following procedure in ASTM C231 [267]. Ten cylinders were cast from each batch of concrete, by placing the mold on a vibrating table and filling it in three approximately equal layers, and compacted by an external vibration for a duration of 60-90 seconds - depending on the workability of the fresh concrete - as detailed in ASTM C192 [265]. After consolidation, each mold was labeled; then covered with a plastic sheet to prevent the evaporation of water from the concrete surface and kept for 24±2 h in the laboratory. After removal from molds, they were continuously cured in a water bath at 23±2 °C before testing.

5.1.3.3 Testing Procedures

This study mainly consists of surface and bulk electrical resistivity measurements of concrete cylinders. For further characterization of the concrete quality, the compressive strength was also determined. After 28 days of curing, compressive strength tests on three cylindrical specimens were conducted on all the mixes in accordance to ASTM C39 [270].

The surface electrical resistivity measurement, following ASTM [WK37880] working document methodology, was performed by commercially available non-destructive four-probe Wenner SR meter with 3.8 cm equally spaced, manufactured by Giatec Scientific Inc. The equipment, shown in Figure 5.2, works on low fixed frequency (13 Hz) alternating current (AC) which is flowing between the outer electrodes and

measures the potential difference between two inner electrodes. All cylinders were removed one by one from water tank before testing on the specified day and tested at Saturated Surface Dry (SSD) condition at 23±2 °C. Readings were taken at a total of eight locations with the four set of probes centered every 90° along the longitudinal direction of the cylinder.

RCON meter was utilized to measure the BR of Φ100mm × 200 mm concrete cylinders. It is another non-destructive instrument, manufactured by Giatec Scientific Inc (Figure 5.2). Since resistance measurement with a DC signal is not recommended due to electrodes' polarization effect, an alternating current (AC) was used to apply the current at a fixed frequency of 1 kHz through the specimen. Such a frequency was selected based on Spragg *et al*. [99], who have found the lowest imaginary impedance at a frequency of about 800 Hz for cement-based mortars in uniaxial impedance measurements. The electrodes consist of circular stainless-steel plates, on which a contact sponge wetted with a dilute solution of soap, was inserted in between two electrodes to ensure that the entire surface is in electrolytic contact with the electrode. The soap is added to lower the surface tension of the water in the sponge to further ensure full contact. Before testing, any free surface water was carefully removed from the specimen's surface with a towel. Figure 5.2 shows schematic diagram of fundamental physics involved for measurement of the BR. The instrument is set up with a voltmeter to measure the voltage drop V, across the specimen and an ammeter to measure the current "I". Once the measurement was taken in the first few seconds, the BR reading appeared unstable and increased at faster rate. It usually took one or two minutes for the data to become stable and then it was recorded. For each mix, three specimens were tested, and an average of these readings was calculated.

It should be noted while using BR, the resistivity is measured over the whole volume of a specimen whereas using the four-point Wenner method, the result is more influenced by the superficial concrete inhomogeneity, porosity and saturation level [287]. In this study, both SR and BR data were used for investigating the resistivity evolution over time for different concrete specimens.

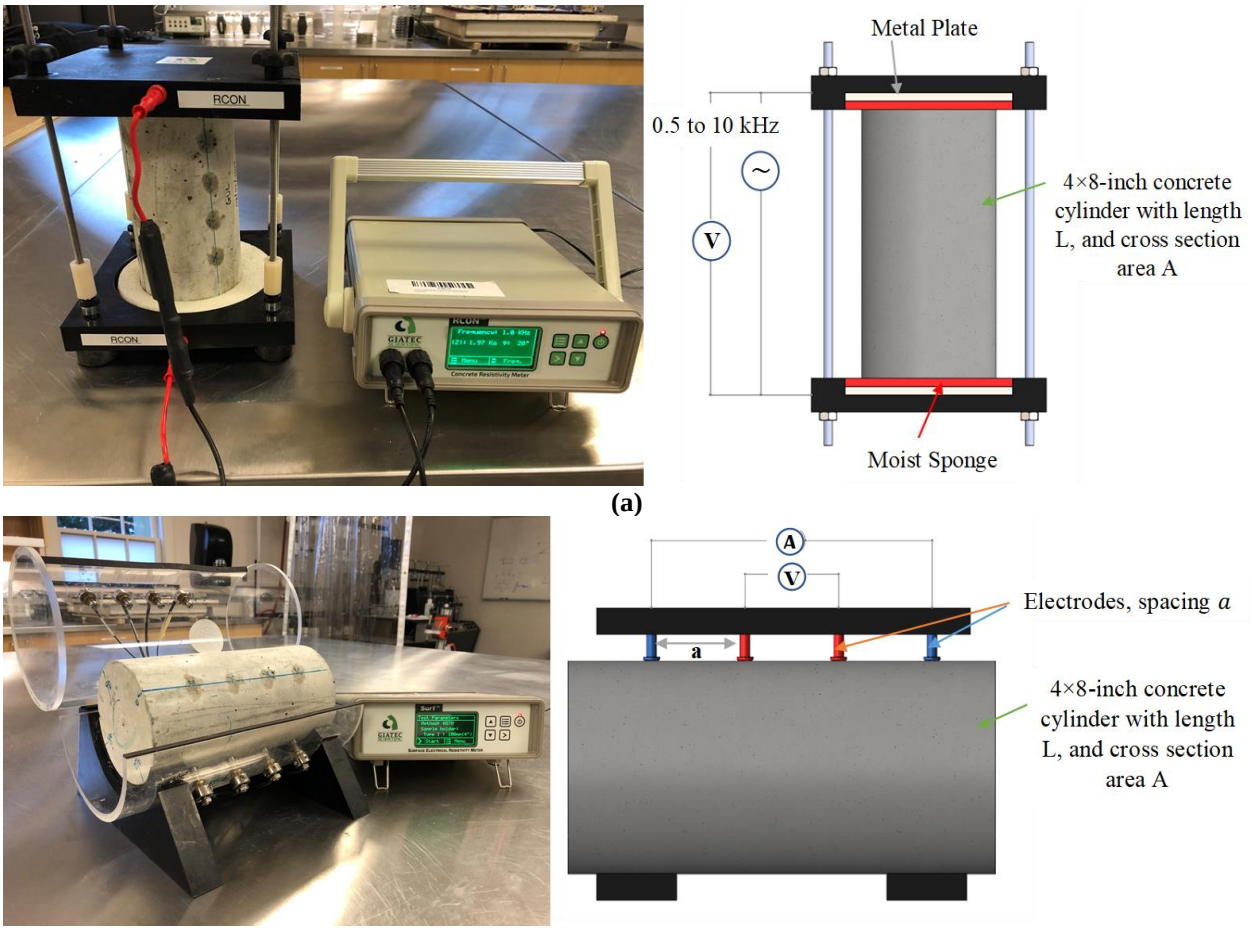

Figure 5.2. Testing concrete specimen & schematic diagram of **(a)** RCON meter **(b)** SR testing instrument.

The effect of water temperature on resistivity measurements was also investigated for the same mixture. The specimens were kept in water at temperatures of 5, 15, 25, 30, 35 and 50 ˚C for three days before testing. To investigate the influence of specimen water content on resistivity measurement, cylinders were first weighed and then kept inside the oven at 110 ˚C for 24±2 hours to reach to dry state. After cooling down, each cylinder's weight at dry stage was measured again to ensure constant mass. Afterward, all specimens were immersed in a water tank under controlled temperature (20±2 ˚C). Specimens were retrieved after 2, 6, 12, 24, 48 h and were surface dried; weighed and thereafter both SR and BR were measured. The measurements have been performed until each cylinder reached a constant weight.

5.1.4 Results and discussion

This section describes the SR and BR results for samples aged from 7 to 700 days. Results are presented for un- and CA treated concrete mixtures. The influences of environmental conditions such as temperature and water content on electrical resistivity measurements are also presented here. Correlation between SR and BR measurement techniques are discussed for concrete with and without crystalline admixtures. Fresh concrete properties including slump, unit weight, air content, and temperature are reported in Table 5.3. From slump and compressive strength values reported in Table 5.3, it can be observed that the slump of all mixes is within 140±20 mm. The addition of crystalline admixtures results in a slight decrease in workability and slight increase in strength. This improvement in strength proves formation of additional CSH gel (responsible for concrete strength) in treated cylinders. Also, incorporation of SCM improved the strength slightly after 28 days of curing while workability also slightly increased. Due to slower pozzolanic reactions of slag, its compressive strength is expected to be fully gained at later age, not at 28 days curing.

Table 5.3. Fresh and hardened properties of concrete mixtures.

Mixture ID	Compressive strength (MPa, 28 Days)		Slump (mm)	Unit weight (kg/m^3)	Air content (%)	Mix temperature (^{o}C)
	Average	COV %				
OPC	56.72	2.61	135	2396	5.3	16
OPC-CA	56.98	1.30	110	2385	5.5	15
OPGGBS	57.35	3.18	150	2370	4.9	18
OPGGBS-CA	58.09	4.58	135	2345	5.1	18
OPMK	59.60	3.45	160	2390	-	17
OPMK-CA	60.61	4.53	140	2340	-	15
PLC	56.95	1.02	140	2395	6.2	16
PLC-CA	57.12	0.89	120	2348	6.4	16
PLGGBS	58.13	1.31	155	2368	6.0	19
PLGGBS-CA	59.16	1.75	130	2360	6.3	17

5.1.4.1 Relationship between compressive strength and electrical resistivity

For all mixtures, the correlation results for both BR and SR of concrete and its compressive strength at 28 days are shown in Figure 5.3. Similar to previous studies [72], [73], [82], [106], [108], [111], [112], [288], as the strength increased, the electrical resistivity correspondingly increased as shown in the plot. Strong linear relationship between strength and resistivity (especially SR) has been observed due to direct

dependency of these parameter on the matrix porosity. As the density of the microstructure increases, both strength and electrical resistivity of concrete will increase, although in later ages they might be affected by the other properties such as the pore solution conductivity, pore connectivity, and the degree of mixture saturation. The proposed equations in the plot can be used to estimate the resistivity or strength of similar concrete mixes used in this study. The presence of metakaolin also resulted in the greatest values for both compressive strength and resistivity of concrete, indicating its filler effect, the acceleration of cement hydration, and the pozzolanic reaction of MK with lime (CH) at early age, reported by [289]. Also, using PLC in the mix did not show an increase in strength and resistivity values when compared to control mix.

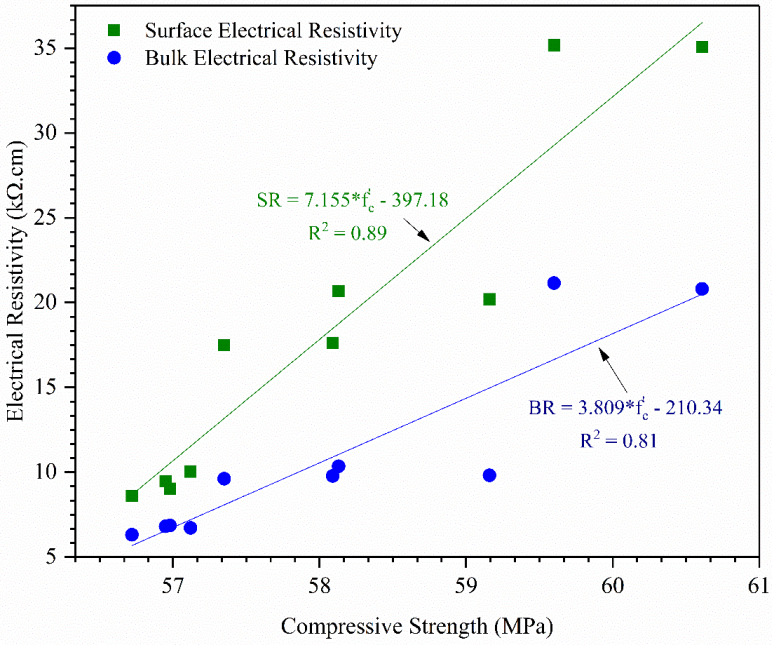

Figure 5.3. Relationship between concrete compressive strength and electrical resistivity.

5.1.4.2 Relationship between concrete curing age and electrical resistivity

The bulk electrical resistivity of concrete values at different ages for mixtures with and without CA are shown in Figure 5.4. The substitution of cement by GGBS and metakaolin effectively increased the electrical resistivity of the concretes at different days and this phenomenon has been reported by other researchers [102], [108], [112], [117], [118]. Considering all concrete ages, the un-treated mixture composed of OPC and 20% GGBS, OPGGBS, showed bulk electrical resistivity values that were between

1.24 and 2.38 times greater than that of control mixture (OPC) while the corresponding values for CA treated mixture (OPGGBS-CA) were between 1.25 and 2.13 times greater. Similar un-treated mixture with Portland limestone cement (PLGGBS) exhibited bulk electrical resistivity values that were between 1.03 and 2.65 times greater than that of reference mixture whereas these values were between 0.96 and 2.49 times greater for CA treated concrete (PLGGBS-CA). The metakaolin mixtures, OPMK and OPMK-CA, had resistivity levels that were 2.6-3.37 and 2.43-3.03 times greater, respectively, than those of the control mixture (OPC). The presence of SCM increased the density of the mixtures, reduced the conductivity of the paste mix and the ionic concentration of the pore solution [102]. Comparing the mixtures containing only Portland cement (control ones), the bulk electrical resistivity of the mixture with limestone was slightly higher (maximum of 20% increase) than that of ordinary one for all the ages tested and also un-/CA-treated.

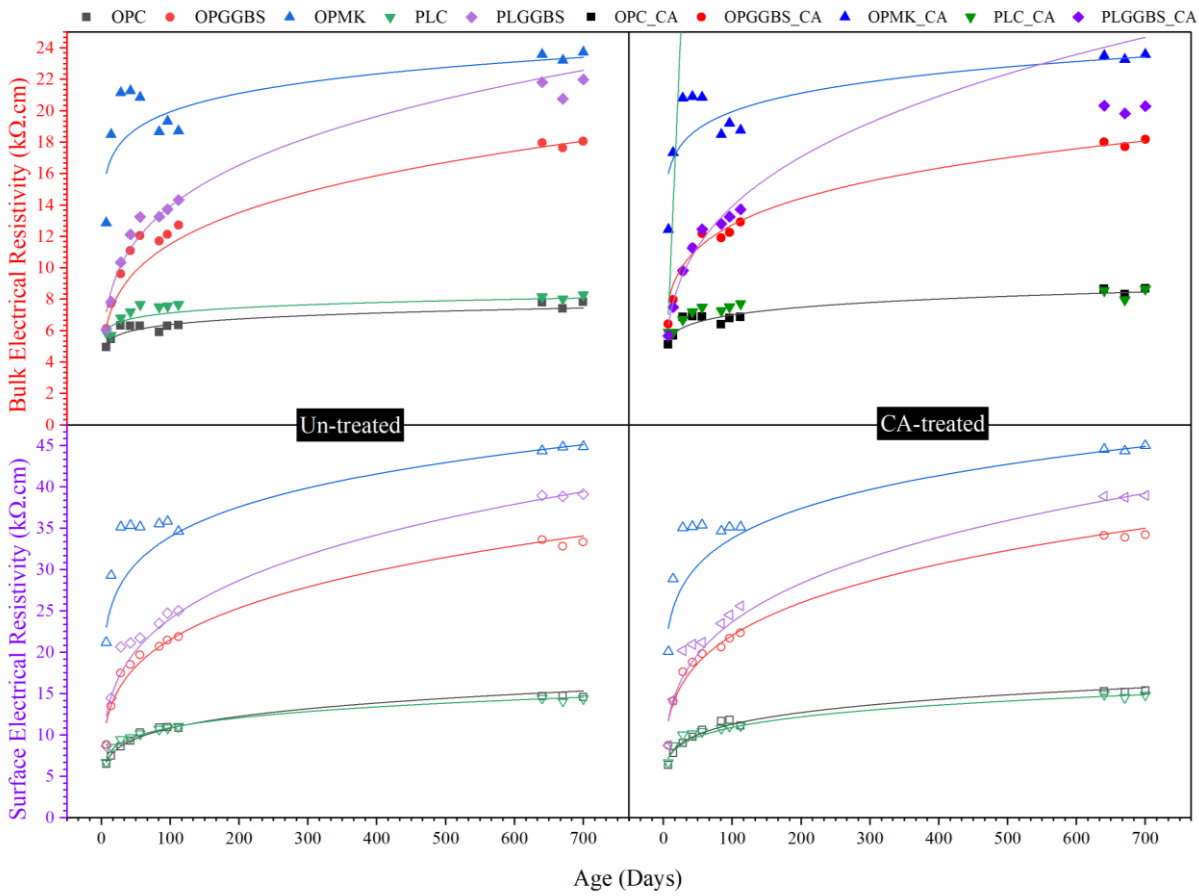

Figure 5.4. Bulk and surface electrical resistivity variation over time.

Due to cement hydration and progressive hardening of concrete, the surface electrical resistivity of concrete cylinders also increased continuously with time over 700 days after preparation while it does at a declining rate, as seen in Figure 5.4. In compliance with other studies [102], [112], [117], [118], the plot suggests that there is tendency to reduce the interconnected pore network of the matrix over time, attributing to increase in the concrete resistivity. For a given cement type, the results clearly indicate that the concrete composition (SCM and CA presence) likewise affects the concrete electrical resistivity. Similarly, concrete prepared using GGBS or metakaolin showed considerable increase in surface electrical resistivity compared to the reference concrete. According to results of resistivity testing, OPMK and OPMK-CA samples have the highest resistivity values, followed by GGBS mixtures. This behavior is explained by high pozzolanic activity of these mixtures. It is also interesting to mention that resistivity of GGBS mixtures closely reached to that of the metakaolin mixtures at 2 years. This suggests that the addition of GGBS seems to react more slowly and consume calcium hydroxide ($Ca(OH)_2$) over time, forming more CSH gel in the matrix due to pozzolanic reactions; this reduces the amount of OH in the pores' solution, increasing the concrete resistivity. It is also appeared that the effect of CA on the lessening of concrete electrical conduction is limited. It is important to note that addition of 2% CA may not sufficient to modify the electrical conductivity results when compared to control concrete.

According to Figure 5.4, the best regression fit to the data was of power type, based on the best determination coefficient (R^2) found. Although Medeiros-Junior & Lima [290] suggests the polynomial adjustment for the long-term resistivity behavior (over 1 year), the power function ($y = ax^b$) appeared to be the most suitable in this study. Power functions, summarized in Table 5.4, are useful to predict the long-term electrical resistivity behavior and its evolution in un- and CA treated samples with two different cement types. In this table, GGBS mixtures are shown the highest coefficient of determination ($R^2 > 0.95$) than other mixtures, indicating consistent and constant development of both bulk and surface electrical resistivity. A fair correlation ($R^2 = 0.6$) was observed for metakaolin mixtures measured using bulk resistivity method. It should be noted that these functions are proposed based on laboratory tests performed

in this study and authors validate these parameters, which will later be used in the service life model based on concrete resistivity, in real concrete structures as part of on-going research study. Generally, for all mixtures, the development of the surface and bulk resistivity has a common rate of development trend; however, surface resistivity measurement represented better correlation than that of bulk resistivity method, as also indicated in Table 5.4. This data will benefit researchers or concrete industry fellows to understand the role of CA and metakaolin as supplementary cementitious materials. Aging factor are also introduced in the next section to investigate more about resistivity evolution vs time for all mixes.

Table 5.4. Summary of power function parameters ($ER=a*t^b$).

Concrete type	Mix ID	Bulk electrical resistivity			Surface electrical resistivity		
		a	b	R^2	a	b	R^2
Untreated	OPC	4.45	0.078	0.94	4.75	0.179	0.98
	OPGGBS	3.96	0.232	0.99	7.26	0.236	0.96
	OPMK	14.15	0.078	0.6	21.24	0.116	0.87
	PLC	5.41	0.067	0.8	5.61	0.144	0.98
	PLGGBS	4.43	0.248	0.97	7.48	0.254	0.98
CA-treated	OPC-CA	4.48	0.097	0.89	5.17	0.17	0.96
	OPGGBS-CA	5.56	0.18	0.99	7.38	0.238	0.95
	OPMK-CA	13.52	0.085	0.65	20.71	0.12	0.86
	PLC-CA	5.25	0.01	0.88	5.71	0.146	0.97
	PLGGBS-CA	3.59	0.294	0.94	7.16	0.26	0.98

5.1.4.3 Aging factor

The transport of chloride ions through microstructure of concrete, typically defined by chloride diffusion coefficient, plays an important role in the control of concrete durability [22]. Chloride diffusion coefficient $D(t)$ usually decreases with time [291] and can be expressed by [292]:

$$D(t) = D_0 \left(\frac{t_0}{t}\right)^m \quad \text{Equation 5.1}$$

where $D(t)$ is the apparent diffusion coefficient at time t; D_0 is the diffusion coefficient at a reference time t_0; m is the aging factor ($0 \leq m \leq 1$) can be derived experimentally from bulk diffusion test values or rapid chloride migration (RCM) test values [291]. The factor depends on the concrete composition and environmental exposure. When chloride ions are charged, then it is the concrete's ability to withstand

transfer of charged ions which is highly dependent upon its electrical resistivity. Hence, m values can be also obtained from resistivity [74]. In theory, the relationship between diffusivity of chloride ions and resistivity can be described by Nernst-Einstein equation:

$$D_{cl} = \frac{K}{\rho} \qquad \text{Equation 5.2}$$

where D_{cl} is the chloride diffusion coefficient; K is a constant and ρ is electrical resistivity of concrete. Combining Equation 5.1 and Equation 5.2 results in the following equation:

$$\rho(t) = \rho_0 \left(\frac{t_0}{t}\right)^{-m} \qquad \text{Equation 5.3}$$

Now m can be calculated by rearranging Equation 5.3 and applying log_{10} as follow:

$$m = \frac{\log\left(\frac{\rho_t}{\rho_0}\right)}{\log\left(\frac{t}{t_0}\right)} \qquad \text{Equation 5.4}$$

Using the resistivity values, therefore, chloride diffusivity evolution as function of time can be estimated under certain conditions. According to Andrade *et al.* [74], [114] and Presuel-Moreno *et al.*'s [104] studies, there is a difference between the aging factor derived from resistivity and diffusivity as ρ represents the evolution of the microstructure (i.e. pore network and tortuosity) while D_{cl} variations indicate the binding capacity and evolution of chloride surface concentration vs time, in addition to microstructure changes. In this study, the aging factor (m), calculated using Equation 5.4 with a reference age of 7 days (t_0) and the concrete resistivity obtained at that age (ρ_0), corresponds to the change in microstructure with time i.e. pore network and connectivity.

Figure 5.5 exhibits the aging factors of specimens treated with CA, calculated from BR data, whereas un-treated mixtures are shown in upper half of the graph. The calculated aging factors (m) are shown in y-axis while x direction indicates specimen age (t). It was observed that the calculated m of cylinders treated with CA range between 0.01 and 0.48; while these values for untreated samples varies from 0.02 to 0.52. In terms of aging factor derived from BR data, not much difference in values has been observed between un-treated and CA treated samples. It can be also seen that the aging factors of all mixtures except ones

containing metakaolin are time-independent and quite constant. For metakaolin mixtures, the trends of m values decrease with time and are initially the highest for both un- and treated samples. Additionally, it is clear that aging factors of control cylinders (not containing SCMs) are slightly lower than those incorporated with SCM. It is also apparent that calculated m values for cylinders with OPC and PLC cement types are similar after 56 days. Figure 5.6 shows the aging factors ($t_0 = 7$) of all mixtures calculated from SR data. Comparing the results shown in Figure 5.5 and Figure 5.6, it was observed that the aging factors of all concrete based on SR data were generally higher than those from BR data. The aging factors of all specimens in Figure 5.6 has a descending trend and reduce with time which is different from what has been observed in Figure 5.5 where the most aging factors reached constant values after 28 days. Therefore, aging factors from SR data indicates more realistic results than corresponding ones from BR data. In the Figure 5.6, the highest aging factor (m) belongs to GGBS mixtures with PLC cement (0.73 for un-treated and 0.7 for CA-treated), followed by similar mixtures with OPC cement; while these factors for control cylinders with OPC and PLC cements are the lowest. Low hydration rate and slow pozzolanic reactions of GGBS is likely responsible for constant decay in aging factors while hydration of metakaolin helps in the faster decay in m values at an early age. All treated mixtures except GGBS mixtures show slightly higher initial aging factors than un-treated samples; thus, it is evident that presence of CA and SCM enhances the electrical resistivity and produce greater aging factors vs. time which in turn is indicative of improved concrete durability. In the case of SCM presence, the trend is similar to what have been reported by Andrade *et al*. [74] and Presuel-Moreno *et al*. [104]. After 56 days, the calculated m values for OPC, PLC and OPMK mixtures are similar. It should be noticed that m values for each mixture decays initially faster and reaches a constant plateau at later ages. From the results shown in Figure 5.5 and specifically Figure 5.6, it can be concluded that aging factors are time dependent and affected by concrete compositions and admixtures. It is also suggested for concrete containing slow reacting mineral admixtures such as GGBS, the long-term resistivity (diffusivity) can be calculated from m values obtained at later ages. Also, it is recommended to consider multiple m values for these mixtures since the m factor can be affected by mixture composition

at different age. Authors suggest m values of 0.2 for concrete with OPC or PLC cement, m values of 0.32 for concrete made with GGBS <20% at later age (0.45 for early age); m values of 0.22 for concrete containing less than 10% metakaolin. Similar m values for OPC mixtures reported in Andrade *et al*. study [74].

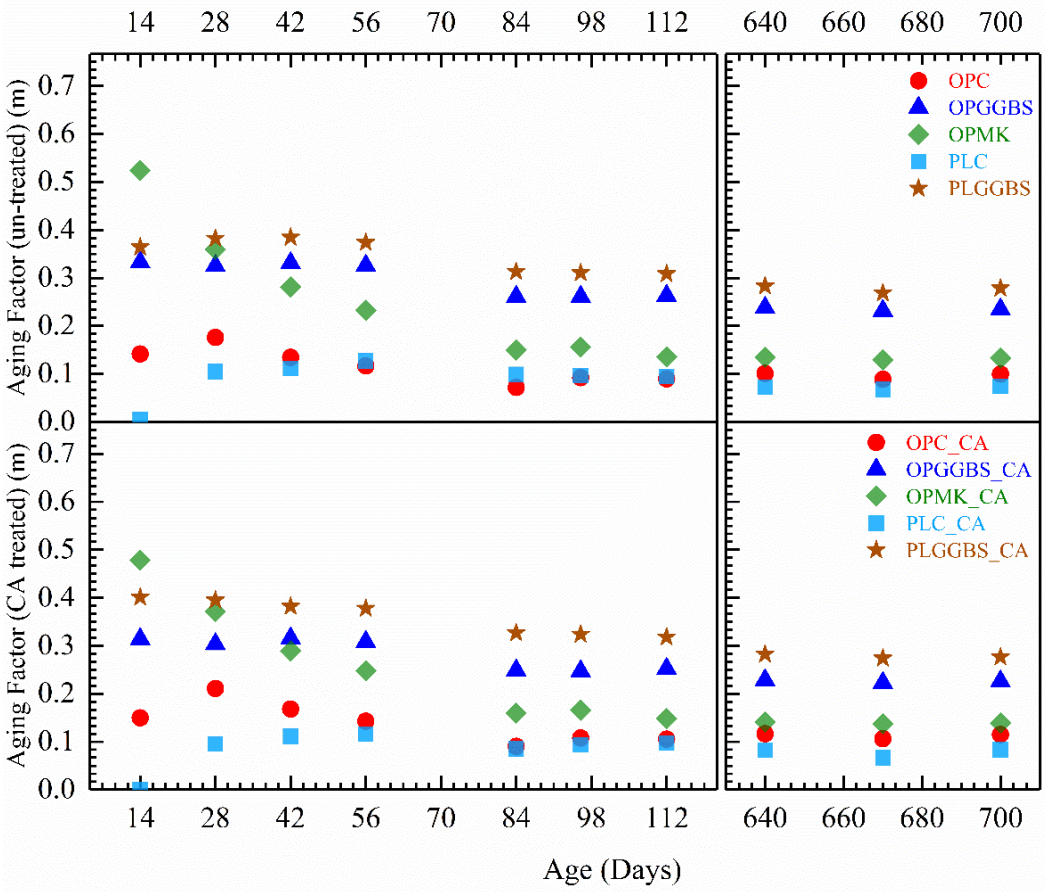

Figure 5.5. Aging factors of CA- and un-treated specimens (based on bulk resistivity data).

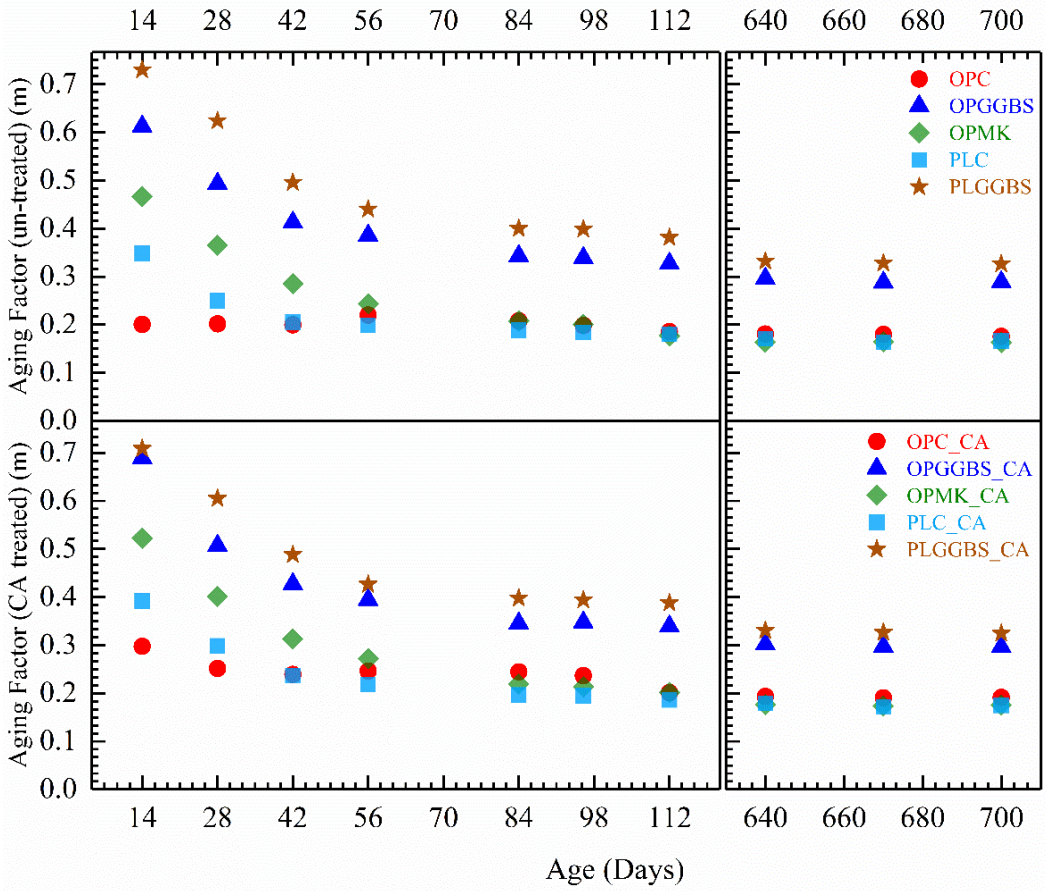

Figure 5.6. Aging factors of CA- and un-treated specimens (based on surface resistivity data).

5.1.4.4 Correlation of electrical resistivity of un- and CA treated mixes

Figure 5.7 shows the relationship between BR vs BR and SR vs SR for un- and CA treated specimens. For regression analysis, linear equation was used to correlate data for un- and CA treated concrete mixtures. There is strong correlation (R^2) between un- and CA treated samples for both BR and SR, indicating effectiveness of resistivity measurement technique. From this graph, it can be concluded that concrete resistivity is not affected by addition of crystalline admixtures. Either dosage of CA added to the mix was not optimal to alter concrete resistivity or chemistry of pore solution was not influenced by CA addition since its presence in the mix showed reduction in matrix porosity by deposition of pore-blocking crystals. It should be noted that no similar study has been found to report this correlation for crystalline admixtures.

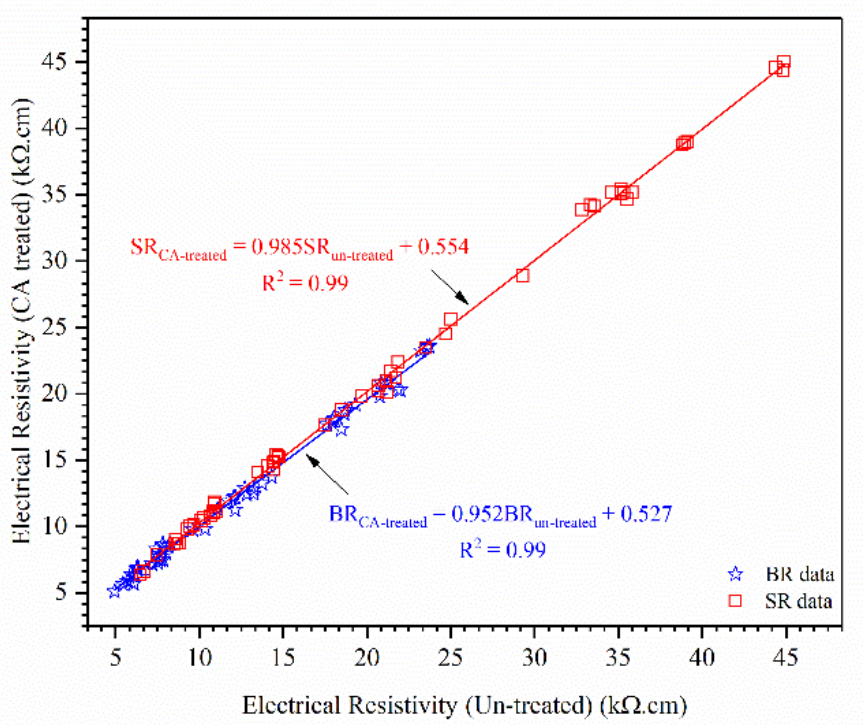

Figure 5.7. Correlation of the resistivites between un-treated and CA-treated specimens.

For all concrete mixtures, the correlations of resistivity of bulk vs bulk and surface vs surface between 700 days and that obtained at 7, 28, 56, 112, 640 days are plotted in Figure 5.8 (a) & (b). Linear equation was used for regression analysis in all cases as best correlation. As times progresses, it can be noted that the determination coefficient increases for both SR and BR. Only at 7-day age, data obtained from BR measurement shows very weak correlation (R^2 = 0.23) due to inadequate development of specimen microstructure and the densification of the matrix. Contrary to Ghosh *et al*. [117] study, the determination coefficient of SR vs SR was higher at early ages and slightly higher at later ages when compared with determination coefficient of BR vs BR.

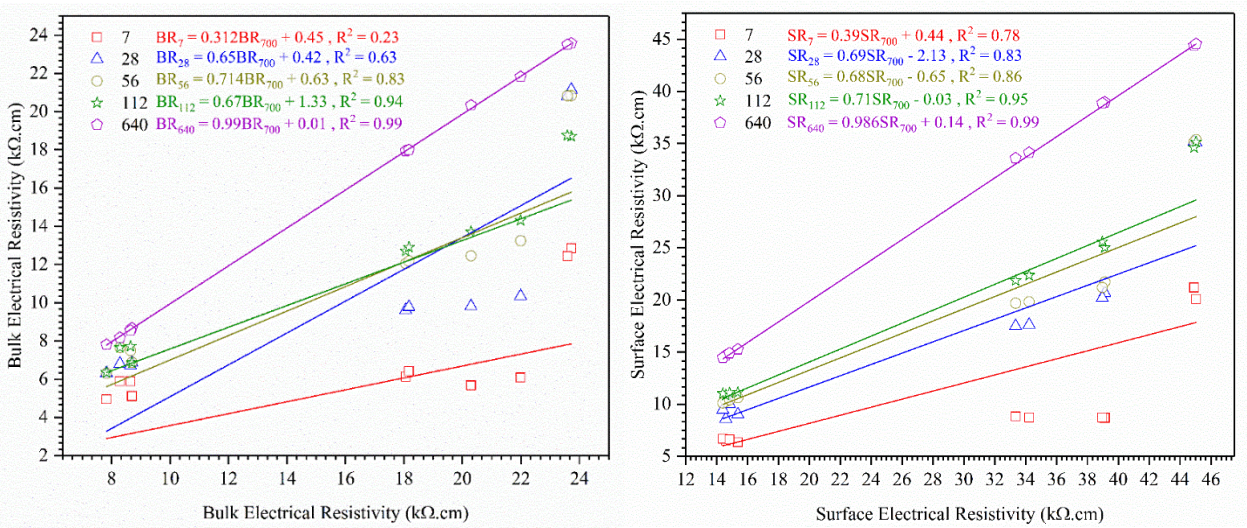

(a) BR vs BR **(b)** SR vs SR

Figure 5.8. Correlation of the resistivites between 7, 28, 56, 112 and 640 vs 700 days **(a)** BR vs BR **(b)** SR vs SR.

5.1.4.5 Comparison of experimental resistivity values

Figure 5.9 exhibits distribution of ratio of experimental surface to bulk resistivity on un-treated and CA treated samples. The box plot indicates the range of average ratios between experimental SR and BR resistivity those lay between the first quartile (Q_1) and third quartile numbers (Q_3) for all cementitious mixtures. The median value of ratio is shown with horizontal line inside the box whereas the remaining values of the ratios excluding the outlier is presented with the vertical line below and above the box. An outlier, shown as a symbol of (°) in the graph, is any data point that is more than 1.5 times the Inter Quartile Range (IQR= $Q_3 - Q_1$) from either end of the box. It can be seen that the ratio falls in between 1.35 to 1.95 (in between first and third quartile numbers) for all mixtures. As mentioned earlier, the ratio of two different resistivity types (ρ_{SR} and ρ_{BR}), proposed by Morris *et al*. [119], is equal to 1.95 for a cylinder with a length of 200 mm (8 inches) and diameter of 100 mm (4 inches) when probe spacing (a) is equal to 38 mm. Considering the theoretical geometric correction factor of 1.95, the ratio of surface vs bulk resistivity is slightly lower but still in good agreement with the theoretical value. Similar studies by Spragg *et al*. [96] and Ghosh *et al*. [117] showed similar trend of results for surface and bulk resistivity comparison. The possible reason for lower value in this than previous ones is the testing operation since several requirements

must be satisfied. One possibility is the need to test the specimen in SSD condition which is not sometimes feasible to control in the laboratory environment. Also, the variation of bulk resistivity measurement can sometimes root in the stress induced in the sponge, soaked in the solution and attached to both ends of the specimen; thus, water from sponge drains out onto the specimen surface. In addition, the moisture content and the pore structure in the surface layer of the concrete might not be similar to that of the bulk concrete. In contrast to OPC and PLC mixtures, the IQR for GGBS mixtures are small (lowest among the other mixtures) and varies between 0.1 to 0.3 for both un- and CA treated samples. Overall, it is evident from Figure 5.9 that CA treated samples show lower IQR than untreated ones (except for OPGGBS mixes), suggesting smaller variations in the results; thus, more reliable measured data points for these mixtures. Also, for GGBS mixtures, the average ratio of surface vs. bulk resistivity closely matches with proposed value of 1.95 although it is smaller for PLGGBS mixtures than other concrete types due to inadequate development of surface resistivity compared to bulk resistivity at early age. In addition, error spread is the largest for the PLC mixes. Using the ratio of surface vs. bulk resistivity called the geometric factor, bulk resistivity can be indirectly obtained from surface resistivity measurement. This ratio also helps in getting the resistivity of in-situ semi-infinite bridge deck slab from bulk resistivity values of a cylindrical specimen measured in the laboratory.

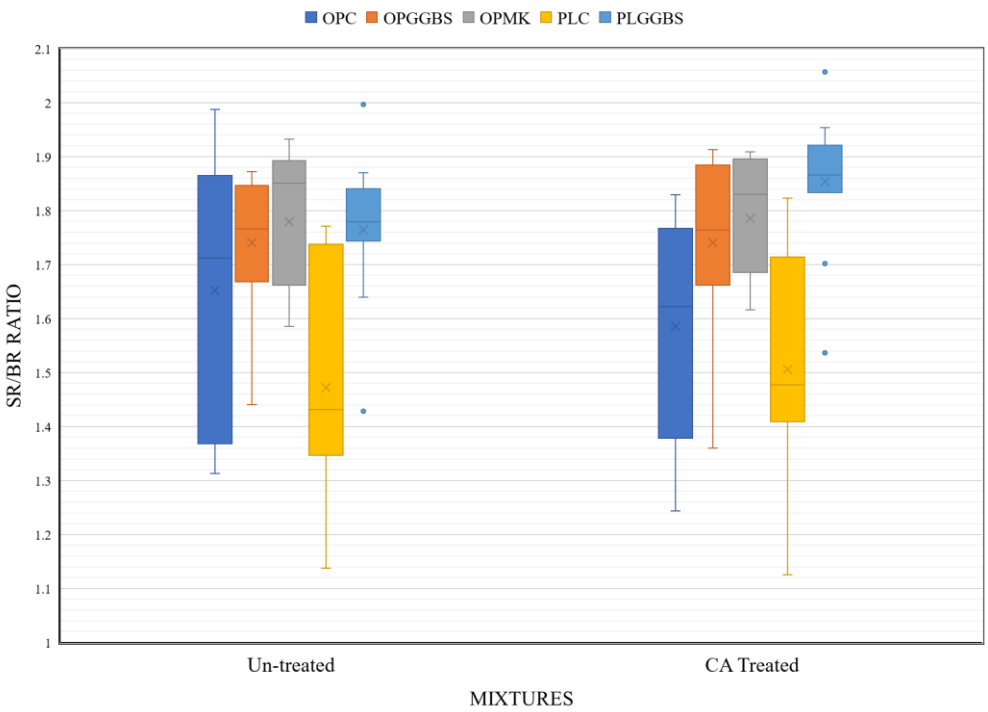

Figure 5.9. Distribution of experimental surface vs. bulk resistivity for all mixtures.

5.1.4.6 Relationship between surface and bulk electrical resistivity

Figure 5.10 shows the relationship between SR and BR measurements for untreated (left) and CA treated (right) specimens at different ages. For sake of better data representation, the figure has been divided into three different groups based on testing days: short-term (early-age) (7-28 days), mid-term (42-112 days), and long-term (640-700 days). The dash lines represent the permeability class limits summarized in Table 5.5. It is evident that only in the long-term, specimens (mostly due to metakaolin and GGBS mixtures) were greater than very low permeability limit. At early age, most specimens showed high penetration class because of inadequate matrix densification. Similar trend has been observed for both un- and CA treated samples, not indicating any difference in resistivity values when CA added. It is interesting to note that BR data shows all mixtures can be classified into moderate to very low permeability group while SR values of similar mixtures indicate high to very low penetration classes. This indicates difference of precision levels between two experimental techniques.

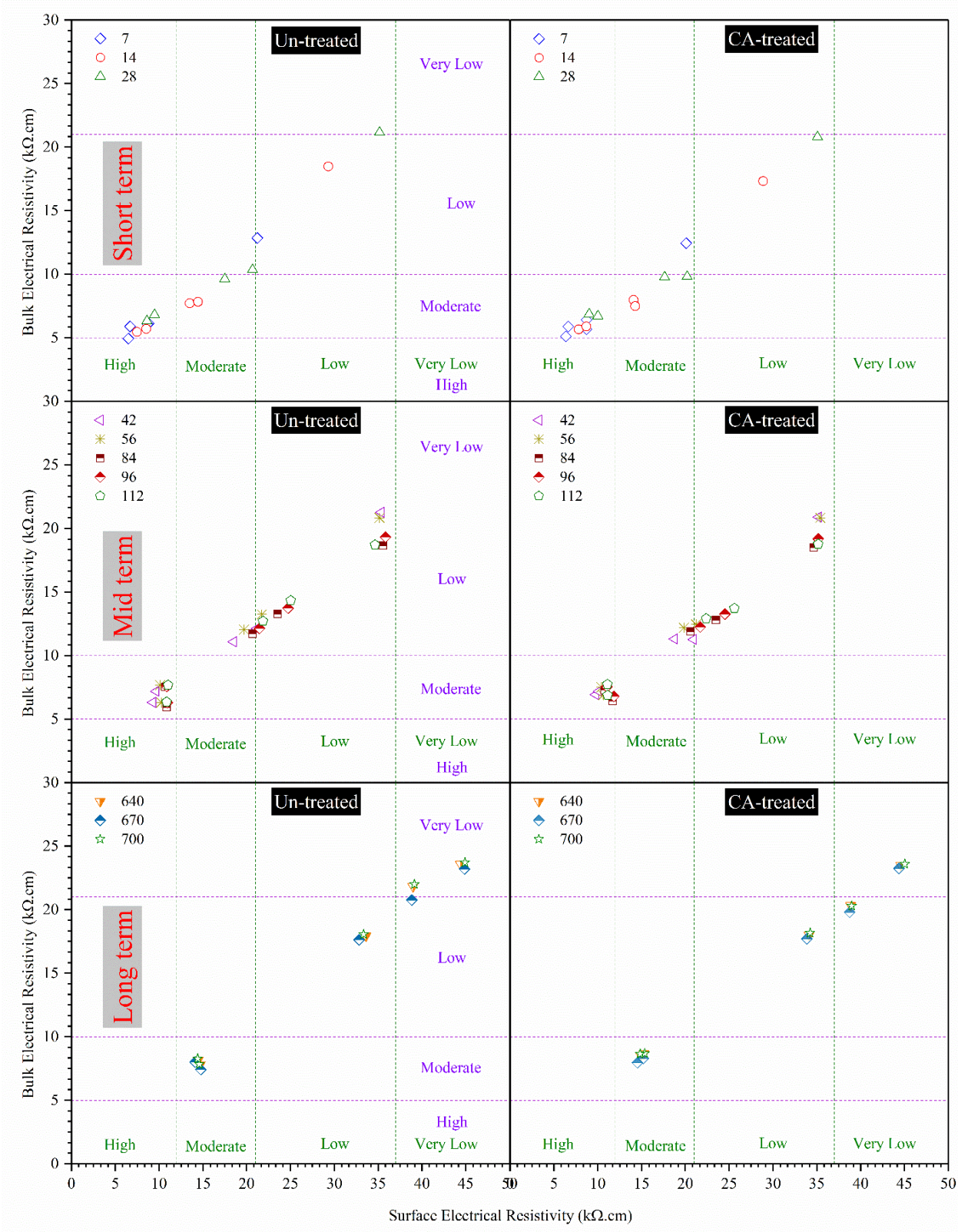

Figure 5.10. Relationship between surface and bulk resistivity at different ages (un-treated mixtures on the left side and CA-treated mixtures on the right side).

Table 5.5. Relationship between permeability class and surface/bulk resistivity.

Chloride ion permeability classification	Surface resistivity (kΩ.cm) (AASHTO TP95-11 [61])	Bulk resistivity (kΩ.cm) [118]
High	<12	<5
Moderate	12-21	5-10
Low	21-37	10-21
Very low	37-254	21-207
Negligible	>254	>207

The best regression fit to the data was of linear type ($BR = slope \times SR + intercept$). Table 5.6 summarizes the intercept, slope, and coefficient of determination (R^2) of linear equation for each age. The ratio of SR over BR for Φ100×200 mm cylinders with 38 mm probe spacing is proposed by Morris *et al*. [119] to be considered as 1.95. In other words, the inverse ratio of BR to SR is $\frac{1}{1.95} = 0.51$. It can be simply observed in the table that the slope of linear fit varies from 0.46 to 0.61 (in average 0.52) which justifies the proposed ratio between SR and BR. Based on the Table 5.6, it can be seen that two measurement techniques correlate extremely well with each other at all ages for both un- and CA-treated samples. The coefficients of determination found were between 0.93 and 0.99. The results agree with findings in other studies, only focused on concrete without crystalline admixtures [117], [118]. From statistical tests, it can be concluded that two test methods can be used interchangeably as they proved to be linearly well-correlated at different test ages. Hence, due to BR measurement's limited application for field evaluation since electrodes access to opposite sides of the concrete element is not possible all the time, the SR measurement technique, as an alternative method, can be used for routine-based quality control of the concrete electrical resistivity during its construction and service life.

Table 5.6. Summary of linear equation parameters (Intercept, slope and coefficient of determination).

Concrete type	Age period	Age (days)	Intercept	Slope	R^2
Untreated	Short term (early-age)	7	1.35	0.54	0.99
		14	0.1	0.61	0.98
		28	0.39	0.58	0.98
	Mid-term	42	0.93	0.55	0.99
		56	1.29	0.55	0.99
		84	0.52	0.52	0.99
		96	0.67	0.52	0.99
		112	1.14	0.53	0.99
	Long-term	640	0.4	0.52	0.99
		670	0.32	0.52	0.99
		700	0.77	0.52	0.99
CA treated	Short term (early-age)	7	0.76	0.57	0.97
		14	0.54	0.57	0.97
		28	-1.8	0.62	0.93
	Mid-term	42	1.74	0.5	0.95
		56	1.33	0.55	0.99
		84	0.67	0.51	0.99
		96	0.82	0.52	0.99
		112	2.1	0.46	0.99
	Long-term	640	1.12	0.49	0.99
		670	0.61	0.5	0.99
		700	1.02	0.5	0.99

To narrow the investigation on SR and BR relationship, Figure 5.11 is plotted to show the effect of two cement types (OPC and PLC) on concrete resistivity at all ages. In the plot, the permeability classes, provided in Table 5.5, are also shown with dash lines. It is evident that there is a strong linear correlation between these resistivity measurement techniques. It is also observed that for both OPC and PLC mixtures, the coefficient of determination values for linear trend line are 0.99 and 0.94, respectively, as seen in Figure 5.11. Over time, PLC mixtures developed greater SR and BR values than that of OPC mixtures. This proves that Portland-Limestone cement can be a better solution and a more sustainable choice for the construction industry as compared to conventional Portland cement because it has a lower carbon footprint with similar or better performance characteristics. During unpublished literature search by the authors, it is worth to mention that no similar study has been found to investigate the effect of PLC on resistivity evolution.

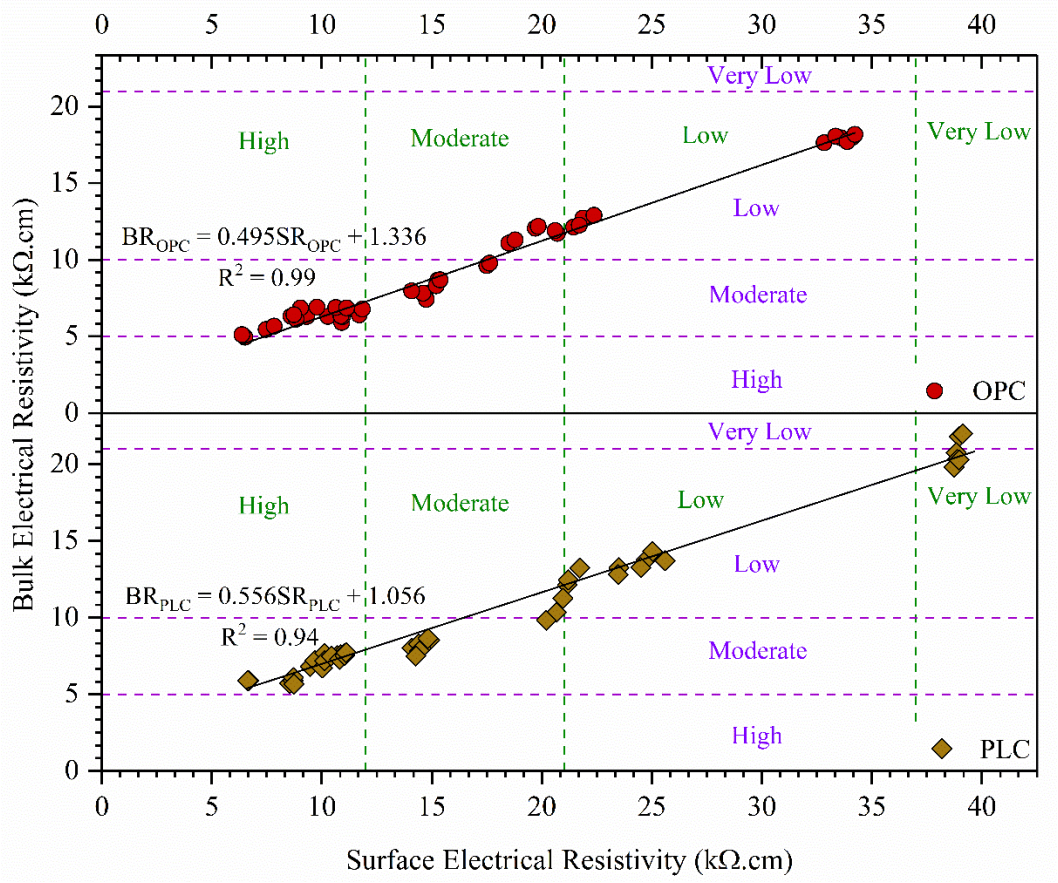

Figure 5.11. Relationship between surface and bulk resistivity for different cement types.

To understand the effectiveness of incorporating GGBS in the mixtures with two different cement types, Figure 5.12 is plotted. This figure shows the relationship between the SR and BR measurement techniques. Similarly, the best trendline adjustment was determined for the data. Both linear trend lines show that when testing Φ100×200 mm cylinders, the BR results are 0.53 and 0.48 times higher than the BR results for OPC and PLC mixtures respectively. Considering only OPC mixtures, other studies [102], [108], [112], [117] reported similar ratio between the SR and BR results for laboratory mixtures. Likewise, the strong coefficient of determination suggests that there is practically no difference of one test over the other to obtain the electrical resistivity. It is also observed that average standard errors of SR and BR measurements were less in PLGGBS mixtures than that of OPGGBS mixtures (both un- and CA-treated) while most errors increase over time for both mixtures.

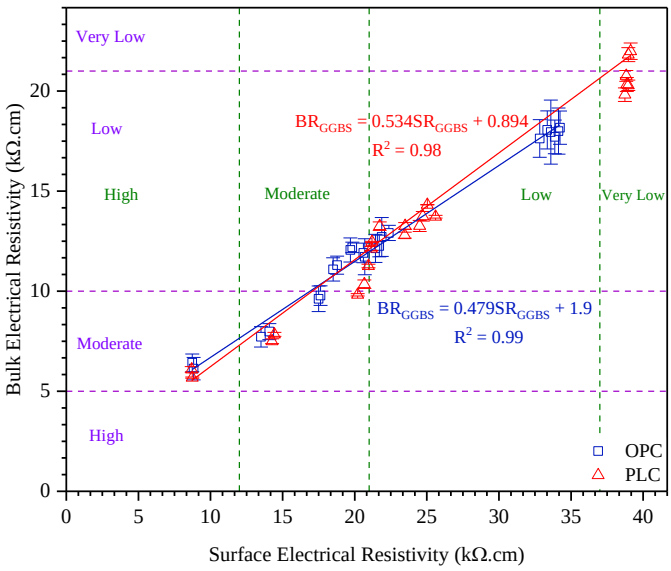

Figure 5.12. Relationship between surface and bulk resistivity for GGBS mixtures.

Figure 5.13 exhibits the effect of metakaolin presence in the mixture on SR and BR values. A strong correlation factor of 0.93 was obtained; similar well-correlated linear trend line to other studies conducted for concrete with metakaolin [102], [108], [112], [117], [118]. Over time, high pozzolanic activity of metakaolin at early age densifies concrete microstructure, consumes more OH ions, results in higher resistivity. The resistivity evolution was observed to be constant after 56 days. It should be noted that OPMK mixtures had the highest electrical resistivity and it was greater for CA treated specimens than that of control mixes.

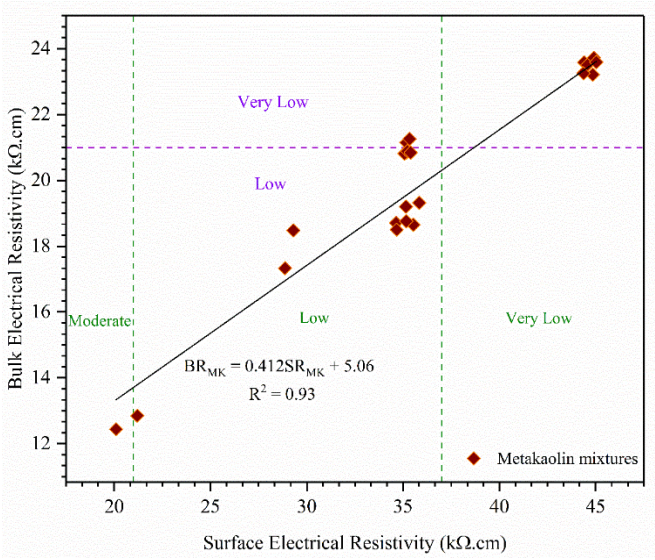

Figure 5.13. Relationship between surface and bulk resistivity for metakaolin mixtures.

5.1.4.7 Effect of temperature on concrete resistivity

The electrical resistivity measurement can significantly be influenced by concrete's moisture content and temperature. Concrete specimens were kept 72 h prior to testing in a water tank at 5, 15, 25, 30, 35, and 50 °C temperatures and tested in SSD condition to investigate the effect of temperature. Figure 5.14 illustrate the temperature effect on BR and SR values, respectively. In agreement with the results reported in the literature [62], [94], [98], [99], as temperature increased, lower resistivity values were observed, mostly because of variation in electron mobility at different temperatures. Electrons move faster in the pore solution when the temperature rises, causing higher electrical conductivity and thus lower resistivity. For instance, the resistivity measured using the same sample can differ by more than two times when temperature of the sample fluctuates between 5 °C to 50 °C. Generally, SR values for CA-treated samples were greater than those of un-treated mixtures when temperature decreased/increased. This indicates less sensitivity of resistivity values of CA added matrix to temperature variation. In the plot, the decrease in both BR and SR is more significant on cylinders with higher resistivity values than those with lower resistivity values. To ensure reliable resistivity measurement, temperature should be kept constant during testing of various specimens at different times.

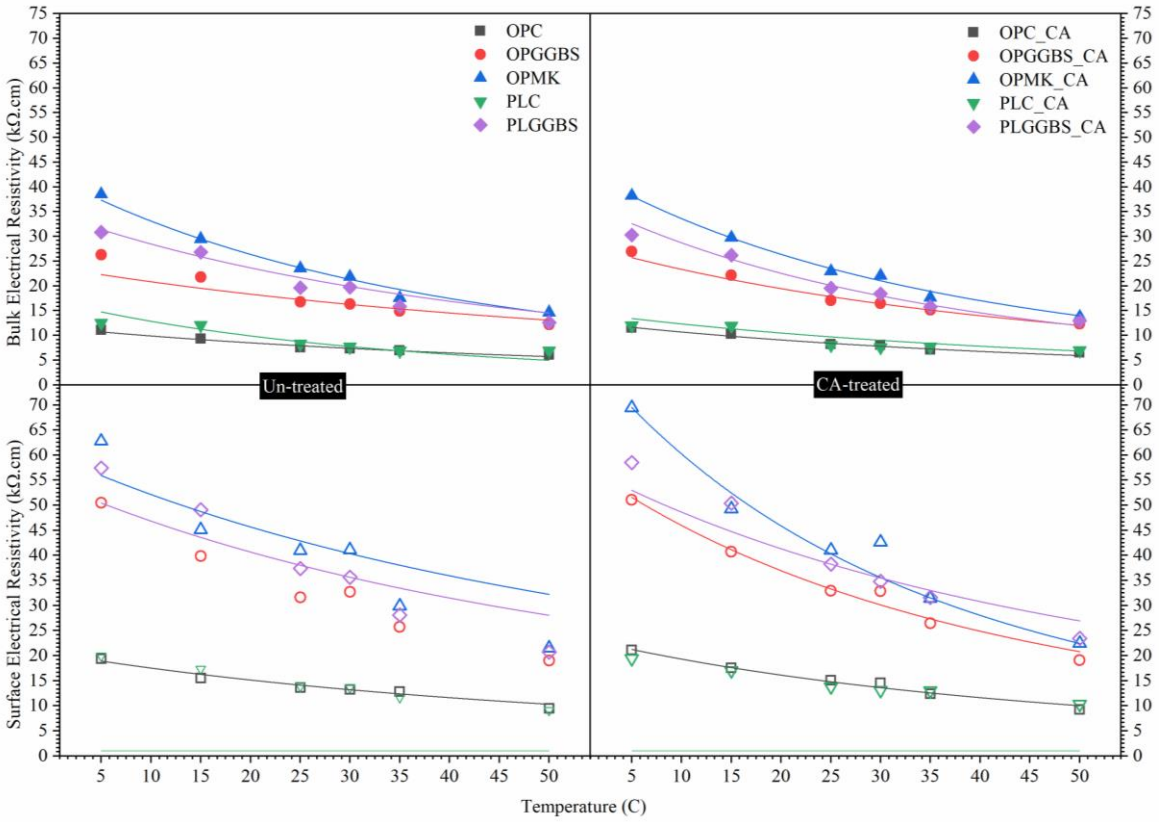

Figure 5.14. Evolution of bulk and surface electrical resistivity with temperature.

The modified version of Arrhenius equation, a popular method to describe the correlation between resistivity and temperature, has been used in this study [98].

$$\rho = A.\exp\left[\frac{E_{a,\rho}}{R.(T+273.15)}\right] \qquad \text{Equation 5.5}$$

where A (Ω.m) is the resistivity when $T(℃) \to \infty$; $E_{a,\rho}$ (J/mol) is the activation energy, mainly determines the temperature sensitivity of concrete resistivity (correlated to the microstructure properties); R is the gas constant (8.31 J/mol/K). For BR and SR dataset, similar to Arrhenius equation, a trend of exponential decay has been observed for all the profiles of resistivity vs temperature. According to Equation 5.5, exponential curve parameters (e.g. activation energy) were obtained for each trend line in Figure 5.14 as summarized in Table 5.7. With regards to BR values, the coefficient of determination (R^2) for all specimens except PLC mixture are higher than 0.95 indicating an excellent fit of the measured values to the Arrhenius law. Contrary to BR values, R^2 value for un-treated GGBS mixtures with PLC cement (equal to 0.75) are the

lowest one when SR values were compared. The activation energy value quantifies the amount of thermal energy needed to promote a mole of ions in the pore solution from equilibrium state to activated state (migrating ions) to carry a current flow under an electric field [98]. With regards to activation energy (E), the mixtures with metakaolin (OPMK) showed the highest value, 17.1 and 17.32 kJ/mol for BR and SR measurement, respectively. Use of SCM in the mixtures showed noticeable increase in the activation energy values relative to control mixtures, similar to McCarter *et al*. study [293]. Overall, activation energy of CA treated samples is generally greater than those of un-treated mixtures. The activation energy for CA treated samples ranges from 11.2 to 17.2 kJ/mol while this value for un-treated cylinders varies from 8.8 to 16.8 kJ/mol.

Table 5.7. Summary of Arrhenius equation parameters ($\boldsymbol{\rho_T = A.exp\left[\frac{E_{a,\rho}}{R.(T+273.15)}\right]}$).

Concrete type	Mix ID	Bulk electrical resistivity			Surface electrical resistivity		
		ρ when $T(°C) \rightarrow \infty$ (A), (Ω.m)	Activation energy ($E_{a,\rho}$) (J/mol)	R^2	ρ when $T(°C) \rightarrow \infty$ (A), (Ω.m)	Activation energy ($E_{a,\rho}$) (J/mol)	R^2
Untreated	OPC	0.1191	10401.98	0.98	0.2429	10069.14	0.96
	OPGGBS	0.4864	8842.56	0.84	0.6798	13106.78	0.92
	OPMK	0.0268	16792.20	0.99	0.0672	15783.02	0.92
	PLC	0.0541	12646.96	0.85	0.0872	12601.80	0.98
	PLGGBS	0.1243	12787.37	0.95	0.7455	9741.10	0.75
CA-treated	OPC-CA	0.0918	11196.61	0.97	0.0975	12445.74	0.98
	OPGGBS-CA	0.1111	12584.96	0.96	0.0761	15067.61	0.93
	OPMK-CA	0.0234	17102.83	0.99	0.038	17328.48	0.95
	PLC-CA	0.0972	11201.72	0.81	0.1995	10593.50	0.98
	PLGGBS-CA	0.0242	16653.56	0.99	0.4128	11220.61	0.89

Figure 5.15 exhibits the relationship between electrical resistivity of un-treated and CA-treated concrete at different temperatures There is strong linear relationship between un-treated and CA-treated mixtures for both SR and BR values (R^2=0.99). This relationship has not been reported elsewhere in the literature. This proves that presence of crystalline admixtures and its chemical composition does not affect the pore solution conductivity although various types of concrete that have different pore solution chemistries were tested at various temperatures. It should be noted that the proposed linear functions can be used to estimate the BR or SR for un- and CA treated concretes interchangeably.

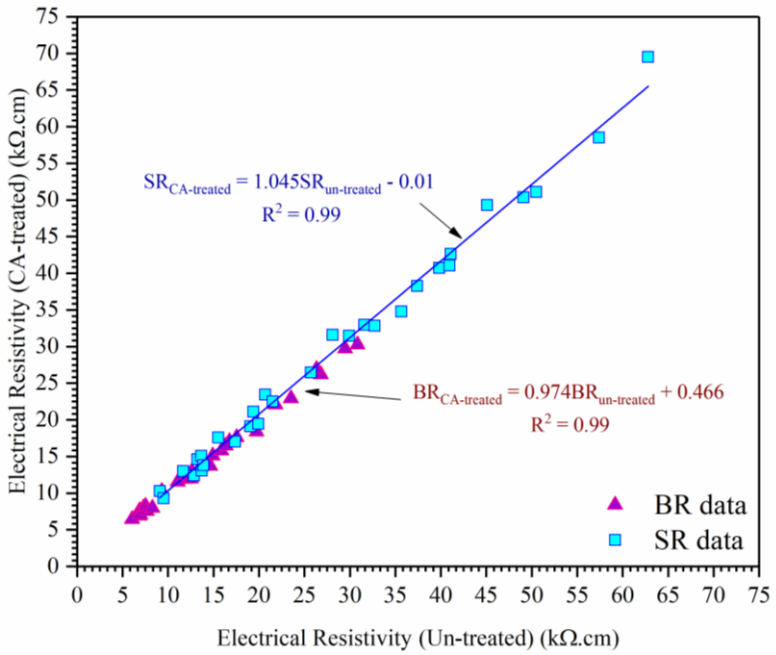

Figure 5.15. Correlation of the electrical resistivites between un-treated and CA-treated mixtures.

Correlations of bulk vs bulk and surface vs surface resistivity were obtained between reference temperature (25 ˚C) and that obtained at 5, 15, 30, 35, 50 ˚C. A linear equation was used ($ER_T = slope \times ER_{25\,^{\circ}C} + intercept$) as best correlation, as presented in Table 5.8. For BR measurements, the lines mostly overlap each other pretty well at different temperatures. As mentioned earlier, the lower the temperature, the higher the resistivity which also can be seen in the table. It was also observed that the slope of trend lines decay as the temperature increases, illustrated in Table 5.8. In addition, it is interesting to note that data are well-correlated where coefficients of determination are greater than 0.96 ($R^2 \geq 0.96$). For mixtures with SCM, the range of variation in the resistivity values are greater than those of control mixtures, indicating greater influence of temperature on these mixtures.

Table 5.8: Summary of linear equation parameters (intercept, slope and coefficient of determination)

Concrete type	Temperature (°C)	Surface Electrical Resistivity			Bulk Electrical Resistivity		
		Intercept	Slope	R^2	Intercept	Slope	R^2
Un-treated	5	-2.19	1.61	0.99	-1.61	1.68	0.99
	15	0.49	1.2	0.96	0.86	1.26	0.99
	30	-0.12	1	0.99	0.1	0.96	0.99
	35	3.27	0.67	0.99	1.55	0.72	0.97
	50	3.01	0.47	0.98	2.41	0.53	0.98

Table 5.8: Summary of linear equation parameters (intercept, slope and coefficient of determination)							
CA treated	5	-5.14	1.74	0.99	-2.42	1.73	0.99
	15	-1.03	1.28	0.99	0.78	1.27	0.99
	30	-0.72	1	0.98	0.06	0.95	0.99
	35	2.08	0.74	0.99	1.75	0.72	0.98
	50	2.43	0.51	0.97	2.81	0.51	0.97

For each concrete mixture, the relationship between SR and BR measurements at all combined temperatures is plotted in Figure 5.16. The overall linear trend from all mixtures is the same and the coefficients of determination are greater than 0.95 for all mixtures except PLC mixtures. This proves that strong linear correlation between SR and BR still exists even though temperature varies. As mentioned before, the ratio of BR over SR for Φ100×200 mm cylinders with 38 mm probe spacing is 0.51 [119]. It is evident that the slope of the linear fit varies from 0.46 to 0.62 for un-treated concrete cylinders and 0.46 to 0.67 for CA-treated samples which closely matches with the proposed BR/SR ratio. For mixtures with SCM, the range of variation in the resistivity values are greater than those of control mixtures, indicating greater influence of temperature on these mixtures, mainly due to their differences in pore solution chemical compositions.

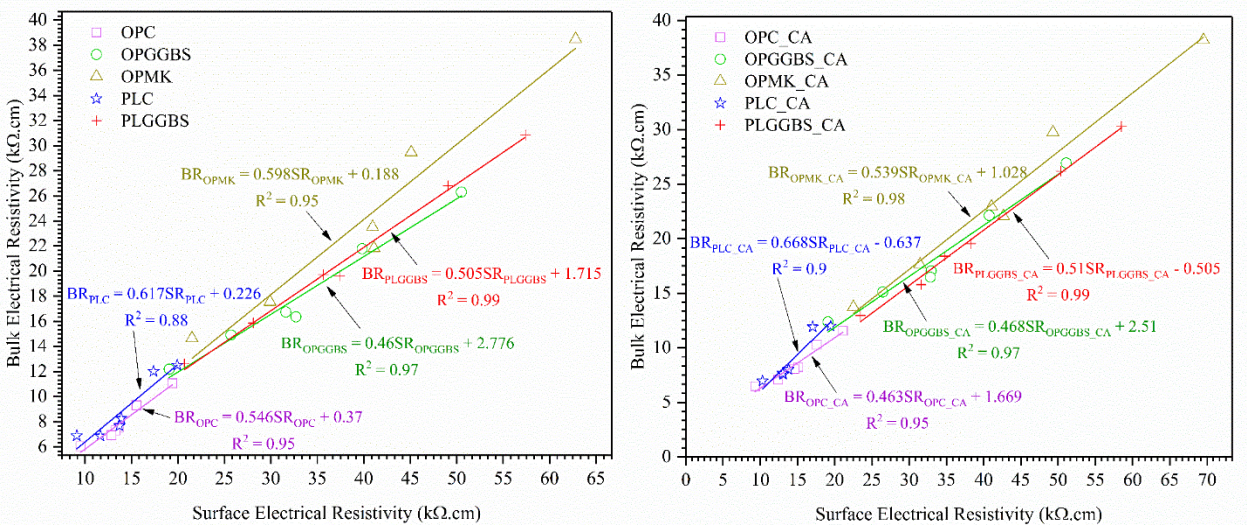

(a) Un-treated **(b)** CA-treated

Figure 5.16. Relationship between surface and bulk electrical resistivity for each concrete mixture at all temperatures.

5.1.4.8 Effect of water content

At the beginning of the testing period, concrete specimens were first weighed and later oven-dried at 110 °C for 24 h to ensure no moisture was left inside. After weighing again, the cylinders were immersed into a water tank with pre-set temperature of 20±2 °C in order to investigate the effect of moisture content on both BR and SR values. Specimens were monitored using SR and BR meter at 2, 6, 12, 24, 48 h after immersion in water until constant weights were achieved. Then, the water content of each specimen was calculated based on measured specimen's weight as follows:

$$WC\% = \frac{\frac{(W - W_D)}{W}}{\frac{(W_{SSD} - W_D)}{W_{SSD}}} \times 100 \qquad \text{Equation 5.6}$$

where $WC\%$ is sample's water content in percentage; W is weight of specimen at time (*t);* W_D and W_{SSD} are specimen weights at dry and SSD conditions. The water content of samples in this study were within 40-80% range after 2 to 48 h measurements. After obtaining samples' water content values, the following equation was used to predict resistivity behavior of concrete cylinders containing various water content level:

$$\rho_{WC\%} = \rho_{100\%} \times \left(1 + \frac{(100 - \mathrm{WC}\%)^{\mathrm{n}}}{(100 - \mathrm{WC_{avg}}\%)^{\mathrm{n}}}\right) \qquad \text{Equation 5.7}$$

where $\rho_{WC\%}$ is resistivity value at certain water content, $\rho_{100\%}$ is resistivity value when sample is in SSD condition, n is an experimental constant value that can be obtained from curve fitting of data, and $\mathrm{WC_{avg}}\%$ is the average of all measured water content. Figure 5.17 shows the SR and BR development during water immersion period for un- and CA-treated cylinders. As seen in the figure, water content of concrete substantially affected its electrical resistivity. Over time, moisture content inside specimen increased, resulting in easier passage of electrical flow; hence, the electrical resistivity observed decreases. Therefore, reduced water content increases the SR and BR for all mixtures especially control mixtures as illustrated in the plot. The parameters related to Equation 5.7, shown by solid lines in the plot, are also summarized in Table 5.9. For all mixtures except MK concretes, coefficient of determinations are greater than 0.9, indicating strong dependency of resistivity on sample's water content and also proficiency of proposed

equation to estimate concrete resistivity with different water content. It is essential to keep the same moisture condition in different mixtures for quality control purposes. Since resistivity is a function of porosity and pore solution, the lower the water content in pore system, the higher resistivity values. For control mixtures, this explains that they have higher porosity level than those of with SCM/CA as their SR and BR values decreased at higher rate when more water penetrated into matrix. For un-treated mixes, the results agree with those reported in other literature [62], [82], [91], [93], [99], [104], [112] and for first time reported for CA-treated mixes in this study.

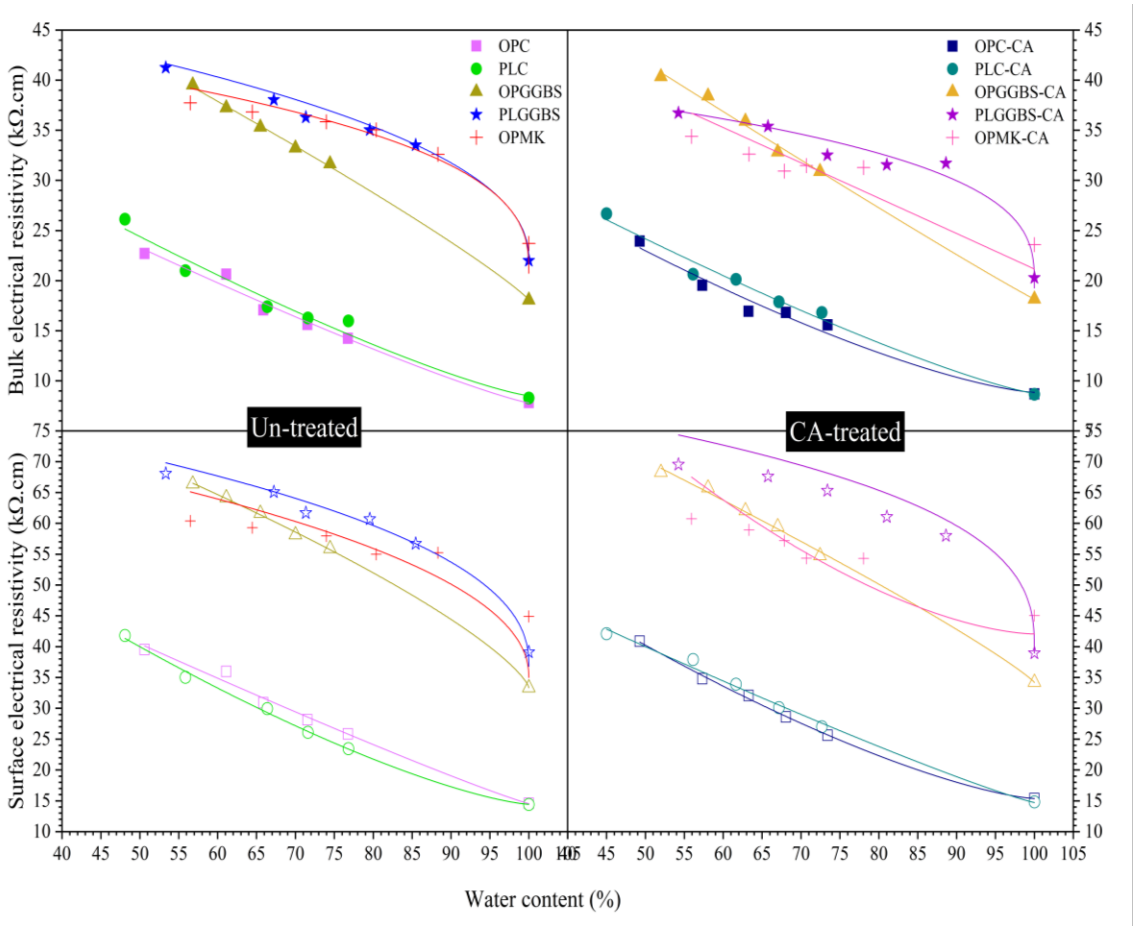

Figure 5.17. Relationship between bulk electrical resistivity and water immersion period **(a)** Un-treated **(b)** CA-treated samples.

Generally, the resistivity of control mixtures after 2 h of immersion were almost two times higher than those of tested at 48 h while for binary and ternary mixes these values were about 1.5 times greater than those tested after 48 h immersion. Such results suggest that the saturation degree of the sample had great

effect on the resistivity, especially in reference mixes. It was also observed that addition of CA in concrete showed similar behavior to un-treated concrete and did not contribute much in enhancing resistivity by the water content more. Additionally, it was attempted to measure SR and BR at dry state but there were significant variations in results, implying that the resistivity of the specimens with little water content cannot be practically detected using this test technique. Generally, SR values showed better correlation with immersion period than those of measured using RCON device. Also, the inclusion of MK and GGBS in the mixes resulted in a decrease in water content effect on resistivity, presumably due to the pore refinement when these minerals were added. In summary, the degree of specimen saturation affected the resistivity of concrete.

Table 5.9. Summary of resistivity equation parameters measured for different water content $\left(\boldsymbol{\rho_{WC\%} = \rho_{100\%} \times \left(1 + \frac{(100-WC\%)^{n}}{(100-WC_{avg}\%)^{n}}\right)}\right)$.

Concrete type	Mix ID	Bulk electrical resistivity (kΩ.cm)			Surface electrical resistivity (kΩ.cm)		
		n	$WC\%_{(avg)}$	R^2	n	$WC\%_{(avg)}$	R^2
Un-treated	OPC	1.16	72.41	0.97	1.09	70.61	0.98
	OPGGBS	0.89	63.95	0.99	0.75	56.49	0.99
	OPMK	0.37	40	0.84	0.47	40	0.2
	PLC	1.24	69.74	0.95	1.36	67.11	0.99
	PLGGBS	0.46	40	0.98	0.44	40	0.96
CA-treated	OPC-CA	1.39	64.32	0.96	1.39	64.61	0.99
	OPGGBS-CA	1.04	61.17	0.99	0.89	52.87	0.99
	OPMK-CA	0.99	40	0.48	1.63	40	0.27
	PLC-CA	1.22	68.6	0.97	1.12	69.19	0.98
	PLGGBS-CA	0.33	40	0.94	0.35	40	0.83

To investigate the correlation between SR and BR values considering all different water content, Figure 5.18 is plotted. For both un- and CA-treated mixes, strong linear correlation has been found. This proves that no matter what saturation degree of specimen is, two resistivity measurement methods are strongly well-correlated. Considering 0.51 as theoretical BR/SR ratio, addition of CA helped in achieving closer value for experimental ratio (0.518) to the theoretical one when compared with un-treated samples (0.594). To conclude, strong relationship between SR and BR measurement techniques has been found for different environmental conditions and concrete mixtures.

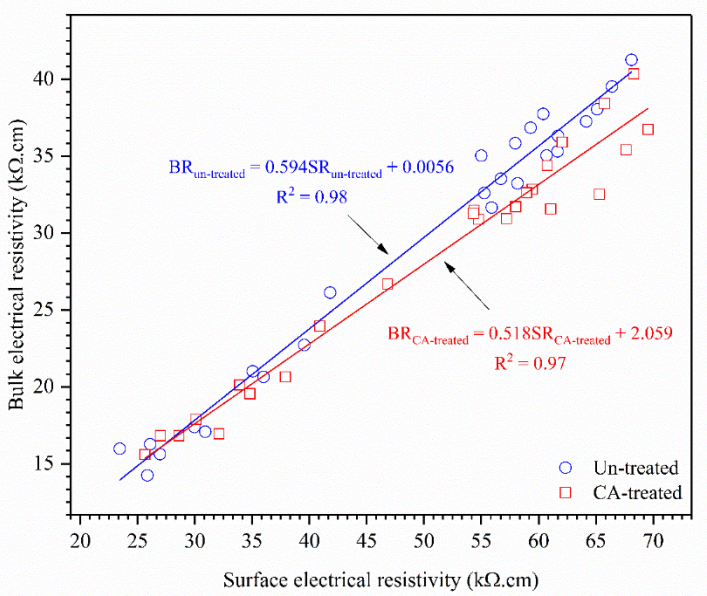

Figure 5.18. Relationship between surface and bulk resistivity for un- and CA-treated mixtures at all water content.

5.1.4.9 Predictive concrete resistivity model

5.1.4.9.1 Model formulation

Based on experimental data gathered from cylinders over a period of time, the surface resistivity model is developed which captures the effect of curing age, SCM, properties of the concrete design mixture and environmental conditions (temperature and water content on surface resistivity of concrete). The SR values can be predicted using multifactor method as follows:

$$\rho_{(t,T,WC\%)} = \rho_{ref(t,T,WC)} \times f_1(t) \times f_2(T) \times f_3(WC\%) \quad \text{Equation 5.8}$$

where ρ (in kΩ.cm) represents the resistivity values at given time (t), temperature (T), and water content ($WC\%$); ρ_{ref} (in kΩ.cm) is the reference resistivity at reference time (t_{ref}) (28 days), 23 ºC temperature (T_{ref}) and 100% water content (WC_{ref}). As discussed earlier, the SR values for a specific mix proportion change with time, temperature and water content. All OPC(-CA) and PLC(-CA) mixes are classified as the control mix in the current model since their resistivity values are very close to each other. Also, OP/PLGGBS-(CA) and OPMK-(CA) mixes are considered as representor of GGBS and Metakaolin groups to predict SCM effects on SR values. In this study, the reference time was considered based on 28 days

curing for control and GGBS mixes and 14 days curing for MK group due to its higher pozzolanic activity in reaching almost constant resistivity values. After employing the curve fitting toolbox of MATLAB software (version 2018a) on the resistivity data, the relationship between control and GGBS/MK mixes is established as follows:

$$\rho_{GGBS} = 0.4544\rho_{ctrl}^{1.6323}\,, \qquad R^2 = 0.96 \qquad \text{Equation 5.9}$$

$$\rho_{MK} = 6.0694\rho_{ctrl}^{0.742}\,, \qquad R^2 = 0.87 \qquad \text{Equation 5.10}$$

where ρ_{GGBS} is the SR of GGBS group; ρ_{MK} is the SR of MK group; ρ_{ctrl} is the SR of control group. The reference SR at an immersion time of 28 days was predicted as a function of the compressive strength by applying regression analysis ($\rho_{28} = 7.155f'_{c\,(28)} - 397.18\,,\ R^2 = 0.89$). It means that concrete compressive strength for all groups can be estimated by taking resistivity values.

The first function, $f_1(t)$, deals with the influence of curing time on the SR values. This function could be estimated using an inverse power function, mentioned previously and is shown below:

$$f_1(t) = \left(\frac{t_{ref}}{t}\right)^{-m} \qquad \text{Equation 5.11}$$

where t represents current time in days, t_{ref} is reference time ($t_{ref} = 28$ days) and m, called aging factor (mentioned earlier), represents the time dependence of the SR values. For the OPC and GGBS groups, the best power function curve showed that $\mathrm{m} = 0.14734$ ($\mathrm{R}^2 = 0.97$) and 0.22057 ($\mathrm{R}^2 = 0.95$) are the best fit for the time element (28 days) for the experimental data expressed in this paper, although, m value for MK group determined at 28 days was not in the acceptable range since coefficient of determination (R^2) was low. Hence, m value of MK group was calculated based on resistivity values taken at 14 days and is equal to 0.11278 (R^2 = 0.89).

The second function, $f_2(T)$, is employed to consider the temperature effect on SR values. As mentioned above, the influence of temperature on electrical resistivity can be incorporated using Arrhenius' law:

$$f_2(T) = \exp\left[\frac{U}{R}.\left(\frac{1}{T} - \frac{1}{T_{ref}}\right)\right] \qquad \text{Equation 5.12}$$

where U (in J mol^{-1}) denotes the activation energy, R is the gas constant (8.314 J mol^{-1} K^{-1}), T presents current temperature in Kelvin and T_{ref} presents reference temperature ($T_{ref} = 296.15$). Using MATLAB curve fitting toolbox and conducting regression analysis on SR data, the activation energy (U) values for all mixture groups were determined (Control: U_{ctrl}=11,640.1 J mol^{-1}, GGBS: U_{GGBS}=14,460.2 J mol^{-1}, MK: U_{MK}=15,384.3 J mol^{-1}).

The third function, $f_3(WC\%)$, takes into account the influence of water content on the resistivity values. No literature has been found to propose a water content function. Hence, regression analysis on the experimental data, reported in the water content section of this paper, was performed in MATLAB to determine a suitable water content function. The $f_3(WC\%)$ function is a power function expressed in Equation 5.13 with R^2 of 0.92.

$$f_3(WC\%) = \left(1 + \frac{(100 - WC\%)^n}{(100 - WC_{avg}\%)^n}\right) \quad \text{Equation 5.13}$$

where $WC\%$ represents the water content of the concrete specimen. In this experiment, the specimens were kept inside curing tank for about 700 days and their WC values were hence assumed to be 100%; and thus $f_3(WC\%)$ function equals to 1. Considering only variation in water content at certain age (700 days) were discussed in previous section. From now on, it is considered that $f_3(WC\%) = 1$ for the proposed model that is summarized for three concrete groups (control, GGBS, and MK). For each representative group, proposed functions are summarized in Table 5.10 and will be validated by experimental data in the following section.

Table 5.10. Predictive concrete resistivity model equations.

Mix group	General formula $\rho_{(t,T,WC\%)} = \rho_{(t_{ref},T_{ref},WC_{ref})} \times f_1(t) \times f_2(T) \times f_3(WC\%)$	$t_{ref} = 28\ days$ $T_{ref} = 296.15\ K$ WC_{ref}=100%
Control	$f_{ctrl}(t) = \left(\frac{28}{t}\right)^{-0.14734}$ $f_{ctrl}(T) = \exp\left(\frac{11640.1}{8.314}\left(\frac{1}{T} - \frac{1}{296.15}\right)\right)$ $f_{ctrl}(WC\%) = 1$	$\rho_{(t_{ref},T_{ref},WC_{ref})} = 9.28\ (k\Omega.cm)$
GGBS	$f_{GGBS}(t) = \left(\frac{28}{t}\right)^{-0.22057}$ $f_{GGBS}(T) = \exp\left(\frac{14460.2}{8.314}\left(\frac{1}{T} - \frac{1}{296.15}\right)\right)$ $f_{GGBS}(WC\%) = 1$	$\rho_{(t_{ref},T_{ref},WC_{ref})} = 18.10\ (k\Omega.cm)$
MK	$f_{MK}(t) = \left(\frac{14}{t}\right)^{-0.11278}$ $f_{MK}(T) = \exp\left(\frac{15384.3}{8.314}\left(\frac{1}{T} - \frac{1}{296.15}\right)\right)$ $f_{MK}(WC\%) = 1$	$\rho_{(t_{ref},T_{ref},WC_{ref})} = 29.09\ (k\Omega.cm)$ $(t_{ref} = 14\ days)$

5.1.4.9.2 Model validation

Comparison to experimental data

The proposed model is validated by using new experimental resistivity data measured at reference temperature ($T_{ref} = 296.15\ K\ or\ 23\ ºC$) and those taken at 700 days with different water temperatures. Equations summarized in Table 5.10 can predict the surface resistivity values for control, GGBS and metakaolin groups. The experimental values of SR versus predicted values calculated from equations in Table 5.10 are plotted in Figure 5.19. The plot indicates that most of the test data especially control group are located within 95% confidence band with adjusted R^2 of 0.99. As a result, the predicted resistivity values fit pretty well with the measured data. Due to high pozzolanic activity of MK, it typically gains its strength and resistivity at early age which leads to constant aging factor over time; thus, m is less dependent on time compared to GGBS and control for this mix. Since proposed model considers the effect of curing age on resistivity for all groups, some tested data in MK group are outliers and are not located inside the confidence

band due to constant aging factor after a certain point. It should be mentioned that this validation is based on resistivity results from laboratory cylinder samples tested for over 2 years. The validation demonstrates that the proposed model is reliable for estimating the resistivity of control, 20% GGBS, or 10% MK concrete containing crystalline admixtures.

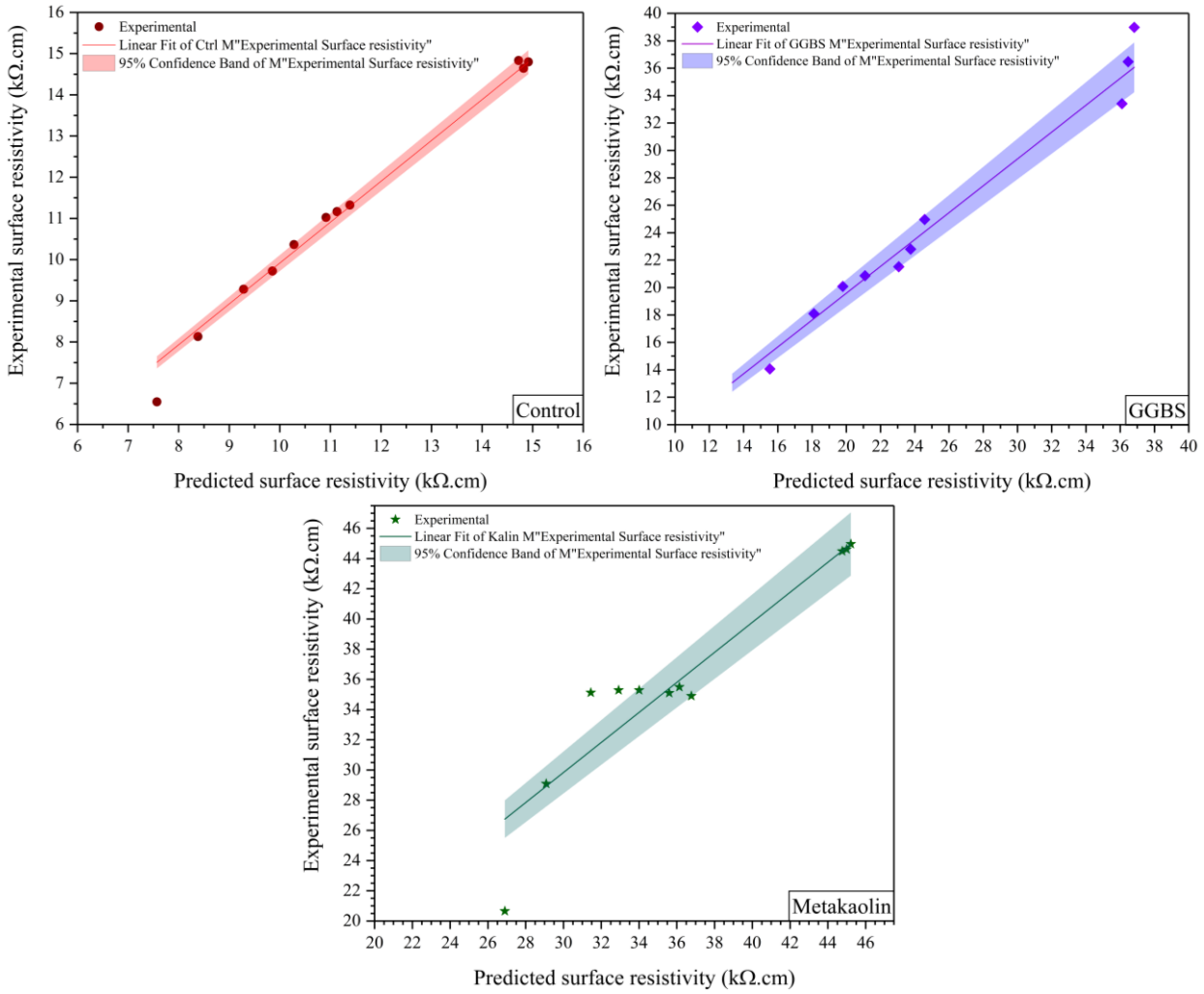

Figure 5.19. Comparison of the predicated and experimental resistivity results of concrete cylinders with w/b ratio of 0.45 **(a)** Control **(b)** GGBS **(c)** MK groups.

Based on the proposed empirical model, Figure 5.20 exhibits the resistivity of three concrete groups over time using both experimental at T = 23 ºC for different ages, at t = 700 days for different temperatures and predicted values considering different temperature profile (T= 5, 15, 23, 25, 30, 35, 50 ºC). As expected, the resistivity increases as concrete ages with higher slope at early period and almost constant rate after a

certain period, especially for MK group. It depends on the type of pozzolanic materials and mix proportions. Also, it can be observed from predictive values that lower the temperature, the higher the resistivity matches with previous findings in this study. As shown in Figure 5.20, the predicted resistivity for reference temperature ($T_{ref} = 23\ ºC$) over curing age correspond reasonably well with actual values taken for all concrete groups. Presence of SCM can lead to overestimating the resistivity values as aging factor becomes gradually constant over time, depending on the type and the content of SCM. To ensure applicability of the proposed model and to validate it with new data points, new resistivity measurements were taken at 30 ºC and 50 ºC assuming sample age is still 700 days. The new experimental data points closely match with the model lines, as shown in Figure 5.20. A minor fluctuation can be observed in the new data set. This is possibly due to the constant aging factor assumption or error during testing operation. As mentioned earlier, several parameters can possibly affect the resistivity readings which needs to be minimized during testing.

Model applicability/limitations

This empirical model is created based on the experimental resistivity values of concrete cylinders kept continuously in water for about two years. Hence, it is more suitable for laboratory verification with similar temperature and water content. In addition, this empirical model is applicable for control, 20% GGBS, and 10% MK concretes with 0.45 *w/b* ratio incorporating PLC cement and CA. No literature could be found that reported similar model for concrete resistivity; hence, it was not possible to verify the proposed model with other similar studies.

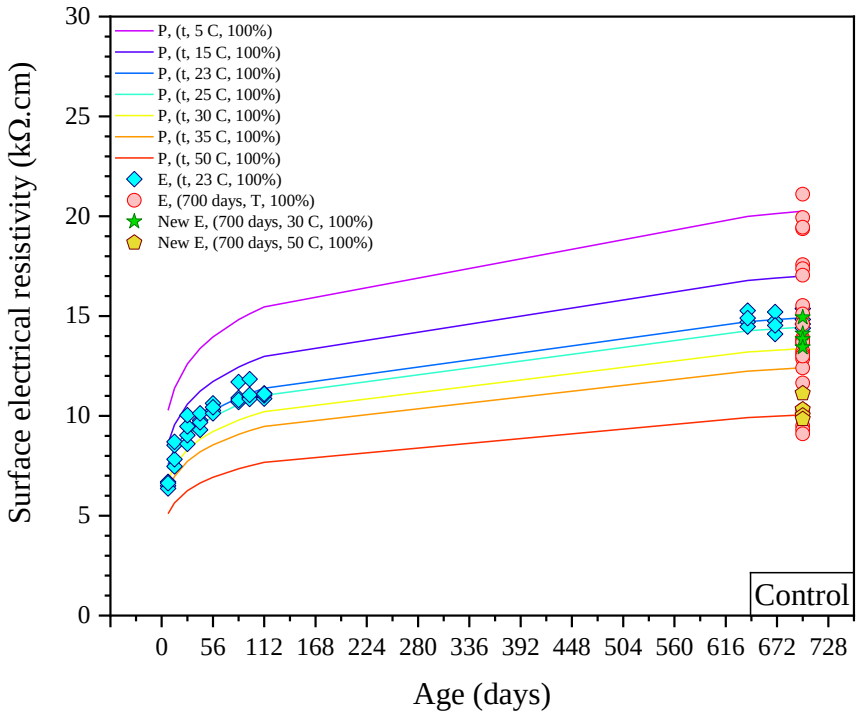
P, (t, 5 C, 100%)
P, (t, 15 C, 100%)
P, (t, 23 C, 100%)
P, (t, 25 C, 100%)
P, (t, 30 C, 100%)
P, (t, 35 C, 100%)
P, (t, 50 C, 100%)
E, (t, 23 C, 100%)
E, (700 days, T, 100%)
New E, (700 days, 30 C, 100%)
New E, (700 days, 50 C, 100%)
Surface electrical resistivity (kΩ.cm)
Age (days)
Control
0
5
10
15
20
25
30
0
56
112
168
224
280
336
392
448
504
560
616
672
728

(a)

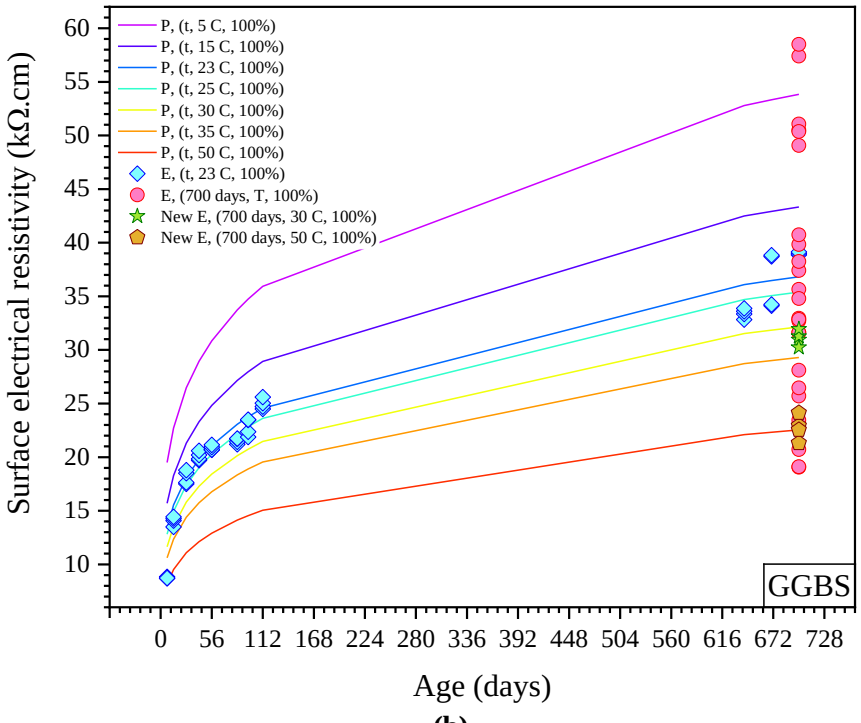
P, (t, 5 C, 100%)
P, (t, 15 C, 100%)
P, (t, 23 C, 100%)
P, (t, 25 C, 100%)
P, (t, 30 C, 100%)
P, (t, 35 C, 100%)
P, (t, 50 C, 100%)
E, (t, 23 C, 100%)
E, (700 days, T, 100%)
New E, (700 days, 30 C, 100%)
New E, (700 days, 50 C, 100%)
Surface electrical resistivity (kΩ.cm)
Age (days)
GGBS
10
15
20
25
30
35
40
45
50
55
60
0
56
112
168
224
280
336
392
448
504
560
616
672
728

(b)

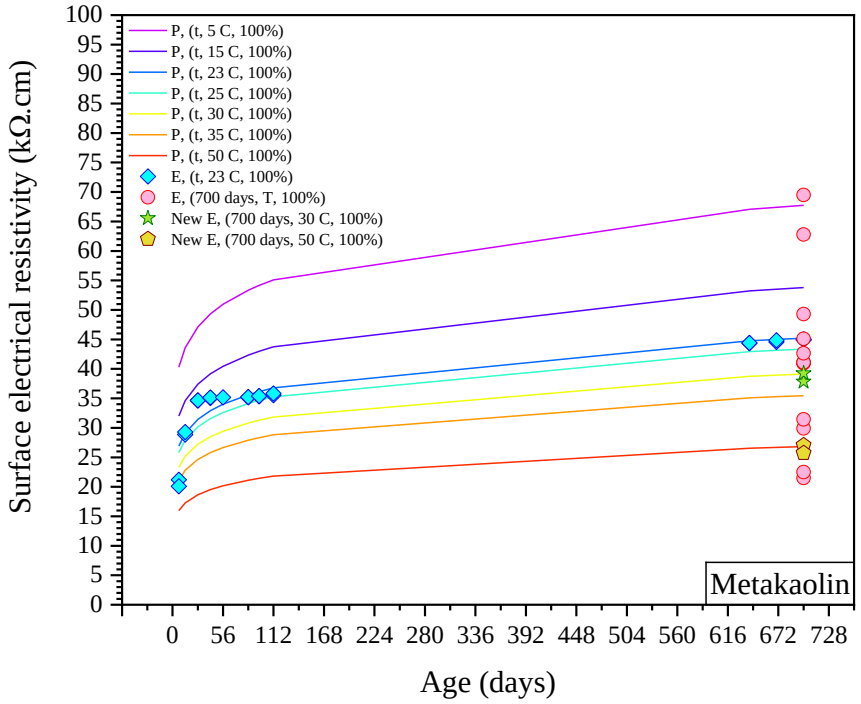

(c)

Figure 5.20. Predictive model and experimental surface resistivity data for **(a)** control, **(b)** GGBS, and **(c)** MK mixes.

5.1.5 Conclusions

From the results obtained, the following conclusions could be drawn in this study:

- Electrical resistivity as an indirect method to evaluate concrete permeability and its chloride diffusivity was utilized. Although CA showed noticeable improvement in healing concrete and decreasing its permeability using direct methods such as DIN 1048-part 5 test according to previous studies, its capability to enhance remarkable resistivity is limited. Strong correlation (R^2 = 0.95) was established between concretes with and without CA which proves limited alternation in resistivity of CA treated system. This is possibility due to dosage of CA used (might be not optimal to alter resistivity of system) or solution chemistry of CA. It is also concluded that resistivity may not be individually a suitable test method to detect performance of system treated with CA and use of additional durability assessment testing (e.g. RCPT) is required. Authors recommend for future work to investigate the pore solution chemistry of CA for detecting any conductive ions and their

concentration which might be possible responsible for limited matrix resistivity improvement compare to control mix. It is suggested that various dosage of CA should be examined to observe how much resistivity of system can increase/decrease. It should be noted that the addition of crystalline admixtures results in a slight decrease in workability and slight increase in strength.

- Electrical resistivity was also proved to be dependent on concrete composition. The presence of SCM in concrete indicated considerable increase in both SR and BR compared to control concrete. Concretes incorporating GGBS or metakaolin have tendency to react more slowly (or rapidly in MK case), consume calcium hydroxide over time, form more CSH gel, densify internal matrix, and also reduce OH^- in the pores' solution; thus, increase concrete electrical resistivity. At end of 2-year testing period, the resistivity of GGBS mixes were very close to that of the MK mixtures while there was initially substantial difference in values for those mixes. For slow reacting mineral admixtures such as GGBS or fly ash, it is suggested to monitor resistivity at later ages since these minerals gain most of their substantial resistivity after 28 days of curing. This can be observed from aging factors established for all mixes in this study.
- PLC cement type when used instead of OPC cement, developed slightly greater SR and BR values over time. Additional limestone amount in PLC cement can provide more $Ca(OH)_2$ in the system which later reacts to form more CSH gel, densifies concrete matrix and eventually results in resistivity improvement. Authors suggest more usage of PLC cement in the construction industry since its manufacturing process has less carbon foot-print with similar or better resistivity evolution as compared to OPC cement. This study is one of the first ones that reports such valuable information on PLC cement and its resistivity performance.
- For all mixtures tested at different ages and environmental conditions, strong relationship ($R^2 > 0.95$) between SR and BR of concretes was drawn for all scenarios. This proves that these testing methods can be simply used interchangeably to obtain concrete resistivity.

- Electrical resistivity of concrete showed also to be under influence of environmental conditions such as temperature variation and degree of saturation. As temperature or water content of concrete decreases, its electrical resistivity greatly increases by more than 2-3 times from reference environmental condition. This is mostly because of variation or accessibility in electron mobility. Specimens with CA additive showed less sensitivity to resistivity variation when temperature decreased/increased as their activation energy values were slightly higher than control samples. Use of SCM in the matrix also indicated significant increase in the activation energy, which proves needs of greater thermal energy than control one to move ions faster from stable state inside matrix.
- Through this study, a concrete resistivity model was developed from lab size cylinders studied for about 2 years which considers effect of age, concrete compositions, and environmental conditions (e.g. temperature). The proposed model can be used as a tool by researcher and industry professionals to estimate resistivity of concrete containing CA and SCM with similar dosage.
- As a part of future work, authors are currently focusing on measuring resistivity of real-world steel reinforced concrete structures with similar mix design and validating the results with current study. Authors also aim to develop a comprehensive model to estimate resistivity evolution in CA treated system for concrete structures in service. Besides that, other durability evaluation techniques will be employed to find any potential correlation between those methods and resistivity technique for concretes containing crystalline admixtures.

5.1.6 Acknowledgement

Thanks are due to the Natural Science and Engineering Research Council of Canada (NSERC) for financial support.

5.2 Long-term Field Investigation of Reinforced Concrete Elements Treated with Crystalline Admixtures Exposed to Simulated Marine Environment

A series of 16 circular hollow reinforced columns were constructed in Civil Engineering Materials Facility (CEMF) at UVic and exposed to a chloride simulated marine environment in order to study the effect of CA and PLC on concrete resistivity and corrosion risk in field specimens. Later, the performance of the 16 specimens were monitored using different NDT methods such as electrical resistivity. More details on column geometry and construction will be discussed in the following sections.

5.2.1 Experimental Program

5.2.1.1 Materials

Ordinary Portland Cement (OPC) and Portland Limestone Cement (PLC) (also referred as Type GUL in CSA A23.1-14 [264]), were investigated in this phase, featuring the same *w/c* ratio and cement contents. The concrete compositions of these two cement types were further modified by adding CA, in powder form, at a dosage equal to 2% by the weight of cement whose behavior is being compared with control specimens (without CA). To target 35 MPa compressive strength which is a typical value for most construction purposes, the *w/c* ratio used was 0.53 in all types of concrete and the mix design is given in Table 5.11. A polycarboxylate Water Reducing Admixture (WRA) was also added into all mixes and its dosage was adjusted in some mixtures to get similar slump (200 mm ± 20 mm). The slump range was chosen to be enough practical to avoid aggregates block the gap between sono-tube mold and steel reinforcement cage.

Table 5.11: Mix design of control and CA concretes.

Material	OPC/PLC	Coarse aggregates	Fine aggregates	Water	CA	WRA
Mix proportions (kg/m^3)	340	1120	820	181	6.8	1.139

5.2.1.2 Specimen design, configuration and geometry

Columns were considered to be approximately 1000 mm (~ 40'') in exterior height with an external diameter of 300 mm (Φ12''). Internal diameter was set to 150 mm (Φ6''). The columns were designed to

be hollow sections in order to use their inside volume as containers for exposure solution (pure water or 3.5% wt. NaCl solution) and also get fairly small cover thicknesses. To get various columns with different rebar cover thickness, steel reinforcements were placed into two different positions from the inside diameter, named type I and II which represent columns with 19.05 mm ($\frac{3}{4}$'') and 31.75 mm ($1\frac{1}{2}$'') rebar cover thickness, respectively. To observe accelerated corrosion occurring in the reinforced columns, such small rebar cover thicknesses were selected. An overview of the final specification of cast specimens is summarized in Table 5.12.

Table 5.12. Specification of columns.

Quantities	Height (mm)		Diameter (mm)		Rebar size (According to CSA standard)	Vertical steel rebar quantities
	Exterior	Interior	Outside	Inside		
16	1000± 100	915 ± 25	300	150	10M	8 (45 degree apart) *

* Three single loops have been considered along the column height to anchor vertical rebar.

The columns' mold was designed using SolidWorks® software and some of its parts were fabricated in house, as illustrated in Figure 5.21.

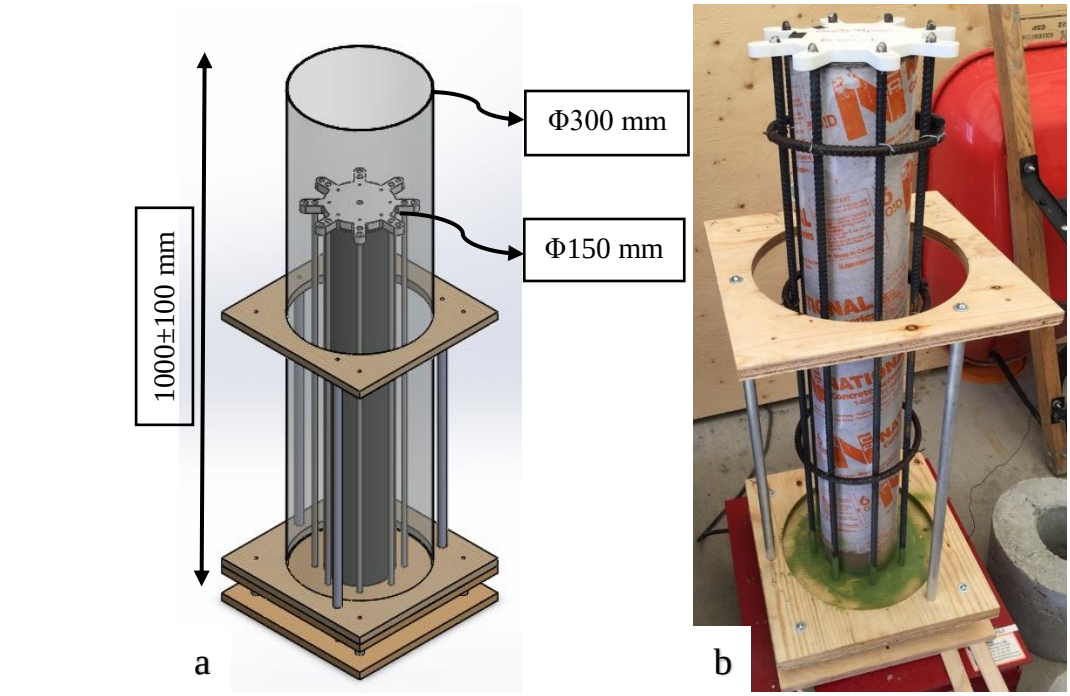

Figure 5.21. Circular hollow-section column **(a)** SolidWorks model **(b)** designed mold.

5.2.1.3 Specimen preparation, curing and exposure conditions

The concretes investigated in this phase were prepared and cast following the standard method described in ASTM C192/C192M-15 [265]. Similar procedures mentioned in section 5.1.3.2 were followed for concrete production and placing. The slump and air content of the concrete mixes were determined for reference purposes, following procedure described in standards ASTM C143/C143M-15a [266] and ASTM C231/231M-14 [267]. Finally, a circular hollow section column and 12 sample cylinders (Φ100×200 mm) (for measuring compressive strength and electrical resistivity) were prepared from each batch of concrete, by placing the column mold on a vibrating table; filling it in four approximately equal layers and compacted by an external vibration for a duration of 60-120 seconds (depending on the workability of the fresh concrete). The cylinders were also cast and cured as detailed in ASTM C192/C192M-15 [265]. After compaction, each column/cylinder was labeled; then covered with a plastic sheet to prevent evaporation and kept overnight in the laboratory.

After 16-24 hours, the concrete columns were stripped from the sono-tube mold and filled up to the brim from inside with tap water for 14 days for curing (Figure 5.22-a). The outside surface of columns was also wrapped with plastic sheet and sprayed with water 2-3 times a day up to 14 days-age. After 14 days, the columns were exposed to air to dry for the next 14 days. Then, once all casting and curing of 16 concrete columns was completed, they were transferred and left outdoors for the exposure period and testing. Also, the 4" × 8" cylinders were cured in a water tank at 23 ± 2 ˚C for 28 days.

After columns were moved outdoors, illustrated in Figure 5.22-b, they were divided in two different exposure conditions. First set involves natural exposure (NE) while they were filled with tap water from inside up to approximately 18 inches (457.2 mm) in height to get three different moisture states (dry, semi-saturated, saturated) along columns' height, whereas the second set involving NaCl solution exposure (CE), was filled up to the same height as NE samples with 3.5% wt. NaCl solution to simulate marine environment and investigate chloride-induced corrosion.

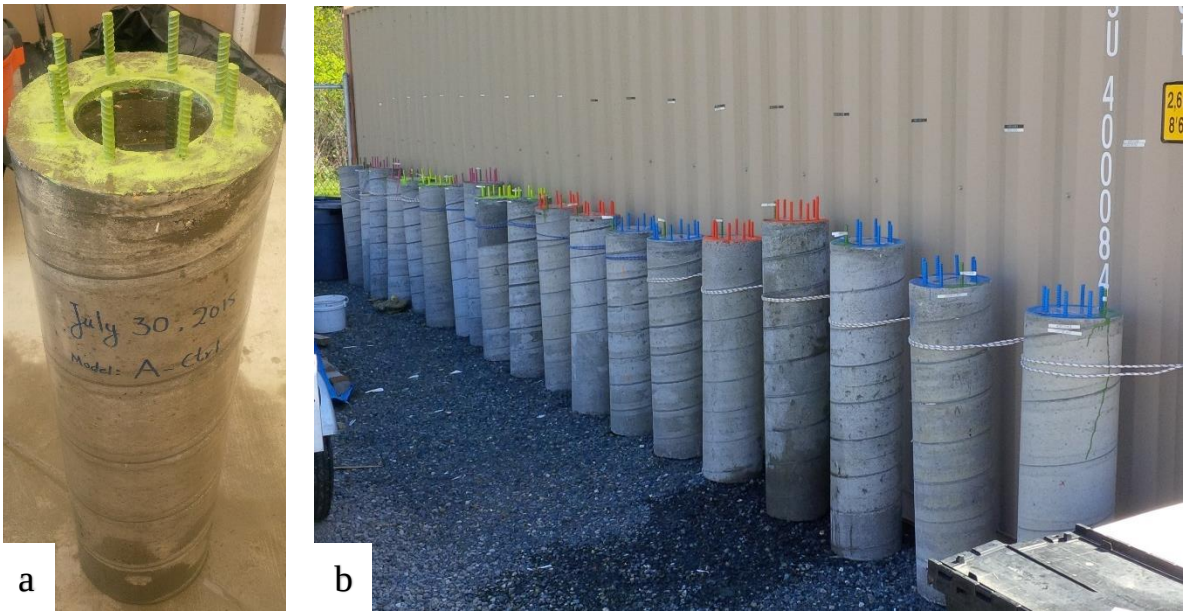

Figure 5.22. Constructed circular hollow-section columns **(a)** curing & **(b)** exposure conditions.

5.2.1.4 Items of investigation

Compressive strength

Three cylindrical specimens with Φ 100×200 mm (Φ 4×8 in.) were tested for all the mixtures on 28 days-age for compressive strength as described in ASTM C39/39M-15a [270]. The average results of three tests were taken as the compressive strength of each mixture and is reported in section 5.2.2.1.

Corrosion potential

There are several electrochemical techniques for monitoring and determining the corrosion potential of steel in RC structures. However, over the period of this study, the most popular method of *in-situ* corrosion testing, known as half-cell potential measurement, was chosen. The use of this method and the interpretation of its results are described in ASTM C876-15 [159]. Readings were taken over 28 pre-defined uniformly distributed spots around the exterior circumference of column and along the height.

Electrical resistivity

In this study, surface electrical resistivity (ρ, in $k\Omega.cm$) measurements were taken from column's surface by commercially available 4 point Wenner probe resistivity meter (Resipod device), manufactured by

Proceq, as detailed in AASHTO TP95 [61]. Then, the values of resistivity (ρ) can be modified based column's geometry as: $\rho = k.R$, where k is a geometrical factor that depends on the shape of the sample. Five resistivity readings were taken at the same positions as corrosion potential and each time, where the four electrodes were moved at least a few millimeters between each reading.

Chloride diffusivity

For this test, a total of 24 cores were extracted through the cross-section of the columns at three locations placed in three moisture states (every 225 mm from column's top surface as shown in Figure 5.23) to measure the chloride content using Germann RCT field testing kit. These locations were chosen in such way to provide information about chloride concentration in individual moisture state region (dry, semi-saturated, and saturated).

5.2.2 Results and Discussion

This section highlights the testing results of columns, prior and after natural exposure (NE) and 3.5% wt. NaCl solution exposure (CE). Results include compressive strength, electrical resistivity (per AASHTO TP95), half-cell corrosion potential (ASTM C876) and chloride diffusion coefficient. The columns are labelled in terms of mix design (OPC/PLC with and without CA), cover depth (I or II) and expected exposure (N or C). Sample IDs are summarized in Table 5.13 by specifying unique code and also an example of one column ID is shown in below.

Table 5.13. Column's identification code.

Cement type		Presence of crystalline admixtures		Exposure conditions		Cover thickness	
Ordinary Portland Cement (OPC)	OP	Treated	CA	Natural exposure (NE)	N	$\frac{3}{4}$,,	I
Portland Limestone Cement (PLC)	PL	Control (No CA)	-	Salt solution exposure (CE)	C	$1\frac{1}{2}$,,	II
Column ID →		OPC cement / NaCl solution exposure / OP-CA-C(I) / Treated with CA / Cover thickness					

For resistivity and half-cell potential measurements, each column was assessed in terms of a defined point height and rotation angle emphasised as Point A – Point G as shown in Figure 5.23. For consistent resistivity

testing, each point (A – G) was aligned with the third probe on the resistivity device. Four separate moisture conditions were considered for each set of electrical resistivity measurement. Data were collected from dry region (Point A & B), semi-saturated region (Point C-D), saturated region (Point E-F), and no rebar region (Point G). The average values of each region (e.g. dry region – Point A & B) around rotation angle will be presented as the equivalent resistivity value for each area. In the following sections, results related to fresh/hardened concrete properties, electrical resistivity, corrosion potential and chloride content will be discussed.

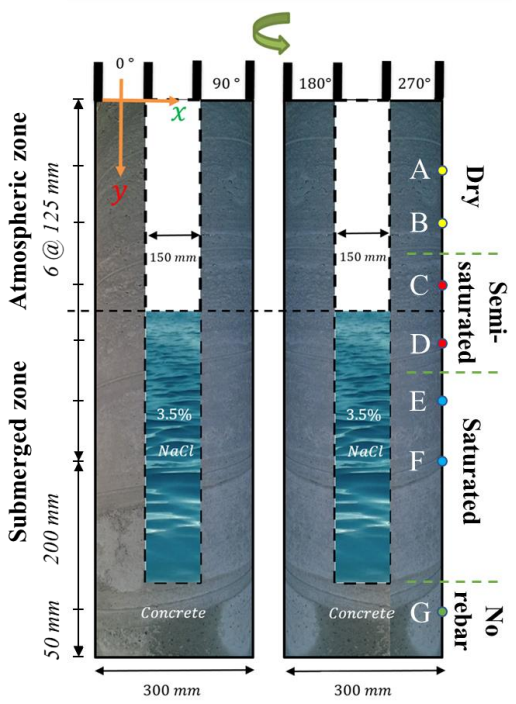

Figure 5.23. Schematic view of testing location and geometry of column exposed to salt solution.

5.2.2.1 Fresh concrete properties and compressive strength results

Fresh concrete properties including slump, unit weight, air content and compressive strength are summarized in Table 5.14. Based on the cement type and columns' treatment (with or without CA), samples are divided into 4 different groups. Group I and III represents mixes with OPC and PLC cement types without additive while group II and IV includes specimens with OPC and PLC treated with CA, respectively. Addition of CA led to a decrease in concrete workability and had a negligible effect on plastic density. As mentioned earlier, slump range was set to be 200±30 mm in order to avoid aggregates from

blocking the gap between the sono-tube mold and the steel reinforcement cage. Compressive strengths of all cylinders range from 34 to 46 MPa which conforms to the target strength and is in line with what is expected for 0.53 *w/c* ratio. Presence of CA in the mix did not result in an increase in concrete compressive strength although it had no negative effects on targeted strength.

Table 5.14. Fresh and hardened properties of concrete mixtures.

Mixture		Fresh properties			Compressive strength	
Group #	Sample ID	Slump (mm)	Air content (%)	Plastic density (kg/m^3)	Average (MPa)	COV (%)
Group I	OP-N(I)	165	3.6	2,388	41.2	2.74
	OP-C(I)	190	4.2	2,405	40.1	1.35
	OP-N(II)	185	4.5	2,384	39.1	3.81
	OP-C(II)	160	2.5	2,391	46.6	4.28
Group II	OP-CA-N(I)	100	4	2,400	38.9	1.21
	OP-CA-C(I)	80	4.5	2,395	40.6	0.74
	OP-CA-N(II)	200	4	2,383	37.6	2.84
	OP-CA-C(II)	135	3.1	2,386	37.3	3.61
Group III	PL-N(I)	200	4	2,402	45.6	2.43
	PL-C(I)	220	3.5	2,397	32.3	0.67
	PL-N(II)	175	3	2,395	42.7	1.74
	PL-C(II)	190	3	2,376	43.7	4.25
Group IV	PL-CA-N(I)	170	3.8	2,381	34.4	1.34
	PL-CA-C(I)	155	4	2,400	38.3	0.93
	PL-CA-N(II)	180	3.2	2,398	36.5	2.46
	PL-CA-C(II)	160	3.5	2,379	40.3	2.83

5.2.2.2 Reinforcement corrosion and half-cell potential results

To investigate the reinforcement corrosion state in the concrete, one of the simplest NDT method was used i.e. half-cell potential (HCP) measurement. Following the ASTM C876 [159] standard procedure, a total of six HCP measurements over 2 years exposure period (0, 3, 6, 12, 18, and 24 months after exposure to NaCl solution) and along columns' height at 7 predefined spots were conducted for all 16 columns. In Figure A8.3-Figure A**8.15** in appendix A (Chapter 8), the results of HCP measurements (E_{corr} in mV) are plotted on a contour map format as a representative for only one column type in each group which was exposed to marine simulated conditions and had $\frac{3}{4}$'' rebar cover thickness (type I). Other HCP contour maps over testing period are also illustrated in appendix A section (Chapter 8) (Figure 8.1-Figure A8.16). Except some

spots in the columns, HCP readings largely indicated absolute potential values less negative than 200 mV in the testing period of 2 years. This in accordance to ASTM C876 [159] norm for Cu-$CuSO_4$ reference electrode, means less than 10% corrosion risk in the vicinity of all reinforcing bars within column. On the other hand, no column indicated corrosion potential values typical of active steel (E_{corr} < -350 mV vs. CSE). No difference in values between treated and un-treated columns was observed. From results obtained for HCP test, it can be concluded that exposure period may not be enough for corrosion initiation that can be detected by this technique. Longer exposure period with continuous HCP monitoring or apply external power supply for corrosion acceleration is suggested to detect time-to-corrosion-initiation, an input parameter for service life modeling of columns.

5.2.2.3 Electrical resistivity

Figure 5.24 represents normalized electrical resistivity values for 4 steel reinforced hollow concrete columns assigned to group I, where a measured electrical resistivity value is the median of five measurements taken at predefined point; then average of 8 different readings in each moisture state was considered as total resistivity value for specific group at certain time. These values for other groups (OPC-CA, PLC, PLC-CA) are shown in the Appendix A section (Figure A8.17-Figure 8.19). To get the normalized resistivity value at each testing time, the measured resistivity value is divided by resistivity of OPC-N(I) mix, considered as the reference electrical resistivity value since this untreated mix represents natural exposure and less rebar cover thickness from inside the hollow column. To consider the effect of different temperatures on the resistivity measurements taken on separate days, the values were normalized by temperature to 25 °C using the Arrhenius law expressed in Equation 5.5. The U/R (activation energy/gas constant) ratio in this equation was considered to be 2900 [294]. When the concrete moisture condition is dry, most of normalized values in each group are close to 1. Only resistivity of OPC-CA-N(I) column at initial reading is 2.5 times higher than that of reference. In some cases, resistivity values were either at most 20-30% higher or lower than the reference value. In this moisture state, $\frac{3}{4}$'' and $1\frac{1}{2}$'' cover thickness (type I and II) and two exposure conditions have closely the same effects on resistivity measurements. Specified

rebar cover thicknesses may not play a role in affecting resistivity measurements in the dry state. This can be mainly due to the restriction of electrical current being passed through the porous medium which does not have connection with the pore network. Hence, rebar is not able to short circuit resistivity measurements when concrete is in dry state. It was observed that presence of CA or PLC did not lead to a significant increase in the resistivity values which these findings were in line with resistivity data taken from laboratory specimens. For a semi-saturated and saturated concrete moisture conditions, comparing different cover thicknesses, mix design and exposure conditions, no trackable trend was observed in resistivity values over time. This is most likely due to uncertain water saturation level and moisture conditions of the pore network as resistivity measurement is highly dependent on saturation degree and chemistry of pore network solution. When considering a saturated moisture condition, a slight increase in resistivity values of all groups over time can be seen in the plot. As mentioned in section 2.2.6.2.1, presence of steel rebar and its mesh density in the concrete typically results in lower resistivity value than virgin concrete. Hence, the resistivity measurements were also taken from the unreinforced concrete area, close to column base, to investigate effect of rebar presence on resistivity values. Except for the PLC group, normalized resistivity values are slightly higher at later age in virgin section of concrete than reinforced region in dry or semi-saturated state due to greater cover thickness and unreinforced area. In the following section, the effects of various components such as cover thickness or moisture conditions on resistivity values of columns will be individually discussed.

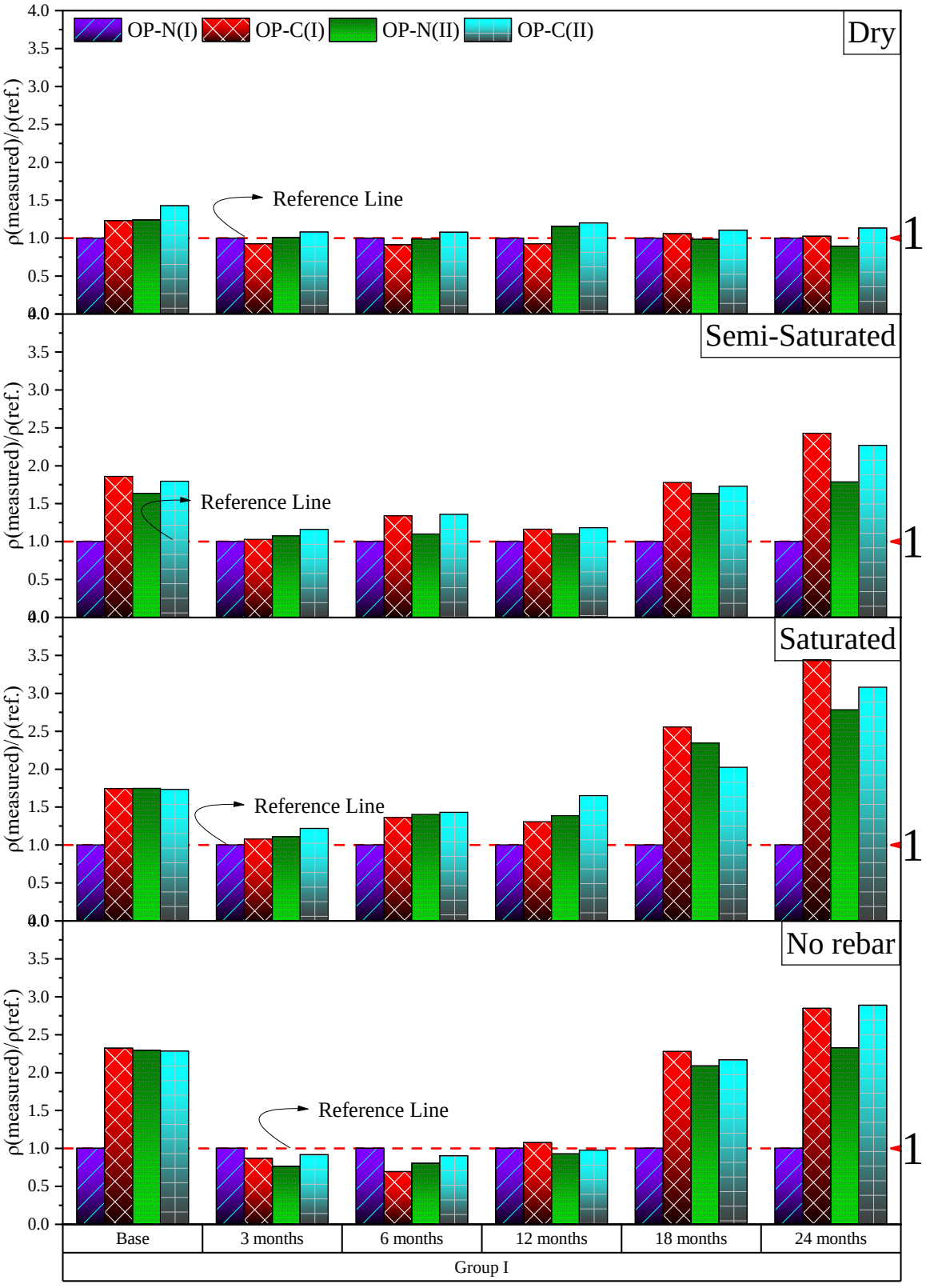

Figure 5.24. Normalized electrical resistivity of group I columns (OPC group without CA).

5.2.2.3.1 Influencing parameters on resistivity measurement

Figure 5.25 shows the influential parameters such as moisture conditions and CA presence on resistivity readings of circular hollow reinforced concrete columns. It was observed that there is only strong linear correlation between two different rebar cover thicknesses ($\frac{3}{4}$'' and $1\frac{1}{2}$") for OPC group (R^2=0.95) while almost no correlation was determined for other groups (Figure 5.25-(a)). Considering effects of moisture conditions and rebar presence on resistivity measurements, there was no detectable trend between different moisture states when compared with no rebar area (R^2<0.7). However, distribution of dry state resistivity data was more scattered than those in semi- and saturated states (Figure 5.25-(b)). It should be noted that specimen's moisture condition has an influence on resistivity measurements as mentioned in section 2.2.6.2.8. Moreover, no linear relationship exists between untreated and CA treated samples (R^2=0.5) (Figure 5.25-(c)) and also between OPC and PLC groups (R^2=0.25) (Figure 5.25-(d)). This indicates that even though a linear relationship between treated and untreated mix was established in section 5.1.4.4 for laboratory cylinders, similar correlation may not be applicable for field specimens due to uncontrolled environmental conditions which may affect concrete properties over time. Poor correlation was also found between two different exposure conditions (natural and 3.5% NaCl solution) in this study (Figure 5.25-(e)).

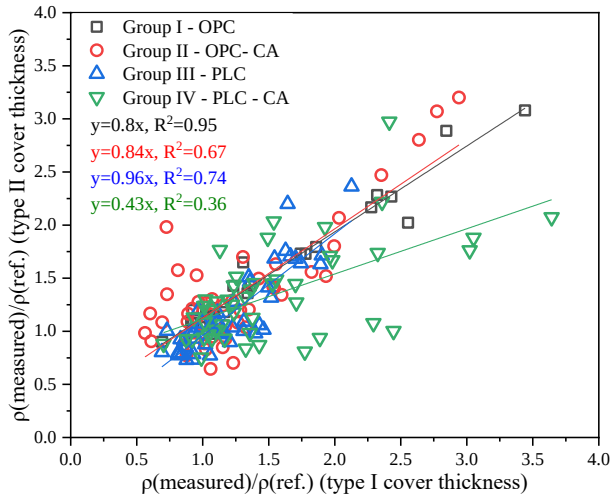

(a) Effect of rebar cover thickness

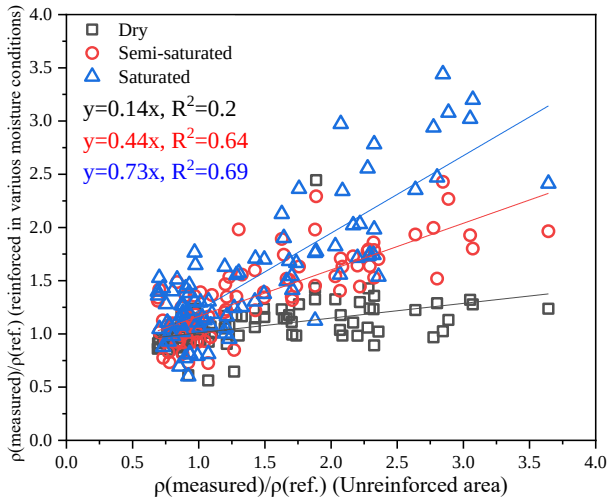

(b) Effect of moisture conditions and rebar presence

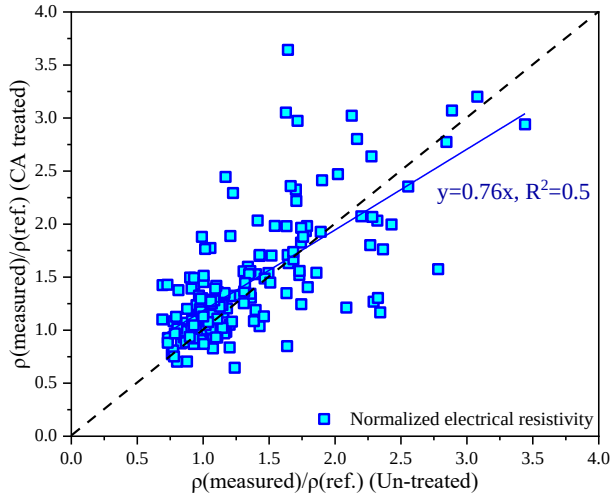

(c) Effect of CA addition

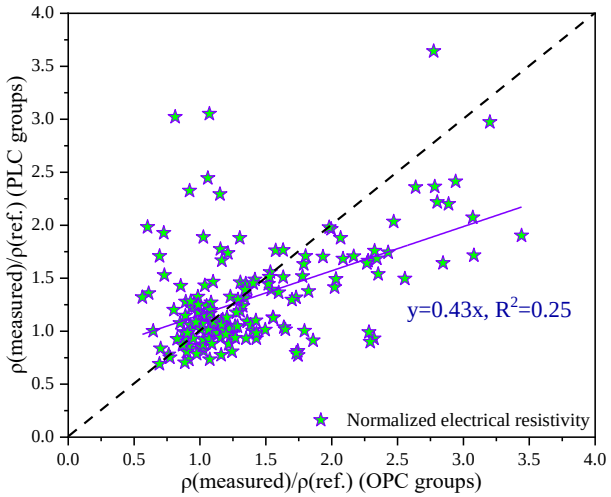

(d) Effect of cement type

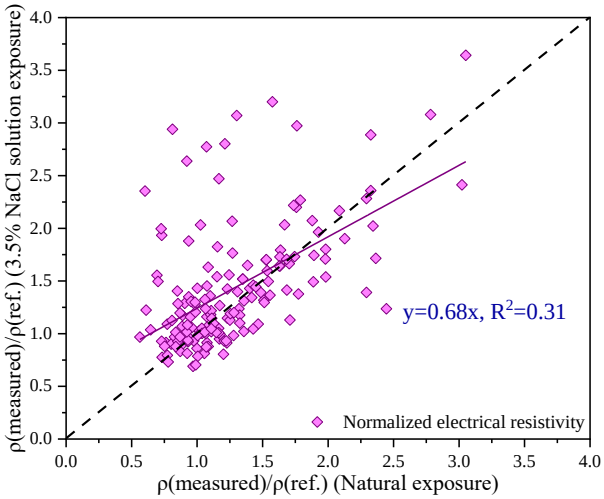

(e) Effect of exposure conditions

Figure 5.25. Influential parameters on electrical resistivity of hollow steel reinforced concrete columns.

5.2.2.4 Chloride content and its concentration distribution

To determine chloride content of the reinforced columns exposed to marine simulated environment for 2 years, 1'' diameter through-depth cores were extracted from three different heights (225, 450, 675 mm from top) at every 90° around the column (total of 12 cores for each column). Since no sign of corrosion was observed using other techniques, the cores were only taken from two columns (OPC-C(I) and OPC-CA-C(I)) in order to only investigate the efficiency of CA addition in corrosive environment. Figure 5.26 shows the measured chloride content in contour format (in percent by weight of cement) at 12 different spots around the column. It should be noted that the chloride samples were taken from portion of the core from

the part that was in contact with salt solution. As expected, measured chloride concentration in saturated zone of individual column indicated the highest values due to direct exposure to NaCl solution while these values were the lowest in the dry zone. For OPC-C(I) and OPC-CA-C(I) columns, the highest average values of chloride content taken from cores inside saturated region are 1.15% and 1.27% weight of cement, respectively. Chloride threshold level, defined as the quantity of chloride at the steel which initiate the corrosion process, could not be determined in this study due to lack of corrosion signs. However, risk of corrosion initiation for the highest measured chloride content in this study, is about 60-70% according to the range defined in Vassie *et al.* study [295]. Also, no reliable difference in chloride content was captured between treated and untreated columns. It should be mentioned that collected data may not be adequate to draw any definite conclusions.

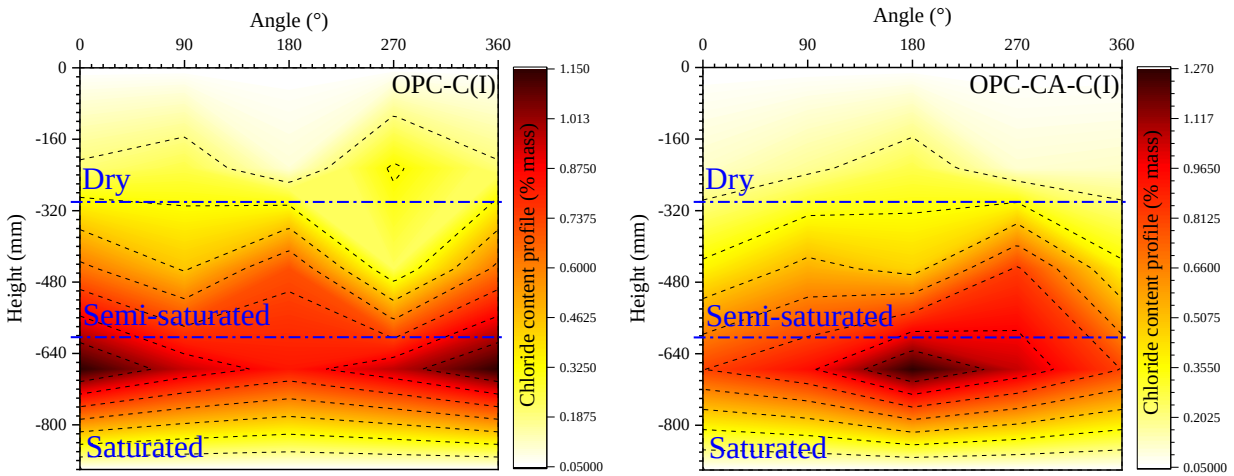

(a) OPC-C(I) column **(b)** OPC-CA-C(I) column

Figure 5.26. Chloride content contour map of hollow concrete columns.

5.2.3 Concluding remarks

The long-term electrical resistivity changes and half-cell potential data for 16 circular steel reinforced concrete columns were determined to fill the technical knowledge gap and provide better understanding about the effects of certain parameters such as addition of CA on concrete durability and steel reinforcement corrosion in simulated real-world conditions. Experimental results showed that electrical resistivity readings were highly influenced by the presence of rebar and concrete moisture conditions. In this study, concrete cover thickness and CA addition into cementitious matrix had a negligible effect on its resistivity.

As over the 2 years, no change was observed, or rebar cover protection was adequate to alter chemical compositions of cement paste or de-passivate steel reinforcement since measured corrosion potential (E_{corr}) values did not indicate high risk corrosion state and were less negative than 200 mV vs CSE. An attempt was made to correlate different influential parameters together although no certain linear relationship was observed between these parameters due to high scattering in collected data. Degree of saturation (or moisture content level) and temperature level of specimen at time of testing had an influence on resistivity measurements, increasing by about 2-4 times higher when specimen's moisture content or temperature is low. Even though it was expected to observe decrease in resistivity values as chloride reaches the embedded rebar surface over 2 years period, corrosion did not occur. This might be due to binding capacity and bound chloride effect which creates discontinuity within the concrete pore network.

Chapter 6 Conclusions and Future Work

The aim of this thesis was to investigate multiscale durability parameters of concretes containing CA and develop a predictive resistivity-based model for them when SCM or PLC presents in the mix. With that general aim in mind, three phases were developed to achieve all proposed objectives. In phase I, microstructural features, morphological aspects, chemical elements and hydration products of cementitious composites treated with CA were studied at submicron level using SEM and STEHM. Phase II includes the results of macro level investigation of durability properties such as chloride diffusivity, corrosion potential, water or chloride permeability and electrical resistivity for specimens with and without CA or PLC. This phase also contributes to knowledge development in the field of concrete electrical resistivity by proposing a predictive model for both CA-treated and control concretes, considering the effect of curing age, SCM or PLC presence, temperature and water content of specimen. Results and recommendations on self-healing and crack-closure capability of concretes modified with CA were included in phase III. A simple empirical model which relates initial water flow rate through crack to crack width was also proposed for control and CA-modified concretes in this phase. In an initial part of this chapter, the main findings of the work completed and conclusions for individual phases are summarized. Considering the findings and limitations of this thesis, several aspects that could potentially serve as a basis for future investigations, are presented in the second part (section 6.2). It should be noted that specific conclusions for various phases were also listed at the end of each chapter.

6.1 Key Findings and Accomplishments

For individual phases, the key findings and scientific contributions of the thesis are presented below

6.1.1 Phase I: Microstructure examination of CA-treated cementitious materials

STEHM analysis of CA particle:

- Using “lifted-out” technique, a fabrication process was developed for FIB the system to manufacture a nano-size CA particle for STEHM analysis. Challenges and advantages of

using unique preparation technique for nanoscale investigation are presented in sections 3.1 and 3.1.3.2.

- Prior to initiating the FIB fabrication process, formation of needle-like crystals was observed in SEM micrographs and also chemical constituents of hydration products were detected by EDX spectrums for 7-days hydrated CA powder (section 3.1.4.1). These results can contribute to better implementations of these admixtures in construction industry.
- A crystalline admixture particle was imaged for the very first time in reported literature by STEHM and its micrographs indicated compact, fine-scale, and homogenous morphology without any substantial defects or dislocation (section 3.1.4.2). To ensure adequate passage of electrons through the sample, the relative thickness map of this particle was obtained which showed particle size between 50 to 80 nm (suitable for STEHM examination) (section 3.1.4.3). Furthermore, SAED patterns for CA particle which provides crystallographic information about particle structure, showed an amorphous structure with evidence of sub-crystalline regions (section 3.1.4.5). Not enough particles and spots of CA were examined by EDX analysis to draw specific conclusions. Unlike cement hydration products, preliminary EDX data showed considerably low Ca/Si ratio in CA particle which needs further investigation to understand significance of this observation (section 3.1.4.6). No study was found to report such microstructure characteristics of crystalline additives. 3.1.4.1

SEM and EDX analysis of CA-treated mortars:

- Four types of crystalline additives, defined in section 3.2.1.1, were examined and compared for the first time in reported literature to provide better insights and in-depth comparison about their microstructures and how needle-shaped crystals (acting as a membrane in the system) form inside the matrix. SEM images illustrated the formation of these crystals inside the hardened cement paste which was not the case for control specimens (3.2.2.1.1).

- These crystals were later examined by X-ray analysis to obtain their chemical elements and were checked for any possible similarity to ettringite's structure or chemical compositions. EDX spectrums indicated that not all, but some CA types have similar calcium, sulfur and aluminum peaks similar to ettringite in their spectrum. These findings can broaden our insights about nature and performance of these crystals inside the cement paste. More samples should be collected with different *w/c* ratio before any conclusive comments about nature of these crystals can be made.
- Hydration products of these mortar mixes did not show any substantial differences between each other and when compared with typical cement hydration phases forming in OPC mortar (section 3.2.2.2).
- To identify different hydration phases and calculate average porosity, image processing was performed on SEM micrographs taken from polished sections of CA-treated cementitious composites. Different hydration phases were quantified and marked according to brightness level of the image and atomic weight of elements. No additional hydration phases other than those presented in typical hardened concrete were identified.
- The average porosity of CA-modified system, calculated from percentage of pore-segmented area (black area in the generated binary image) to the cement paste area, showed slightly lower values than control mortars (less than 10%), indicating possible formation of pore-blocking crystals which results in lower porosity of HCP.

6.1.2 Phase II: Investigation of transport properties and resistivity parameters for concretes containing CA

- Durability of a porous medium is typically controlled by transport of ions into its matrix. To study durability properties of CA-treated concrete, parameters related to different transport mechanisms such as permeation, diffusion and electro-migration were measured experimentally by different test methods and then these parameters were correlated to each

other. The investigated durability parameters include water penetration, chloride diffusivity, corrosion potential, and electrical resistivity of concrete.

- Water permeability coefficient of concretes with CA, determined by following standard procedure reported in DIN 1048-part 5, were 2-3 times smaller than those for control ones, no matter which cement types were used (OPC or PLC). The CA-treated system showed considerable positive effect on preventing water penetration, possibly due to formation of needle-shaped crystals (acting as a membrane) or development of finer microstructure (section 4.4.4). This is one of the major accomplishments through this thesis to identify CA behavior in a cementitious system which was under water permeation transport mechanism. When compared with OPC group, PLC concrete group indicated 20% and 37.5% lower water penetration depth for un- and CA-treated, respectively. Additionally, strong correlation between average and maximum water penetration depth and also between these parameters and water permeability coefficients were found. Comparing the water penetration depth based on maximum or average values, it was observed that standard errors of results were lower for average penetration depth, suggesting reliability of using average depth instead of maximum one as recommended in standards.
- Due its simplicity, rapid-measurement, and low-cost nature of this non-destructive testing technique, concrete electrical resistivity can be a great alternative to time-consuming permeability indicator test methods such as RCP or DIN 1048. Prior to studying the effect of CA on concrete electrical resistivity, comprehensive literature review has been done to identify the effect of influential parameters such as reinforcement presence or environmental conditions on concrete resistivity and its relationship with other durability parameters. Through this published review, research and industry knowledge gap was identified on understanding the effect of following parameters: rebar or crack presence, temperature, SCM, chemical admixtures, and water saturation degree on concrete resistivity; also, the gap was found in grasping the correlation of this parameter and other

durability properties (especially for in-service field concrete elements). Hence, through this thesis, an attempt was made to investigate the influence of the abovementioned parameters on concrete resistivity and possibly close gaps between current research and industry knowledge. Generally, addition of CA showed negligible effects on resistivity values even when SCM or PLC presented in the mix with 0.53 or 0.42 *w/c* ratio. It was hypothesized that either dosage of CA added to concrete was not sufficient to result in resistivity alteration and/or resistivity measurement method may not be a suitable technique to indirectly provide information about the CA's role in decreasing permeability. This is in contrast with results obtained from water penetration tests which showed significant improvement.

- Concretes incorporating GGBS and MK respectively indicated almost 2.1 and 2.9 times higher resistivity values than OPC concretes, mainly due to reduction in matrix porosity and alteration of pore solution chemistry. This is the first study which reports resistivity data on interaction of CA, PLC and SCM. PLC concrete showed relatively similar resistivity values to OPC group. About 10% additional limestone in PLC did not appear to change in resistivity values.
- Strong linear correlation was observed between SR and BR measurements, indicating the use of these resistivity test methods interchangeably (section 5.1.4.6). Considering the effect of curing time, aging factor was introduced for specimens containing CA, SCM and PLC which can be used to predict long-term behavior of different mixes. When specimens' water temperature was increased from 5 °C to 50 °C, the resistivity values almost increased two times (section 5.1.4.7). This suggests that resistivity is highly influenced by concrete's temperature due to faster ion-mobility inside pore solutions. The resistivity values also showed noticeable variation when specimens water content was altered (section 5.1.4.8). Equations were proposed which considers the effect of temperature, curing time, and water content level.

- Predicative long-term empirical resistivity-based model which considers the effect of curing time, SCM, environmental conditions, has been developed through this study for concrete specimens treated with CA (section 5.1.4.9). Most of experimental data points were placed in 95% confidence band when compared with proposed model data values. This model can be a good predictive tool to estimate long-term resistivity behavior of cement-based system incorporating MK and GGBS.
- Resistivity data, taken from 16 hollow-section steel reinforced concrete elements exposed to natural and marine simulated environment for over 24 months, were highly affected by concrete's moisture content, surface temperature, and rebar presence (section 5.2.2.3). Three different moisture states were investigated in this study which showed that dryer the concrete pores, the higher the resistivity readings. This is mostly due to less availability of solution in pores which may not allow passage of electrical current. Presence of steel reinforcement led to decrease in resistivity values. According to corrosion risk ranges defined in ASTM C876 [159], corrosion potential (E_{corr}) results of concrete columns did not indicate any sign of corrosion in steel reinforcement over 2 years exposure to NaCl solution. Chloride profile mapping of CA-treated and control columns were also obtained to study the effect of CA on chloride ion penetration which showed quite similar trend for both concrete types.
- The average cumulative charge, taken from RCP test to provide indirect information about concrete chloride diffusivity, was 5538 Coulombs for OPC at 28 days, and was approximately 25%, 35%, and 30% higher for OPC-CA, PLC, and PLC-CA, respectively (section 4.4.3). This value was 2315 Coulombs for OPC at 56 days, roughly 5% higher than OPC-CA, and was 11% and 19% lower for PLC and PLC-CA mixes, respectively.
- It was found that the specimen curing time and presence of CA can affect the penetration of chloride ions into different depth of concrete cylinders exposed to NaCl solution for 6 months. Improvement in chloride penetration depth from further water curing is mostly

due to gradual enhancement of the extent of the concrete hydration, density and inner pore structures with time. Implementing Fick's second law, equations were proposed in the thesis to predict chloride content of CA-modified and control (OPC or PLC) specimens cured for 28 and 56 days (section 4.4.5).

- Through this thesis, an attempt was made to find a correlation between concrete resistivity and durability parameters. Lack of strong linear correlation between resistivity, water permeability, RCPT data, and apparent chloride diffusion coefficient was observed (section 4.4.6). This poor correlation could be valuable to understanding that having a certain durability parameter such as resistivity does not necessarily indicate or predict the complete behavior of the concrete system (e.g. water permeability) when exposed to different transport mechanisms.

6.1.3 Phase III: Investigation of self-healing and crack-closure capability for concretes modified with CA

- Efficiency of CA-based concretes in self-healing process was investigated using an innovative technique [1] to determine whether presence of CA accelerates the crack sealing process or speeds up the reduction in water flow (section 4.4.7). Results showed that CA-modified concretes were able to reduce water flow by a higher rate than control specimens. Full water-flow termination was observed in CA-treated concrete within the chosen test period while full water-flow stoppage was not observed in control samples. PLC self-healing potential is reported for the first time in this work.
- The experimental values of initial water flow measured at the beginning of self-healing test versus the corresponding initial average crack width were correlated. The following equation was proposed to correlate these parameters: $q = 6.81 \times CW^3$. The obtained results corroborate with some of the results reported in the literature for natural healing.

6.2 Recommendations for Future Work

Based on the findings of this thesis, the following recommendations can be drawn for future:

6.2.1 Phase I: Microstructure examination of CA-treated cementitious materials

- Study of the effect of SCM or fiber addition and *w/b* ratio on microstructural features, morphology and hydration products of fracture surface and polished sections of CA-treated cementitious composites compared to control specimens using SEM.
- Develop a nano-structure model by performing additional FIB fabrication process and further TEM analysis of CA particles.
- Study of the effect of matrix cracking on formation of needle-shaped crystals and self-healing properties of different cementitious composites.
- Conduct X-ray Diffraction (XRD) analysis on CA-treated mortar to obtain information about its chemical compositions and possible further improvement of this admixture.

6.2.2 Phase II: Investigation of transport properties and resistivity parameters for concretes containing CA

- Verification of the resistivity-based model for a wide range of concrete types and environmental conditions is proposed.
- Study of the effect of concrete cracking on electrical resistivity, corrosion potential, self-healing and corrosion rate in the presence of CA.
- Develop a numerical resistivity model for CA treated concrete using COMSOL software which considers the effect of curing time, SCM, temperature and water content level.
- Collect more resistivity data from field concrete elements and correlate them with laboratory data exposed to different environmental conditions. Field data was considered in just a few investigations and thus, it is of high interest to gather more field experience.
- Further investigation on resistivity data to understand how much time is needed for water to infiltrate into the concrete to obtain constant moisture level through bulk specimens and

how multilayered resistivity systems (e.g. concrete with carbonated layers) can be experimentally measured.

6.2.3 Phase III: Investigation of self-healing and crack-closure capability for concretes modified with CA

- XRD or EDX analysis of CA-based healing products to obtain chemical and mineralogical compositions of the healing materials and their evolution with time under different conditions.
- Integration of resistivity measurement technique into self-healing apparatus to gather live data on resistivity enhancement of different concrete types during crack healing process.
- Investigation on the strength or durability recovery of the fiber reinforced composites containing SCM and crystalline additives.

Chapter 7 Bibliography

[1] R. Gupta and A. Biparva, "Innovative Test Technique to Evaluate 'Self-Sealing' of Concrete," *J. Test. Eval.*, vol. 43, no. 5, p. 20130285, Sep. 2015.

[2] E. Cailleux and V. Pollet, "Investigations on the development of self-healing properties in protective coatings for concrete and repair mortars," in *In Proceedings of 2nd International Conference on Self Healing Materials*, Chicago, IL, USA, 2009.

[3] Mark Yunovich and Neil G. Thompson, "Corrosion of Highway Bridges: Economic Impact and Control Methodologies," *Concr. Int.*, vol. 25, no. 1, Jan. 2003.

[4] J. Woudhuysen and I. Abley, *Why is construction so backward?* Chichester ; Hoboken, NJ: Wiley-Academy, 2004.

[5] K. Van Tittelboom and N. De Belie, "Self-Healing in Cementitious Materials—A Review," *Materials*, vol. 6, no. 6, pp. 2182–2217, May 2013.

[6] J. Y. Wang, D. Snoeck, S. Van Vlierberghe, W. Verstraete, and N. De Belie, "Application of hydrogel encapsulated carbonate precipitating bacteria for approaching a realistic self-healing in concrete," *Constr. Build. Mater.*, vol. 68, pp. 110–119, Oct. 2014.

[7] B. Boh Podgornik and B. Sumiga, *Microencapsulation technology and its applications in building construction materials*, vol. 55. 2008.

[8] K. Van Tittelboom, N. De Belie, D. Van Loo, and P. Jacobs, "Self-healing efficiency of cementitious materials containing tubular capsules filled with healing agent," *Cem. Concr. Compos.*, vol. 33, no. 4, pp. 497–505, Apr. 2011.

[9] Z. Yang, J. Hollar, X. He, and X. Shi, "A self-healing cementitious composite using oil core/silica gel shell microcapsules," *Cem. Concr. Compos.*, vol. 33, no. 4, pp. 506–512, Apr. 2011.

[10] V. Wiktor and H. M. Jonkers, "Quantification of crack-healing in novel bacteria-based self-healing concrete," *Cem. Concr. Compos.*, vol. 33, no. 7, pp. 763–770, Aug. 2011.

[11] D Palin and V Wiktor and H M Jonkers, "A bacteria-based bead for possible self-healing marine concrete applications," *Smart Mater. Struct.*, vol. 25, no. 8, p. 084008, 2016.

[12] J. Wang, K. Van Tittelboom, N. De Belie, and W. Verstraete, "Use of silica gel or polyurethane immobilized bacteria for self-healing concrete," *Constr. Build. Mater.*, vol. 26, no. 1, pp. 532–540, Jan. 2012.

[13] K. Van Tittelboom, N. De Belie, W. De Muynck, and W. Verstraete, "Use of bacteria to repair cracks in concrete," *Cem. Concr. Res.*, vol. 40, no. 1, pp. 157–166, Jan. 2010.

[14] A. Al-Otoom, A. Al-Khlaifa, and A. Shawaqfeh, "Crystallization Technology for Reducing Water Permeability into Concrete," *Ind. Eng. Chem. Res.*, vol. 46, no. 16, pp. 5463–5467, Aug. 2007.

[15] K. Sisomphon, O. Copuroglu, and E. A. B. Koenders, "Self-healing of surface cracks in mortars with expansive additive and crystalline additive," *Cem. Concr. Compos.*, vol. 34, no. 4, pp. 566–574, Apr. 2012.

[16] L. Ferrara, V. Krelani, and M. Carsana, "A 'fracture testing' based approach to assess crack healing of concrete with and without crystalline admixtures," *Constr. Build. Mater.*, vol. 68, pp. 535–551, Oct. 2014.

[17] M. Roig-Flores, S. Moscato, P. Serna, and L. Ferrara, "Self-healing capability of concrete with crystalline admixtures in different environments," *Constr. Build. Mater.*, vol. 86, pp. 1–11, Jul. 2015.

[18] M. Roig-Flores, F. Pirritano, P. Serna, and L. Ferrara, "Effect of crystalline admixtures on the self-healing capability of early-age concrete studied by means of permeability and crack closing tests," *Constr. Build. Mater.*, vol. 114, pp. 447–457, Jul. 2016.

[19] L. Ferrara, V. Krelani, and F. Moretti, "On the use of crystalline admixtures in cement-based construction materials: from porosity reducers to promoters of self healing," *Smart Mater. Struct.*, vol. 25, no. 8, p. 084002, Aug. 2016.

[20] R. Gupta and A. Biparva, "Do crystalline water proofing admixtures affect restrained plastic shrinkage behavior of concrete?" *Rev. ALCONPAT*, vol. 7, no. 1, p. 15, Jan. 2017.

[21] ACI Committee 212, *ACI 212. 3R-16 Report on Chemical Admixtures for Concrete*. American Concrete Institute, 2016.

[22] P. Azarsa and R. Gupta, "Electrical Resistivity of Concrete for Durability Evaluation: A Review," *Adv. Mater. Sci. Eng.*, vol. 2017, pp. 1–30, 2017.

[23] P. Azarsa and R. Gupta, "Specimen preparation for nano-scale investigation of cementitious repair material," *Micron*, vol. 107, pp. 43–54, Apr. 2018.

[24] Y. M. Malinskii, V. V. Prokopenko, N. A. Ivanova, and V. A. Kargin, "Investigation of self-healing of cracks in polymers," *Polym. Mech.*, vol. 6, no. 2, pp. 240–244, 1970.

[25] Carolyn Dry, “Matrix cracking repair and filling using active and passive modes for smart timed release of chemicals from fibers into cement matrices,” *Smart Mater. Struct.*, vol. 3, no. 2, p. 118, 1994.
[26] C. Dry, “Procedures developed for self-repair of polymer matrix composite materials,” *Compos. Struct.*, vol. 35, no. 3, pp. 263–269, Jul. 1996.
[27] S. R. White *et al.*, “Autonomic healing of polymer composites,” *Nature*, vol. 409, no. 6822, pp. 794–797, Feb. 2001.
[28] B. J. Blaiszik, S. L. B. Kramer, S. C. Olugebefola, J. S. Moore, N. R. Sottos, and S. R. White, “Self-Healing Polymers and Composites,” *Annu. Rev. Mater. Res.*, vol. 40, no. 1, pp. 179–211, Jun. 2010.
[29] V. C. Li, Y. M. Lim, and Y.-W. Chan, “Feasibility study of a passive smart self-healing cementitious composite,” *Compos. Part B Eng.*, vol. 29, no. 6, pp. 819–827, Nov. 1998.
[30] Mo Li and Victor C. Li, “Cracking and Healing of Engineered Cementitious Composites under Chloride Environment,” *Mater. J.*, vol. 108, no. 3, May 2011.
[31] Y. Yang, E.-H. Yang, and V. C. Li, “Autogenous healing of engineered cementitious composites at early age,” *Cem. Concr. Res.*, vol. 41, no. 2, pp. 176–183, Feb. 2011.
[32] H. X. D. Lee, H. S. Wong, and N. R. Buenfeld, “Potential of superabsorbent polymer for self-sealing cracks in concrete,” *Adv. Appl. Ceram.*, vol. 109, no. 5, pp. 296–302, May 2010.
[33] D. Snoeck, S. Steuperaert, K. Van Tittelboom, P. Dubruel, and N. De Belie, “Visualization of water penetration in cementitious materials with superabsorbent polymers by means of neutron radiography,” *Cem. Concr. Res.*, vol. 42, no. 8, pp. 1113–1121, Aug. 2012.
[34] D. Snoeck, K. Van Tittelboom, S. Steuperaert, P. Dubruel, and N. De Belie, “Self-healing cementitious materials by the combination of microfibres and superabsorbent polymers,” *J. Intell. Mater. Syst. Struct.*, vol. 25, no. 1, pp. 13–24, Jan. 2014.
[35] M. Şahmaran, S. B. Keskin, G. Ozerkan, and I. O. Yaman, “Self-healing of mechanically-loaded self consolidating concretes with high volumes of fly ash,” *Cem. Concr. Compos.*, vol. 30, no. 10, pp. 872–879, Nov. 2008.
[36] P. Termkhajornkit, T. Nawa, Y. Yamashiro, and T. Saito, “Self-healing ability of fly ash–cement systems,” *Cem. Concr. Compos.*, vol. 31, no. 3, pp. 195–203, Mar. 2009.
[37] S. H. Na, Y. Hama, M. Taniguchi, O. Katsura, T. Sagawa, and M. Zakaria, “Experimental Investigation on Reaction Rate and Self-healing Ability in Fly Ash Blended Cement Mixtures,” *J. Adv. Concr. Technol.*, vol. 10, no. 7, pp. 240–253, 2012.
[38] L. Sun, W. Y. Yu, and Q. Ge, “Experimental Research on the Self-Healing Performance of Micro-Cracks in Concrete Bridge,” *Adv. Mater. Res.*, vol. 250–253, pp. 28–32, May 2011.
[39] Z. H. Zhou, Z. Q. Li, D. Y. Xu, and J. H. Yu, “Influence of Slag and Fly Ash on the Self-Healing Ability of Concrete,” *Adv. Mater. Res.*, vol. 306–307, pp. 1020–1023, Aug. 2011.
[40] T.-H. Ahn and T. Kishi, “Crack Self-healing Behavior of Cementitious Composites Incorporating Various Mineral Admixtures,” *J. Adv. Concr. Technol.*, vol. 8, no. 2, pp. 171–186, 2010.
[41] A. M. Abd_Elmoaty, “Self-healing of polymer modified concrete,” *Alex. Eng. J.*, vol. 50, no. 2, pp. 171–178, Jun. 2011.
[42] X. Yuan, W. Sun, X. Zuo, and H. Li, “The crack self-healing properties of cement-based material with EVA heat-melt adhesive,” *J. Wuhan Univ. Technol.-Mater Sci Ed*, vol. 26, no. 4, pp. 774–779, 2011.
[43] X. Z. Yuan, W. Sun, and X. B. Zuo, “Study of Feasibility of Heat Melt Adhesive Being Used in Crack Self-Healing of Cement-Based Materials,” *Appl. Mech. Mater.*, vol. 99–100, pp. 1087–1091, Sep. 2011.
[44] H. M. Jonkers, “Self Healing Concrete: A Biological Approach,” in *Self Healing Materials: An Alternative Approach to 20 Centuries of Materials Science*, S. van der Zwaag, Ed. Dordrecht: Springer Netherlands, 2007, pp. 195–204.
[45] H. Mihashi and T. Nishiwaki, “Development of Engineered Self-Healing and Self-Repairing Concrete-State-of-the-Art Report,” *J. Adv. Concr. Technol.*, vol. 10, no. 5, pp. 170–184, 2012.
[46] D. J. Hannant and J. G. Keer, “Autogenous healing of thin cement-based sheets,” *Cem. Concr. Res.*, vol. 13, no. 3, pp. 357–365, May 1983.
[47] R. J. Gray, “Autogenous healing of fibre/matrix interfacial bond in fibre-reinforced mortar,” *Cem. Concr. Res.*, vol. 14, no. 3, pp. 315–317, May 1984.
[48] Y. Yang, M. D. Lepech, E.-H. Yang, and V. C. Li, “Autogenous healing of engineered cementitious composites under wet–dry cycles,” *Cem. Concr. Res.*, vol. 39, no. 5, pp. 382–390, May 2009.
[49] S. Qian, J. Zhou, M. R. de Rooij, E. Schlangen, G. Ye, and K. van Breugel, “Self-healing behavior of strain hardening cementitious composites incorporating local waste materials,” *Cem. Concr. Compos.*, vol. 31, no. 9, pp. 613–621, Oct. 2009.

[50] S. Z. Qian, J. Zhou, and E. Schlangen, “Influence of curing condition and pre-cracking time on the self-healing behavior of Engineered Cementitious Composites,” *Cem. Concr. Compos.*, vol. 32, no. 9, pp. 686–693, Oct. 2010.
[51] C. M. S. Ravindra Kumar Dhir and John G. L. Munday, “Strength and Deformation Properties of Autogenously Healed Mortars,” *J. Proc.*, vol. 70, no. 3, Mar. 1973.
[52] A. H. N. Ali S. Ngab and Floyd O. Slate, “Shrinkage and Creep of High Strength Concrete,” *J. Proc.*, vol. 78, no. 4, Jul. 1981.
[53] Kenneth R. Lauer and Floyd 0. Slate, “Autogenous Healing of Cement Paste,” *J. Proc.*, vol. 52, no. 6, Jun. 1956.
[54] H.-W. Reinhardt and M. Jooss, “Permeability and self-healing of cracked concrete as a function of temperature and crack width,” *Cem. Concr. Res.*, vol. 33, no. 7, pp. 981–985, Jul. 2003.
[55] D. Jaroenratanapirom and R. Sahamitmongkol, “Effects of different mineral additives and cracking ages on self-healing performance of mortar,” presented at the Annual Concrete Conference 6, 2011.
[56] D. Jaroenratanapirom and R. Sahamitmongkol, “Self-Crack Closing Ability of Mortar with Different Additives,” *J. Met. Mater. Miner.*, vol. 21, pp. 9–17, 2011.
[57] K. Sisomphon, O. Copuroglu, and E. A. B. Koenders, “Effect of exposure conditions on self healing behavior of strain hardening cementitious composites incorporating various cementitious materials,” *Constr. Build. Mater.*, vol. 42, pp. 217–224, May 2013.
[58] British Standards Institution, *Testing hardened concrete. Part 8*, London: BSI, 2009.
[59] P. K. Mehta and P. J. M. Monteiro, *Concrete: microstructure, properties, and materials*, 3rd ed. New York: McGraw-Hill, 2006.
[60] ASTM C1760-12, “Standard Test Method for Bulk Electrical Conductivity of Hardened Concrete,” *ASTM Int.*, 2012.
[61] AASHTO TP 95, “Method of Test for Surface Resistivity Indication of Concrete’s Ability to Resist Chloride Ion Penetration,” *Am. Assoc. State Highw. Transp. Off.*, 2011.
[62] O. Sengul, “Use of electrical resistivity as an indicator for durability,” *Constr. Build. Mater.*, vol. 73, pp. 434–441, Dec. 2014.
[63] F. Rajabipour, J. Weiss, and D. M. Abraham, “In-situ electrical conductivity measurements to assess moisture and ionic transport in concrete (A discussion of critical features that influence the measurements),” presented at the International RILEM Symposium on Concrete Science and Engineering: A Tribute to Arnon Bentur, 2004.
[64] H. Layssi, P. Ghods, A. R. Alizadeh, and M. Salehi, “Electrical Resistivity of Concrete,” *Concrete International*, pp. 41–46, May-2015.
[65] K. Hornbostel, C. K. Larsen, and M. R. Geiker, “Relationship between concrete resistivity and corrosion rate – A literature review,” *Cem. Concr. Compos.*, vol. 39, pp. 60–72, May 2013.
[66] D. A. Whitting and M. A. Nagi, “Electrical Resistivity of Concrete,” Portland Cement Association, Sookie, IL, 2457, 2003.
[67] RILEM TC 154-EMC, “Recommendations of RILEM TC 154-EMC: Electrochemical techniques for measuring metallic corrosion Half-cell potential measurements - Potential mapping on reinforced concrete structures,” *Mater. Struct.*, vol. 36, no. 261, pp. 461–471, Jun. 2003.
[68] R. B. Polder, “Test methods for on site measurement of resistivity of concrete — a RILEM TC-154 technical recommendation,” *Constr. Build. Mater.*, vol. 15, no. 2–3, pp. 125–131, Mar. 2001.
[69] F. Wenner, “A method of measuring earth resistivity,” *Bull. Bur. Stand.*, vol. 12, no. 4, p. 469, May 1916.
[70] J. F. Lataste, C. Sirieix, D. Breysse, and M. Frappa, “Electrical resistivity measurement applied to cracking assessment on reinforced concrete structures in civil engineering,” *NDT E Int.*, vol. 36, no. 6, pp. 383–394, Sep. 2003.
[71] R. Ranade, J. Zhang, J. P. Lynch, and V. C. Li, “Influence of micro-cracking on the composite resistivity of Engineered Cementitious Composites,” *Cem. Concr. Res.*, vol. 58, pp. 1–12, Apr. 2014.
[72] A. Lübeck, A. L. G. Gastaldini, D. S. Barin, and H. C. Siqueira, “Compressive strength and electrical properties of concrete with white Portland cement and blast-furnace slag,” *Cem. Concr. Compos.*, vol. 34, no. 3, pp. 392–399, Mar. 2012.
[73] A. L. G. Gastaldini, G. C. Isaia, T. F. Hoppe, F. Missau, and A. P. Saciloto, “Influence of the use of rice husk ash on the electrical resistivity of concrete: A technical and economic feasibility study,” *Constr. Build. Mater.*, vol. 23, no. 11, pp. 3411–3419, Nov. 2009.
[74] C. Andrade, M. Castellote, and R. d’Andrea, “Measurement of ageing effect on chloride diffusion coefficients in cementitious matrices,” *J. Nucl. Mater.*, vol. 412, no. 1, pp. 209–216, May 2011.

[75] J. W. Bryant Jr., R. E. Weyers, and J. M. Garza, "In-Place Resistivity of Bridge Deck Concrete Mixtures," *ACI Mater. J.*, vol. 106, no. 2, Mar. 2009.
[76] R. B. Polder and W. H. Peelen, "Characterisation of chloride transport and reinforcement corrosion in concrete under cyclic wetting and drying by electrical resistivity," *Cem. Concr. Compos.*, vol. 24, no. 5, pp. 427–435, Oct. 2002.
[77] F. Presuel-Moreno, A. Suares, and Y. Liu, "Characterization of New and Old Concrete Structures Using Surface Resistivity Measurements," Florida Department of Transportation, Dania Beach, FL, Aug. 2010.
[78] D. P. Bentz, K. A. Snyder, and A. Ahmed, "Anticipating the Setting Time of High-Volume Fly Ash Concretes Using Electrical Measurements: Feasibility Studies Using Pastes," *J. Mater. Civ. Eng.*, vol. 27, no. 3, p. 04014129, Mar. 2015.
[79] R. Weydert and C. Gehlen, "Electrolytic Resistivity of Cover Concrete: Relevance, Measurement and Interpretation," presented at the CIB W078 Workshop on Information Technology in Construction, Rotterdam, Netherlands, 1999.
[80] O. Sengul and O. E. Gjorv, "Effect of Embedded Steel on Electrical Resistivity Measurements on Concrete Structures," *ACI Mater. J.*, vol. 106, no. 1, Jan. 2009.
[81] F. Presuel-Moreno, Y. Liu, and M. Paredes, "Understanding the Effect of Rebar Presence and/or Multilayered Concrete Resistivity on the Apparent Surface Resistivity Measured via the Four Point Wenner Method." NACE International, 2009.
[82] C.-T. Chen, J.-J. Chang, and W. Yeih, "The effects of specimen parameters on the resistivity of concrete," *Constr. Build. Mater.*, vol. 71, pp. 35–43, Nov. 2014.
[83] A. J. Garzon, J. Sanchez, C. Andrade, N. Rebolledo, E. Menéndez, and J. Fullea, "Modification of four-point method to measure the concrete electrical resistivity in presence of reinforcing bars," *Cem. Concr. Compos.*, vol. 53, pp. 249–257, Oct. 2014.
[84] Y.-C. Lim, T. Noguchi, and C.-G. Cho, "A quantitative analysis of the geometric effects of reinforcement in concrete resistivity measurement above reinforcement," *Constr. Build. Mater.*, vol. 83, pp. 189–193, May 2015.
[85] W. Morris, A. Vico, and M. Vázquez, "Chloride induced corrosion of reinforcing steel evaluated by concrete resistivity measurements," *Electrochimica Acta*, vol. 49, no. 25, pp. 4447–4453, Oct. 2004.
[86] U. M. Angst and B. Elsener, "On the Applicability of the Wenner Method for Resistivity Measurements of Concrete," *ACI Mater. J.*, vol. 111, no. 6, Nov. 2014.
[87] M. Goueygou, O. Abraham, and J.-F. Lataste, "A comparative study of two non-destructive testing methods to assess near-surface mechanical damage in concrete structures," *NDT E Int.*, vol. 41, no. 6, pp. 448–456, Sep. 2008.
[88] N. Wiwattanachang and P. H. Giao, "Monitoring crack development in fiber concrete beam by using electrical resistivity imaging," *J. Appl. Geophys.*, vol. 75, no. 2, pp. 294–304, Oct. 2011.
[89] T. D. Rupnow and P. Icenogle, "Evaluation of Surface Resistivity Measurements as an Alternative to the Rapid Chloride Permeability Test for Quality Assurance and Acceptance," Performing Organization Name and Address Louisiana Transportation Research Center, Baton Rouge, LA, Technical FHWA/LA.11/479, Jul. 2011.
[90] F. J. Presuel-Moreno and Y. Liu, "Temperature Effect on Electrical Resistivity Measurement on Mature Saturated Concrete," presented at the NACE - International Corrosion Conference Series 7, Salt Lake City, 2012.
[91] R. Van Noort, M. Hunger, and P. Spiesz, "Long-term chloride migration coefficient in slag cement-based concrete and resistivity as an alternative test method," *Constr. Build. Mater.*, vol. 115, pp. 746–759, Jul. 2016.
[92] J. Su, C. Yang, W. Wu, and R. Huang, "Effect of moisture content on concrete resistivity measurement," *J. Chin. Inst. Eng.*, vol. 25, no. 1, pp. 117–122, Jan. 2002.
[93] M. Saleem, M. Shameem, S. E. Hussain, and M. Maslehuddin, "Effect of moisture, chloride and sulphate contamination on the electrical resistivity of Portland cement concrete," *Constr. Build. Mater.*, vol. 10, no. 3, pp. 209–214, Apr. 1996.
[94] O. Sengul and O. E. Gjorv, "Electrical Resistivity Measurements for Quality Control During Concrete Construction," *ACI Mater. J.*, vol. 105, no. 6, Nov. 2008.
[95] M. D. Newlands, M. R. Jones, S. Kandasami, and T. A. Harrison, "Sensitivity of electrode contact solutions and contact pressure in assessing electrical resistivity of concrete," *Mater. Struct.*, vol. 41, no. 4, pp. 621–632, May 2008.
[96] R. Spratt, J. Castro, T. Nantung, E. Paredes, and W. J. Weiss, "Variability Analysis of the Bulk Resistivity Measured Using Concrete Cylinders," Purdue University Press, West Lafayette, IN, Technical, 2011.

[97] W. J. McCarter, G. Starrs, S. Kandasami, M. R. Jones, and M. Chrisp, "Electrode Configurations for Resistivity Measurements on Concrete," *ACI Mater. J.*, vol. 106, no. 3, May 2009.
[98] Y. Liu and F. J. Presuel-Moreno, "Normalization of Temperature Effect on Concrete Resistivity by Method Using Arrhenius Law (with Appendix)," *ACI Mater. J.*, vol. 111, no. 4, Jul. 2014.
[99] R. Spragg, C. Villani, K. Snyder, D. Bentz, J. Bullard, and J. Weiss, "Factors That Influence Electrical Resistivity Measurements in Cementitious Systems," *Transp. Res. Rec. J. Transp. Res. Board*, vol. 2342, pp. 90–98, Dec. 2013.
[100] Y. Liu and F. Presuel-Moreno, "Effect of Elevated Temperature Curing on Compressive Strength and Electrical Resistivity of Concrete with Fly Ash and GGBS," *ACI Mater. J.*, vol. 111, no. 5, Sep. 2014.
[101] W. J. McCarter, T. M. Chrisp, G. Starrs, P. A. M. Basheer, and J. Blewett, "Field monitoring of electrical conductivity of cover-zone concrete," *Cem. Concr. Compos.*, vol. 27, no. 7–8, pp. 809–817, Aug. 2005.
[102] K. M. Smith, A. J. Schokker, and P. J. Tikalsky, "Performance of Supplementary Cementitious Materials in Concrete Resistivity and Corrosion Monitoring Evaluations," *ACI Mater. J.*, vol. 101, no. 5, Sep. 2004.
[103] H. Minagawa and M. Hisada, "Consideration about Chloride Ion Diffusion Coefficient Estimated by Electric Resistivity of Concrete Exposed in Tidal Zone," presented at the Third International Conference on Sustainable Construction Materials and Technologies, Kyoto, 2013.
[104] F. Presuel-Moreno, Y.-Y. Wu, and Y. Liu, "Effect of curing regime on concrete resistivity and aging factor over time," *Constr. Build. Mater.*, vol. 48, pp. 874–882, Nov. 2013.
[105] E. Güneyisi, T. Özturan, and M. Gesoğlu, "A study on reinforcement corrosion and related properties of plain and blended cement concretes under different curing conditions," *Cem. Concr. Compos.*, vol. 27, no. 4, pp. 449–461, Apr. 2005.
[106] T. Y. D. Lim, S. Teng, B. Divsholi Bahador, and O. E. Gjorv, "Durability of Very-High-Strength Concrete with Supplementary Cementitious Materials for Marine Environments," *ACI Mater. J.*, vol. 113, no. 01, Jan. 2016.
[107] R. J. Kessler, R. G. Powers, E. Vivas, M. A. Paredes, and Y. P. Virmani, "Surface Resistivity as an Indicator of Concrete Chloride Penetration Resistance," presented at the Concrete Bridge Conference, 2008, p. 18.
[108] J. Gudimettla and G. Crawford, "Resistivity Tests for Concrete—Recent Field Experience," *ACI Mater. J.*, vol. 113, no. 04, Jul. 2016.
[109] A. Jenkins, "Surface Resistivity as an Alternative for Rapid Chloride Permeability Test of Hardened Concrete," Kansas Department of Transportation Bureau of Research, Topeka, Kansas, FHWA-KS-14-15, Mar. 2015.
[110] Y. Liu, F. J. Presuel-Moreno, and M. A. Paredes, "Determination of Chloride Diffusion Coefficients in Concrete by Electrical Resistivity Method," *ACI Mater. J.*, vol. 112, no. 05, Sep. 2015.
[111] A. A. Ramezanianpour, A. Pilvar, M. Mahdikhani, and F. Moodi, "Practical evaluation of relationship between concrete resistivity, water penetration, rapid chloride penetration and compressive strength," *Constr. Build. Mater.*, vol. 25, no. 5, pp. 2472–2479, May 2011.
[112] P. A. Basheer, P. R. Gilleece, A. Long, and W. Mc Carter, "Monitoring electrical resistance of concretes containing alternative cementitious materials to assess their resistance to chloride penetration," *Cem. Concr. Compos.*, vol. 24, no. 5, pp. 437–449, Oct. 2002.
[113] D. T. Y. Lim, B. Sabet Divsholi, D. Xu, and S. Teng, "Evaluation of High Performance Concrete Using Electrical Resistivity Technique," presented at the Our World in Concrete and Structures, Singapore, 2011.
[114] C. Andrade, R. d'Andrea, and N. Rebolledo, "Chloride ion penetration in concrete: The reaction factor in the electrical resistivity model," *Cem. Concr. Compos.*, vol. 47, pp. 41–46, Mar. 2014.
[115] W. Morris, A. Vico, M. Vazquez, and S. de Sanchez, "Corrosion of reinforcing steel evaluated by means of concrete resistivity measurements," *Corros. Sci.*, vol. 44, no. 1, pp. 81–99, Jan. 2002.
[116] R. P. Spragg, C. Villani, and J. Weiss, "Surface and Uniaxial Electrical Measurements on Layered Cementitious Composites having Cylindrical and Prismatic Geometries," presented at the International Conference on the Durability of Concrete Structures, West Lafayette, IN, 2014.
[117] P. Ghosh and Q. Tran, "Correlation Between Bulk and Surface Resistivity of Concrete," *Int. J. Concr. Struct. Mater.*, vol. 9, no. 1, pp. 119–132, Mar. 2015.
[118] P. Ghosh and Q. Tran, "Influence of parameters on surface resistivity of concrete," *Cem. Concr. Compos.*, vol. 62, pp. 134–145, Sep. 2015.
[119] W. Morris, E. I. Moreno, and A. A. Sagüés, "Practical evaluation of resistivity of concrete in test cylinders using a Wenner array probe," *Cem. Concr. Res.*, vol. 26, no. 12, pp. 1779–1787, Dec. 1996.
[120] J. Weiss, K. Snyder, J. Bullard, and D. Bentz, "Using a Saturation Function to Interpret the Electrical Properties of Partially Saturated Concrete," *J. Mater. Civ. Eng.*, vol. 25, no. 8, pp. 1097–1106, Aug. 2013.

[121] S. G. Millard, “Reinforced Concrete Resistivity Measurement Technique,” in *Institution of Civil Engineers*, 1991, pp. 71–88.
[122] K. R. Gowers and S. G. Millard, “Measurement of Concrete Resistivity for Assessment of Corrosion Severity of Steel Using Wenner Technique,” *ACI Mater. J.*, vol. 96, no. 5, Sep. 1999.
[123] F. Presuel-Moreno, Y. Liu, and Y.-Y. Wu, “Numerical modeling of the effects of rebar presence and/or multilayered concrete resistivity on the apparent resistivity measured via the Wenner method,” *Constr. Build. Mater.*, vol. 48, pp. 16–25, Nov. 2013.
[124] M. Salehi, P. Ghods, and O. Burkan Isgor, “Numerical investigation of the role of embedded reinforcement mesh on electrical resistivity measurements of concrete using the Wenner probe technique,” *Mater. Struct.*, vol. 49, no. 1–2, pp. 301–316, Jan. 2016.
[125] M. Salehi, “Numerical investigation of the role of embedded reinforcement mesh on electrical resistivity measurements of concrete using the Wenner probe technique,” Master, Carleton University, Ottawa, ON, 2013.
[126] J. Sanchez, C. Andrade, J. Torres, N. Rebolledo, and J. Fullea, “Determination of reinforced concrete durability with on-site resistivity measurements,” *Mater. Struct.*, vol. 50, no. 1, Feb. 2017.
[127] M. Morales, “Experimental Investigation of the Effects of Embedded Rebar, Cracks, Chloride Ingress and Corrosion on Electrical Resistivity Measurements of Reinforced Concrete,” Master, Oregon State University, 2015.
[128] A. A. Shah and Y. Ribakov, “Non-destructive measurements of crack assessment and defect detection in concrete structures,” *Mater. Des.*, vol. 29, no. 1, pp. 61–69, Jan. 2008.
[129] M. Chouteau and S. Beaulieu, “An Investigation on Application of the Electrical Resistivity Tomography Method to Concrete Structures.”, *Geophysics*, 2002.
[130] E. Taillet, J. F. Lataste, P. Rivard, and A. Denis, “Non-destructive evaluation of cracks in massive concrete using normal dc resistivity logging,” *NDT E Int.*, vol. 63, pp. 11–20, Apr. 2014.
[131] M. Salehi, P. Ghods, and O. B. Isgor, “Numerical Study on the Effect of Cracking on Surface Resistivity of Plain and Reinforced Concrete Elements,” *J. Mater. Civ. Eng.*, vol. 27, no. 12, p. 04015053, Dec. 2015.
[132] A. Ewins, “Resistivity Measurements in Concrete,” *Br. J. NDT*, vol. 32, no. 3, pp. 120–126, 1990.
[133] R. Henkensiefken, J. Castro, D. Bentz, T. Nantung, and J. Weiss, “Water absorption in internally cured mortar made with water-filled lightweight aggregate,” *Cem. Concr. Res.*, vol. 39, no. 10, pp. 883–892, Oct. 2009.
[134] M. D. A. Thomas, “The use of conductive gel.” 2008.
[135] J. D. Shane, “Electrical Conductivity and Transport Properties of Cement-based Material Measured by Impedance Spectroscopy,” PhD., Nothwestern University, Evanston, IL, 2000.
[136] R. Spragg, Y. Bu, K. Snyder, D. Bentz, and J. Weiss, “Electrical Testing of Cement-Based Materials: Role of Testing Techniques, Sample Conditioning,” Purdue University, Technical FHWA/IN/JTRP-2013/28, Dec. 2013.
[137] A. Shahroodi, “Development of Test Methods for Assessment of Concrete Durability for Use in Performance-based Specifications,” Master, University of Toronto, Toronto, ON, 2010.
[138] J. M. S. Marquez, “Influence of Saturation and Geometry on Surface Electrical Resistivity Measurements,” Master, Concordia University, Montreal, Quebec, 2015.
[139] M. Castellote, C. Andrade, and M. C. Alonso, “Standardization, to a Reference of 25 °C, of Electrical Resistivity for Mortars and Concretes in Saturated or Isolated Conditions,” *ACI Mater. J.*, vol. 99, no. 2, Mar. 2002.
[140] Y. A. Villagrán Zaccardi, J. Fullea García, P. Huélamo, and á. A. Di Maio, “Influence of temperature and humidity on Portland cement mortar resistivity monitored with inner sensors,” *Mater. Corros.*, vol. 60, no. 4, pp. 294–299, Apr. 2009.
[141] S. Poyet, “Experimental investigation of the effect of temperature on the first desorption isotherm of concrete,” *Cem. Concr. Res.*, vol. 39, no. 11, pp. 1052–1059, Nov. 2009.
[142] S. G. Millard, J. A. Harrison, and K. R. Gowers, “Practical measurement of concrete resistivity,” *Br. J. Non-Destr. Test.*, vol. 33, pp. 59–63, 1991.
[143] W. Elkey and E. J. Sellevold, “Electrical Resistivity of Concrete,” Norwegian Road Research Laboratory, Oslo, Norway, 80, 1995.
[144] T. M. Chrisp, G. Starrs, W. J. McCarter, E. Rouchotas, and J. Blewett, “Temperature-conductivity relationships for concrete: An activation energy approach,” *J. Mater. Sci. Lett.*, vol. 20, no. 12, pp. 1085–1087, 2001.

[145] DuraCrete R17, "DuraCrete – Probabilistic Performance based Durability Design of Concrete Structures, includes General Guidelines for Durability Design and Redesign," The European Union – Brite EuRam III, CUR, Gouda, Technical BE95-1347/R17, May 2000.
[146] M. Pour-Ghaz, O. B. Isgor, and P. Ghods, "The effect of temperature on the corrosion of steel in concrete. Part 1: Simulated polarization resistance tests and model development," *Corros. Sci.*, vol. 51, no. 2, pp. 415–425, Feb. 2009.
[147] C. K. Larsen, E. J. Sellevold, Østvik, and Ø. Vennesland, "Electrical resistivity of concrete - Part II: Influence of moisture content and temperature," in *2nd International RILEM Symposium on Advances in Concrete through Science and Engineering*, 2006.
[148] Y. Liu, "Accelerated Curing of Concrete With High Volume Pozzolans -Resistivity, Diffusivity And Compressive Strength," PhD, Florida Atlantic University, Boca Raton, Florida, 2012.
[149] X. Lu, "Application of the Nernst-Einstein equation to concrete," *Cem. Concr. Res.*, vol. 27, no. 2, pp. 293–302, Feb. 1997.
[150] K. R. Backe, O. B. Lile, and S. K. Lyomov, "Characterizing Curing Cement Slurries by Electrical Conductivity," *SPE Drill. Complet.*, vol. 16, no. 04, pp. 207–207, Dec. 2001.
[151] FDOT, "Florida Method of Test For Concrete Resistivity as an Electrical Indicator of its Permeability," FM 5-578, 2004.
[152] R. J. Kessler, R. G. Powers, and M. A. Paredes, "Resistivity Measurements of Water Saturated Concrete as an Indicator of Permeability," presented at the Corrosion, Houston, TX, 2005.
[153] ASTM C1202-12, "Standard Test Method for Electrical Indication of Concrete's Ability to Resist Chloride Ion Penetration," *ASTM Int.*, 2012.
[154] R. K. Dhir, M. J. McCarthy, and M. D. Newlands, Eds., *Challenges of Concrete Construction: Volume 6, Concrete for Extreme Conditions: Proceedings of the International Conference held at the University of Dundee, Scotland, UK on 9–11 September 2002*. Thomas Telford Publishing, 2002.
[155] E. Vivas, A. Boyd, and H. R. Hamilton III, "Permeability of Concrete-Comparison of Conductivity and Diffusion Methods," Florida Department of Transportation, Tallahassee, FL, Technical 4910 45 04 992–12 (0026899), Jun. 2007.
[156] A. Bentur, S. Diamond, and Berke Neal Steven, *Steel corrosion in concrete: fundamentals and civil engineering practice*, 1st ed. London; New York: E & FN Spon, 1997.
[157] G. K. Glass, C. L. Page, and N. R. Short, "Factors affecting the corrosion rate of steel in carbonated mortars," *Corros. Sci.*, vol. 32, no. 12, pp. 1283–1294, Jan. 1991.
[158] L. Bertolini and R. Polder, "Concrete resistivity and reinforcement corrosion rate as a function of temperature and humidity of the environment," Netherlands Organisation for Applied Scientific Research, Delft, The Netherlands, TNO 97-BT-R0574, 1997.
[159] ASTM C876, "Test Method for Corrosion Potentials of Uncoated Reinforcing Steel in Concrete," *ASTM Int.*, 2015.
[160] N. J. Carino, "Non-destructive techniques to investigate corrosion status in concrete structures," *J. Perform. Constr. Facil.*, vol. 13, no. 3, pp. 96–106, 1999.
[161] N. Gucunski, F. Romero, S. Kruschwitz, R. Feldmann, A. Abu-Hawash, and M. Dunn, "Multiple Complementary Nondestructive Evaluation Technologies for Condition Assessment of Concrete Bridge Decks," *Transp. Res. Rec. J. Transp. Res. Board*, vol. 2201, pp. 34–44, Dec. 2010.
[162] N. Gucunski, "Non-destructive Testing to Identify Concrete Bridge Deck Deterioration," Transportation Research Board, Washington, DC, S2-R06A-RR-1, 2013.
[163] L. Sadowski, "Methodology for Assessing the Probability of Corrosion in Concrete Structures on the Basis of Half-Cell Potential and Concrete Resistivity Measurements," *Sci. World J.*, vol. 2013, pp. 1–8, 2013.
[164] "Operating Instructions Resipod Family Manual." Proceq.
[165] "SURF™ Surface Electrical Resistivity of Concrete Manual." Giatec Scientific Inc.
[166] H.-W. Song and V. Saraswathy, "Corrosion monitoring of reinforced concrete structures-a," *Int. J. Electrochem. Sci.*, vol. 2, pp. 1–28, 2007.
[167] C. Alonso, C. Andrade, and J. A. González, "Relation between resistivity and corrosion rate of reinforcements in carbonated mortar made with several cement types," *Cem. Concr. Res.*, vol. 18, no. 5, pp. 687–698, Sep. 1988.
[168] C. Andrade and C. Alonso, "Corrosion rate monitoring in the laboratory and on-site," *Constr. Build. Mater.*, vol. 10, no. 5, pp. 315–328, Jul. 1996.
[169] J. Gulikers, "Theoretical considerations on the supposed linear relationship between concrete resistivity and corrosion rate of steel reinforcement," *Mater. Corros.*, vol. 56, no. 6, pp. 393–403, Jun. 2005.

[170] C. Andrade and C. Alonso, "Test methods for on-site corrosion rate measurement of steel reinforcement in concrete by means of the polarization resistance method," *RILEM*, vol. 37, pp. 623–643, Nov. 2004.
[171] E. Vesikari and M.-K. Soderqvist, "Life Cycle Management of Concrete Infrastructures for Improved Sustainability," presented at the 9th International Bridge Management Conference, 2003, pp. 15–28.
[172] A. Sharif, "Review on advances in nanoscale microscopy in cement research," *Micron*, vol. 80, pp. 45–58, Jan. 2016.
[173] I. G. Richardson and G. W. Groves, "Microstructure and microanalysis of hardened ordinary Portland cement pastes," *J. Mater. Sci.*, vol. 28, no. 1, pp. 265–277, 1993.
[174] A. Grudemo, *The Chemistry of Cements*, H. F. W. Taylor. New York: Academic Press, 1964.
[175] E. E. Lachowski, K. Mohan, H. F. W. Taylor, and A. E. Moore, "Analytical Electron Microscopy of Cement Pastes: II, Pastes of Portland Cements and Clinkers," *J. Am. Ceram. Soc.*, vol. 63, no. 7–8, pp. 447–452, Jul. 1980.
[176] E. E. Lachowski, K. Mohan, H. F. W. Taylor, C. D. Larsen, and A. E. Moore, "Analytical Electron Microscopy of Cement Pastes: III, Pastes Hydrated for Long Times," *J. Am. Ceram. Soc.*, vol. 64, no. 6, pp. 319–321, Jun. 1981.
[177] E. E. Lachowski and S. Diamond, "Investigation of the composition and morphology of individual particles of portland cement paste: 1. C-S-H gel and calcium hydroxide particles," *Cem. Concr. Res.*, vol. 13, no. 2, pp. 177–185, Mar. 1983.
[178] T. D. Ciach, J. E. Gillott, E. G. Swenson, and P. J. Sereda, "Microstructure of calcium silicate hydrates," *Cem. Concr. Res.*, vol. 1, no. 1, pp. 13–25, Jan. 1971.
[179] H. M. Jennings and P. L. Pratt, "The Use of a High Voltage Electron Microscope and Gas Reaction Cell for the Microstructural Investigation of Wet Portland Cement," *J. Mater. Sci. Lett.*, no. 15, pp. 250–3, 1980.
[180] H. F. W. Taylor, K. Mohan, and G. K. Moir, "Analytical Study of Pure and Extended Portland Cement Pastes: I, Pure Portland Cement Pastes," *J. Am. Ceram. Soc.*, vol. 68, no. 12, pp. 680–685, Dec. 1985.
[181] T. N. Tiegs, "Investigation of Ion Thinned Tricalcium Silicate Pastes by Transmission Electron Microscopy," M. Sc. Thesis, University of Illinois, Urbana- Champaign, 1975.
[182] B. J. Dalgleish, P. L. Pratt, and R. I. Moss, "Preparation techniques and the microscopical examination of portland cement paste and C3S," *Cem. Concr. Res.*, vol. 10, no. 5, pp. 665–676, Sep. 1980.
[183] H. M. Jennings, B. J. Dalgleish, and P. L. Pratt, "Morphological Development of Hydrating Tricalcium Silicate as Examined by Electron Microscopy Techniques," *J. Am. Ceram. Soc.*, vol. 64, no. 10, pp. 567–572, Oct. 1981.
[184] J. A. Card, K. Mohan, H. F. W. Taylor, and G. Cliff, "Analytical Electron Microscopy of Cement Pastes: I, Tricalcium Silicate Pastes," *J. Am. Ceram. Soc.*, vol. 63, no. 5–6, pp. 336–337, May 1980.
[185] B. J. Dalgleish and K. Ibe, "Thin-foil studies of hydrated Portland cement," *Cem. Concr. Res.*, vol. 11, no. 5–6, pp. 729–739, Sep. 1981.
[186] G. W. Groves, P. J. Le Sueur, and W. Sinclair, "Transmission Electron Microscopy and Microanalytical Studies of Ion-Beam-Thinned Sections of Tricalcium Silicate Paste," *J. Am. Ceram. Soc.*, vol. 69, no. 4, pp. 353–356, Apr. 1986.
[187] G. W. Groves and S. A. Rodger, "The hydration of C3S and ordinary Portland cement with relatively large additions of micro silica," *Adv. Cem. Res.*, vol. 2, no. 8, pp. 135–140, Oct. 1989.
[188] M. W. Grutzeck and D. M. Roy, "Electron Microprobe Studies of the Hydration of 3CaO.SiO2," *Nature*, vol. 223, no. 5205, pp. 492–494, Aug. 1969.
[189] D. D. Double, A. Hellawell, and S. J. Perry, "The Hydration of Portland Cement," *Proc. R. Soc. Math. Phys. Eng. Sci.*, vol. 359, no. 1699, pp. 435–451, Mar. 1978.
[190] R. Javelas, J. C. Maso, and J. P. Ollivier, "Realisation de lames ultra-minces de mortier pour observation directe au microscope electronique par transmission," *Cem. Concr. Res.*, vol. 4, no. 2, pp. 167–168, Mar. 1974.
[191] G. W. Groves, "TEM Studies of Cement Hydration," *MRS Proc.*, vol. 85, Jan. 1986.
[192] E. Henderson and J. E. Bailey, "Sheet-like structure of calcium silicate hydrates," *J. Mater. Sci.*, vol. 23, no. 2, pp. 501–508, 1988.
[193] S. A. Rodger and G. W. Groves, "Electron Microscopy Study of Ordinary Portland Cement and Ordinary Portland Cement–Pulverized Fuel Ash Blended Pastes," *J. Am. Ceram. Soc.*, vol. 72, no. 6, pp. 1037–1039, Jun. 1989.
[194] I. G. Richardson and G. W. Groves, "Microstructure and microanalysis of hardened cement pastes involving ground granulated blast-furnace slag," *J. Mater. Sci.*, vol. 27, no. 22, pp. 6204–6212, 1992.
[195] I. G. Richardson, "The nature of C-S-H in hardened cements," *Cem. Concr. Res.*, vol. 29, no. 8, pp. 1131–1147, Aug. 1999.

[196] I. G. Richardson, “Electron microscopy of cements,” in *Structure and performance of cements*, 2nd ed., London; New York: Spon Press, 2002.
[197] I. G. Richardson, “Tobermorite/jennite- and tobermorite/calcium hydroxide-based models for the structure of C-S-H: applicability to hardened pastes of tricalcium silicate, β-dicalcium silicate, Portland cement, and blends of Portland cement with blast-furnace slag, metakaolin, or silica fume,” *Cem. Concr. Res.*, vol. 34, no. 9, pp. 1733–1777, Sep. 2004.
[198] E. Gallucci, P. Mathur, and K. Scrivener, “Microstructural development of early age hydration shells around cement grains,” *Cem. Concr. Res.*, vol. 40, no. 1, pp. 4–13, Jan. 2010.
[199] J. Plank, Z. Dai, and P. R. Andres, “Preparation and characterization of new Ca–Al–polycarboxylate layered double hydroxides,” *Mater. Lett.*, vol. 60, no. 29–30, pp. 3614–3617, Dec. 2006.
[200] Y. Sun, Z. Zhang, and C. P. Wong, “Study on mono-dispersed nano-size silica by surface modification for underfill applications,” *J. Colloid Interface Sci.*, vol. 292, no. 2, pp. 436–444, Dec. 2005.
[201] F. Zhang, Q. Jin, and S.-W. Chan, “Ceria nanoparticles: Size, size distribution, and shape,” *J. Appl. Phys.*, vol. 95, no. 8, pp. 4319–4326, Apr. 2004.
[202] H. Borchert *et al.*, “Determination of Nanocrystal Sizes: A Comparison of TEM, SAXS, and XRD Studies of Highly Monodisperse CoPt3 Particles,” *Langmuir*, vol. 21, no. 5, pp. 1931–1936, Mar. 2005.
[203] K. L. Lin, W. C. Chang, D. F. Lin, H. L. Luo, and M. C. Tsai, “Effects of nano-SiO_2 and different ash particle sizes on sludge ash–cement mortar,” *J. Environ. Manage.*, vol. 88, no. 4, pp. 708–714, Sep. 2008.
[204] R. Ziel, A. Haus, and A. Tulke, “Quantification of the pore size distribution (porosity profiles) in microfiltration membranes by SEM, TEM and computer image analysis,” *J. Membr. Sci.*, vol. 323, no. 2, pp. 241–246, Oct. 2008.
[205] P. Hou, X. Cheng, J. Qian, R. Zhang, W. Cao, and S. P. Shah, “Characteristics of surface-treatment of nano-SiO2 on the transport properties of hardened cement pastes with different water-to-cement ratios,” *Cem. Concr. Compos.*, vol. 55, pp. 26–33, Jan. 2015.
[206] P. Chaunsali and S. Peethamparan, “Influence of the composition of cement kiln dust on its interaction with fly ash and slag,” *Cem. Concr. Res.*, vol. 54, pp. 106–113, Dec. 2013.
[207] A. A. Ramezanianpour, S. A. Ghahari, and M. Esmaeili, “Effect of combined carbonation and chloride ion ingress by an accelerated test method on microscopic and mechanical properties of concrete,” *Constr. Build. Mater.*, vol. 58, pp. 138–146, May 2014.
[208] H. L. Xin, K. Niu, D. H. Alsem, and H. Zheng, “In Situ TEM Study of Catalytic Nanoparticle Reactions in Atmospheric Pressure Gas Environment,” *Microsc. Microanal.*, vol. 19, no. 06, pp. 1558–1568, Dec. 2013.
[209] A. V. Crewe, M. Isaacson, and D. Johnson, “A Simple Scanning Electron Microscope,” *Rev. Sci. Instrum.*, vol. 40, no. 2, pp. 241–246, Feb. 1969.
[210] A. V. Crewe, J. Wall, and J. Langmore, “Visibility of Single Atoms,” *Science*, vol. 168, no. 3937, pp. 1338–1340, Jun. 1970.
[211] K. L. Scrivener, “The development of microstructure during the hydration of Portland cement,” PhD thesis, University of London, 1984.
[212] K. L. Scrivener and P. L. Pratt, “Characterisation of Portland Cement Hydration by Electron Optical Techniques,” *MRS Proc.*, vol. 31, Jan. 1983.
[213] K. L. Scrivener and P. Pratt, “Microstructural studies of the hydration of C3A and C4AF independently and in cement paste,” presented at the Proceedings of the British Ceramic Society, 1984, vol. 35, pp. 207–219.
[214] M. Kumar, N. P. Singh, and N. B. Singh, “Effect of water proofing admixture on the hydration of Portland cement,” *Indian J. Chem. Technol.*, vol. 16, pp. 499–506, Nov. 2009.
[215] B. Ersoy, S. Dikmen, T. Uygunoğlu, M. G. İçduygu, T. Kavas, and A. Olgun, “Effect of mixing water types on the time-dependent zeta potential of Portland cement paste,” *Sci. Eng. Compos. Mater.*, vol. 20, no. 3, Jan. 2013.
[216] L. A. Giannuzzi and F. A. Stevie, “A review of focused ion beam milling techniques for TEM specimen preparation,” *Micron*, vol. 30, no. 3, pp. 197–204, Jun. 1999.
[217] L. A. Giannuzzi, B. W. Kempshall, S. M. Schwarz, J. K. Lomness, B. I. Prenitzer, and F. A. Stevie, “FIB Lift-Out Specimen Preparation Techniques,” in *Introduction to Focused Ion Beams: Instrumentation, Theory, Techniques and Practice*, L. A. Giannuzzi and F. A. Stevie, Eds. Boston, MA: Springer US, 2005, pp. 201–228.
[218] D. Viehland, J.-F. Li, L.-J. Yuan, and Z. Xu, “Mesostructure of Calcium Silicate Hydrate (C-S-H) Gels in Portland Cement Paste: Short-Range Ordering, Nanocrystallinity, and Local Compositional Order,” *J. Am. Ceram. Soc.*, vol. 79, no. 7, pp. 1731–1744, Jul. 1996.
[219] H. F. Taylor, *Cement chemistry*. Thomas Telford, 1997.

[220] P. Stutzman, “Scanning electron microscopy imaging of hydraulic cement microstructure,” *Cem. Concr. Compos.*, vol. 26, no. 8, pp. 957–966, Nov. 2004.
[221] H. S. Wong, N. R. Buenfeld, and M. K. Head, “Estimating transport properties of mortars using image analysis on backscattered electron images,” *Cem. Concr. Res.*, vol. 36, no. 8, pp. 1556–1566, Aug. 2006.
[222] H. S. Wong, M. K. Head, and N. R. Buenfeld, “Pore segmentation of cement-based materials from backscattered electron images,” *Cem. Concr. Res.*, vol. 36, no. 6, pp. 1083–1090, Jun. 2006.
[223] J.-I. Escalante-Garcia and J. H. Sharp, “The chemical composition and microstructure of hydration products in blended cements,” *Cem. Concr. Compos.*, vol. 26, no. 8, pp. 967–976, Nov. 2004.
[224] S. Diamond, “The microstructure of cement paste and concrete—a visual primer,” *Cem. Concr. Compos.*, vol. 26, no. 8, pp. 919–933, Nov. 2004.
[225] C. Famy, K. Scrivener, and A. Crumbie, “What causes differences of C-S-H gel grey levels in backscattered electron images?” *Cem. Concr. Res.*, vol. 32, no. 9, pp. 1465–1471, Sep. 2002.
[226] K. L. Scrivener, “Backscattered electron imaging of cementitious microstructures: understanding and quantification,” *Cem. Concr. Compos.*, vol. 26, no. 8, pp. 935–945, Nov. 2004.
[227] National Institutes of Health, *ImajeJ*. National Institutes of Health, 2018.
[228] D. J. Hassett, G. J. McCarthy, P. Kumarathasan, and D. Pflughoeft-Hassett, “Synthesis and characterization of selenate and sulfate-selenate ettringite structure phases,” *Mater. Res. Bull.*, vol. 25, no. 11, pp. 1347–1354, Nov. 1990.
[229] N. B. Winter, *Scanning electron microscopy of cement and concrete*. Woodbridge: WHD Microanalysis, 2012.
[230] J. Newman and B. S. Choo, Eds., *Advanced concrete technology*. Amsterdam ; Boston: Elsevier Butterworth-Heinemann, 2003.
[231] A. El-Newihy, P. Azarsa, R. Gupta, and A. Biparva, “Effect of Polypropylene Fibers on Self-Healing and Dynamic Modulus of Elasticity Recovery of Fiber Reinforced Concrete,” *Fibers*, vol. 6, no. 1, p. 9, Feb. 2018.
[232] W. Ramm and M. Biscoping, “Autogenous healing and reinforcement corrosion of water-penetrated separation cracks in reinforced concrete,” *Nucl. Eng. Des.*, vol. 179, no. 2, pp. 191–200, Feb. 1998.
[233] N. Hearn and C. T. Morley, “Self-sealing property of concrete—Experimental evidence,” *Mater. Struct.*, vol. 30, no. 7, pp. 404–411, Aug. 1997.
[234] Adam Neville, “Autogenous Healing—A Concrete Miracle?” *Concr. Int.*, vol. 24, no. 11, Nov. 2002.
[235] S. Granger, A. Loukili, G. Pijaudier-Cabot, and G. Chanvillard, “Experimental characterization of the self-healing of cracks in an ultra high performance cementitious material: Mechanical tests and acoustic emission analysis,” *Cem. Concr. Res.*, vol. 37, no. 4, pp. 519–527, Apr. 2007.
[236] W. Zamorowski, “The phenomenon of self-regeneration of concrete,” *Int. J. Cem. Compos. Lightweight Concr.*, vol. 7, no. 3, pp. 199–201, Aug. 1985.
[237] N. Hearn, “Self-sealing, autogenous healing and continued hydration: What is the difference?” *Mater. Struct.*, vol. 31, no. 8, p. 563, Oct. 1998.
[238] S. Jacobsen and E. J. Sellevold, “Self healing of high strength concrete after deterioration by freeze/thaw,” *Cem. Concr. Res.*, vol. 26, no. 1, pp. 55–62, Jan. 1996.
[239] C.-M. Aldea, W.-J. Song, J. S. Popovics, and S. P. Shah, “Extent of Healing of Cracked Normal Strength Concrete,” *J. Mater. Civ. Eng.*, vol. 12, no. 1, pp. 92–96, Feb. 2000.
[240] M. L. Mustafa Sahmaran and Victor C. Li, “Transport Properties of Engineered Cementitious Composites under Chloride Exposure,” *Mater. J.*, vol. 104, no. 6, Nov. 2007.
[241] S. Jacobsen, J. Marchand, and L. Boisvert, “Effect of cracking and healing on chloride transport in OPC concrete,” *Cem. Concr. Res.*, vol. 26, no. 6, pp. 869–881, Jun. 1996.
[242] D. Snoeck and N. De Belie, “Mechanical and self-healing properties of cementitious composites reinforced with flax and cottonised flax, and compared with polyvinyl alcohol fibres,” *Biosyst. Eng.*, vol. 111, no. 4, pp. 325–335, Apr. 2012.
[243] D. Homma, H. Mihashi, and T. Nishiwaki, “Self-Healing Capability of Fibre Reinforced Cementitious Composites,” *J. Adv. Concr. Technol.*, vol. 7, no. 2, pp. 217–228, 2009.
[244] Carola Edvardsen, “Water Permeability and Autogenous Healing of Cracks in Concrete,” *Mater. J.*, vol. 96, no. 4, Jul. 1999.
[245] V. C. Li and E. Herbert, “Robust Self-Healing Concrete for Sustainable Infrastructure,” *J. Adv. Concr. Technol.*, vol. 10, no. 6, pp. 207–218, 2012.
[246] H. Mihashi, Y. Kaneko, T. Nishiwaki, and K. Otsuka, *Fundamental Study on Development of Intelligent Concrete Characterized by Self-Healing Capability for Strength*, vol. 11. 2000.
[247] A. Jefferson, C. Joseph, R. Lark, B. Isaacs, S. Dunn, and B. Weager, “A new system for crack closure of cementitious materials using shrinkable polymers,” *Cem. Concr. Res.*, vol. 40, no. 5, pp. 795–801, May 2010.

[248] G. Song, N. Ma, and H.-N. Li, "Applications of shape memory alloys in civil structures," *Eng. Struct.*, vol. 28, no. 9, pp. 1266–1274, Jul. 2006.
[249] C. Joseph, A. D. Jefferson, B. Isaacs, R. Lark, and D. Gardner, "Experimental investigation of adhesive-based self-healing of cementitious materials," *Mag. Concr. Res.*, vol. 62, no. 11, pp. 831–843, Nov. 2010.
[250] T. D. P. Thao, T. J. S. Johnson, Q. S. Tong, and P. S. Dai, "Implementation of self-healing in concrete – Proof of concept," *IES J. Part Civ. Struct. Eng.*, vol. 2, no. 2, pp. 116–125, May 2009.
[251] T. Nishiwaki, H. Mihashi, B.-K. Jang, and K. Miura, "Development of Self-Healing System for Concrete with Selective Heating around Crack," *J. Adv. Concr. Technol.*, vol. 4, no. 2, pp. 267–275, 2006.
[252] J. W. C. Pang and I. P. Bond, "A hollow fibre reinforced polymer composite encompassing self-healing and enhanced damage visibility," *Compos. Sci. Technol.*, vol. 65, no. 11, pp. 1791–1799, Sep. 2005.
[253] S. Bleay, C. Loader, V. Hawyes, L. Humberstone, and P. Curtis, "A smart repair system for polymer matrix composites," *Compos. Part Appl. Sci. Manuf.*, vol. 32, no. 12, pp. 1767–1776, Dec. 2001.
[254] M Motuku and U K Vaidya and G M Janowski, "Parametric studies on self-repairing approaches for resin infused composites subjected to low velocity impact," *Smart Mater. Struct.*, vol. 8, no. 5, p. 623, 1999.
[255] Carolyn Dry and William McMillan, "Three-part methylmethacrylate adhesive system as an internal delivery system for smart responsive concrete," *Smart Mater. Struct.*, vol. 5, no. 3, p. 297, 1996.
[256] H.-S. S. Li-Li Kan Aaron R. Sakulich, and Victor C. Li, "Self-Healing Characterization of Engineered Cementitious Composite Materials," *Mater. J.*, vol. 107, no. 6, Nov. 2010.
[257] E. Herbert and V. Li, "Self-Healing of Microcracks in Engineered Cementitious Composites (ECC) Under a Natural Environment," *Materials*, vol. 6, no. 7, pp. 2831–2845, Jul. 2013.
[258] M. S. Erdogan Ozbay Mohamed Lachemi, and Hasan Erhan Yucel, "Self-Healing of Microcracks in High-Volume Fly-Ash- Incorporated Engineered Cementitious Composites," *Mater. J.*, vol. 110, no. 1, Jan. 2013.
[259] M. Sahmaran, G. Yildirim, and T. K. Erdem, "Self-healing capability of cementitious composites incorporating different supplementary cementitious materials," *Cem. Concr. Compos.*, vol. 35, no. 1, pp. 89–101, Jan. 2013.
[260] M. Şahmaran, G. Yildirim, E. Ozbay, K. Ahmed, and M. Lachemi, "Self-healing ability of cementitious composites: effect of addition of pre-soaked expanded perlite," *Mag. Concr. Res.*, vol. 66, no. 8, pp. 409–419, Apr. 2014.
[261] G. Yildirim, M. Sahmaran, and H. U. Ahmed, "Influence of Hydrated Lime Addition on the Self-Healing Capability of High-Volume Fly Ash Incorporated Cementitious Composites," *J. Mater. Civ. Eng.*, vol. 27, no. 6, p. 04014187, Jun. 2015.
[262] ASTM C1556, "Standard Test Method for Determining the Apparent Chloride Diffusion Coefficient of Cementitious Mixtures by Bulk Diffusion." ASTM International, 2016.
[263] DIN 1048, "Testing Concrete: Testing of Hardened Concrete (Specimens prepared in mould)." Deutscher Ausschuß für Stahlbeton of the Normenausschuß Bauwesen, 1991.
[264] CSA A23.1-14, "Standard for concrete materials and methods of concrete construction." Canadian Standard Association (CSA), 2014.
[265] ASTM C192 / C192M-15, "Standard Practice for making and Curing Concrete Test Specimens in the Laboratory." ASTM International, 2015.
[266] ASTM C143 / C143M-15a, "Standard Test Method for Slump of Hydraulic-Cement Concrete." ASTM International, 2015.
[267] ASTM C231 / C231M-14, "Standard Test Method for Air Content of Freshly Mixed Concrete by the Pressure Method." ASTM International, 2014.
[268] ASTM C138 / C138M-17a, "Standard Test Method for Density (Unit Weight), Yield, and Air Content (Gravimetric) of Concrete." ASTM International, 2017.
[269] ASTM C1064 / C1064M-12, "Standard Test Method for Temperature of Freshly Mixed Hydraulic-Cement Concrete." ASTM International, 2012.
[270] ASTM C39 / C39M-15a, "Standard Test Method for Compressive Strength of Cylindrical Concrete Specimens." ASTM International, 2015.
[271] M. Ibrahim and M. Issa, "Evaluation of chloride and water penetration in concrete with cement containing limestone and IPA," *Constr. Build. Mater.*, vol. 129, pp. 278–288, Dec. 2016.
[272] E. G. Moffatt, M. D. A. Thomas, and A. Fahim, "Performance of high-volume fly ash concrete in marine environment," *Cem. Concr. Res.*, vol. 102, pp. 127–135, Dec. 2017.
[273] M. M. Khotbehsara, B. M. Miyandehi, F. Naseri, T. Ozbakkaloglu, F. Jafari, and E. Mohseni, "Effect of SnO_2 , ZrO_2 , and $CaCO_3$ nanoparticles on water transport and durability properties of self-compacting mortar

containing fly ash: Experimental observations and ANFIS predictions," *Constr. Build. Mater.*, vol. 158, pp. 823–834, Jan. 2018.
[274] S. A. Bernal, R. Mejía de Gutiérrez, and J. L. Provis, "Engineering and durability properties of concretes based on alkali-activated granulated blast furnace slag/metakaolin blends," *Constr. Build. Mater.*, vol. 33, pp. 99–108, Aug. 2012.
[275] A. A. Ramezanianpour and H. Bahrami Jovein, "Influence of metakaolin as supplementary cementing material on strength and durability of concretes," *Constr. Build. Mater.*, vol. 30, pp. 470–479, May 2012.
[276] M. Khoshroo, A. A. Shirzadi Javid, and A. Katebi, "Effects of micro-nano bubble water and binary mineral admixtures on the mechanical and durability properties of concrete," *Constr. Build. Mater.*, vol. 164, pp. 371–385, Mar. 2018.
[277] R. J. Thomas, E. Ariyachandra, D. Lezama, and S. Peethamparan, "Comparison of chloride permeability methods for Alkali-Activated concrete," *Constr. Build. Mater.*, vol. 165, pp. 104–111, Mar. 2018.
[278] Min-Hong Zhang and Odd E. Gjorv, "Permeability of High-Strength Lightweight Concrete," *Mater. J.*, vol. 88, no. 5, Sep. 1991.
[279] S. E. Hedegaard and T. C. Hansen, "Water permeability of fly ash concretes," *Mater. Struct.*, vol. 25, no. 7, pp. 381–387, Aug. 1992.
[280] J. Zhang and Z. Lounis, "Sensitivity analysis of simplified diffusion-based corrosion initiation model of concrete structures exposed to chlorides," *Cem. Concr. Res.*, vol. 36, no. 7, pp. 1312–1323, Jul. 2006.
[281] A. da Costa, M. Fenaux, J. Fernández, E. Sánchez, and A. Moragues, "Modelling of chloride penetration into non-saturated concrete: Case study application for real marine offshore structures," *Constr. Build. Mater.*, vol. 43, pp. 217–224, Jun. 2013.
[282] A. Neville, "Chloride attack of reinforced concrete: an overview," *Mater. Struct.*, vol. 28, no. 2, p. 63, Mar. 1995.
[283] A. Keulen, Q. L. Yu, S. Zhang, and S. Grünewald, "Effect of admixture on the pore structure refinement and enhanced performance of alkali-activated fly ash-slag concrete," *Constr. Build. Mater.*, vol. 162, pp. 27–36, Feb. 2018.
[284] J. Plank, E. Sakai, C. W. Miao, C. Yu, and J. X. Hong, "Chemical admixtures — Chemistry, applications and their impact on concrete microstructure and durability," *Cem. Concr. Res.*, vol. 78, pp. 81–99, Dec. 2015.
[285] P. Azarsa, R. Gupta, and A. Biparva, "Crystalline Waterproofing Admixtures Effects on Self-healing and Permeability of Concrete," presented at the International Conference on New Horizons in Green Civil Engineering, Victoria, BC, 2018.
[286] ASTM C33, "Standard Specification for Concrete Aggregates." ASTM International, 2016.
[287] R. Polder *et al.*, "Test methods for on site measurement of resistivity of concrete," *Mater. Struct.*, vol. 33, no. 10, pp. 603–611, Dec. 2000.
[288] N. Singh and S. P. Singh, "Carbonation and electrical resistance of self compacting concrete made with recycled concrete aggregates and metakaolin," *Constr. Build. Mater.*, vol. 121, pp. 400–409, Sep. 2016.
[289] S. Wild, J. M. Khatib, and A. Jones, "Relative strength, pozzolanic activity and cement hydration in superplasticised metakaolin concrete," *Cem. Concr. Res.*, vol. 26, no. 10, pp. 1537–1544, Oct. 1996.
[290] R. A. Medeiros-Junior and M. G. Lima, "Electrical resistivity of unsaturated concrete using different types of cement," *Constr. Build. Mater.*, vol. 107, pp. 11–16, Mar. 2016.
[291] P. S. Mangat and B. T. Molloy, "Prediction of long term chloride concentration in concrete," *Mater. Struct.*, vol. 27, no. 6, p. 338, Jul. 1994.
[292] S. H. Magne Maage Ervin Poulsen, Oystein Vennesland, and Jan Erik Carl, "Service Life Prediction of Existing Concrete Structures Exposed to Marine Environment," *Mater. J.*, vol. 93, no. 6, Nov. 1996.
[293] W. McCarter, G. Starrs, and T. Chrisp, "Electrical conductivity, diffusion, and permeability of Portland cement-based mortars," *Cem. Concr. Res.*, vol. 30, no. 9, pp. 1395–1400, Sep. 2000.
[294] Brian B. Hope and Alan K. C. Ip, "Chloride Corrosion Threshold in Concrete," *Mater. J.*, vol. 84, no. 4, Jul. 1987.
[295] P. Vassie, D. Swenson, D. Gregg, K. Vine-Lott, M. Arshad, and K. V.- Lott, "Reinforcement Corrosion and the Durability of Concrete Bridges," *Proc. Inst. Civ. Eng.*, vol. 78, no. 5, pp. 1253–1256, Oct. 1985.

Chapter 8 Appendix A

Figure A8.3 to Figure A8.16 illustrates the HCP mapping of 16 steel reinforced columns in different exposure conditions.

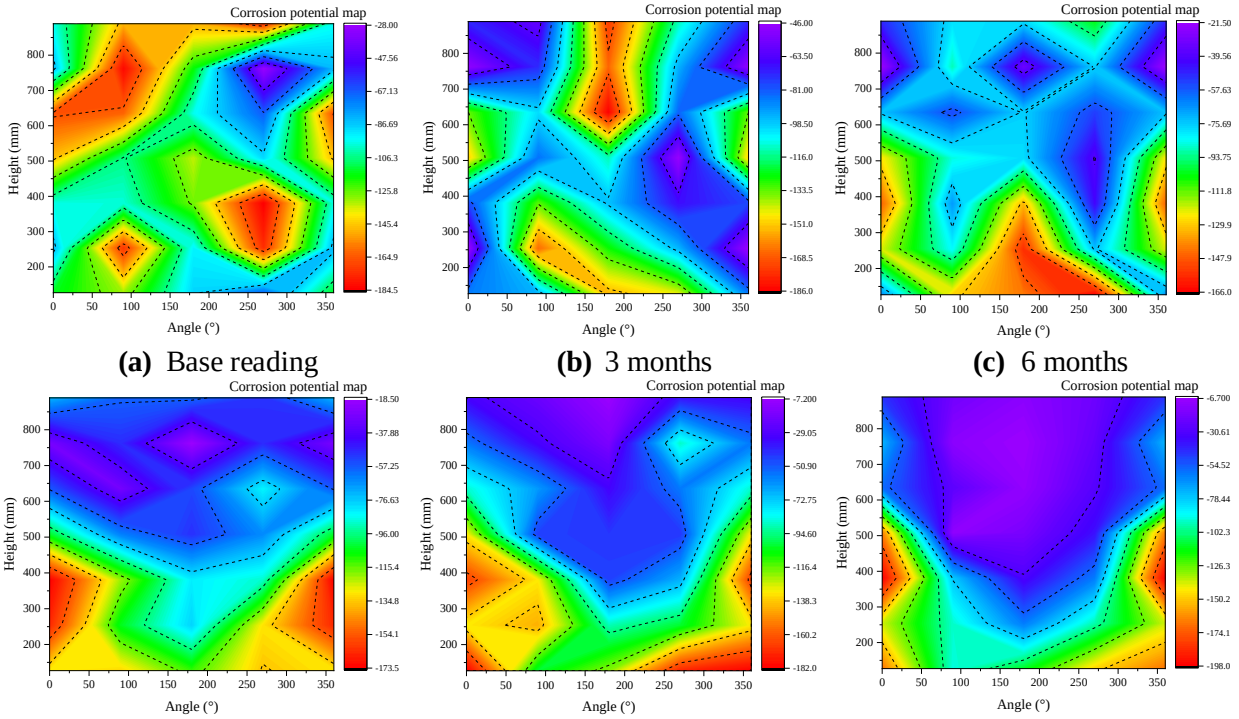

(a) Base reading **(b)** 3 months **(c)** 6 months

(d) 12 months **(e)** 18 months **(f)** 24 months

Figure 8.1. Half-cell corrosion mapping of OP-N(I) column.

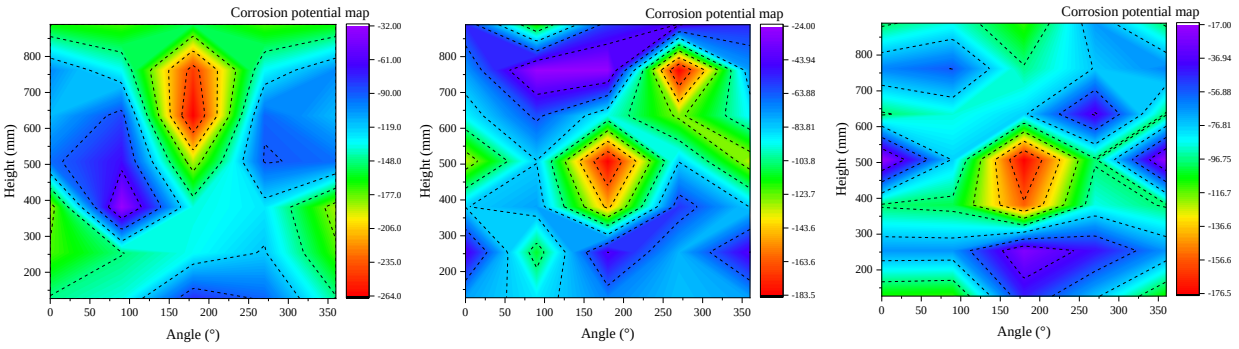

(a) Base reading **(b)** 3 months **(c)** 6 months

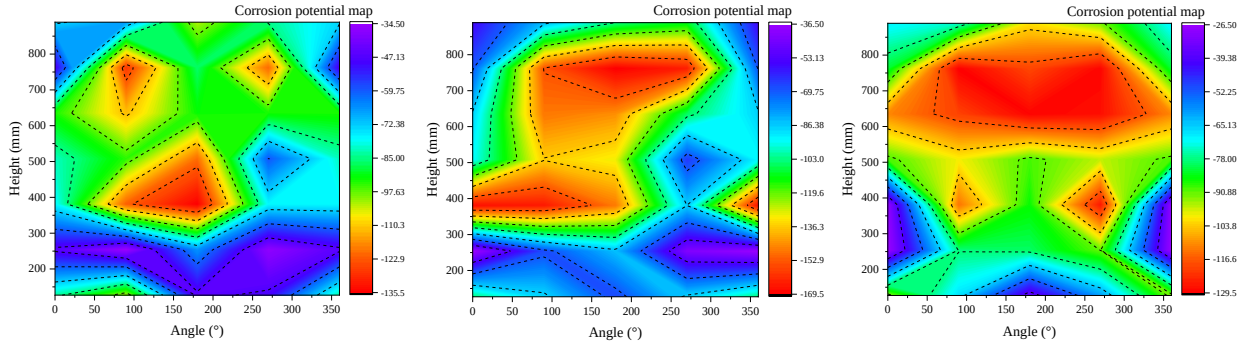

(d) 12 months **(e)** 18 months **(f)** 24 months

Figure A8.2. Half-cell corrosion mapping of OP-N(II) column.

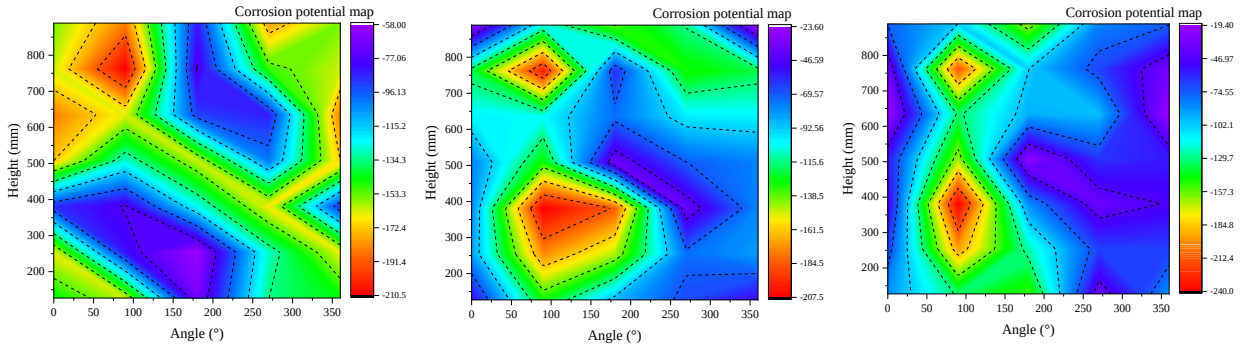

(a) Base reading **(b)** 3 months **(c)** 6 months

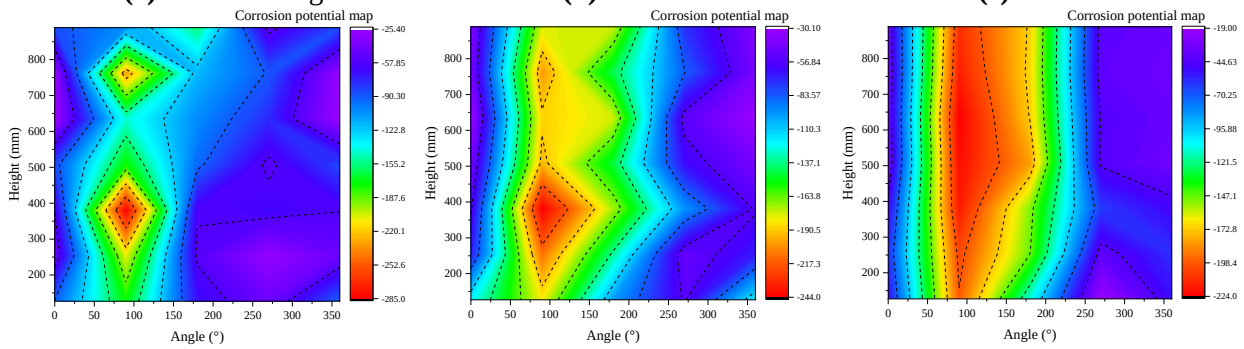

(d) 12 months **(e)** 18 months **(f)** 24 months

Figure A8.3. Half-cell corrosion mapping of OP-C(I) column.

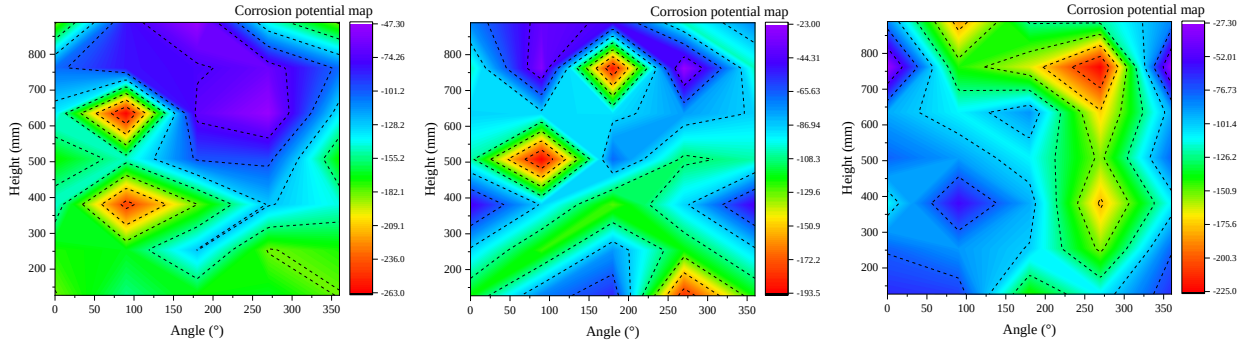

(a) Base reading **(b)** 3 months **(c)** 6 months

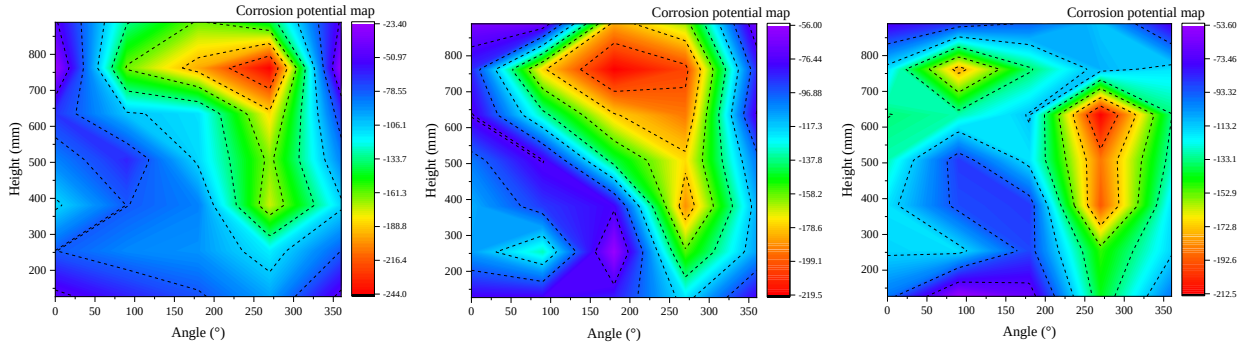

(d) 12 months **(e)** 18 months **(f)** 24 months

Figure 8.4. Half-cell corrosion mapping of OP-C(II) column.

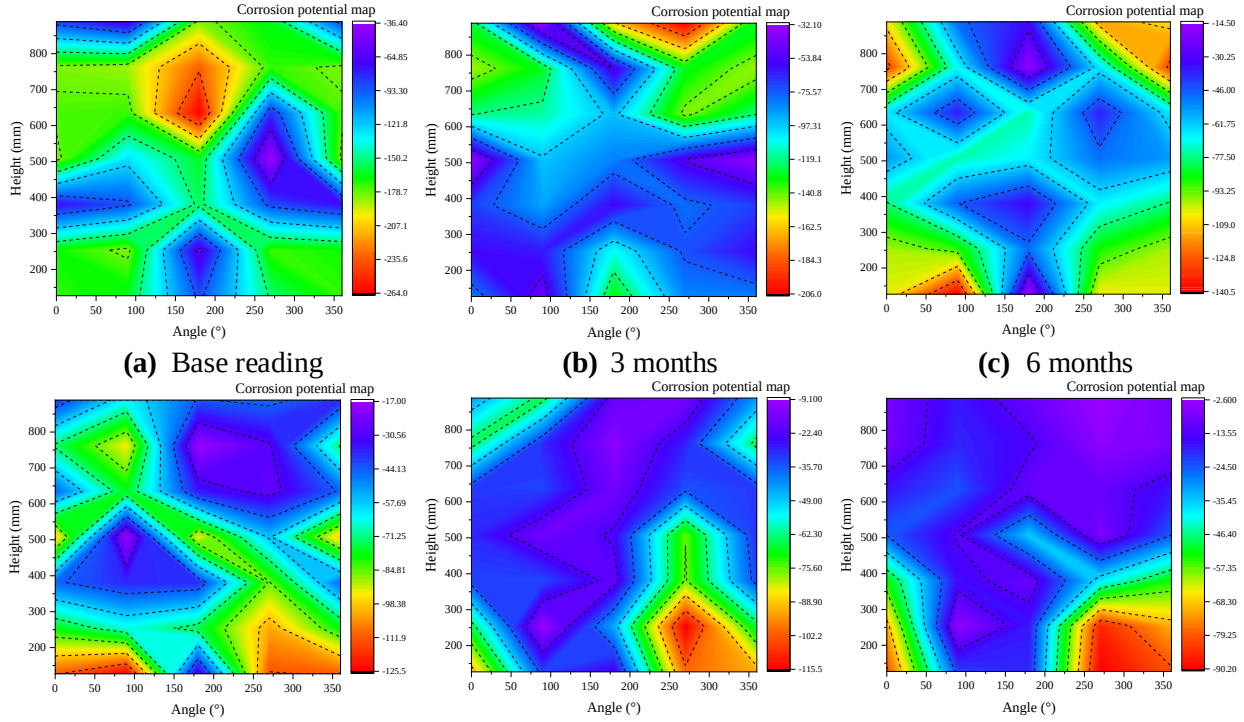

(a) Base reading **(b)** 3 months **(c)** 6 months

(d) 12 months **(e)** 18 months **(f)** 24 months

Figure 8.5. Half-cell corrosion mapping of OP-CA-N(I) column.

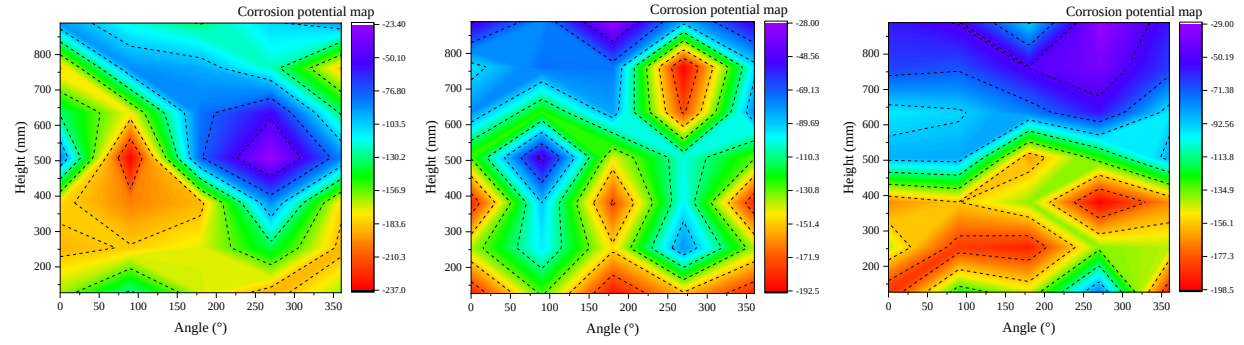

(a) Base reading **(b)** 3 months **(c)** 6 months

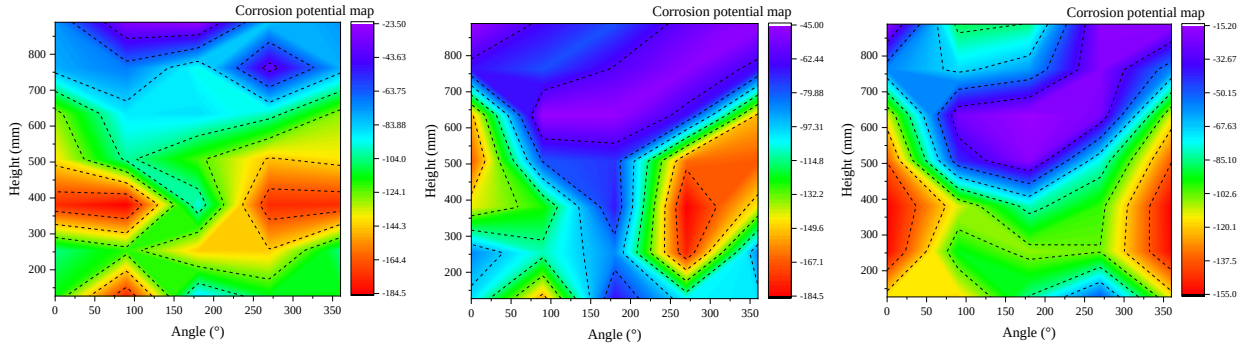

(d) 12 months **(e)** 18 months **(f)** 24 months

Figure A8.6. Half-cell corrosion mapping of OP-CA-N(II) column.

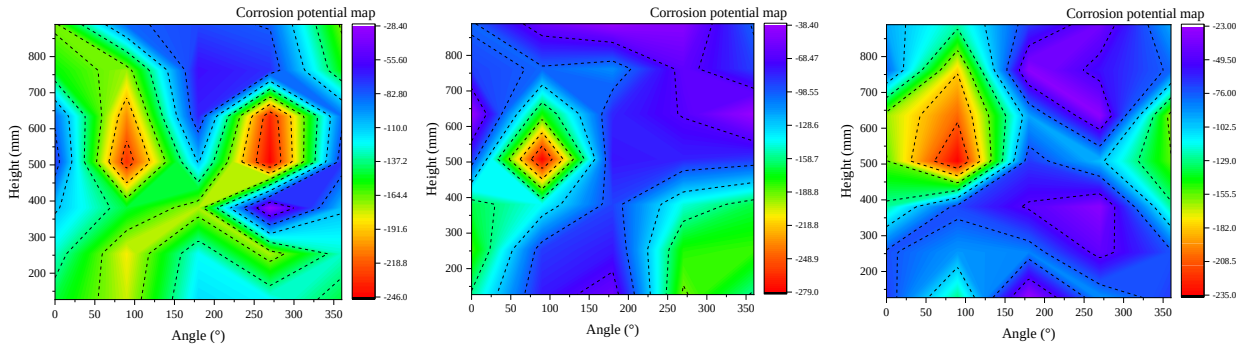

(a) Base reading **(b)** 3 months **(c)** 6 months

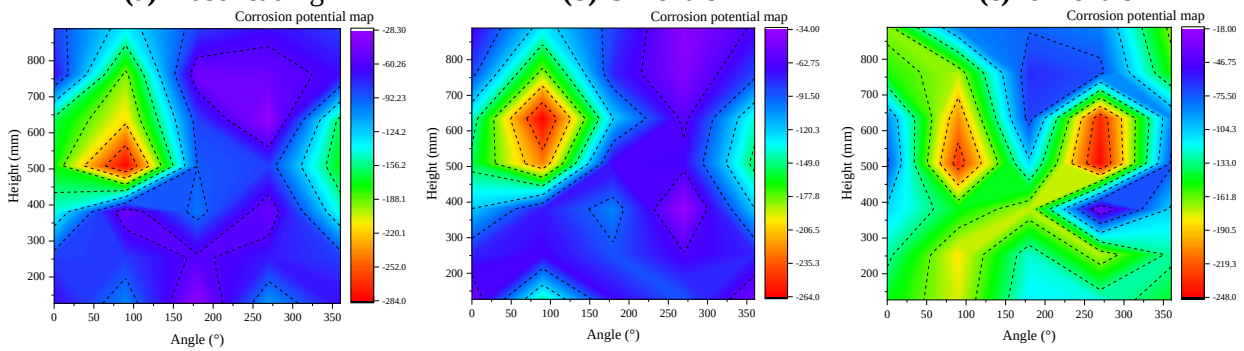

(d) 12 months **(e)** 18 months **(f)** 24 months

Figure A8.7. Half-cell corrosion mapping of OP-CA-C(I) column.

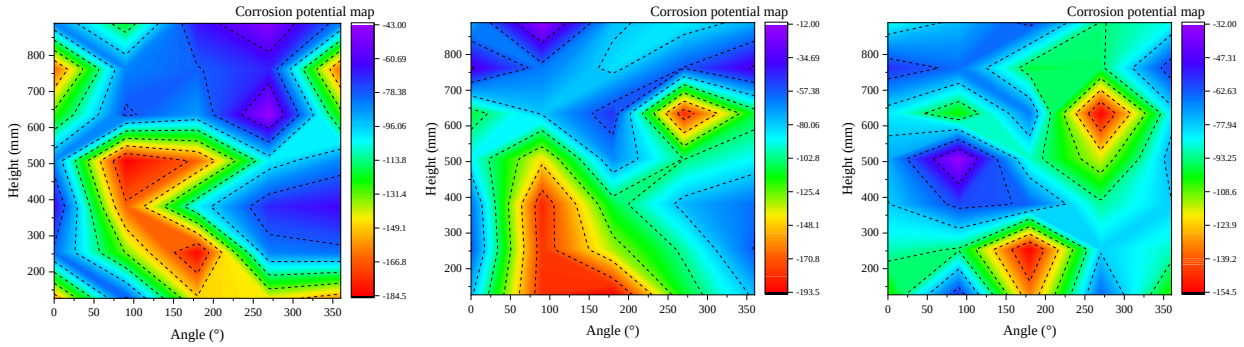

(a) Base reading **(b)** 3 months **(c)** 6 months

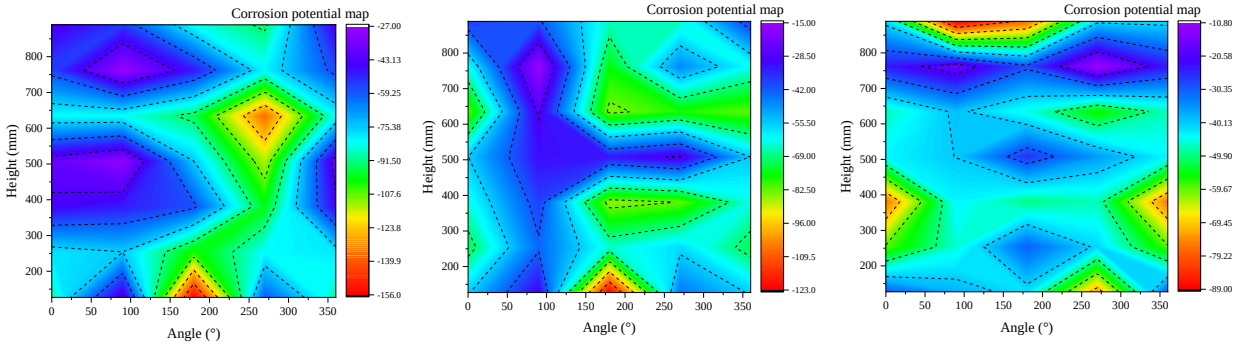

(d) 12 months **(e)** 18 months **(f)** 24 months

Figure A8.8. Half-cell corrosion mapping of OP-CA-C(II) column.

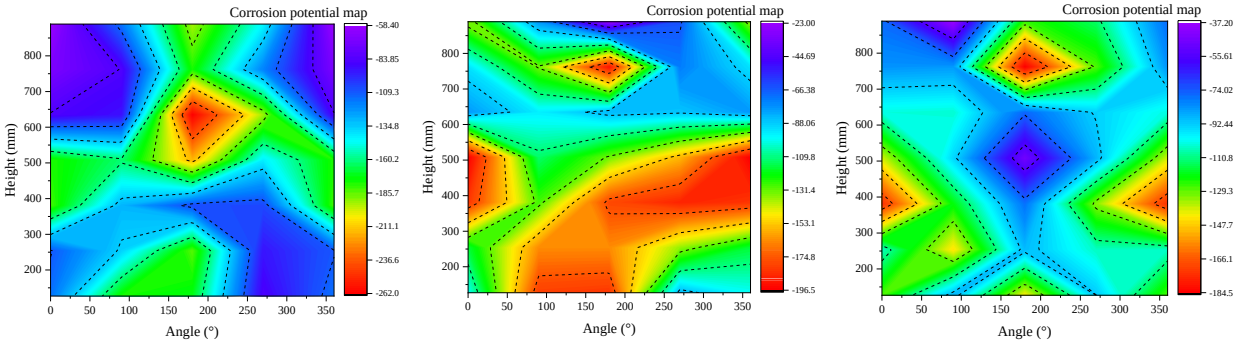

(a) Base reading **(b)** 3 months **(c)** 6 months

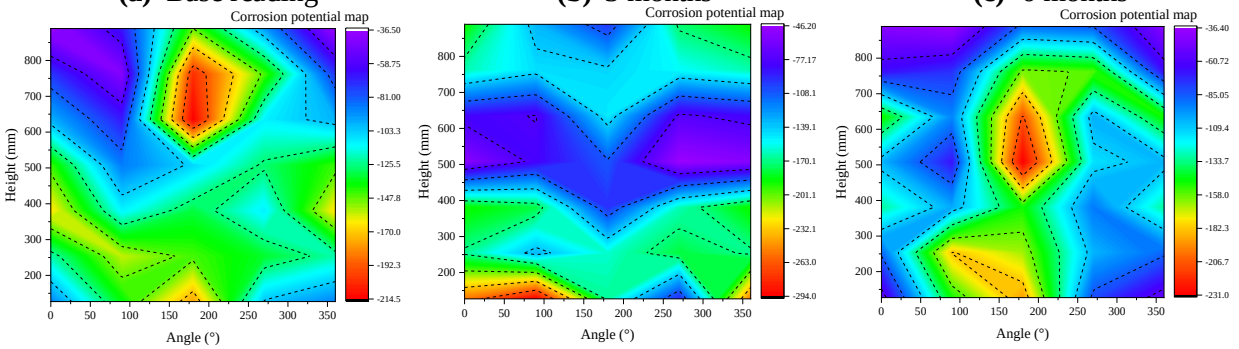

(d) 12 months **(e)** 18 months **(f)** 24 months

Figure 8.9. Half-cell corrosion mapping of PL-N(I) column.

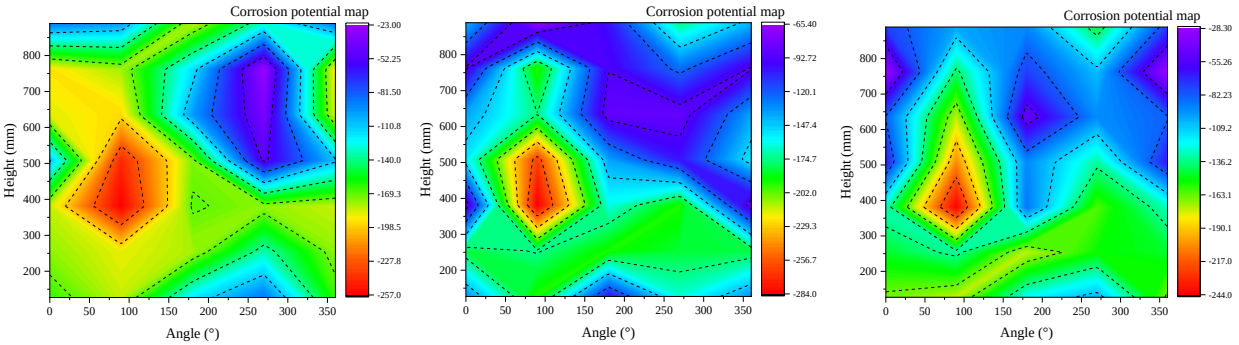

(a) Base reading **(b)** 3 months **(c)** 6 months

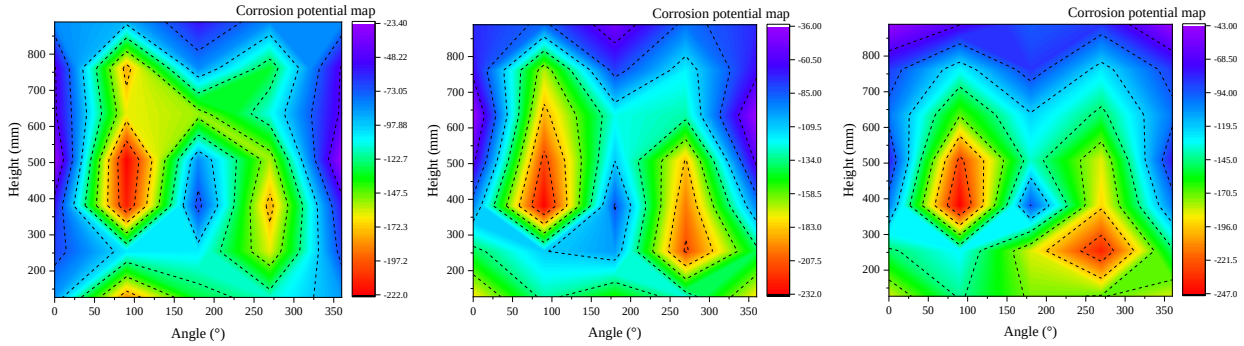

(d) 12 months **(e)** 18 months **(f)** 24 months

Figure 8.10. Half-cell corrosion mapping of PL-N(II) column.

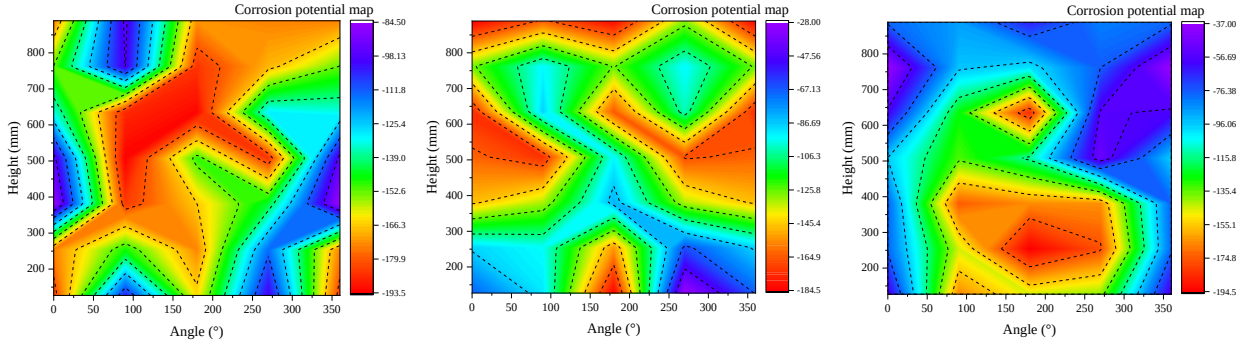

(a) Base reading **(b)** 3 months **(c)** 6 months

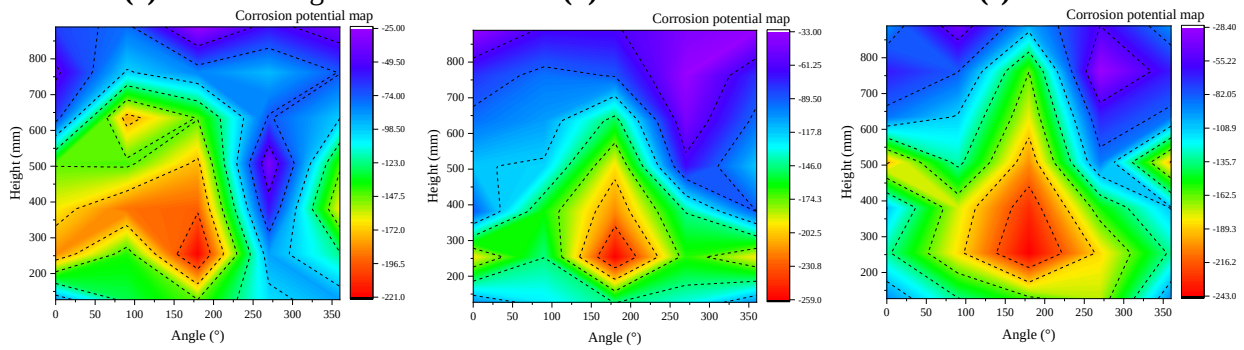

(d) 12 months **(e)** 18 months **(f)** 24 months

Figure A8.11. Half-cell corrosion mapping of PL-C(I) column.

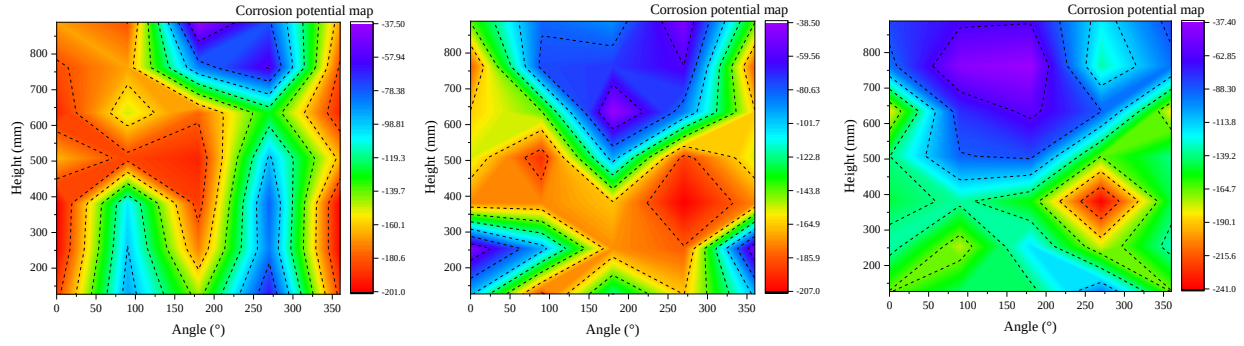

(a) Base reading **(b)** 3 months **(c)** 6 months

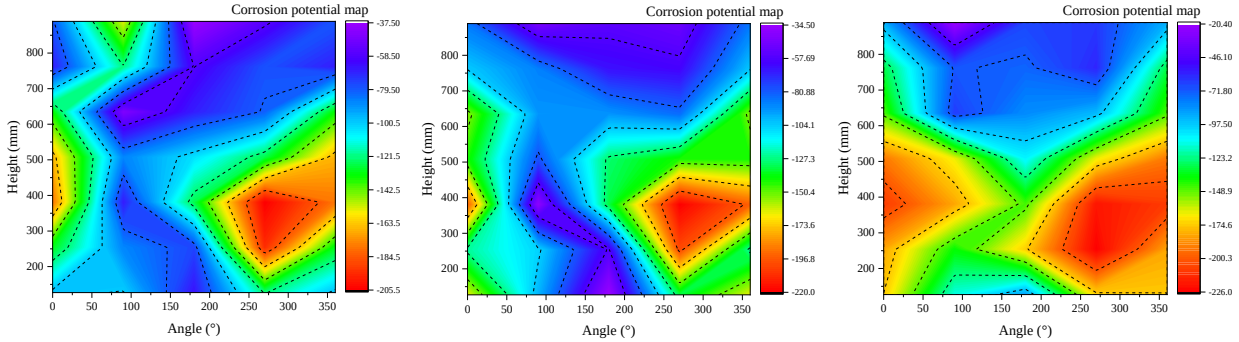

(d) 12 months **(e)** 18 months **(f)** 24 months

Figure A8.12. Half-cell corrosion mapping of PL-C(II) column.

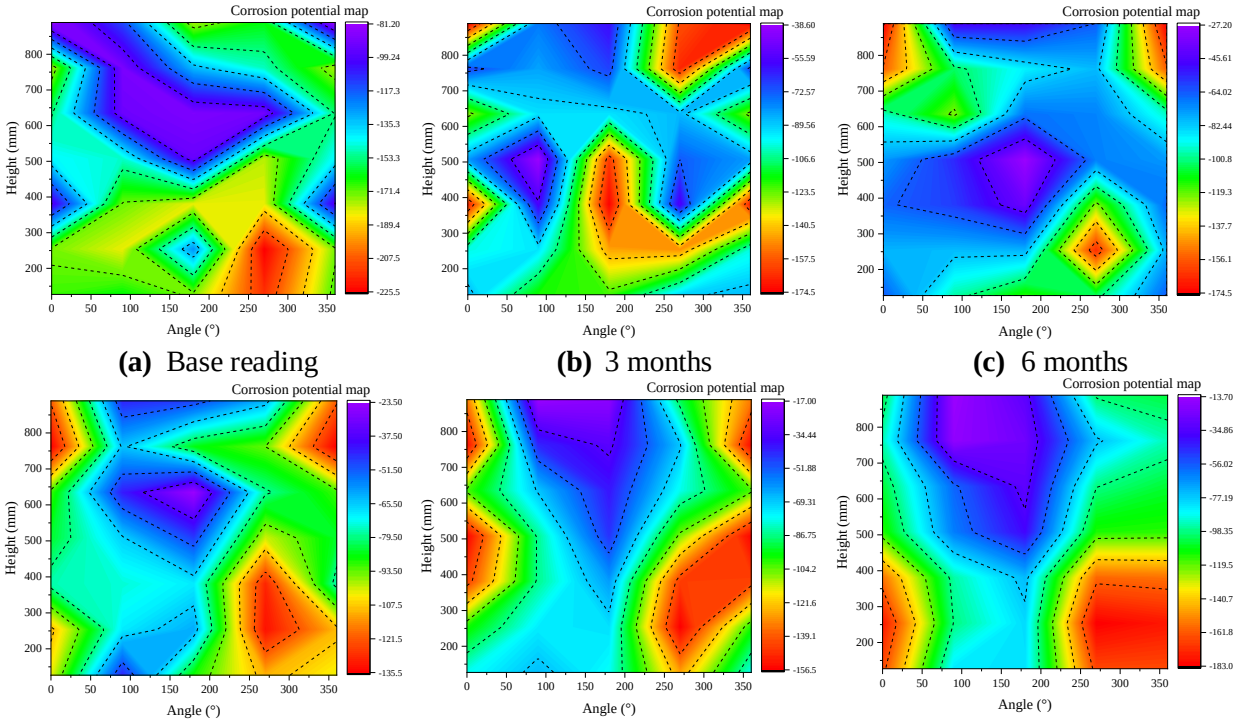

(a) Base reading **(b)** 3 months **(c)** 6 months

(d) 12 months **(e)** 18 months **(f)** 24 months

Figure A8.13. Half-cell corrosion mapping of PL-CA-N(I) column.

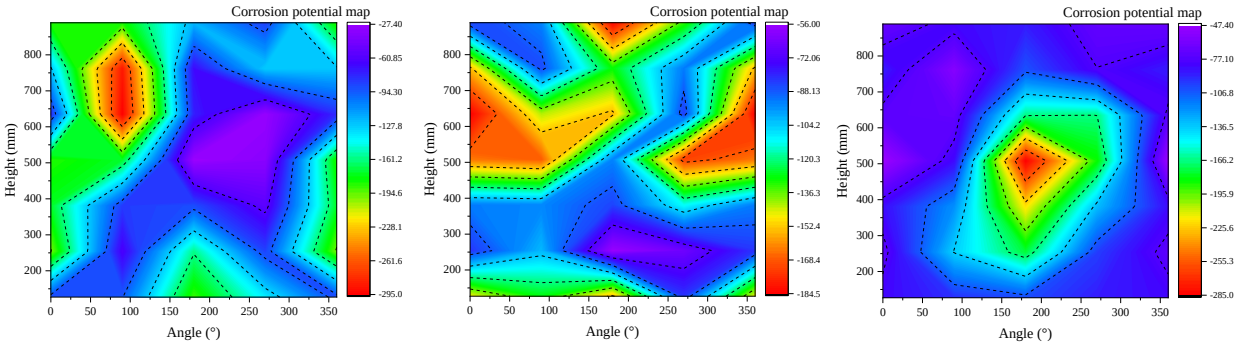

(a) Base reading **(b)** 3 months **(c)** 6 months

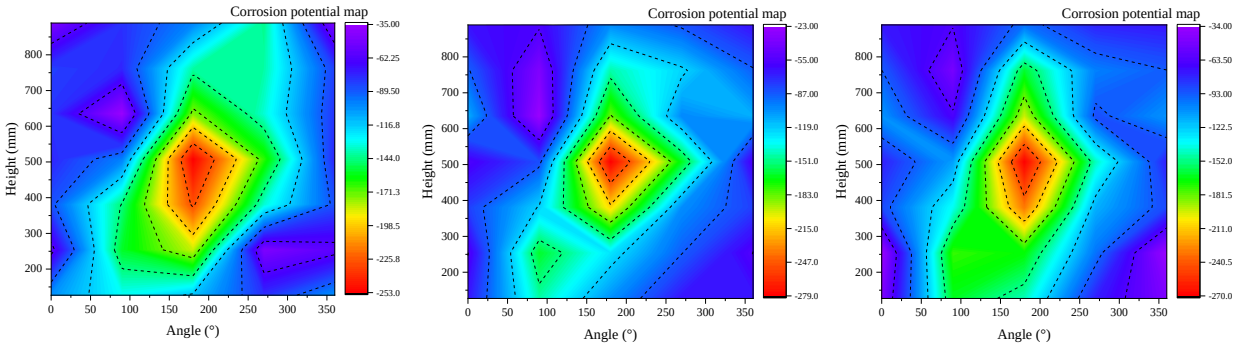

(d) 12 months **(e)** 18 months **(f)** 24 months

Figure A8.14. Half-cell corrosion mapping of PL-CA-N(II) column.

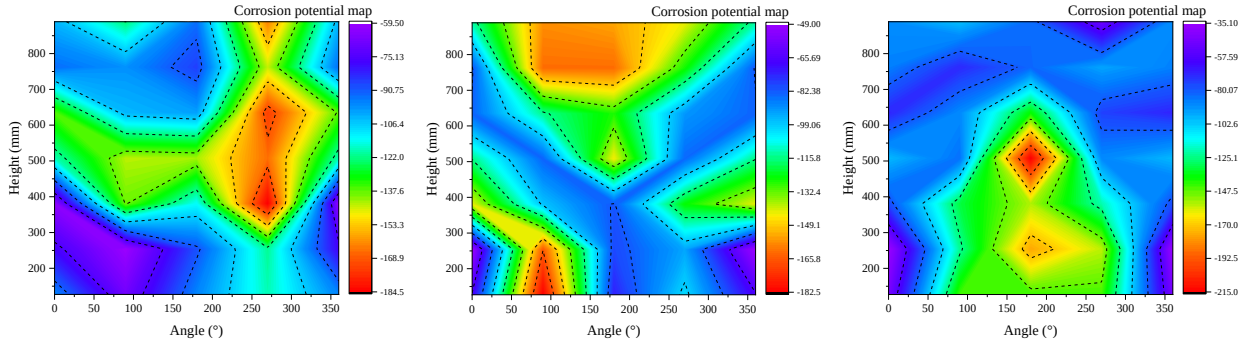

(a) Base reading **(b)** 3 months **(c)** 6 months

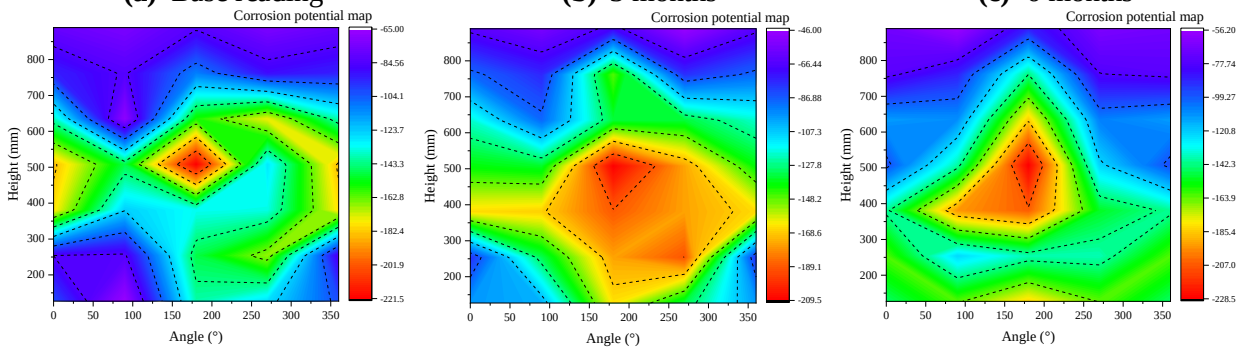

(d) 12 months **(e)** 18 months **(f)** 24 months

Figure A8.15. Half-cell corrosion mapping of PL-CA-C(I) column.

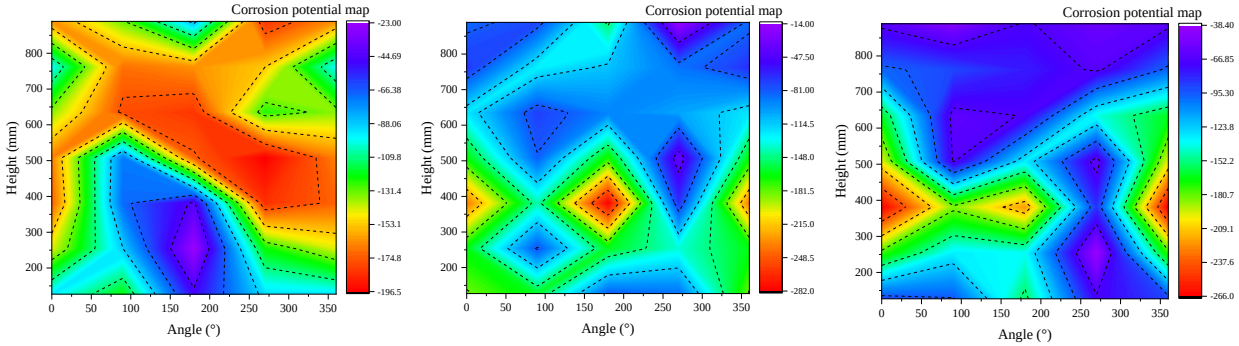

(a) Base reading **(b)** 3 months **(c)** 6 months

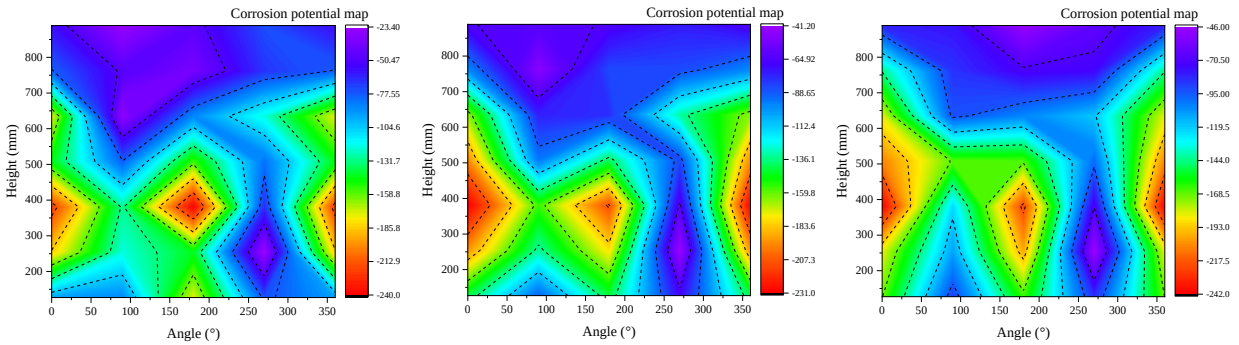

(d) 12 months **(e)** 18 months **(f)** 24 months

Figure A8.16. Half-cell corrosion mapping of PL-CA-C(II) column.

Figure A8.17-Figure 8.19 illustrate the normalized resistivity data of steel reinforced columns for three groups (OPC-CA, PLC, and PLC-CA groups) in different exposure conditions.

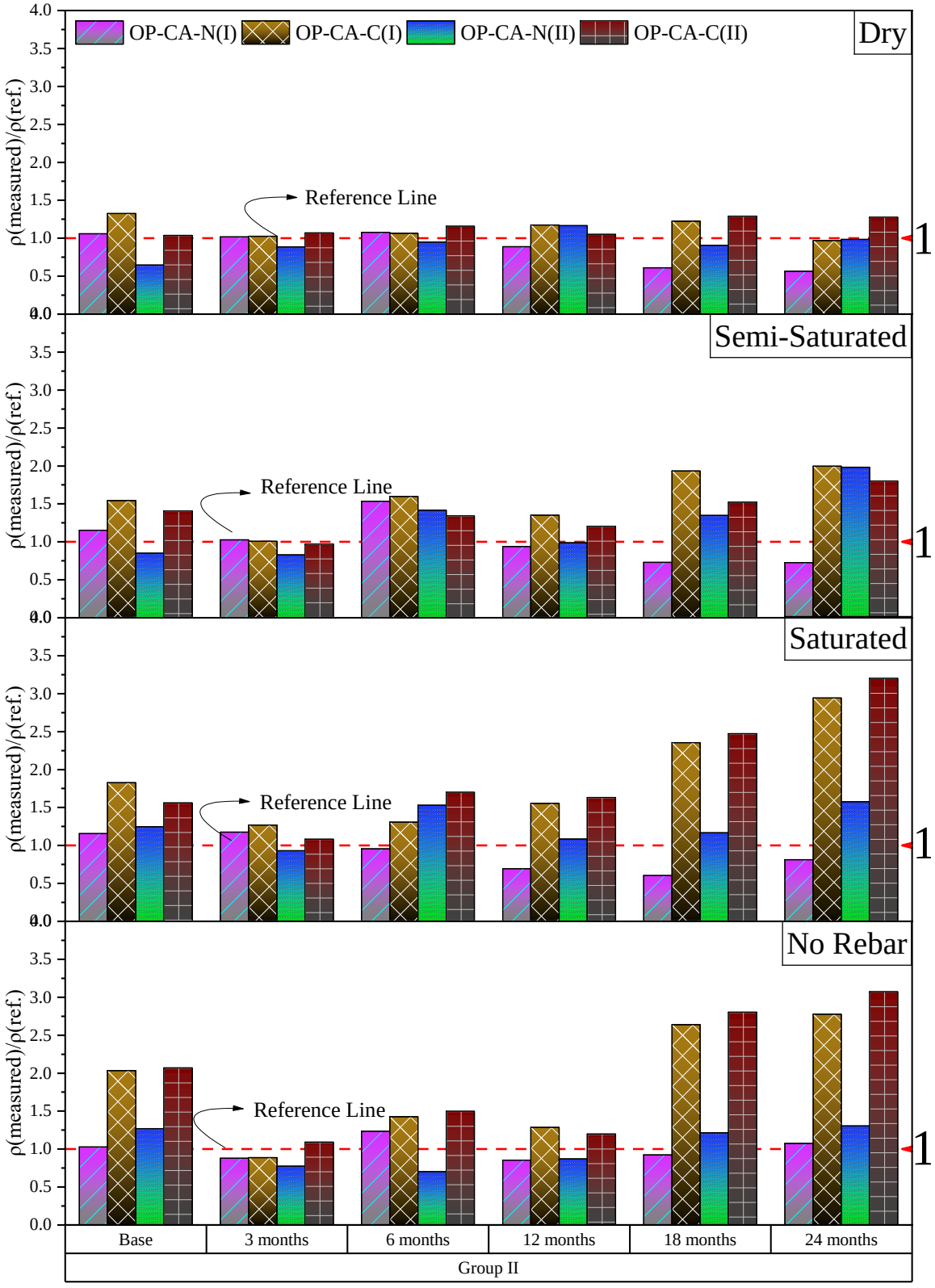

Figure A8.17. Normalized electrical resistivity of group II columns (OPC group with CA).

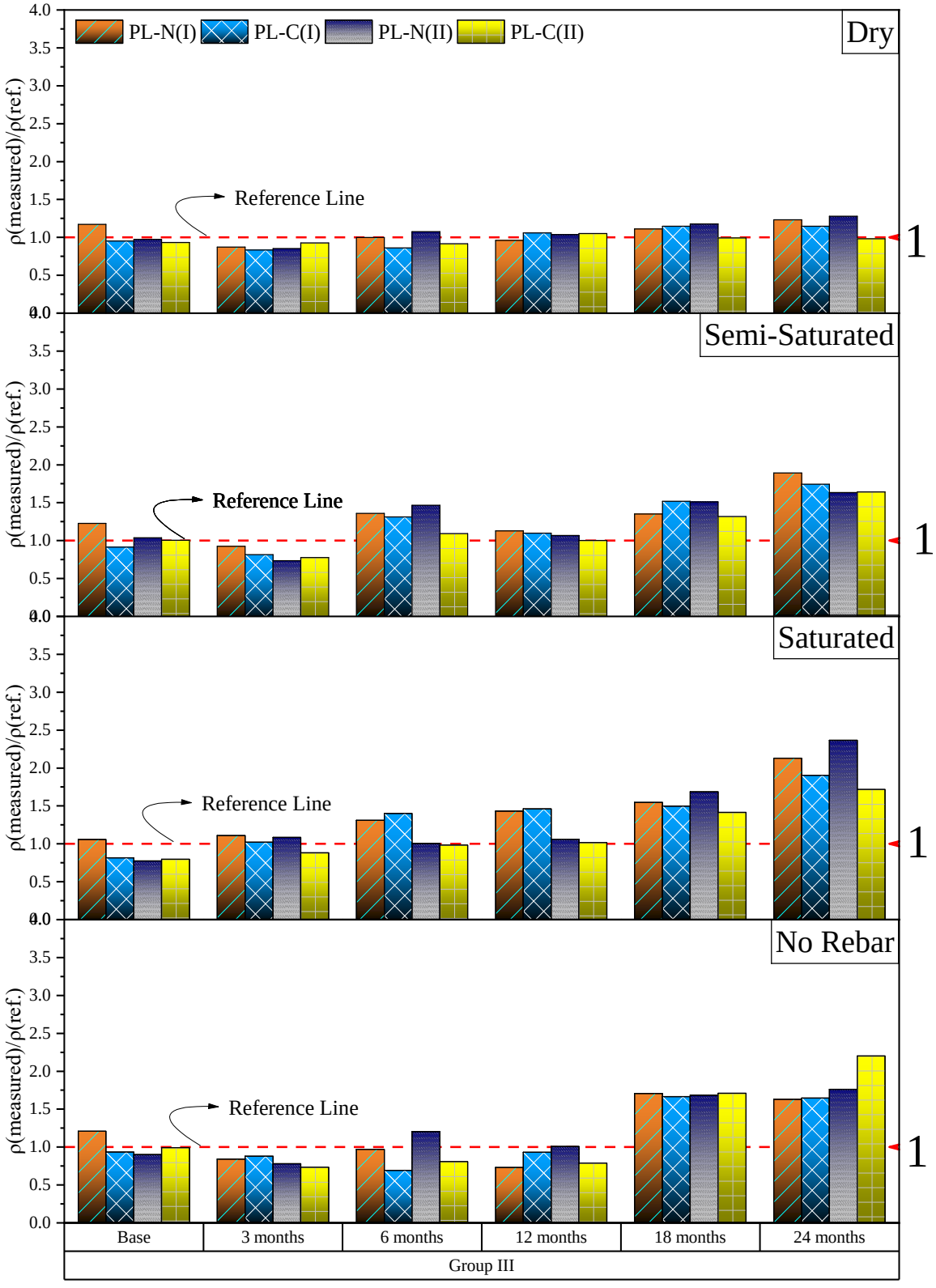

Figure A8.18. Normalized electrical resistivity of group III columns (PLC group without CA).

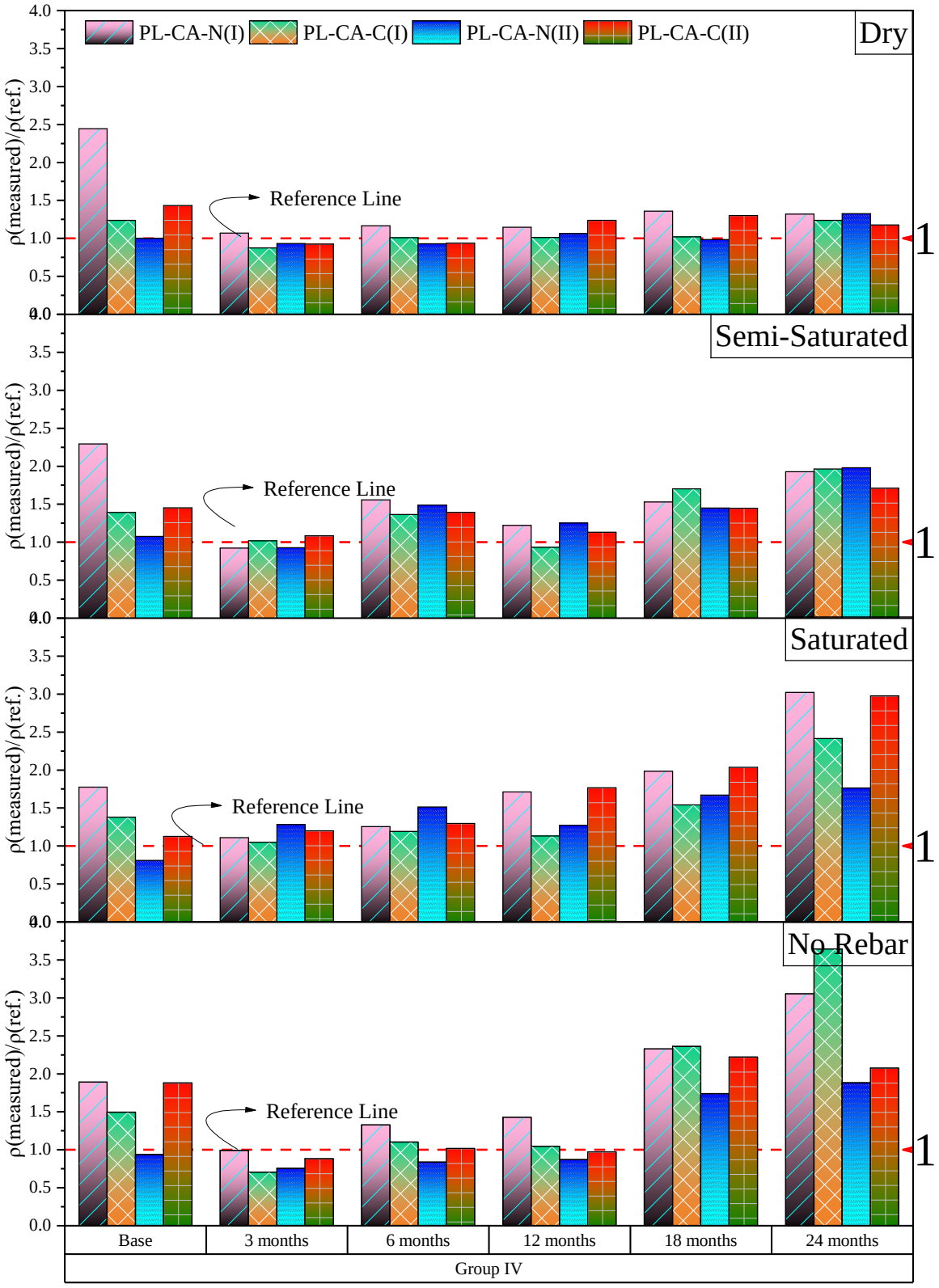

Figure 8.19. Normalized electrical resistivity of group IV columns (PLC group with CA).